Additive Manufacturing of Soft, Functional Structures for Next-Generation Soft Robotics

BY

DJEN TIMO KÜHNEL

A dissertation submitted to the University of Bristol in accordance with the requirements for award of the degree of DOCTOR OF PHILOSOPHY in the Faculty of Engineering.

JUNE 2019

Word count: seventy-seven thousand five hundred

Abstract

Soft electroactive structures like dielectric elastomers (DEs) show great potential for many applications in soft robotics or wearable devices. However, high-quality fabrication of soft devices, and particularly DEAs, remains a great challenge both in terms of materials and manufacturing methods. Many different fabrication techniques have been developed but these are often very time- and labour intensive or require very expensive, specialised equipment that is not accessible to every researcher or company interested in this technology. In this thesis, novel, low-cost materials and manufacturing methods for soft, functional structures are explored.

A method to fabricate patterned, stretchable electrodes for DE actuators (DEAs) from laser-scribed graphene oxide (LSGO) is proposed. The method uses a simple drop casting technique and a low-cost laser engraver to produce arbitrary electrode patterns with 100 µm resolution. LSGO has previously been used in various electronic devices but never to produce stretchable electrodes for soft actuators. LSGO DEAs are shown to have similar performance compared to DEAs made by more conventional methods.

To move towards fully automated fabrication of soft 3D structures, a novel 3D printing technique is proposed. This technique, called Laser-Assisted Multi-material Direct-write Assembly (LAMDA), combines simple direct ink writing and laser scribing into one integrated process. Laser scribing is used to alter the chemical composition and properties of the deposited materials. This allows fabrication of multi-material structures without the need for multi-material deposition, making the required 3D printer hardware very simple and affordable (~£1000). The LAMDA process is capable of producing electrically conductive layers and traces throughout the printed part. It can also incorporate layer separations for inflatable cavities. This technique could pave the way for easier fabrication and prototyping of DE devices and might enable completely new shapes and functionality that would not be accessible by conventional manufacturing methods.

Author's declaration

I declare that the work in this dissertation was carried out in accordance with the requirements of the University's *Regulations and Code of Practice for Research Degree Programmes* and that it has not been submitted for any other academic award. Except where indicated by specific reference in the text, the work is the candidate's own work. Work done in collaboration with, or with the assistance of, others, is indicated as such. Any views expressed in the dissertation are those of the author.

SIGNED: ..... DATE: .....

Acknowledgements

First of all, I want to thank my supervisors Prof. Charl FJ Faul and Prof. Jonathan Rossiter for their invaluable encouragements, inspiring discussions and brilliant ideas they contributed over the course of this work, as well as many helpful comments and suggestions on my writing. Of course, my thanks also go to EPSRC and everyone involved with the FARSCOPE CDT for making this project possible in the first place.

I want to thank my many great colleagues and friends in the Faul Group, in the Soft Robotics Group, and on the FARSCOPE CDT for countless interesting conversations, helpful ideas and moral support over the years. Specifically, I wish to thank Thekla, Alix, Hatem, Chanelle, Ben, Anouk, Tom, and Luke who all helped me greatly by proofreading parts of my thesis and providing many helpful comments. Special thanks go to my good friend Jay for also proofreading a chapter of my thesis, for many valuable, helpful, in-depth discussions about my research and about life in general, and for making my time in Bristol such a great experience altogether. My thank also go to my amazing (former) housemates James, Chris, Stephen, Esther, Marco, Diego, Bhargavi and Faegheh who really made me feel at home in Bristol and enjoy my time here.

Lastly, I want to thank my parents and my sister for their great support over the years, particularly in the final stages, and of course my girlfriend Sabrina for her love, her encouragements, her patience, and for putting up with me and taking good care of me during the tougher parts of my writeup.

Table of contents

List of figures

List of tables

List of publications

Peer-reviewed journal articles:

Kühnel, D. T., Helps, T. & Rossiter, J. **Kinematic Analysis of VibroBot: A Soft, Hopping Robot with Stiffness- and Shape-Changing Abilities.** *Front. Robot. AI* **3**, 60 (2016).

Contributions: DK and TH contributed in equal parts to the design and construction of the robot, acquisition and evaluation of experimental data, and writing of the article. JR helped in developing fundamental locomotion concepts, provided general project guidance, and reviewed written content.

Kuhnel, D. T., Rossiter, J. M. & Faul, C. F. J. **Laser-Scribed Graphene Oxide Electrodes for Soft Electroactive Devices.** *Adv. Mater. Technol.* **4**, 1800232 (2019).

Contributions: Development and refinement of the laser scribing process, fabrication and testing of laser-scribed samples, analysis of experimental data, and writing of the article were performed by DK. JR and CF helped to develop the fundamental concept of the laser scribing process, provided general project guidance and reviewed written content.

Conference proceedings:

Kuhnel, D. T., Rossiter, J. M. & Faul, C. F. J. **3D printing with light: Towards additive manufacturing of soft, electroactive structures.** in *Proceedings of SPIE - The International Society for Optical Engineering* **10594**, (2018).

Contributions: Design and construction of the 3D printer, development of the laser scribing process for silicone rubber, fabrication and testing of samples, analysis of experimental data, and writing of the article were performed by DK. JR and CF helped to develop fundamental concepts, provided general project guidance and reviewed written content.

List of abbreviations

- 2D: two-dimensional
- 3D: three-dimensional
- AgNW: silver nanowire
- AM: additive manufacturing
- CAD: computer-aided design
- CB: carbon black
- CG: carbon grease
- CNT: carbon nanotube
- DE: dielectric elastomer
- DI: de-ionised
- DEA: dielectric elastomer actuator
- DIW: direct ink writing
- DLP: digital light processing
- DLZ: dielectrophoretic liquid zipping
- DoD: drop on demand
- EA: electroadhesion
- EDX: energy-dispersive X-ray spectroscopy
- FDM: fused deposition modelling
- FFF: fused filament fabrication
- FTIR: Fourier-transform infrared spectroscopy
- GO: graphene oxide
- HV: high voltage
- LAA: L-ascorbic acid
- LAMDA: laser-assisted multi-material direct-write assembly
- LIG: laser-induced graphene
- LSGO: laser-scribed graphene oxide
- LSSR: laser-scribed silicone rubber
- LV: low voltage
- PCP: progressive cavity pump
- PDMS: polydimethylsiloxane
- PMMA: polymethyl methacrylate
- PU: polyurethane
- PWM: pulse width modulation
- rGO: reduced graphene oxide
- RMS: root mean square

- RMSE: root mean square error
- ROI: region of interest
- S3D: Simplify3D (software)
- SEM: scanning electron microscopy
- SMA: shape memory alloy
- SMD: surface-mount device
- SWCNT: single-wall carbon nanotube
- TCR: triblock copolymer rubber
- TG: thermogravimetry
- TPU: thermoplastic polyurethane
- UoB: University of Bristol
- VHB: “Very High Bond” – a brand of adhesive tapes from 3M

Chapter 1

Introduction

1.1. Background and motivation

For many decades now, even before robots started to take over much of our industrial manufacturing, people have been dreaming of robots that assist us in our daily lives, do chores at home, help out at work, and can follow us anywhere we go.[1] Alas, even in 2019, one struggles to find any robots outside of factories and research laboratories. The problem, which early robotics enthusiasts have always greatly underestimated, is that robots as we have come to know them – with rigid limbs, made of metal, and driven by electric motors – do not operate well in uncontrolled and uncertain environments with unpredictable agents like humans walking around.[2] Probably the biggest concern, which in industrial robotics has always been avoided rather than solved, is safety. A heavy, rigid metal robot, which has tremendous strength but lacks such things as perception of its surroundings and situational awareness, can be a serious danger to a human operating in the same environment.[3] This is why robots and people have been kept strictly separated in the past. To change this, a new approach is necessary. We are currently on the verge of a great paradigm shift in robotics that will bring us a new generation of robots which are nothing like their bulky metal ancestors and much more like us, like most living things: soft.[4,5]

1.1.1. Soft robotics

Humans and animals largely consist of soft tissues. It is, to a large extent, this softness that allows us to walk on uneven terrain, securely grasp delicate objects and interact with each other safely. These are all tasks that traditional robots still struggle with today. But a new generation of soft robots might soon be able to overcome these

challenges.[5] The emerging field of soft robotics is about embracing the complexity of soft bodies with many redundant degrees of freedom in order to exploit their inherent safety, robustness, and their ability to react "intelligently" to external stimuli without cognition or active control.[6]

Increased safety arises naturally from the use of soft, lightweight materials. A robot that is lightweight and inherently compliant moves with less kinetic energy and will yield to external forces, like when encountering an unexpected obstacle. In case of an accident, such a robot is much less likely to cause serious damage or injury. Softness is always desirable where robots operate near, in contact with, or perhaps even inside humans. It is not only safer but also much more natural for us to interact with something that feels soft and organic and can conform to our bodies, which are largely soft themselves.[7]

A soft body also makes robots more robust to unknown, uncertain environments. A compliant body can react, even without sensors or active control, to stimuli from the environment, deforming around objects or conforming to uneven terrain.[8] This robustness is crucial for robots to operate safely and effectively in unstructured, chaotic environments with humans and other unpredictable agents present.

There are still a great many challenges to overcome before we see soft robots on our streets and in our homes, but their fundamental advantages over traditional, rigid robots give soft robotics the great potential to bring robots out of our factories and into our daily lives.

1.1.2. Artificial muscles

One of the key enabling technologies for soft robotics are lightweight and inherently compliant actuators, so-called artificial muscles.[9] An artificial muscle is a material or structure that deforms mechanically in response to some (non-mechanical) stimulus. It does not necessarily mimic the structure or functioning principle of biological muscles. There are different types of artificial muscles that work by very different principles. They each have their distinct advantages and disadvantages and tend to be suited for different applications (see Section 2.2). Probably the most widely used artificial muscles today are pneumatic actuators (Section 2.2.1). These are made

entirely of soft materials and can generate complex movement and substantial force output. Another promising artificial muscle technology are dielectric elastomer actuators (DEAs, see Section 2.2.3). DEAs combine almost all the desirable properties for an artificial muscle.[10] They are completely soft and made of lightweight polymer materials. They have high energy and power densities and fast response time, allowing operation over a broad range of frequencies, up to several kilohertz. Their operation is completely silent and very smooth, giving them an incredibly convincing organic look and feel. Despite their many favourable properties, DEAs have not yet found very widespread use in soft robotics. One reason for this is the high voltage required for actuation, which is typically in the range of 1 to 10 kV. Such high voltages raise safety concerns and make the driving electronics bulky and expensive. The second major limiting factor for widespread DEA adoption is materials and manufacturing. DEAs consist of alternating thin layers of conductive and insulating elastic materials. There are not many materials available with the required properties, particularly elastic, conductive materials (see Section 2.3). The layers must also be very thin with low variation, requiring very precise manufacturing. Simple DEAs can easily be made by hand but for most practical applications, stacked actuators made up of many DEA layers are required, making fabrication difficult without highly specialised equipment.

Artificial muscles such as soft pneumatic actuators and DEAs as well as the bodies of soft robots are, for the most part, made of elastomers such as silicone rubber. To achieve a particular response or actuation, these materials need to be made into complex shapes and intricate multi-material structures which can be difficult to manufacture by traditional methods. New fabrication techniques for elastomer materials, including functional materials such as conductive rubbers, could therefore greatly benefit the field of soft robotics.

1.1.3. Manufacturing of soft structures and actuators

To enable a new generation of soft robotics, sophisticated manufacturing methods for soft structures are required. Unfortunately, processing techniques for soft materials are still very limited compared to more traditional engineering materials such as metals and plastics. Casting with liquid silicone rubber is probably the most common method to make soft robot parts. Unfortunately, certain geometries or multi-material

structures are very difficult or even impossible to produce in a casting process. E.g., hollow structures for pneumatic actuators must be cast in a two-step process which is very time-consuming. In addition, casting always requires pre-fabricated moulds which means that each alteration to a part's design requires a new mould to be made.

3D printing has emerged in recent years as an incredibly valuable tool for prototyping and small-scale manufacturing. It allows automated fabrication of almost arbitrary shapes and geometries with great detail and high complexity. No part-specific, prefabricated moulds are required which reduces the time and cost of manufacturing, particularly for bespoke parts and prototypes. Many soft robotics researchers already use 3D printing with rigid materials to fabricate moulds for casting soft parts. Direct 3D printing of soft structures could greatly accelerate the process and increase design flexibility.

In addition to faster prototyping, 3D printing could even enable completely new structures that would not be possible to manufacture by any other method. Multi-material printing in particular can enable the fabrication of functional parts with intricate internal structures and embedded functionality. Some very impressive examples of entirely soft, muscular structures can be found in nature, such as arms of an octopus, tentacles of a squid, trunk of an elephant, or the tongues of mammals and reptiles. All of these structures can display amazing dexterity and delicate manipulation while also being able to exert substantial forces. These capabilities are enabled by a complex arrangement of interacting groups of muscles,[11] as shown in Figure 1 on the example of an elephant trunk. Assembling such a structure from prefabricated units, such as the DEA stack modules that can currently be mass-manufactured,[12] would be impossible. In contrast, a sophisticated 3D printer capable of printing artificial muscles could deposit them in any arbitrary arrangement, allowing us to make structures of similar complexity as natural systems like the elephant trunk. This might finally allow our robots to match the astounding capabilities of their organic counterparts.

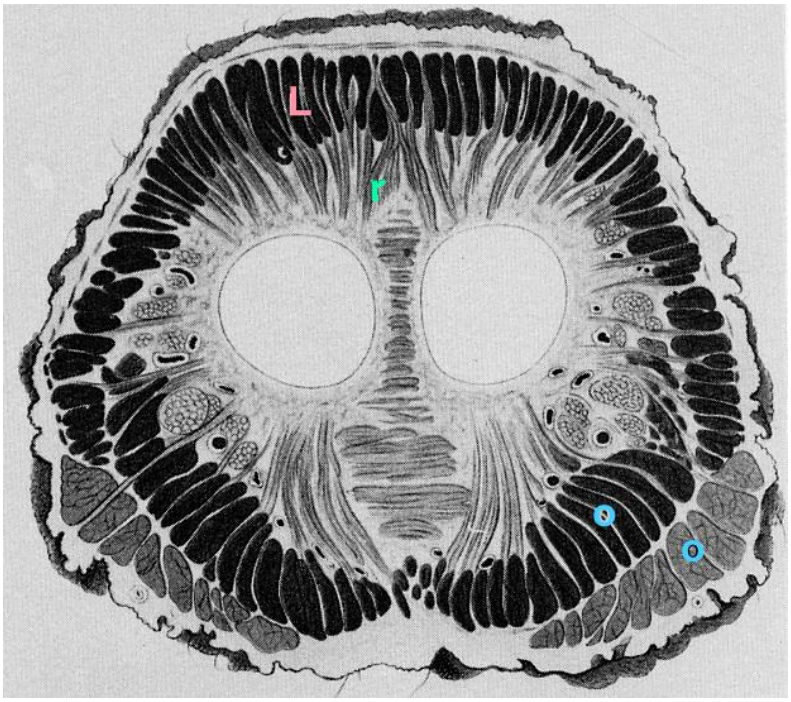

Figure 1. Schematic cross-section of an elephant trunk showing muscle arrangement. Radial muscles (r) are arranged between bundles of longitudinal muscles (L). Two groups of oblique muscles (o) with opposite handedness provide torsional motion in both directions. (modified from [11])

Unfortunately, most current 3D printing techniques are not able to process high-performance elastomers such as silicone rubber. Some elastic materials for common 3D printing platforms are available, but their properties generally fall short of what is required in soft robotics applications (see Section 2.3). 3D printing with silicone rubber and other soft, functional materials is possible, but so far only with highly-expensive laboratory-grade 3D printers (see Section 2.4) which most people, including most researchers, do not have access to. Some experimental, low-cost printing platforms have been developed that allow printing with soft materials, but these are often difficult to use and limited in their capabilities. A 3D printer with the ability to print a complex, soft, functional structure with sufficient precision to produce, for instance, a good-quality DEA has not yet been presented.

A low-cost printing process capable of printing 3D structures from silicone rubber could greatly accelerate soft robotics research. Furthermore, multi-material 3D printing with elastic, conductive materials would enable fully 3D-printed DEAs as well as other functional structures. Indeed, entire soft robots including actuators, sensors and soft and rigid structural body parts could be printed in a single, automated

process. This capability would dramatically accelerate the development of artificial muscle technology and soft robotics as a whole.

1.2. Research aim and objectives

The overarching aim of this project is to develop new processes and materials for simple, low-cost 3D printing of soft, functional structures such as artificial muscles and soft robots. To enable such a process, two key capabilities were chosen as the main objectives of our research:

- 3D printing with high-performance elastomers such as silicone rubber. This is crucial for the fabrication of soft artificial muscles with competitive performance.
- Multi-material 3D printing with electrically conductive materials to make functional soft devices. This would enable the fabrication of electrically driven artificial muscles as well as soft robots with integrated sensors and other electronic components.

3D printing with silicone rubber and printing of soft, conductive materials have both already been demonstrated (see Sections 2.4) but never in combination on an easy-to-use, low-cost 3D printing platform. We consider low cost and usability of such a process a priority because only through wide-spread accessibility can such a technology have a significant impact on the scientific community (and beyond). Excessive cost as well as other practical aspects such as process time, robustness and repeatability, material preparation, post-processing, and clean-up can be great barriers for the adoption of a 3D printing process. Our efforts therefore focus on the development of a low-cost and easy-to-use 3D printing platform with the aforementioned capabilities. This is something that all previously reported processes with similar capabilities still lack (see Section 2.4).

For 3D printing of artificial muscles and soft devices, silicone rubber was chosen as the most appropriate material (see Section 5.3.2.5) since it combines excellent mechanical properties with easy processability (see Section 2.3.2.1). The development of a low-cost 3D printing process for silicone rubber is described in Chapter 5. Our process

allows 3D printing of silicone rubber parts with complex geometries and comparable resolution to commercial silicone 3D printers.

Adding multi-material printing capability was found to add significant complexity to the 3D printer hardware. To keep the printing process and hardware as simple as possible, we explored the idea of single-material printing with a state-changing material that can function as both a structural, insulating material and as an electrical conductor, after selective conversion from a non-conductive to a conductive state. One example of such a material is graphene oxide (GO), which can be converted from a non-conductive to a conductive material using a very simple, low-cost laser-scribing process (see Section 2.6.1). To prove the feasibility of this approach, the use of GO for the fabrication of artificial muscles, which had not been reported before in the published literature, is investigated in Chapter 3. We show that laser scribing of GO is a simple, low-cost method for precise, in-situ, mask-less patterning of DEA electrodes and that functional DEAs can be produced with this technique, although the material only remains conductive up to moderate strains around 40 %.

As an alternative to GO that is more easily integrated with our 3D printing process, direct conversion of silicone rubber via laser scribing is explored in Chapter 4. We show that direct laser scribing can generate conductive material from silicone rubber, a phenomenon that had not been reported in the literature at the time of our discovery. Laser scribing and 3D printing were then integrated into a novel additive manufacturing process called laser-assisted, multi-material direct-write assembly (LAMDA), as described in Chapter 5. Fabrication of simple electric and pneumatic soft devices was demonstrated using the LAMDA process. Several technical challenges still need to be overcome and printing of functional DEAs has unfortunately not yet been achieved. Nevertheless, we believe that, with future improvements, the LAMDA process could be developed into a simple, low-cost 3D printing platform for artificial muscles and soft devices that will make soft robotics more accessible to a wider community of researcher and enthusiasts, which could greatly accelerate innovation in the field.

Chapter 2

Literature review

This literature review is structured in five subsections that review the state of the art of different disciplines and technologies which are relevant to our work, including soft robotics applications, soft materials, and manufacturing processes. Section 2.1 presents a brief overview of the field of soft robotics, with a focus on actuation. In Section 2.2, various artificial muscle technologies and their actuation properties are discussed. Section 2.3 reviews some of the common materials used for fabrication of soft devices and artificial muscles, with a particular focus on DEAs. Section 2.4 discusses some current fabrication techniques and their limitations to highlight the benefits of 3D printing in this context. Following that, Section 2.5 provides a review of existing 3D printing technologies with regard to their suitability for multi-material printing with soft materials. Lastly, Section 2.6 gives an overview of published work on laser-scribed materials. These are of interest in the context of the laser scribing methods used for DEA fabrication in Chapters 3 and 4, and as part of the LAMDA printing process described in Chapter 5.

2.1. Soft robotics

Soft robotics is a fairly young discipline within the broad field of robotics that has only emerged over the last two decades.[5] Even though the first pneumatic artificial muscles were developed in the 1950s,[13] it was only after the year 2000 that soft robotics started to emerge as a new discipline, as some of the first entirely soft-bodied robots using shape memory alloy coils[14,15] and later PneuNets (a type of soft, pneumatic actuator),[16,17] and dielectric elastomer actuators (DEAs)[18] were developed. Since then, the list of new, often bio-inspired, soft robotics applications has been growing steadily,

as can be seen by the steeply increasing number of publications in the field in recent years (see Figure 2).

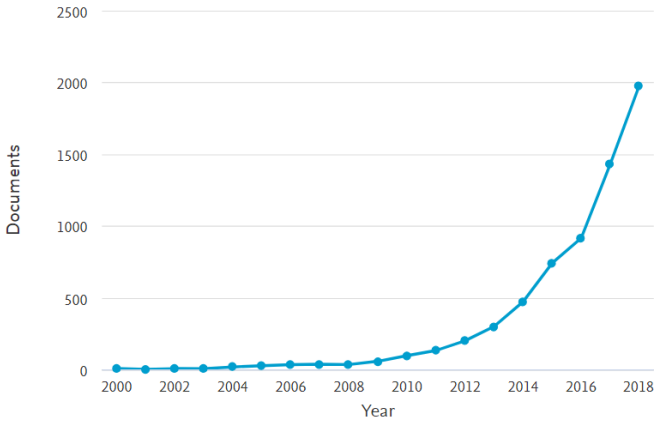

Figure 2. Number of soft robotics publications. The graph shows the numbers of publications mentioning "soft robotics" or "soft robot" per year since 2000. (source: Scopus, March 2019)

The term soft robotics generally includes a wide range of smart, soft devices – anything that uses soft, compliant structures and soft actuators and sensors to provide a specific function. Examples are wearable assistive technology (soft exoskeletons),[19] haptic displays,[20,21] soft surgical tools,[22] as well as grippers[23] and other end-effectors[24,25] that may form part of a soft robot or expand the capabilities of traditional robots. An astounding variety of soft robots and devices has already emerged, with some examples presented below. A more comprehensive overview of the state of the art of soft robotics is given by several recent reviews on the subject.[4,5,7,23,26]

Some of the first soft robotic devices were soft end-effectors such as grippers for handling of delicate and irregularly shaped objects. One of the most prominent examples that showcases the advantages of soft devices is the Universal Gripper (Figure 3A) which works by changing stiffness through jamming of a granular material.[27] Another type of soft gripper uses positive pressure to deform around an object (Figure 3B).[17] More recently, a sophisticated soft gripper has been demonstrated that employs a combination of active deformation through electrostatic actuators and electroadhesion for increased holding force (Figure 3C).[28]

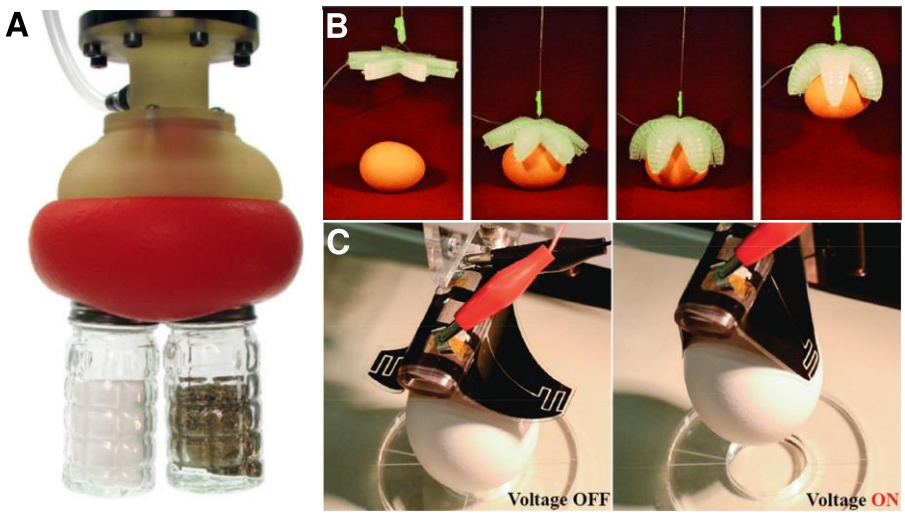

Figure 3. Soft robotic grippers. A) Universal gripper using granular jamming.[29] B) Soft pneumatic gripper.[17] C) Electrostatically actuated electroadhesive gripper.[28]

There is great interest in soft devices for medical applications. Devices range from manipulators for minimally invasive surgery[22] (Figure 4C) to actuated rehabilitation gloves[19] (Figure 5A) or assistive clothing for the disabled and elderly.[30] Other soft robotics applications include tuneable lenses[31] (Figure 5C) and haptic displays[21,32,33] (Figures 5E-F) that might be used in a range of applications from robot teleoperation to virtual reality entertainment. Soft robotic locomotion is also being explored as a way to develop robust locomotion mechanisms and allowing robots to access hard-to-reach places. PneuNet crawlers[16] and DEA-powered crawlers[34] (Figure 4B) have been developed, as well as various inchworm robots,[15,35] hopping robots[36] and even soft jumping robots propelled by internal combustion[37–39] (Figure 4E).

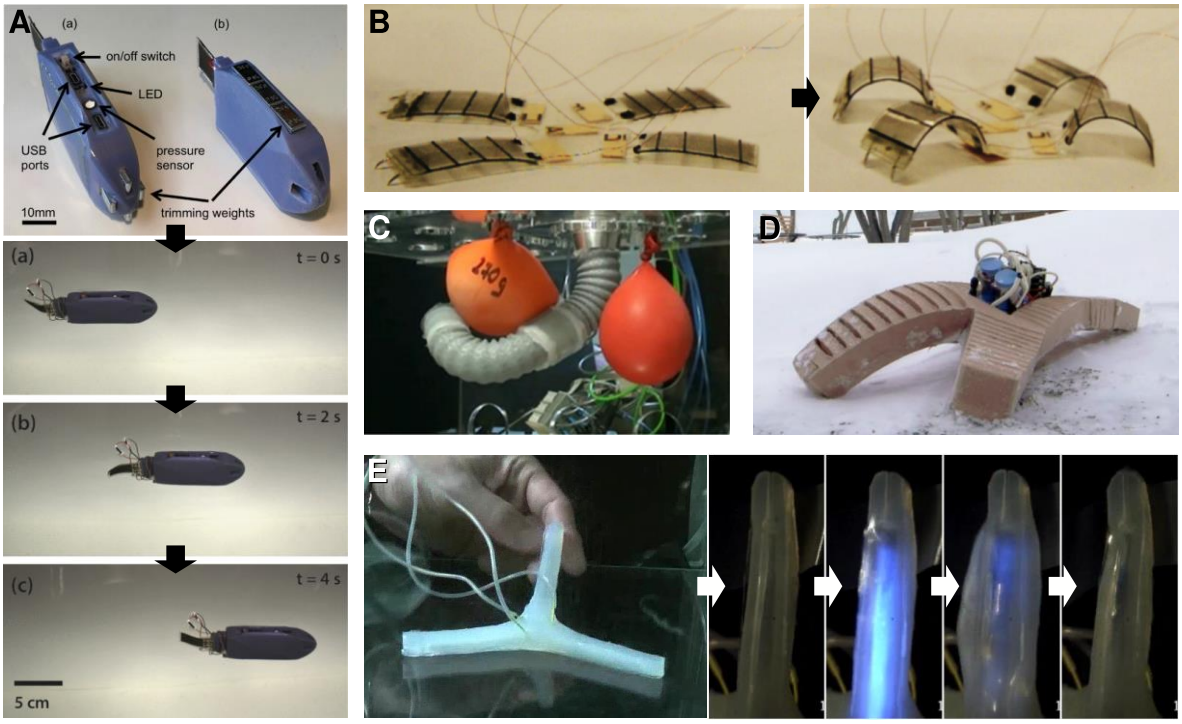

Figure 4. Examples of soft robots. A) DEA-driven, untethered fish robot; image sequence shows swimming by caudal fin movement.[40] B) Fast, DEA-actuated crawler, shown with extended legs (left) and contracted legs (right).[34] C) Soft robotic tool for minimally invasive surgery.[22] D) Untethered PneuNet crawler.[41] E) Soft jumping robot powered by internal combustion; image sequence shows combustion and resulting short-term expansion in one of the robot's arms.[37]

For the most part, these robots have been built to test out different locomotion mechanisms rather than solve any real-world task, but recently, the first untethered soft robots have emerged which are able to move with some degree of autonomy and could potentially carry payloads.[42] Examples are an untethered PneuNet crawler[41] (Figure 4D), a DEA-powered crawler with electroadhesive feet[43] (Figure 5B), and a DEA-powered robot fish[40] (Figure 4A), all of which carry their own power supply and electronics. Another notable example, taking soft robotics to the limit, is OctoBot.[44] Although not currently capable of locomotion, it is the first truly soft, untethered robot as its body does not contain a single rigid component. This is achieved by the use of microfluidic logic implemented on a soft microfluidic controller. The robot is powered by oxygen gas generated through catalytic decomposition of hydrogen peroxide. It is programmed, without any electronics, to lift its arms in an alternating pattern. The robot does not currently perform any function, but it serves to demonstrate that soft

robots can indeed be made without any rigid components whatsoever, even for energy storage or control.

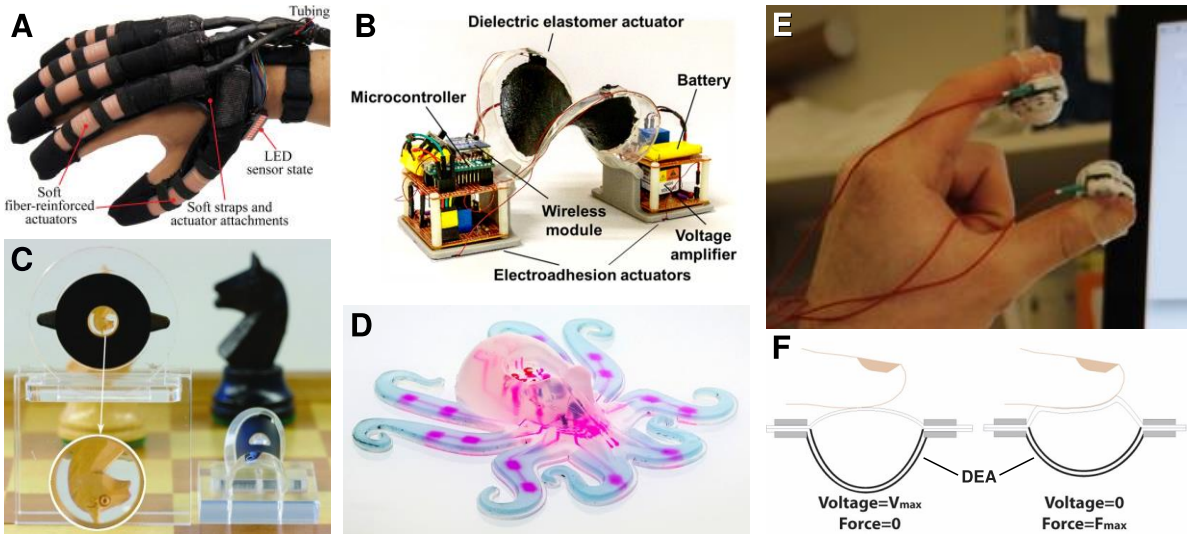

Figure 5. Examples of soft robots and devices. A) Rehabilitation glove with soft fluidic actuators.[19] B) Untethered, DEA-powered crawler that uses electroadhesion to modulate ground friction of its feet.[43] C) DEA-actuated tuneable soft lens (left) with a deformable frame (right).[31] D) OctoBot, an untethered, soft robot powered by oxygen gas generated from hydrogen peroxide decomposition, and controlled through microfluidic logic to move its arms in an alternating pattern without electronics.[44] E) DEA-driven tactile fingertip display.[21] F) Schematic of hydrostatically-coupled, DEA-driven tactile display shown in (E).[21]

2.2. Artificial muscles

The term "artificial muscles" is used to describe a family of soft actuators with muscle-like properties. There are various types of such actuators that all work by different fundamental principles and have different advantages and disadvantages. What they have in common is their inherent compliance and the ability to undergo deformation and exert forces in response to a stimulus, which can be used to perform mechanical work. Most artificial muscles are made from lightweight, polymeric materials. This potentially gives them a high power-to-weight ratio compared to conventional actuators such as electric motors, which are largely made of metals and therefore comparatively heavy.

In this section, the most important and widely used types of artificial muscle technology will be introduced, grouped in several families based on their underlying actuation principles. As there are many subtypes of these artificial muscles for very

specific purposes, this list is not exhaustive. A more comprehensive recent review of the subject can be found under ref.[9]

2.2.1. Pneumatic actuators

The earliest and still some of the most widely used types of artificial muscles are pneumatic muscles. These are soft structures which use pressurised air to drive deformation and exert forces. The first of these to be developed were so-called McKibben actuators, named after J. L. McKibben who popularised their use in the 1960s.[13] A McKibben actuator consists of an elastic tube surrounded by a helical mesh sleeve. The mesh restricts the deformation of the combined structure in such a way that an increase in diameter, caused by an increase in air pressure inside the tube, leads to a decrease in length.

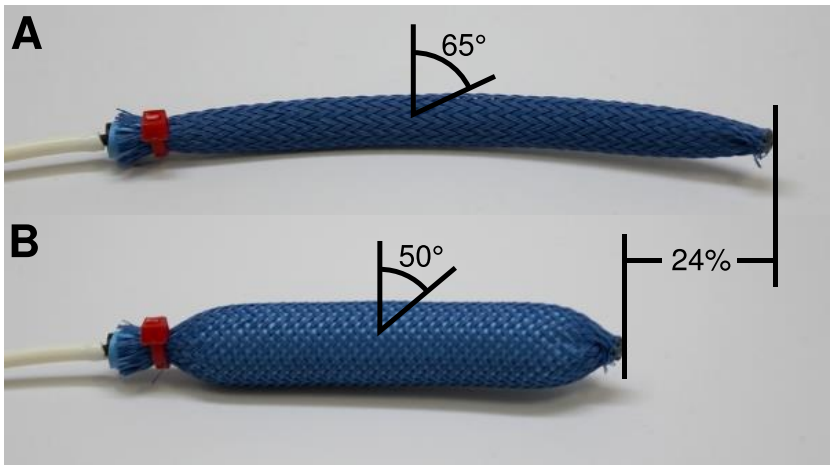

Figure 6. McKibben pneumatic actuator in relaxed state (A) and contracted state (B). Upon inflation, the actuator undergoes an increase in diameter and a decrease in length, typically around 25 %. At the same time, the helical, cross-woven mesh undergoes a change in fibre angle from 65° to 50° in this case. (adapted from softroboticstoolkit.com)

An example of a McKibben actuator is shown in Figure 6. This type of muscle generates linear contraction and behaves very similar to bundles of biological muscles.[45] It can typically contract to 75 % of its original length and generate forces from a few newton to several kilonewton, depending on the geometry, materials and actuation pressure.[46,47] The German company Festo has developed a commercial version of the McKibben actuator marketed as the FESTO Fluidic Muscle.[47] The Soft Robotics Toolkit describes a simple procedure for fabricating McKibben actuators by hand from

rubber balloons and nylon mesh.[48] McKibben actuators can be scaled in length to generate greater stroke and in diameter to generate higher force.[49]

PneuNets (pneumatic networks) are another type of pneumatic actuator that is widely used in soft robotics.[16,17] A PneuNet consist of a soft material with several interconnected cavities. When the cavities are filled with pressurised air, each cavity inflates and changes in size and shape like a balloon, leading to a change in shape of the overall structure. To produce meaningful, directed motion, expansion is usually restricted in a particular direction by incorporation of a fabric that can bend but not stretch, like in the case of the bending actuator shown in Figure 7. PneuNets are typically made of silicone rubber and can be produced using a simple two-part moulding process which is also described in the Soft Robotics Toolkit.[48] As with any bending actuator, scalability is limited. Scaling in length increases bending angle but does so at the cost of actuation force (due to leverage). PneuNets can be scaled in width to increase force but scaling in height has very limited effect. Force output can also be increased by increasing the stiffness of the actuator and the actuation pressure.[41] A similar concept to PneuNets but using buckling structures under negative pressure has been used to create linear contractile pneumatic muscles.[50] Recently, shape-morphing pneumatic structures have been developed that can assume complex, programmable 3D shapes upon inflation.[51,52]

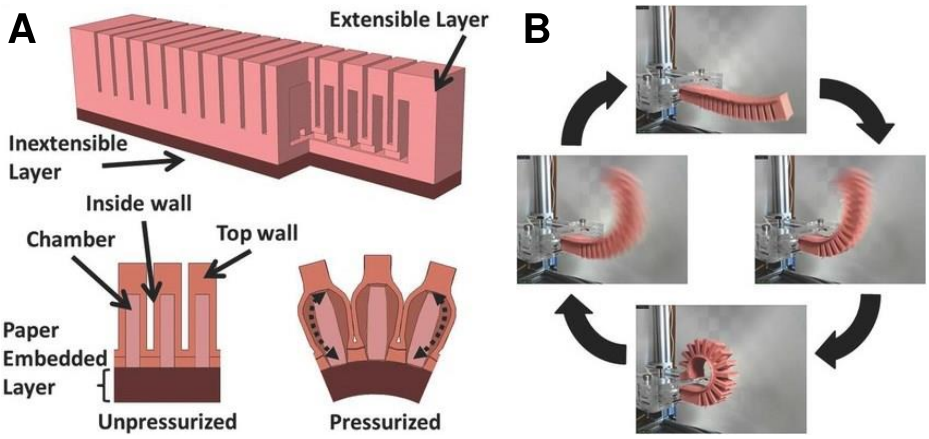

Figure 7. PneuNet bending actuator. A) Schematic of the actuator with individual, connected chambers that expand upon inflation. B) Actuation cycle of the bending actuator made of silicone rubber reinforced with paper. (adapted from [53])

In general, pneumatic muscles show large deformation and high power output. Unfortunately, their practical usability in robotics or wearable technology is limited by the dependency on an external source of pressurised air. Conventional air compressors tend to be very heavy and are not suited for use with a lightweight, soft, mobile robot. Miniature air compressors exist but these have very low flow rates and thus actuation is very slow.[41] Storage of pressurised gas is inefficient and requires heavy, high-pressure containers which is not feasible for a small, lightweight robot. Generating gas through a chemical reaction, as demonstrated in OctoBot,[44] might be a way to overcome this limitation.

2.2.2. Thermally driven actuators

Practically all materials deform with changes in temperature. This phenomenon can be exploited for actuation. A bilayer laminate of two materials with different thermal expansion coefficients will bend upon heating due to non-uniform thermal expansion of the two bonded layers. This principle has been exploited to make bending actuators[54] as well as an untethered, light-powered rolling microrobot (see Figure 8B).[55] Soft bilayer actuators can be made from silicone rubber and a carbon composite that is highly absorbent to visible and infrared light, which are used as a remote power/heat source. Thin bilayer structures can easily be fabricated by spin coating, drop casting or blade casting. They show reasonable response times of the order of several seconds and large bending angles of over 360°, depending on actuator geometry.[55] The downside of soft, thermal bending actuators is their very low actuation force. Scalability is also limited to the in-plane directions because the actuation mechanism relies on the thin, layered structure of the actuator, thus actuation force cannot be scaled up effectively.

Another type of actuator that uses thermal expansion as the driving mechanism for actuation is the class of coiled fibre actuators, the simplest examples of which is the fishing line muscle (see Figure 8A).[56] This actuator consists of a polyamide filament (fishing line) which is twisted into a coil. Thermal expansion of the polymer results in length contraction and unwinding of the coil which can be exploited for contractile or torsional actuation. Depending on how the filament is coiled, the muscle can generate up to 50 MPa actuation stress or 49 % strain, at a power-to-weight ratio of 27.1 kW/kg.[56] Fishing line muscles are extremely cheap and simple to make. Single

coiled fibres can be made into hierarchically twisted or braided bundles to increase force output. Actuation stroke scales with actuator length.

Coiled fibre actuators have also been made from carbon nanotube (CNT) yarns which where infiltrated with another "guest" material such as paraffin wax.[57] Thermal expansion of the guest drives torsional or contractile actuation. CNT actuators have high work- and power density and even faster response time than the fishing line actuators.[57] However, the higher cost of carbon nanotube yarn makes fishing line muscles a much more cost-effective option.[56]

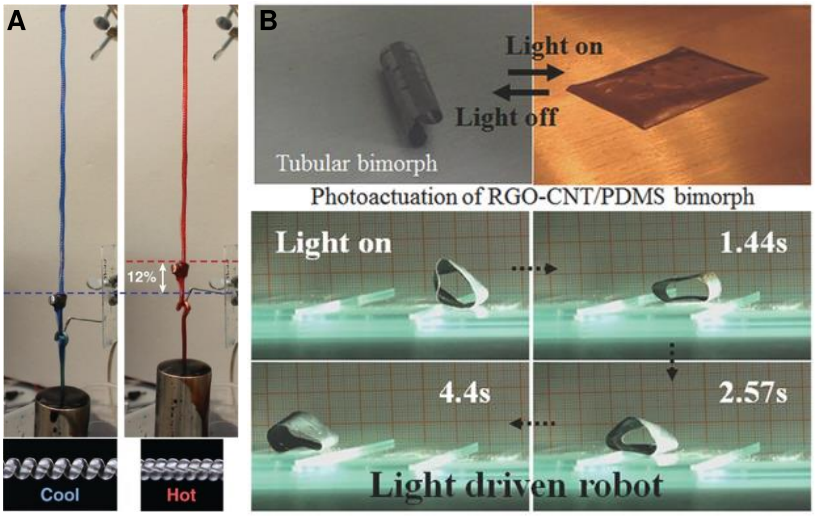

Figure 8. Thermally driven actuators. A) Fishing line muscle in the cold, relaxed state (left) and in the hot, contracted state (right), lifting a 500 g weight.[56] B) Bending bilayer actuator (top) which can be used to make a light-powered rolling microrobot (bottom) capable of untethered locomotion.[55]

Shape memory alloy (SMA) actuators are another type of thermally driven artificial muscle. The shape memory effect allows a material that has been deformed plastically at room temperature to return to its original shape once heated above a specific temperature. The restoring force generated by the shape memory effect can be used for actuation. SMA actuators of various types have been used since the 1980s and have already found widespread use in robotics and many other fields.[58] The most commonly used SMA is a nickel-titanium alloy known as Nitinol. Bulk Nitinol can undergo recoverable strain of 8 % and generate substantial stress of 200 MPa.[9] Coil springs made from SMA wire display very muscle-like properties. The coil spring configuration allows SMA actuators to generate large displacement, above 100% of its original

length,[59] but actuation stress is reduced.[35] SMA springs have been used in a variety of soft robots, including robotic worms and a biomimetic octopus arm.[60–62] SMAs are very easy to use because the heat necessary to induce the shape memory effect can be generated through Joule heating by passing an electric current through the SMA wire itself. No external heating element is necessary. Nitinol springs are inexpensive and can be bought off-the-shelf and ready to use. They are scalable both in length and thickness, allowing their use in applications with different stress/strain requirements. SMA actuation is on-way only. To achieve two-way actuation, an antagonistic configuration of two actuators can be used.

The main drawback of all thermally driven actuators, including SMA springs and coiled fibre muscles, is their low energy efficiency and actuation frequency, which results in low mechanical power density. A large amount of energy is required to heat the actuator, only a small fraction of which, less than 2 %,[57] is converted to mechanical energy. The heat energy is not easily recoverable, leading to great energy losses in each cycle. Cycle frequency is limited by the heating and cooling rate of the actuator. Most thermal actuators are passively cooled, which limits their cycle frequency to less than 1 Hz. SMA micro-actuators can achieve cycle frequencies up to 100 Hz, but heat transfer is slower for larger actuators and thus cycle frequency is reduced.[9] This also limits the scalability of such thermally driven actuators. Active water cooling can be used to increase cycle frequency by a factor of 100 but this adds significant bulk, weight and complexity to the actuator and increases energy consumption.[9]

2.2.3. Dielectric elastomer actuators

DEAs are a type of soft, electrostatic actuator with many favourable characteristics. They can produce high force, high strain, operate over a large range of frequencies and are operated directly by an electric field, which gives them potentially high energy conversion efficiency.[10] In addition, they have inherent sensing and energy harvesting capabilities, making them suitable for an extremely wide range of applications.[63,64]

Dielectric elastomers (DEs) are fundamentally very simple structures. They consist of an insulating elastomer membrane, sandwiched between two compliant electrodes, forming a soft parallel-plate capacitor. When a voltage is applied, the capacitor is

charged. Electrostatic attraction between the oppositely charged electrodes results in Maxwell stress acting on the dielectric membrane that separates the electrodes. By applying a sufficiently large voltage, this effect results in a macroscopic deformation of the membrane, which contracts in thickness and expands in area under the applied stress (see Figure 9).

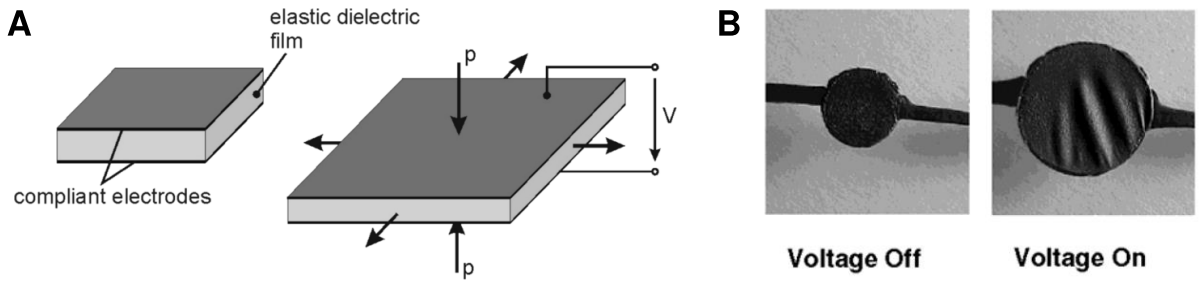

Figure 9. Dielectric elastomer actuators. A) Schematic of basic working principle. A voltage applied to the compliant electrodes on either side of the elastic membrane generates electrostatic forces that result in compressive stress on the membrane. The incompressible elastomer expands in area as it contracts in thickness.[20] B) Planar DEA, showing expansion of the active region covered in carbon black electrodes after a voltage is applied.[65]

The electromechanical coupling in a DE works both ways. Deformation of the membrane changes the thickness and area of the soft capacitor, thus changing its capacitance. This change in capacitance can be measured to obtain feedback on the deformation state of the membrane.[64] The same mechanism can also be used to harvest electrical energy from mechanical deformation. At constant charge, voltage increases as capacitance decreases. The capacitor is charged at high strain, when the capacitance is high. When the membrane is relaxed and the capacitance decreases, voltage across the membrane will increase. The DE can now be discharged at a higher voltage, resulting in a net gain in electrical energy.[63]

DEs are very attractive for use as artificial muscles because they are very simple structures, are generally made from inexpensive, lightweight materials, and they have work- and energy densities that exceed those of biological muscles.[10] The fact that they are driven directly by an electric field makes actuation fast and efficient. Electromechanical conversion efficiency is typically around 30 % but could theoretically be as high as 90 % if energy is recovered during the discharge cycle.[66] Actuation bandwidth is mainly limited by the resistivity of the compliant electrodes

and viscoelastic effects in the elastomer. Depending on the materials used, cycle frequencies up to 20 kHz can be achieved.[67] DEA actuation involves no moving parts and is completely silent, which is another very attractive property of an artificial muscle.

For a DE actuator, the effective compressive stress p experienced by the membrane is described by Equation (1).[65] It depends on the relative permittivity ε_r of the membrane material (the constant ε_0 is the permittivity of free space), and the applied electric field E, which in turn depends on the thickness t of the membrane, and the applied voltage U.

$$p = \varepsilon_0 \varepsilon_r E^2 = \varepsilon_0 \varepsilon_r \frac{U^2}{t^2} \tag{1}$$

All three of these parameters (ε_r, U, and t) can be altered to influence actuation. Increasing the applied voltage will increase actuation stress but is limited by the dielectric strength of the elastic membrane. The relative permittivity is a material property which can be altered by changing the composition of the membrane material (see Section 2.3.2). Decreasing the thickness is another way to produce a higher electric field and thus larger deformation at lower voltage.[68] It is generally desirable to make the dielectric membrane as thin as possible to reduce the required actuation voltage. However, because of the quadratic relationship between thickness and actuation stress, small variations in thickness can lead to large variations in stress over the membrane area.[69] This is exacerbated by the so-called pull-in effect, which occurs because a decrease in thickness leads to higher compressive stress, which in turn leads to a further decrease in thickness. This positive feedback can cause electromechanical instability and lead to membrane failure.[70] To prevent premature breakdown and generate uniform deformation, the dielectric membrane must have a very consistent thickness. Thickness variations are less critical in thicker membranes, but these require higher voltage to actuate.

The actuation stress is counteracted by the elastic restoring force of both the membrane and the compliant electrodes. To achieve high actuation strain, both should have very low stiffness. The electrodes are passive during actuation, serving only to

transport charges to the surface of the membrane (indeed, electrode-less DEAs are possible[71]). Electrodes should therefore be made as thin and soft as possible to limit their mechanical influence on the actuator. The development of high-strain, low-voltage DEAs therefore becomes a materials and manufacturing challenge. It requires the fabrication of extremely thin (to reduce actuation voltage), highly uniform (to avoid premature breakdown) elastomer membranes with even thinner and highly elastic electrodes (to avoid restricting actuation strain), which must nonetheless be capable of transporting electrical charges across the membrane surface with low resistive losses (to increase efficiency and avoid overheating).

Pre-strain is often applied to DEA membranes to tune the mechanical behaviour of the actuator and maximise actuation strain. By applying pre-strain, the elastomer can be put in the "plateau" region of its stress-strain curve (see Section 2.3.1, Figure 14) such that a small change in actuation pressure can effect a large change in actuator strain.[72] Pre-strain can also be used to suppress electromechanical instability which can allow the DEA to operate at higher voltages and thus increases maximum actuation strain.[70] In order to maintain the pre-strain, a rigid frame is necessary which can add bulk to the DEA and decrease its power-to-weight ratio. In addition, mechanical straining of the membrane is difficult to implement as part of an automated manufacturing process. It is therefore desirable to design DEAs that exhibit large actuation strain without pre-strain. Interpenetrating polymer networks have been suggested as a way to "lock" pre-strain into the soft material itself.[73,74] This eliminates the need for rigid frames, but still requires mechanical stretching of the primary network. Instead, specific polymer blends have been developed that display the desired stress-strain behaviour without pre-strain[75,76] (see Section 2.3.2.2).

DEAs can be configured in many different ways to make use of either the area expansion or the thickness contraction of the membrane. Area expansion is used for example in bending bi-layer actuators or diaphragm actuators. In contrast, contractile stack actuators (Figure 10C) make use of the thickness contraction and usually consist of several tens or hundreds of layers in order to increase absolute actuation strain. Some examples of DEA devices such as grippers,[28] crawling[34,43] and swimming[40] robots, haptic feedback devices[21] and tuneable lenses,[31] have already been presented in

Section 2.1. Other applications include tactile displays,[20,32] fluidic pumps[77,78] and valves,[79–81] as well as elevons in a micro air vehicle.[82] The scalability of DEAs has been demonstrated in an arm wrestling robot (Figure 10A) built to compete against a human and capable of generating 200 N of arm wrestling force.[83] The force is generated by 144 spring roll DEAs (Figure 10B). These consist of a DEA membrane wrapped around a compressed coil spring that provides pre-strain.

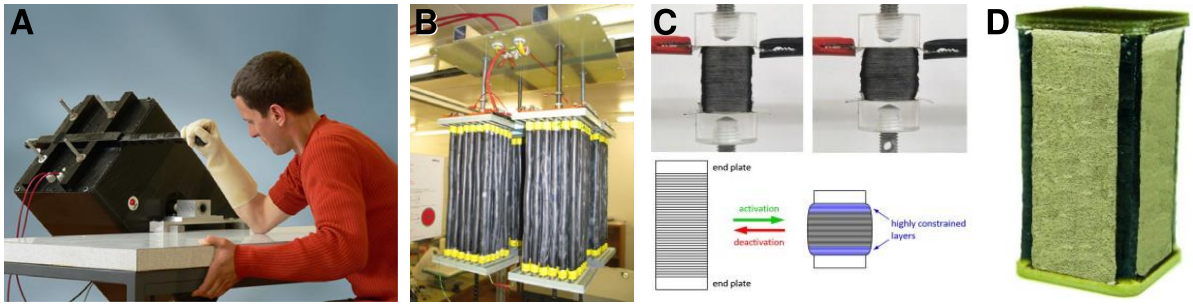

Figure 10. DEA devices. A) DEA-powered arm-wrestling robot.[83] B) Inside of the arm-wrestling robot, showing four batteries of 36 spring roll DEAs.[83] C) Contractile stack DEA and schematic of stack DEA deformation under an applied voltage.[84] D) Commercial stack DEA unit (Gabor Kovacs, CTsystems).

Despite much research interest, few commercial applications for DE technology have arisen as of yet. New Zealand-based company StretchSense Ltd. is the first company to launch a commercially successful product based on DE technology. They supply soft tactile sensors (stretch and pressure), as individual modules or integrated into smart garments, for body pose and motion tracking.[85] DE sensors are the simplest DE devices as they do not require high voltage to operate and are therefore easier to fabricate and safer to use. DEA-based energy harvesting technology is also being explored for commercial applications. Dutch company SBM Offshore is currently developing DE generators to harvest wave power.[86] There are no commercial products using DEs as actuators currently on the market. Much of the reason is due to the lack of cost-effective, large-scale production methods for DEAs. Swiss company CTsystems is the first to develop a fully automated production line for commercially viable DEA stack actuators (see Figure 10D). This might pave the way towards the first commercial DEA applications.

Nevertheless, for DEAs to realise their full potential, a lot of research into materials, fabrication techniques, and device design is still necessary. In our work, we explore

new materials and methods for low-cost, facile, customisable manufacturing of DEAs in order to make this technology accessible to more researchers and accelerate innovation in the field.

2.2.3.1. HASEL actuators

An interesting variation of the DEA is the Hydraulically Amplified Self-healing Electrostatic (HASEL) actuator.[87] The difference to a regular DEA is that the dielectric layer is split into two layers that enclose an insulating liquid such as vegetable oil between them. A schematic of the structure is shown in Figure 11A. Instead of directly using the electrostatic pressure between the electrodes, hydraulic pressure caused by the displacement of the liquid can be used for actuation. This enables new actuator configurations such as the donut actuator shown in Figures 11B-D. As the name implies, the liquid dielectric layer also adds self-healing capabilities because it prevents the creation of a permanent electrical connection between the electrodes when dielectric breakdown occurs (see Figure 11E).

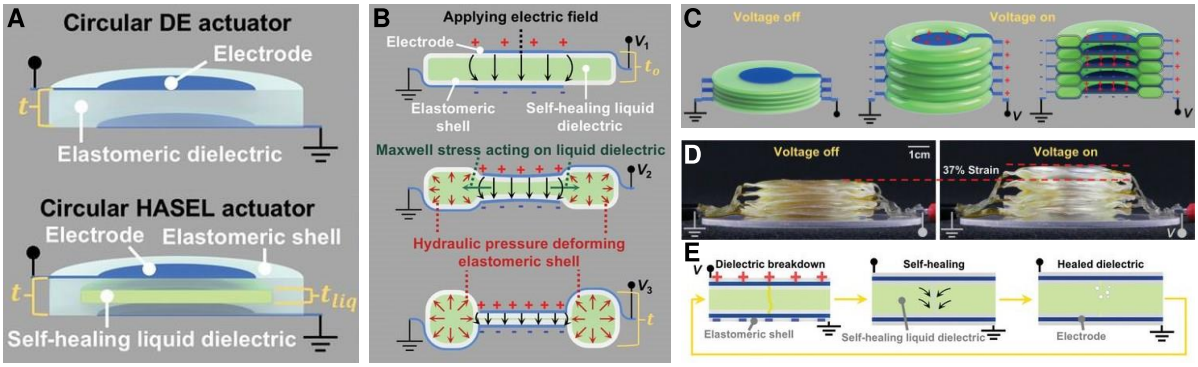

Figure 11. HASEL actuators.[87] A) Basic structure of a HASEL actuator compared to a conventional DEA. B) Donut HASEL actuator which expands in thickness upon actuation due to internal fluid pressure. C) Schematic of a stacked donut actuator. D) Stacked donut actuator prototype. E) Schematic of the self-healing mechanism enabled by the liquid dielectric.

The downside of HASEL actuators is that they inevitably require higher actuation voltage than a conventional DEA because of the increased distance between the electrodes. Assuming that the same limitations for manufacturing of thin dielectric layers apply, a DEA can be made much thinner, because the HASEL actuator needs to incorporate two solid and one liquid dielectric layer whereas the DEA only uses a single solid layer. There is also a danger of leakage of the liquid dielectric in case of

physical damage. Our research therefore focuses on fabrication of conventional DEAs. However, the LAMDA process presented in Chapter 5 might also be suitable for fabrication of HASEL actuators.

2.2.3.2. Other dielectric actuators

Another variant of dielectric actuator combines HASEL actuators with a type of fluidic muscle known as a Peano actuator,[88] and is thus called a Peano-HASEL actuator.[89] It uses dielectric forces to displace a fluid inside a flexible but inextensible pouch which causes it to increase in thickness and contract in length. This mechanism is illustrated in Figure 12A. Figure 11B shows a Peano-HASEL actuator made of a flexible polymer film.

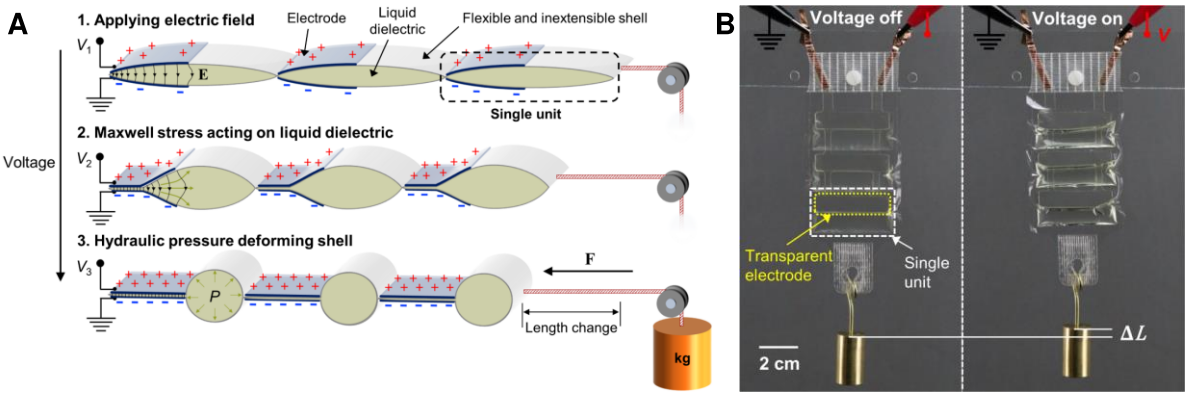

Figure 12. Peano-Hasel actuator.[89] A) Schematic showing the working principle. The fluid is displaced from between the electrodes and the increased pressure causes the passive part of the actuator to assume a round cross-section and contract in length. B) Peano-HASEL prototype in relaxed (left) and actuated state (right), lifting a weight of 20 g.

Another interesting, novel type of dielectric actuators are electro-ribbon actuators, which use a mechanism called dielectrophoretic liquid zipping (DLZ).[90] In a DLZ ribbon actuator, two ribbons of oppositely charged flexible electrodes, which are in close contact on one end, are gradually pressed flat against each other by electrostatic pressure. Actuation force is amplified by a small bead of a liquid dielectric between the ribbons. A simple ribbon actuator demonstrating the basic actuation mechanism is shown in Figure 12. Folding of the ribbons allows interesting actuator configurations in what is called electro-origami.[90]

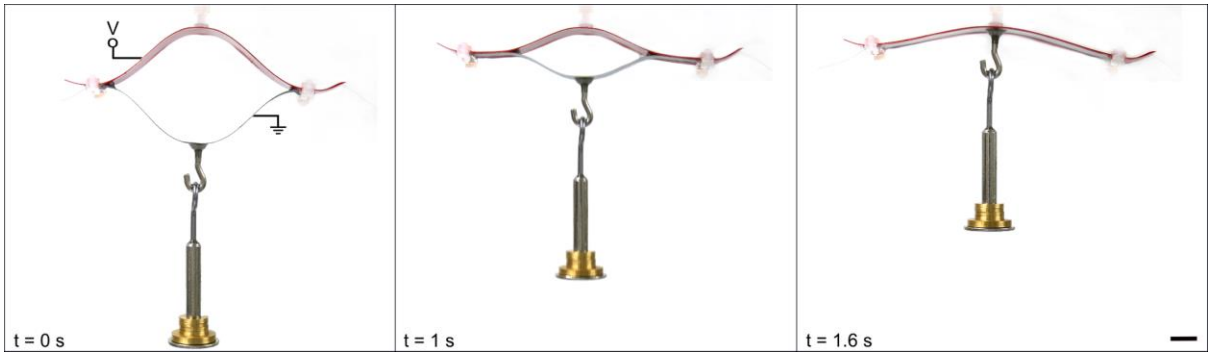

Figure 13. Electro-ribbon actuator using dielectrophoretic liquid zipping.[90] The two oppositely charged flexible ribbons gradually zip closed. A small bead of liquid dielectric between the ribbons amplifies actuation force. Scale bar is 10 mm, lifted mass is 20 g, and actuation voltage is 8 kV.

The same zipping mechanism used in DLZ actuators is also exploited in Peano-HASEL actuators to increase actuation force. However, the DLZ actuator uses a much smaller amount of liquid to gain almost the same benefit, which allows it to be more lightweight.[90]

Both Peano-HASEL and DLZ actuators do not require inherently elastic materials and can be made from flexible polymer films and thin metal electrodes. From a manufacturing perspective, this is a distinct advantage over conventional DEAs because it potentially allows them to be manufactured cheaply and at large scale using existing roll-to-roll manufacturing processes.[89] This could be a great advantage with regard to commercialisation. However, the use of inextensible materials also means that they are mechanically more constrained than DEAs and cannot be considered truly soft actuators.

2.3. Materials for artificial muscles

The different artificial muscles presented in Section 2.2 fall into one of two categories: those that are made of soft materials which have inherent compliance, and those that are made from soft structures where compliance arises from the geometry rather than the inherent material properties. Almost all thermal actuators fall in the latter category. The former category mainly contains DEAs and PneuNets. Our work is focused on developing additive manufacturing (AM) techniques for soft materials to fabricate these types of truly soft actuators as well as soft structural parts for soft robot bodies. For this purpose, Section 2.3.2 reviews a range of commonly used soft

materials with regard to their material properties and suitability for AM. Furthermore, Section 2.3.3 reviews soft, conductive materials which are important for fabrication of DEAs as well as soft bodies with integrated sensors and other electronic components. Before introducing specific materials, Section 2.3.1 briefly introduces some common behaviours and characteristics of elastomer materials which are important for artificial muscle applications.

2.3.1. Elastomer material behaviour

Characteristic for elastomers is a non-linear, hyperelastic stress-strain behaviour (see Figure 14). Near 0 % strain, strain-softening behaviour is observed, meaning that the elastic modulus decreases with increasing strain. It then reaches a "plateau" where the elastic modulus is very low and relatively constant. In this region, the elastomer undergoes a very large increase in strain with very little increase in stress. Finally, the elastic modulus increases again as the material approaches its maximum elongation. In addition to the non-linear stress-strain behaviour, some elastomers display large hysteresis and time-dependent effects such as viscoelasticity and relaxation.[91] Their properties also vary with external factors such as temperature and humidity.[72] All of these interacting, highly non-linear effects combined make soft actuators difficult to model and control.[13,91]

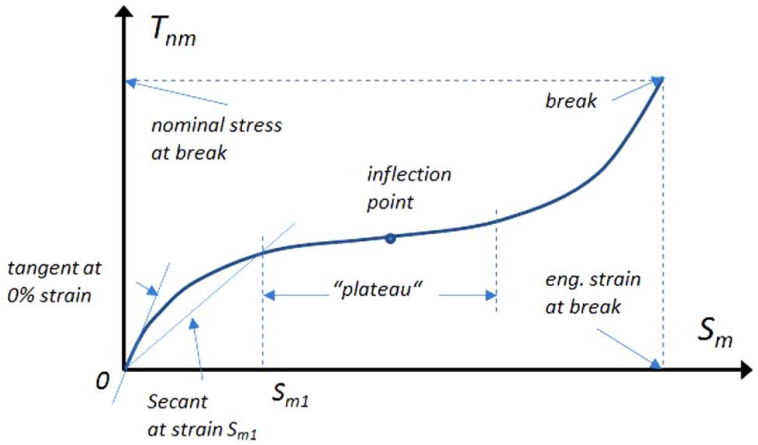

Figure 14. Typical stress-strain diagram of an elastomer displaying hyperelastic behaviour.[72]

Many rubber materials also experience strain softening through the Mullins effect.[92] This is a phenomenon whereby the elastic modulus of an elastomer at any given strain depends on the maximum strain that it has experienced previously. During first

deformation to a certain level of strain, the rubber shows a higher elastic modulus than during subsequent deformation cycles up to the same strain. When stretching past the maximum strain previously experienced by the material, a higher modulus can again be observed during the first cycle. The softening continues over a few strain cycles, but the most-pronounced change occurs between the first and second cycle. The Mullins effect is mostly observed in filled rubbers. It is therefore particularly relevant for DEAs that use elastomer composite electrodes (see Section 2.3.3.3). Because of the Mullins effect, soft actuators often need to be "trained" before use by repeated straining to or past the intended maximum actuation strain in order to achieve the maximum possible strain output and ensure that actuator behaviour is consistent.

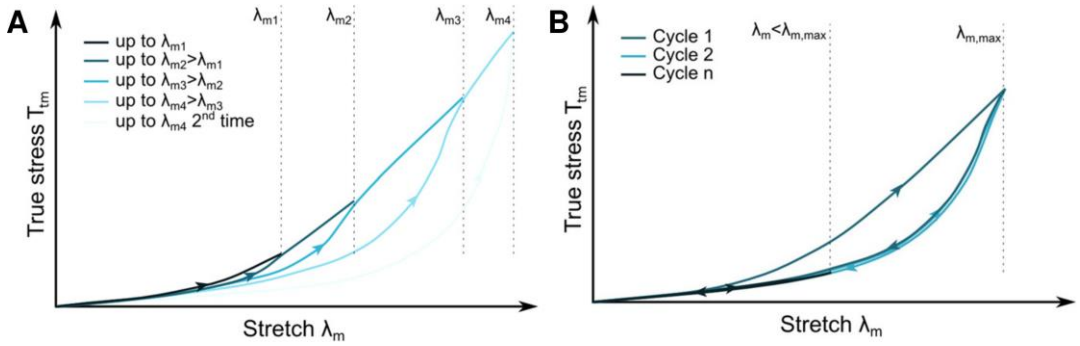

Figure 15. Illustration of the Mullins effect in elastomer materials.[72] A) Typical stress-strain curve showing an elastic modulus dependent on the maximum strain previously experienced. B) Softening occurs mostly during the first stretching cycle but several cycles are required to reach steady material behaviour.

2.3.2. Soft structural materials

Soft materials for artificial muscles and soft robotics must fulfil certain requirements. It is generally desirable to use materials which have high elongation at break (>300 %) so that the actuator can exhibit large strain during actuation. The Young's modulus needs to be chosen appropriate to the application. A higher modulus may be necessary for applications that require higher force.[41,50] However, in most soft robotics applications, materials with very low elastic modulus (<100 kPa) are used to make structures that are highly compliant and reminiscent of soft living tissues. Another important mechanical factor is viscoelasticity. Viscous behaviour leads to energy losses and limits actuation frequency. As mentioned in the Section 2.3.1, viscoelasticity also leads to hysteretic and time-dependent behaviour which makes modelling and control

of the device more difficult. For these reasons, viscoelastic behaviour is generally not desired in soft materials for artificial muscles.

In the particular case of DEAs, the elastic membrane material must fulfil another function: that of the dielectric in a capacitor. This function dictates desirable electrical properties of the material. To achieve large strain at low voltage, the permittivity of the material should be high. Unfortunately, most known elastomers have fairly low permittivity (see following subsections). High permittivity is therefore an interesting characteristic in the selection of soft materials for DEAs. Another important electrical property is the dielectric strength of the material. This parameter determines the maximum electric field that the material can withstand before dielectric breakdown occurs. Membrane materials for DEAs should have a very high dielectric strength since a high electric field is required to produce large deformation.

In the following subsections, different materials are presented that are commonly used in soft robotics and as dielectric membranes in DEAs. Both their mechanical and electrical properties are discussed, as well as their suitability for additive manufacturing processes.

2.3.2.1. Silicone rubber

Silicone rubbers, elastomers based on polysiloxanes, are some of the most versatile elastomer materials available today. Silicone rubber mainly consist of polydimethylsiloxane (PDMS), but compositions vary and wide range of silicones with different mechanical properties are available for different applications. It has some of the highest elongations of any known rubber materials. Several commercial silicone rubbers achieve an elongation at break of 1000 %,[93,94] with some novel, specialist silicone rubbers allowing elongation of up to 5000 %, according to the manufacturer.[95] They can also be extremely soft (Shore A hardness 5) and strong (tensile strength 2.4 MPa) at the same time.[93] Importantly, silicone can offer this amazing softness without significant viscoelastic behaviour.[96] From a mechanical perspective, this makes silicone rubber an excellent material for soft robots and DEA membranes. Silicone rubber also has a wide operating temperature range, from below -50 °C to over 230 °C,[94] which is important for practical applications with outdoors use. In addition

to the outstanding mechanical properties, silicone rubbers are also non-toxic and biocompatible, which is crucial for use in wearables and medical robotics that operate on or in the human body. Silicone rubber tends to have high dielectric strength of up to 350 MV/m (pre-strained).[10] Unfortunately, the permittivity of silicone (without fillers or functionalisation) is low at around 3.

Because of its excellent mechanical properties, silicone rubber is the go-to material for most soft robotics applications. The large majority of PneuNet devices reported in the literature is made from silicone rubber (e.g. [16,17,41,50]) and many other soft robot bodies are made of silicone materials (e.g. [36,37,44,61,62,97]). DEA devices are also often made from silicone rubber, despite the low permittivity (e.g. [28,31,77,82,98–101]).

From a manufacturing perspective, silicone rubber is relatively easy to work with. The most commonly used commercial silicone rubbers for soft robot fabrication are two-component, room temperature vulcanising rubbers. They are supplied as two liquid precursors, one containing a crosslinker and the other a catalyst. These are mixed together to start the crosslinking reaction which will cause the elastomer to cure at room temperature in a matter of several minutes to a few hours. Heat can be used to accelerate the curing process. Examples of commonly used silicone rubbers for soft robotics and DEAs are Ecoflex and DragonSkin (Smooth-On, USA), Sylgard (Dow Corning, USA), Elastosil (Wacker Chemie, Germany), and NuSil (Avantor Performance Materials, The Netherlands), all of which are available in various grades. In recent years, several UV-curable silicone rubbers have become available, such as UV Electro 225-1 (Momentive Performance Materials, USA), KER-4690 (Shin-Etsu Chemical Co., Japan), Loctite SI 5084 (Henkel, Germany), and SEMICOSIL UV (Wacker Chemie AG, Germany).[102–104] These use a UV-activated catalyst to delay activation of the curing reaction until the material has been exposed to UV light. This mechanism provides long pot life of the pre-mixed material (several days) while allowing fast curing (within seconds) after UV exposure. Such materials are highly suited for use in 3D printing, where fast, selective curing is required. Since silicone rubbers are chemically cross-linked, they cannot be melt-processed.

Thin, pre-fabricated silicone membranes made specifically for DEA applications are also available from Wacker.[105] Thin, defect-free membranes are crucial for DEA fabrication (see Section 2.2.3) and can be difficult to produce without specialist equipment and a cleanroom.

2.3.2.2. Acrylic elastomers

Acrylic elastomers are polymers derived from acrylic monomers or oligomers. They are usually supplied as low-viscosity, UV-curable monomer/oligomer resins. The commercial adhesive tape 3M VHB™ is also a type of acrylic elastomer. However, due to its special status as one of the most widely used dielectric membrane materials for DEAs, this material is presented separately in Section 2.3.2.3.

The ability to produce an elastic material from a low-viscosity precursor resin using UV-photopolymerisation is very attractive for 3D printing applications. Hence, most soft materials for stereolithography or inkjet 3D printers are acrylate-based.[106–108] Commercial, soft 3D printing materials have been used to make 3D-printed DEAs[109] and pneumatic actuators.[110,111] Special formulations of UV-curable acrylic oligomer resins have been used to make dielectric membranes without pre-stretch for high-strain (>300 %) diaphragm DEAs[75] as well as multi-layer bending DEAs[76] that have been used to drive crawling[34] and swimming[40] robots. Unfortunately, acrylic elastomers tend to exhibit strong viscoelasticity which leads to hysteretic strain behaviour, high mechanical losses, and a limited dynamic range.[109] Because of this, the aforementioned bending actuators have a maximum actuation frequency of 20 Hz,[34,76] compared with 20 kHz and more in silicone-based DEAs.[10] In general, acrylic elastomers tend to have inferior mechanical properties (elongation at break, tensile strength, toughness) compared with silicone rubbers. However, their relative permittivity tends to be somewhat higher than in silicones, around 4 or 5.[75] Specialised acrylate oligomer formulations have been used successfully for DEA applications and achieved high actuation strain without pre-stretch,[76] which makes them particular attractive for 3D-printed DEAs where pre-stretching of the membranes (during the printing process) is not feasible.

2.3.2.3. VHB

One of the most widely known and still widely used dielectric materials for DEA fabrication is 3M VHB™ 4910. VHB is a commercial adhesive tape made of a clear, highly elastic acrylic elastomer. The exact material composition is proprietary. The first high-strain DEAs that achieved more than 100 % area strain during actuation were made using highly pre-stretched VHB.[112] VHB, like other acrylic elastomers (see Section 2.3.2.2), has strong viscoelastic properties which greatly limit its actuation bandwidth. Its operating temperature range is from -35 °C to 90 °C,[113] much narrower than for silicone rubber. However, VHB, similar to other acrylic elastomers, has a higher relative permittivity than silicone (between 4.5 and 6, depending on conditions).[114] It also has the rather unique property that its dielectric strength increases with strain, from 18 MV/m at rest to 218 MV/m at 500 % biaxial strain.[115] This allows very high actuation strain to be achieved in VHB-based DEAs. Area strain up to 488 % was observed in a VHB DEA under dead load,[116] which is the largest actuation strain of any DEA reported to date.

VHB is also very easy to use. It is commercially available as a 1 mm (VHB 4910) or 0.5 mm (VHB 4905) thin tape on a roll, backed with a polyethylene liner. It can be easily cut to size with scissors. Due to its inherent adhesive properties, it can be easily attached to a frame for pre-straining without the need for adhesive or fasteners. The good adhesion can also be helpful in applying electrodes (depending on the electrode material and application process). For these reasons, VHB is featured by the Soft Robotics Toolkit as the material of choice for easy DEA manufacture.[48] The Toolkit suggests painting on electrodes with carbon grease by hand. Using VHB with carbon grease electrodes is probably the easiest way to make a simple DEA. It requires no expensive equipment and is therefore readily accessible to anyone.

VHB DEAs have been used to fabricate a wide range of devices including valves,[81] tactile displays,[21,32] grippers,[117] and swimming and crawling robots.[43,118,119] VHB membranes have also been used to fabricate other devices such as strain sensors.[120]

VHB is still a popular choice for DEA fabrication due to its ease of use and the high actuation strain that can be achieved with pre-strained membranes. VHB is only

available as pre-fabricated films. Because the material is cross-linked, it cannot be reprocessed and is therefore unsuitable for use as a 3D printing material.

2.3.2.4. Polyurethane

Polyurethane (PU) is a class of synthetic elastomers with a very wide range of properties. It is used for varied applications ranging from medical devices over mattresses to automobile parts. Some PU block copolymers exist which are thermoplastic, making them solution- or melt-processable. Such thermoplastic PU (TPU) is therefore suitable for 3D printing.

TPU is the most widely used soft or flexible material for fused filament fabrication (FFF) printing (see Section 2.5.1). TPU filaments are available from various manufacturers, with NinjaFlex from NinjaTek (USA) probably being the most well-known example. It is also one of the softest 3D printing filaments with a Shore Hardness of 85A and elongation at break of 660 %. This is relatively rigid compare to other rubber materials, including other grades of PU, but because the FFF process relies on a mechanical drive that pushes the filament into the heated extruder, a certain amount of rigidity in the filament is required. Softer materials cannot easily be processed by an FFF-type printer.

NinjaFlex has been used to print fully functional PneuNet actuators on a commercial FFF printer.[121] Direct-write 3D printing with solvent-based TPU inks have been used to create printed, stretchable circuits with embedded rigid electrical components.[122]

PU has also been investigated as a dielectric material for DEAs.[66,123] It can achieve high actuation pressure at relatively low electric fields due to its high permittivity (typically around 7, compared to ~3 for common silicone rubbers) but suffers from creep, low dielectric strength and a limited operating temperature range.[10] For these reasons, PU has so far not been widely used in DEA applications.

2.3.2.5. Triblock copolymer rubbers

Block copolymers are polymers where each individual polymer chain is made up of several segments ("blocks") of at least two different types of polymer. A triblock copolymer consists of a block of one polymer that is capped on either end with blocks

of other polymers. A typical triblock copolymer rubber (TCR) has identical outer blocks, which are able to form crystalline domains that act as non-covalent crosslinking sites. The inner block is generally longer and has only weak interactions so it can provide elasticity between the crystalline domains. The non-covalent cross linking makes these rubbers thermoplastic, which facilitates processing and recycling.

The TCR poly[styrene-b-(ethylene-co-butylene)-b-styrene] has been used as a dielectric material for DEAs.[124] In this case, mineral oil was used to solvate the non-crystalline phase of the polymer and reduce the elastic modulus of the rubber to as little as 2 kPa. At this low modulus, area strain of 245 % was achieved at a very low electric field of 22 V/µm. Recently, another TCR was developed specifically as a dielectric material for DEAs that has both high permittivity and high dielectric strength. The polymer poly[styrene-b-(n-butyl acrylate)-b-styrene] was compounded with partially reduced graphene oxide to make a rubber composite with relatively low modulus (0.51 MPa), high relative permittivity (~11), and high dielectric breakdown strength (33 V/µm).[125] With this material, 21.3% area strain was achieved without pre-stretch. Taylor-made elastomer materials such as this promise great improvements in DEA performance in the future, however, such materials are still in the early stages of development and not yet widely known and accessible. The fact that TCRs are thermoplastic makes them potentially suitable for 3D printing.

2.3.3. Soft conductive materials

Elastic, conductive materials are necessary to produce soft electroactive devices. All types of soft or stretchable electronics, including electrically driven artificial muscles, require conductors that are able to deform while maintaining their conductivity. DEAs in particular require electrode materials that are extremely soft yet conductive even at very high strain. The most widely used electrical conductors today are metals which are generally too stiff to serve as compliant electrodes or conductors in soft electronics. Because of this, soft conductive materials have been the subject of extensive research over the last decade. A great variety of solutions has been proposed, using a wide range of different materials and processes and tailored to specific applications in wearable electronics, electronic skin or artificial muscles. In the following subsections, some of the most common and most promising types of elastic, conductive materials for use in

soft electronics and as electrodes for DEAs are presented. These materials are also assessed with regard to their suitability for 3D printing.

2.3.3.1. Carbon particles

Loose, conductive particles can be applied to an elastic membrane to create a conductive surface. Because of overlap between the particles, the surface remains conductive under strain. Due to the lack of strong adhesion between the particles, the loose powder behaves neither elastically nor viscous and has minimal influence on the mechanical properties of the membrane. This is a very useful property for DEA electrodes. Most commonly, carbon black (CB) or graphite powder is used. CB consists of paracrystalline carbon particles ranging from 15 nm to 320 nm in size, depending on material grade, which form branched aggregates (see Figures 16A and B).[126] Graphite powders typically have primary particle sizes of the order of a few µm, although some sub-µm graphite powders are available.[127] Such fine powders ensure uniform surface coverage and relatively good interconnection between particles, making thin layers of such powders sufficiently conductive for use as DEA electrodes.

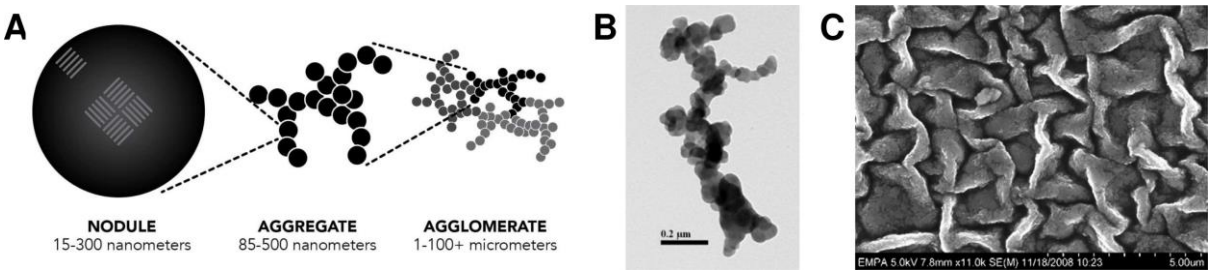

Figure 16. Carbon black as electrode material. A) Hierarchical structure of carbon black (from monolithmaterials.com). B) TEM image of a branched CB aggregate (from mccrone.com). C) SEM image of corrugated single-layer CB film on a relaxed elastomer membrane.[84]

Some of the earliest DEAs were made with graphite powder[128] or carbon black[66] brushed onto silicone membranes. Loose carbon black has been shown to have good cycle stability, but patterning is difficult as powder may spread during or after application.[129] In addition, the lack of adhesion between particles makes such electrodes very sensitive to abrasion. Airborne particles, particularly of carbon black, can also pose a health hazard. For these reasons, loose powder is rarely used these days. The automated fabrication process for DEAs developed by Schlaak et al.[77] uses spray deposition of a

binder-free graphite ink, which leaves only the graphite powder after solvent evaporation. However, the process ensures that electrode layers are encapsulated in silicone elastomer and the graphite powder is never exposed. Inkjet printing has been used to fabricate electrodes using carbon black ink.[130] The ink consist of CB dispersed in an organic solvent using a dispersing agent. After deposition, the solvent evaporates, leaving a thin layer of CB. These printed CB films are fairly resistant to abrasion which is likely due to the dispersing agent acting as a binder that stabilises the film.

The lack of cohesion in loose particle films can be overcome by applying single-layer films whose thickness is the same as the primary particle size of the powder.[84] To ensure that conductivity is maintained under strain, the powder is applied to the pre-strained membrane. Upon relaxation, the powder-coated surface adopts a corrugated morphology (see Figure 16C) which allows in-plane strain without conductive particles becoming disjointed. Unfortunately, this process is difficult to automate since it requires stretching of the elastomer membrane to apply the electrodes. Even the spray deposition method mentioned above is not suitable for integration in a 3D printing process since it relies on pre-fabricated masks to produce the desired electrode geometry.

2.3.3.2. Carbon grease

Carbon grease (CG) is a paste made of conductive carbon black particles dispersed in oil. The oil makes the carbon black easy to apply and prevents the formation of breathable dust which might pose a health risk. CG is one of the most commonly used electrode materials for DEAs. Manually brushing CG on a pre-stretched VHB membrane (Figure 17A) is the basic method for making a DEA described in the Soft Robotics Toolkit.[48] The conductivity of CG is below 1 S/m (properties can vary with composition).[131] This is very low compared with metal conductors, many of which have conductivities above 10^7 S/m. Nevertheless, CG can make effective DEA electrodes. Because it is a paste, CG deforms readily with the dielectric membrane and does not restrict actuation strain under static conditions. However, due to its viscosity, it reduces the actuators response time and maximum actuation frequency.[132]

Some of the first DEAs were made with CG after it replaced the use of loose particles due to easier handling and better compliance.[65,112,115] CG has been used in many DEA devices documented in the literature,[18,21,32,133] including some very recent examples of DEA-driven soft robots.[43,117,119] CG has been recommended as the preferred electrode material for standardised DEA performance evaluation because of its negligible mechanical stiffness.[72]

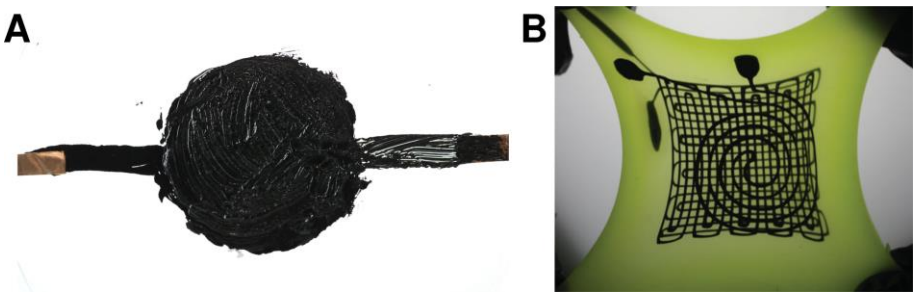

Figure 17. Carbon grease as electrode material. A) DEA with hand-painted, circular carbon grease electrodes (Malcolm Moreno, YouTube). B) Printed patterns of carbon grease traces in a silicone rubber matrix.[134]

The fact that CG does not dry or cure makes it highly compliant but is also one of its main disadvantages. Although better contained than mere loose particles, CG still easily rubs off if not encased. Great care must be taken when applying CG and when using CG-based devices to avoid contamination of equipment and the general work environment, including hands and clothing. Contamination with CG is problematic not only because of the black stains it leaves, but more importantly because of potential health risks[135] and the electrical hazard that can arise from conductive material accidentally deposited in unwanted places near high-voltage power sources. Encapsulation can limit the risk of contamination. However, this adds bulk to the device and contamination can still occur during fabrication. In addition to being messy, CG can also degrade the dielectric membrane.[129,136] Depending on the chemical composition, the oil contained in CG can infiltrate the membrane, weakening the elastomer while simultaneously drying out the CG film. Care must therefore be taken when using CG to ensure that the oil and dielectric material are compatible.

CG, being a paste, is readily 3D-printable using a direct ink writing method (see Section 2.5.2). 3D-printed strain sensors have been fabricated using this method by depositing CG into a volume of uncured silicone rubber (see Figure 17B).[134]

Nonetheless, its suitability for conventional 3D printing processes is limited because it does not cure or dry and remains liquid and unable to support successive layers of deposited material (see Section **5.3.3**).

Besides CG, silver grease is another conductive paste that is sometimes used as compliant electrode material. It consists of silver flakes dispersed in oil and has much higher conductivity than CG (10^4 S/m)[137] but appears to be far less popular, likely due to its much higher cost.

2.3.3.3. Elastomer composites

The most common alternative to CG is the use of conductive elastomer composites, where conductive particles, instead of being applied directly or dispersed in a liquid, are incorporated into an elastomer to produce an elastic, conductive composite. Because the elastomer is crosslinked, the conductive particles are fixed and do not rub off easily. Several conductive filler materials can be used to make conductive composites.

CB is a very common filler for elastomers because it is cheaply available and easy to compound with elastomer precursors. CB is added to many common rubber products as pigment and reinforcing filler, e.g., in car tires where it increases stiffness and abrasion resistance. When used to make stretchable conductors, the reinforcing effect of the CB filler is not desired and low filler ratios are preferable. However, the filler loading must be above the percolation threshold for bulk conductivity to occur. This threshold varies between fillers and matrix materials. At least 3 wt% loading of CB in silicone is required to produce a conductive composite.[136] At these concentrations, the filler has a notable influence on the mechanical properties of the elastomer, leading to an increase in elastic modulus and a decrease in maximum elongation. A CB/PDMS composite with 3 wt% of CB has an elongation at break of only 150%.[138] Its conductivity is around 0.1 S/m at rest and 10^{-3} S/m at 100 % linear strain.[138]

The percolation threshold and achievable conductivity vary with the type of filler and the type of elastomer in the composite. For graphite powder, the percolation threshold is much higher at 23 wt%.[136] Nanoparticles, particularly carbon nanotubes CNTs and graphene, have attracted much attention as conductive fillers because they can have

very low percolation thresholds. In TPU, a percolation threshold of 0.35 wt% for CNTs[139] and 0.1 wt% for graphene[140] has been reported. Hybrid nanofillers, combining CB or graphene with CNTs, have also been used to make conductive composites with enhanced conductivity and elasticity (see Figures 18A-B), however their conductivity remains relatively low at around 0.1 S/m.[140,141] The conductivity of such composites is sufficient for application as DEA electrodes but will not suffice to replace metal conductors in stretchable circuit boards. Various templating methods can be used to tailor the 3D structure of nanofillers within the composite. Such methods have been used to produce highly conductive graphene/PDMS composites, of the order of 1000 S/m, with filler loading of only 0.5 wt%.[142] However, the production of such templated composites is much more complex than simple dispersion-based composites and they have not found widespread use so far.

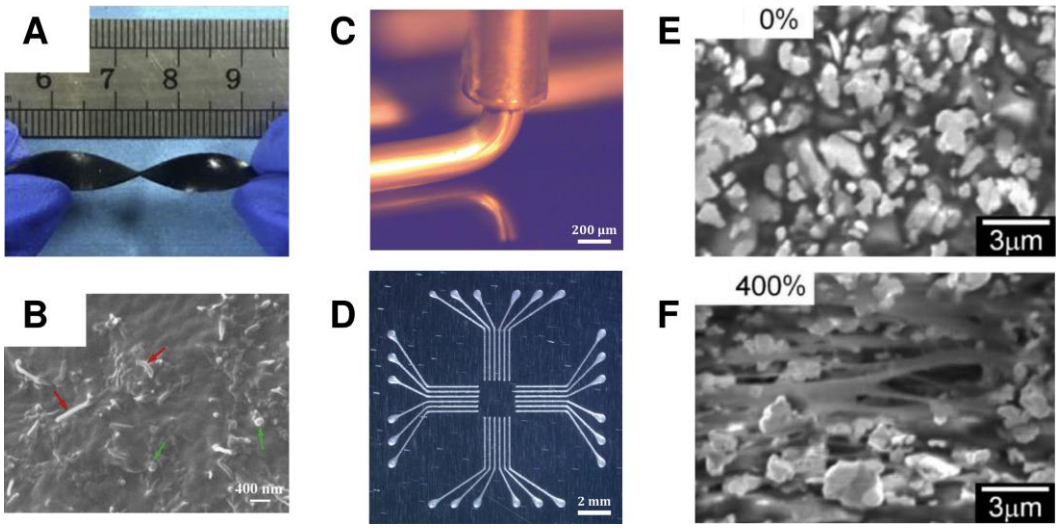

Figure 18. Conductive elastomer composites. A-B) Stretchable, conductive CB+CNT/PDMS composite and SEM micrograph showing CNTs (red arrows) and CB particles (green arrows) in the elastomer matrix.[141] C-D) Silver/TPU composite extruded from a 3D printer nozzle and the resulting conductive traces.[122] E-F) SEM micrograph of silver/TPU composite at 0 % strain and 400 % uniaxial strain.[143]

Metal fillers are also used in elastomer composites, most commonly silver particles, due to their high conductivity and resistance to oxidation. Silver composites in polyurethane have been produced with high strain up to 600 % and high conductivity between 10^7 S/m at 0 % strain and 10^3 S/m at 400 % strain (see Figures 18E-F).[143] However, metal composites typically require high filler loading, in this case 91 wt% (56 vol%) making them very stiff. Such materials are suited for conductive

interconnects in stretchable devices, but not as DEA electrodes, where low stiffness is crucial.

In practice, CB is still the most widely used filler for conductive rubbers. Various DEA devices made with CB/PDMS composite electrodes have been reported, such as folded stack actuators[144] or tuneable lenses,[31] among many others. When used as DEA electrodes, conductive rubber composites must be applied as very thin films compared to the thickness of the dielectric in order to limit the influence of electrode stiffness on the actuation performance of the DEA. Patterning of carbon/elastomer composite electrodes can be achieved, e.g., using pad printing of the uncured composite[145] or via laser ablation of a cured composite film.[146]

Conductive rubber composites can also serve as soft, resistive strain sensors. For this application, a large relative increase in resistance under strain is desirable. This property is known as the gauge factor. Many conductive composites with high gauge factor have been developed specifically for use as strain sensors.[147] These types of composites do not serve well as electrodes, where a large increase in resistance under strain is unfavourable.

In principle, conductive composites can be used for 3D printing in the same way that the different elastomers without conductive fillers can. However, the incorporation of conductive fillers changes the rheological properties of the materials and also makes them opaque. This means that the ability to photo-cure these composites is limited. When 3D printing conductive composites, other curing mechanisms such as thermal curing must be used instead. Direct ink writing of thermoplastic polyurethane with silver flakes has been used to make stretchable circuits that support up to 30 % strain (see Figures 18C-D).[122] Multi-material direct-write printing with PDMS and Ag/PDMS composites has also been demonstrated to make printed tactile sensors.[148] In this case the filler loading was 68 wt% and the method relied on non-selective thermal curing.

2.3.3.4. Nanoparticle films

For DEAs, the trend towards thinner dielectric membranes to reduce the driving voltage brings with it a need for extremely thin electrodes.[69] To make such thin

electrodes, various techniques have been used to apply conductive nanoparticles to the surface of the dielectric membrane which can yield conductive films with a thickness of no more than a few nanometres. Thin mats of single-wall CNTs (SWCNTs), shown in Figure 19B have been demonstrated as effective, thin DEA electrodes.[149] These mats are produced by filtration of a CNT suspension and then transferred onto an adhesive dielectric membrane using a simple stamping method. At 19 mg/m^2, the CNT electrodes had a sheet resistance around 100 kΩ/sq and optical transmittance of 72 % (see Figures 19C-D). Actuation strain of 80 % was observed at 300 V/µm, same as a comparable DEA with CG electrodes. The same type of CNT electrodes has since been used to fabricate multilayer bending DEAs and the electrode thickness has been determined to be below 100 nm.[76] Because the thickness of the dielectric membrane used was comparatively large at ~38 µm, actuation voltage for these DEAs was still in the range of several kilovolts. Electrodes made the same way out of silver nanowires (AgNWs) have lower sheet resistance but require much higher density (780 mg/m^2). They show lower actuation strain (max. 60 %) as well as lower optical transmittance (38 %) due to their much larger diameter of 90 nm compared to 1 nm for SWCNTs (see Figure 19A,C-D).[149] Hybrid electrodes made of a combination of AgNWs and SWCNTs show very low resistance of ~25 Ω/sq with an optical transmittance of 90 % and high strain up to 460 % (linear).[150] Layer thickness was not reported but must be larger than the diameter of the AgNWs used which was 150 nm.

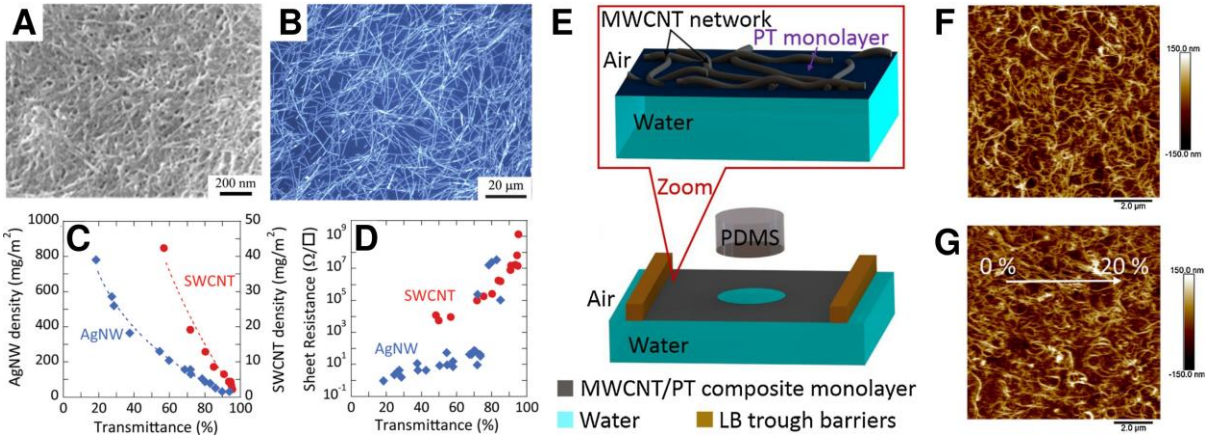

Figure 19. Conductive nanoparticle films. A-B) SEM micrographs of AgNW (A) and SWCNT (B) mats made via filtration.[149] C-D) Visible light transmittance and sheet resistance for AgNW and SWCNT mats of varying density.[149] E) Langmuir-Schaefer method for monolayer fabrication.[68] F-G) AFM height maps of multi-wall CNT/poly(3-decylthiophene) films on PDMS, at 0 % strain (F) and at 20 % uniaxial strain (G).[68]

To push electrode thickness even lower, monolayer electrodes from multi-walled CNTs in polythiophene have been produced via the Langmuir-Schaefer method (Figures 19E-G).[68] These electrodes have an average thickness of 30 nm and have been used to make DEAs with 4 % area strain at 100 V. The monolayer films have relatively high sheet resistance, ranging from ~20 MΩ/sq at 0 % strain to ~5 GΩ/sq at 100 % strain, which limits their actuation frequency and efficiency. They also have notable mechanical stiffness, increasing the elastic modulus of the DEA membrane. Nonetheless, such monolayer electrodes enable the fabrication of ever thinner DEAs and help to push existing limits on driving voltage.

Integration of nanoparticle deposition into a 3D printing process could be difficult since both the filtration method and the Langmuir-Schaefer method presented above consist of at least two separate steps, one for nanoparticle film preparation and one for transfer to the elastomer substrate, and both rely on masks for patterning. Alternative deposition mechanisms need to be developed that allow direct patterning and don't require a separate transfer step.

2.3.3.5. Ionic conductors

Ionic conductors transport electrical charges in the form of ions rather than electrons. Such conductors are only suitable in alternating-current applications because a direct current leads to electrochemical reactions taking place at the electrodes, even at very low voltage. They are, however, suitable as DEA electrodes where the voltage is applied across an insulating membrane and no electron transfer can take place. DEAs with hydrogel electrodes haven been demonstrated and show large strain comparable to other common electrode materials, with the added benefit of being perfectly transparent to visible light (see Figure 20A).[151] Hydrogel electrodes were also used to make the transparent Peano-HASEL actuators shown in Figure 12B.[89] The disadvantage of hydrogels is that they suffer from loss of water through evaporation which reduces conductivity over time. Encapsulation can slow this process, but most elastomers are permeable to water vapor and cannot completely prevent drying. By forming gels with a non-volatile ionic liquid instead of water, ionic conductors can be made that are stable at ambient conditions without encapsulation, as shown in Figure 19B. Ionic gels for DEA electrodes with a low elastic modulus of ~3 kPa, high

elongation of ~360 %, and good electrical conductivity of 0.22 S/m have been demonstrated.[152] A range of soft devices including sensors, displays, and energy storage devices have been developed using ionic gels as a conductor.[153]

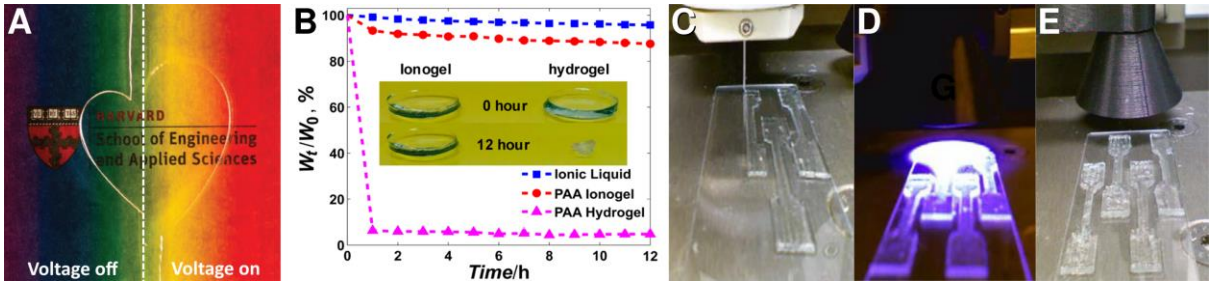

Figure 20. Ionic conductors. A) Transparent DEA with hydrogel electrodes in un-actuated and actuated state.[151] B) Weight loss due to evaporation for a hydrogel and ionic gel in comparison.[152] C-E) 3D printing with UV-curable hydrogels.[154] The gel is deposited through a thin nozzle (C) and then cross-linked using UV light (D) to fabricate dog-bone specimen for tensile testing (E).

Ionic gels are made via a polymerisation/crosslinking reaction from liquid precursors. Depending on the formulation, this reaction can be triggered by external stimuli such as light. UV-curable hydrogels have been 3D-printed using a direct ink writing method, depicted in Figures 20C-E.[154] Functional devices such as strain sensors[155] and bending DEAs[156] have been printed from conductive hydrogels.

2.3.3.6. Metallic conductors

Metals are excellent electrical conductors. Unfortunately, their intrinsic elasticity is not sufficient for use in artificial muscles and other soft, stretchable devices. The use of metal particles allows the fabrication of stretchable, conductive films and composites,[157] such as the Ag/TPU composites presented in Section 2.3.3.3 or the AgNW films shown in Section 2.3.3.4. Such composites tend to suffer from a large reduction in conductivity under strain as conductive particles become separated. As an alternative, there are several ways to make continuous metal structures with sufficient structural elasticity for use in soft devices. For instance, shaping metal traces in undulating patterns as in Figure 21A is one way to enhance their elasticity. Thin conductive traces in zig-zag or horseshoe patterns have been shown to withstand up to 100 % uniaxial strain with negligible increase in resistance.[66,158] Well-established industrial processes such as vapor deposition, sputtering, or electroplating in combination with photolithography can be used to produce such patterns with high

precision and at a large scale. The disadvantage of this approach is that it reduces the overall surface coverage of the metal film. This is problematic for use as DEA electrodes where uniform distribution of charges is important but is of no concern for conductive interconnects between components on soft substrates. Stretchable circuits such as arrays of LEDs or CMOS devices have been fabricated with serpentine interconnects that can withstand strains up to 140 % (Figure 21B).[159,160]

Out-of-plane structuring is another way to achieve stretchable metallic films that allows full surface coverage. This can be done by two methods. In the first method, a thin metal film is plated on an elastomer substrate with a corrugated surface structure. This approach has been used to make conductive films that withstand over 80 % strain without damage.[161] These films have a linear, sinusoidal surface pattern which makes them elastic in only one direction. This can be a useful feature e.g., in DEAs where uniaxial actuation is desired. These corrugated conductive films have been used to make DEAs with actuation strain of 14 % at 72 V/µm.[161] The second method consists of metal plating a pre-stretched elastomer membrane to form a crumpled metal film once the elastomer is released as can be seen in Figures 21C-D. Silver thin films on biaxially pre-stretched VHB membranes have been used to fabricate planar DEAs with large area strain of up to 128 % at 102 V/µm, making them comparable to graphite powder electrodes.[162] A major downside of this approach is the need for pre-straining, which is difficult to integrate into an automated manufacturing process. Another drawback of both buckled and corrugated metal films, if used as DEA electrodes, is their non-flat surface structure. For example, feature height of the corrugated films is 7 µm.[161] If the overall membrane thickness is of a similar scale, these variations will lead to stress concentrations and premature membrane failure. This limits the use of these electrodes in small-scale and low-voltage DEAs.

Metal ion implantation, by means of filtered cathode vacuum arc plasma (Figure 21E), is a method that allows embedding of metal nanoclusters beneath the surface of PDMS membranes to form conductive, stretchable films.[163] The metal clusters form up to 60 nm under the surface (see Figure 21F). They are close enough to be in contact and form a continuous conductive network but are able to move relative to each other, allowing the membrane to deform with little mechanical resistance and without losing

contact. Gold ion implantation in particular has yielded membranes with good electrical conductivity that remain conductive under strains up to 175 %. These have been successfully used to fabricate DEAs.[164] Electrode patterning can be achieved by the use of a mask. The stiffness of the implanted nanocluster layers is fairly low compared to other electrode materials, but has been shown to become more pronounced for very thin membranes.[136] The suitability of this process for low-voltage DEAs is therefore limited.

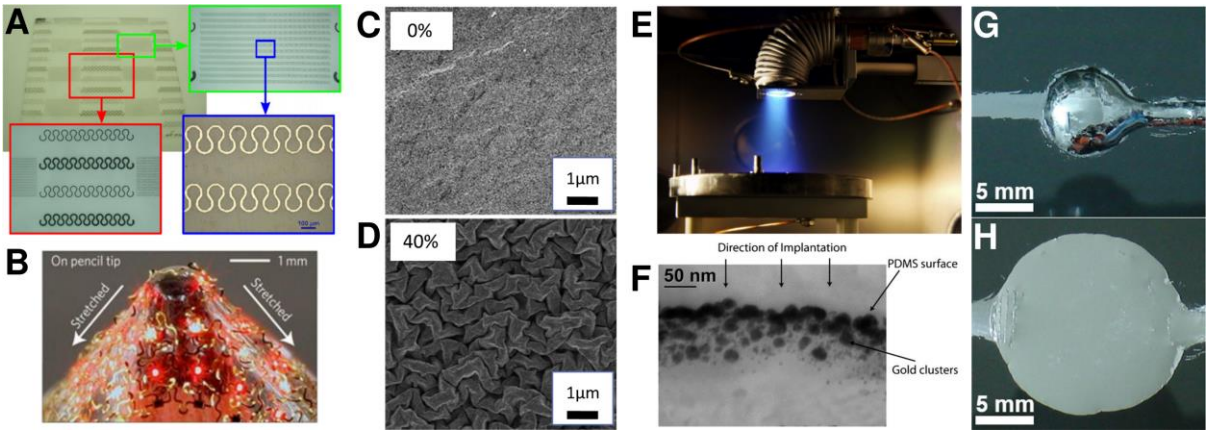

Figure 21. Stretchable metal conductors. A) Undulating pattern for interconnects that are stretchable up to 100 %.[158] B) Stretchable micro LED array.[160] C-D) Silver film deposited on pre-stretched membrane (C) assumes a crumpled surface structure after relaxation of the membrane, resulting in 40 % compressive strain (D).[162] E) Photograph of the filtered cathode vacuum arc plasma gun used for metal ion implantation.[165] F) TEM micrograph showing the cross-section of a PDMS membrane with implanted gold nanoclusters.[163] G-H) DEA with liquid metal (EGaIn) electrodes in the un-actuated (G) and actuated (H) state.[166]

Yet another approach to making compliant electrodes and circuits is to use liquid metal, which is, by definition, highly compliant. Eutectic alloys such as gallium-indium (EGaIn) or gallium-indium-tin (EGaInSn) have attracted much interest in this area since they are liquid at room temperature and fairly non-toxic (compared to mercury). It has been shown that EGaInSn can be directly applied to a pre-stretched VHB membrane to make planar DEAs with more than 300 % area strain at 3.5 kV (see Figures 21G-H), displaying better compliance than silver grease.[166] Mask-less patterning of EGaIn on a silicone elastomer substrate has been demonstrated using microcontact printing.[167] In this method, a small pin mounted on the print head is dipped into a reservoir of EGaIn to pick up small droplets which are then transferred onto the silicone substrate upon contact. This way, arbitrary 2D patterns with lateral

dimensions down to ~200 µm can be generated droplet by droplet. Recently, inks composed of EGaIn micro- or nanodroplets have been used to make films which can be selectively sintered through mechanical pressure to form conductive traces and patterns.[168,169] This method has also been used as part of a hybrid 3D printing process to produce stretchable circuits and devices.[170] A whole range of different techniques for printing with low melting point metal alloys has been developed.[171] Like with carbon grease, liquid metal electrodes require encapsulation to ensure their mechanical stability. In addition, liquid metal has very high density compared to polymeric materials, making devices heavier and reducing power-to-weight ratio. Liquid metal is not suited for devices that might be exposed to low temperatures which could cause the metal to solidify. Nonetheless, liquid metal shows great potential for stretchable electronics due to its high compliance and excellent conductivity.

2.4. Conventional soft robot fabrication

This section discusses some of the limitations of current, "conventional" methods used to fabricate soft robot parts. The discussion is based around practical experience gained during the building of VibroBot, a soft, hopping robot that we developed to compete in the RoboSoft Grand Challenge in 2016.[172] A detailed description and analysis of the kinematics and locomotion performance of VibroBot was published in Frontiers in Robotics in 2016.[36]

VibroBot's body consists of soft inflatable bladders attached to a rigid core. The core is made of acrylic glass sheets and plastic connectors. The use of conventional, rigid engineering materials made prototyping of the core very quick and straight-forward. By using rapid prototyping methods like laser cutting and FFF printing, several iterations of these rigid parts could easily be manufactured and tested within the same day. Much more challenging was the fabrication of the inflatable bladders which form VibroBot's soft outer body. The bladders (design shown in Figure 22A) were made from highly elastic silicone rubber (DragonSkin 10 MEDIUM, Smooth-On, USA) so they would be able to undergo large volumetric deformation and sustain enough pressure to carry the weight of the robot.

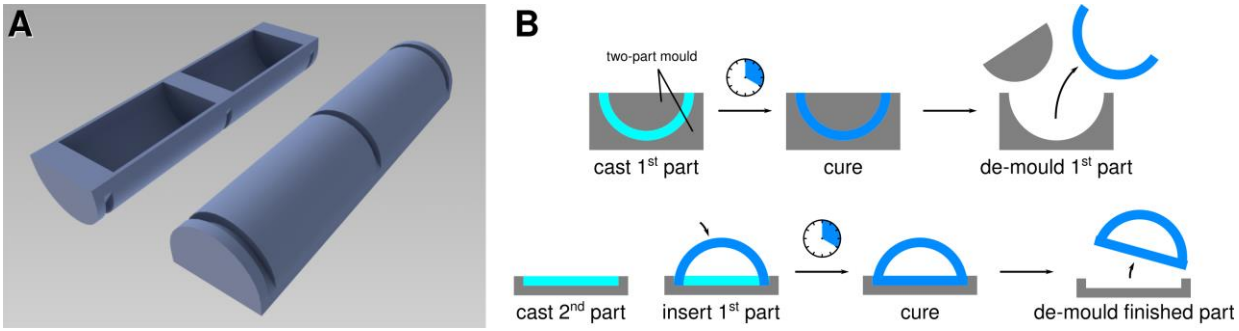

Figure 22. Inflatable bladders cast from silicone rubber. A) 3D rendering of the outer part of the inflatable bladder in two different orientations to show the inside (left) and the outside (right). B) Schematic of the two-step casting process used to make the bladders.

The bladders had to be made in a two-step casting process, as shown in Figure 22B. This method is commonly used to fabricate hollow parts from soft materials. A very similar process is described in the Soft Robotics Toolkit for manufacturing of PneuNet actuators.[48] In the first step, the outer shell of the bladder is cast in a two-part mould. Once cured, the back wall, which also attaches to the rigid body, is cast in a separate mould and the first part of the bladder is set into the uncured silicone rubber to form a continuous, seamless part. In each step, the two components of the liquid silicone rubber need to be mixed thoroughly and degassed in a vacuum chamber to remove air bubbles before the mixture could be cast into the moulds and left to cure.[94] Cure time for DragonSkin 10 MEDIUM is 5 h.

With this type of casting process, cycle time is a major limitation to the design process. Two-step casting is time-consuming, particularly because the two steps cannot be done in parallel. Mixing, degassing, casting and curing (for at least 5 h) has to be done separately for each step. Typically, it took two days to manufacture a bladder. With two identical moulds, two bladders were made in parallel. Nevertheless, a full prototyping cycle of the bladders took three days at the very least, since new moulds had to be made every time the design was changed. Because of this, only three iterations of bladders could be completed, leaving many potential improvements untested.

The use of faster-curing silicone rubber could accelerate the casting process, however, rubber with a shorter pot life is also more difficult to process since mixing, degassing and moulding have to be done very quickly but nonetheless thoroughly to achieve good

results. Curing at elevated temperatures could reduce cure time but can have a detrimental impact on material properties and may also lead to warping of the moulds if those are made from thermoplastic materials.

We also found that the use of mould release agent caused serious problems with the two-step casting process. Depending on the shape and material of the mould, a release agent was necessary to remove the moulded part cleanly and without damaging it. However, even very small quantities of mould release on the first part of the bladder would severely weaken its bond with the second part. Upon inflation, bladders cast using mould release agent would burst even at low pressures, with the two parts separating cleanly. Even washing of the first silicone part with soap and water did not fully remove the mould release agent. Therefore, compromises had to be made in the shape and material of the moulds to allow de-moulding without a mould release agent.

Many of the challenges and limitations of conventional moulding methods could be overcome if current rapid prototyping capabilities, specifically 3D printing, could be extended to high-performance elastomers such as silicone rubbers. Even more enticing is the potential of multi-material 3D printing with soft and rigid materials.

Fundamentally, there are two significant advantages of 3D printing compared with the silicone casting process. Firstly, 3D printing requires no prefabricated moulds. That entirely removes one step of the prototyping process and thus reduces the time and cost associated with each design iteration. The second advantage is that the process is largely automated. Although 3D printing may be slower in terms of absolute process time than casting (especially if existing moulds are used), the man hours required are much fewer. Even a 12-hour print, if started at the end of one workday and retrieved at the beginning of the next, easily allows for a 24-hour prototyping cycle. For VibroBot, this could have tripled the number of possible design iterations and allowed for more experimentation with additional features such as embedded sensors.

3D printing would also have allowed for more complex shapes of the bladders. The silicone casting process is limited to fairly simple geometries. Hollow structures always require two-part moulds and a two-step casting process, and more complex internal structures are impossible to achieve in a simple moulding process. Techniques like

rotational moulding could be used to produce hollow parts with more complex geometries, but these have other limitations. For instance, the wall thickness of parts made by rotational moulding has a variation of ±10 % or more,[173] making this technique unsuitable for the fabrication of inflatable structures. 3D printing also has its limitations when it comes to hollow structures because each 3D-printed layer needs to be supported during printing, but these limitations can be overcome. Some hollow geometries can be printed directly if overhang angles are sufficiently steep, and almost arbitrary shapes can be realised by the use of sacrificial support structures (in a multi-material printing process). That way, a sort of mould would be printed on the fly, but only where it is really necessary to support the rubber part.

The "holy grail" of soft robotics prototyping and manufacturing would be multi-material 3D printing with a selection of several soft and rigid materials that also have various other functional properties, like electrical conductivity. This would allow the incorporation of functional devices such as dielectric elastomer sensors and actuator. It could also allow the creation of a gradual, seamless transitions from soft to rigid materials, as demonstrated by Stratasys' PolyJet printers (see Section 2.5.3). Entire functional assemblies could be printed in a single process. In the case of VibroBot, strain sensors could have easily been incorporated directly into the bladders during manufacture. Air inlets and anchors for attachment could also have been implemented while simultaneously reducing the weight of the bladders by removing excess material in certain areas. Faster prototyping cycles would have allowed further optimisation of the structure and potentially led to a great increase in performance. The development of sophisticated 3D printing methods for soft materials would therefore be highly beneficial for soft robotics and artificial muscle research.

2.5. 3D printing techniques for soft, functional, structures

3D printing is a term commonly used to describe a variety of additive manufacturing processes that are capable of producing 3D objects. Different 3D printing techniques use very different methods and materials for building 3D structures. Four of the most common printing techniques are shown in the schematic in Figure 23. In the following subsections, these techniques are reviewed in more detail with regard to their

suitability for fabricating functional, soft, multi-material structures. Some examples of 3D printed soft structures and devices are given along with the printing platforms used to fabricate them.

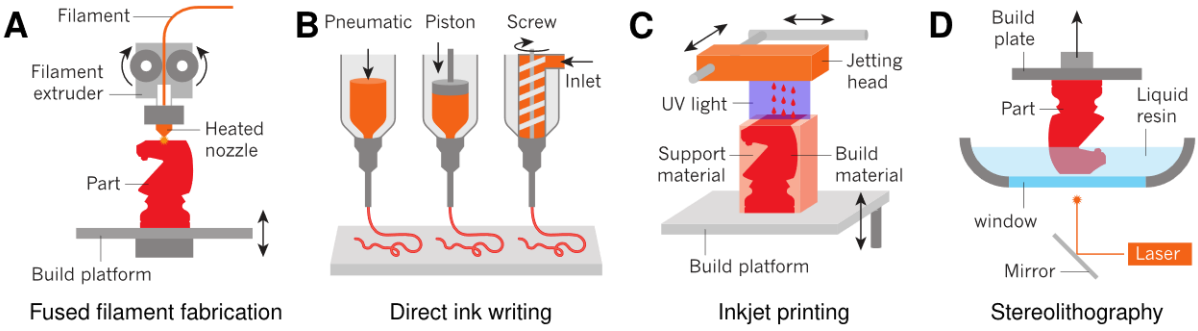

Figure 23. Schematic of different 3D printing techniques. A) Fused filament fabrication, which deposits a melted thermoplastic filament. B) Direct ink writing, which deposits a liquid or paste. C) Inkjet printing, which deposits individual droplets or a spray. D) Stereolithography, which selectively solidifies a volume of liquid. (modified from [174])

2.5.1. Fused filament fabrication

FFF is probably the most widely known and widely used 3D printing technique today. It is also known as fused deposition modelling (FDM), which is a trademark of Stratasys (USA). FFF works by extruding a bead of melted thermoplastic to deposit each layer of a 3D shape (see Figure 23A). Typically, a continuous filament of thermoplastic material is fed by a motor into a heated nozzle where it is melted and extruded on the other end. Once the material is deposited, it cools down and solidifies so that the next layer can be printed on top. Freshly deposited material will melt the surface of the layer below and the material will fuse, ensuring good adhesion between layers.

FFF-printed parts are relatively coarse compared to other 3D printing techniques. The most common nozzles used for FFF printing have a diameter of 0.4 mm, producing a bead of around 0.5 mm width. This dictates the minimum feature size. Layer height is generally between 0.05 mm and 0.2 mm. This gives FFF-printed parts a characteristic surface roughness because each layer produces a small bulge (see Figure 24A).

Since FFF printing relies on melting and cooling processes to solidify the deposited material, it is limited to thermoplastic materials. There is a great range of FFF materials on the market but most of these are rigid thermoplastics. Some flexible and

elastic filaments exist, mostly made of thermoplastic polyurethane, and these have been used to fabricate soft pneumatic actuators (see Section 2.3.2.4). Because the extrusion mechanism relies on a hobbed gear pushing the filament into the heated nozzle, the filament must have a certain amount of stiffness, otherwise it could buckle and jam the material path. This puts a limit on the elasticity of FFF-printable materials. Multi-material FFF printing is relatively simple and fairly commonplace. It can be achieved by using multiple nozzles on the same print head, multiple independent print heads, or by feeding multiple materials into the same nozzle.

Many commercial FFF printers are available over a large size and price range. Stratasys (MN, USA), who owns the FDM trademark and also held many early patents on the technology, is probably the best-known brand for large, industrial scale FFF printers. These machines offer a large build volume and high reliability but prints of comparable quality can also be achieved with desktop 3D printers, which are much more affordable. For desktop-size printers, MakerBot (NY, USA) and Ultimaker (The Netherlands) are probably two of the best-known brands. Both offer a basic FFF printer for around £2000 and more advanced models for up to £7000. Many smaller companies sell 3D printer kits to assemble at home. Most notably among them is probably the Original Prusa i3 by Prusa Research (Czech Republic), shown in Figure 24B. Their 3D printer kits start at around £600, with an extra £200 for a multi-material upgrade. Off-brand models are available for as little as £150. However, these tend to use low-quality parts and therefore have lower print quality. The great advantage of FFF printer kits, for research applications, is their adaptability. Most 3D printer kits are based on open-source designs and can easily be modified and expanded by the user which can be very useful for experimental printing applications.

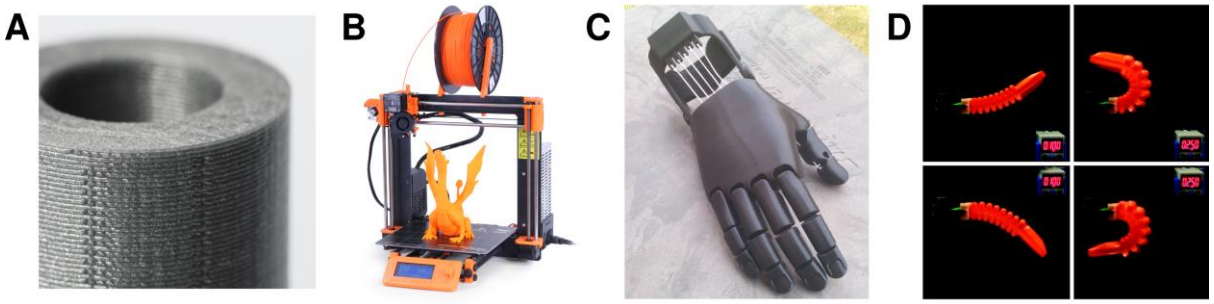

Figure 24. Fused filament fabrication. A) FFF-printed part with visible lines on the vertical walls indicating individual printed layers as well as slight irregularities where extrusion started and stopped on each perimeter (3dhubs.com). B) Original Prusa i3 FFF-type 3D printer, basic single-material model (3dhubs.com). C) Flexy-Hand 2, a 3D-printed prosthetic hand (Gyrobot, Thingiverse). D) FFF-printed bimorph PneuNet actuator made of NinjaFlex.[121]

Because the range of different printing materials is fairly limited, FFF printing is mostly used for rigid plastic parts. The structural strength of such parts is generally inferior to injection-moulded parts, but functional load-bearing parts can nevertheless be printed. 3D printing is particularly useful where customisability is important, e.g., for prosthetics: Many different versions of 3D-printable prosthetic hands have been developed over the years.[175] Some of these designs also make use of flexible materials for 3D-printed joints (see Figure 24C). Multi-material printing with PLA and a conductive graphene/PLA composite has been used to make 3D-printed variable stiffness structures, however, these can only transition from rigid to plastically deformable, but not elastic.[176] Possibly the only example of truly soft FFF-printed devices are PneuNet actuators made with NinjaFlex (Figure 24D).[121] NinjaFlex is currently the most elastic FFF material available, but it is still very stiff compared to elastomers like silicone rubber. Because of this, FFF printing is not suitable for soft devices or artificial muscles where large strain is required.

2.5.2. Direct ink writing

Direct ink writing (DIW) is a rather broad term used for any type of extrusion-based 3D printing using liquid or past-like materials (see Figure 23B). It is similar to FFF in so far as both techniques deposit a continuous bead of material to build a 3D structure layer by layer. In direct ink writing however, the material that is being deposited is liquid and can therefore be extruded without the need to melt it. That removes the requirement for a heated extruder, but it adds a requirement for a

hardening or curing mechanism to ensure that the deposited material maintains its shape as subsequent layers are deposited on top. Depending on the material, or "ink", this is typically achieved by drying or chemical crosslinking which can be triggered or accelerated through heat or UV light.[155,177–179] The process must be selective so that undeposited material remains processable while deposited material solidifies quickly to maintain its shape. Often, shear-thinning materials are used that can be extruded through a thin nozzle at high shear rates using moderate pressure. Once deposited, such materials hold their shape against gravity. Some materials are even able to support the weight of a few additional layers printed on top. This allows printing of thin parts without the need for a selective curing mechanism.[180]

Extrusion of liquids and pastes is typically done by one of two mechanisms, either pneumatically or mechanically driven. Mechanically driven systems are generally cheaper as they use conventional electric motors to drive a syringe plunger or a feed screw to exert pressure on the fluid.[181] Pneumatic systems use air pressure to extrude the fluid. These require digitally controlled pressure regulators which are relatively expensive. Nevertheless, pressure-driven extruders are the most common type because they allow almost instant switching of material flow rates and can also be used to prevent oozing by applying negative pressure.

DIW is probably the most versatile 3D printing method, allowing multi-material printing with a very wide range of materials. It is particularly interesting for soft structures because many elastomer materials are derived from a liquid or paste-like precursor which is easily processable in a DIW process.

A range of commercial DIW printers are available, mostly marketed as bioprinters. Bioprinters can print with living cells and biocompatible gels or other biomaterials, allowing 3D printing of biological tissues and organs. These printers generally offer multi-material extrusion and can process many types of liquids, gels or pastes. They can hence be used for a wide range of applications other than bioprinting. Some of the most well-known commercial bioprinters are the 3D Bioplotter by EnvisionTEC (USA), the 3DDiscovery by regenHU (Switzerland) or the BIO X 3D Bioprinter by Cellink (Sweden). These printers generally cost upwards of £100,000 which greatly

limits their accessibility. Recently, several more affordable bioprinters have entered the market like the BioBot™ (Advanced Solutions, USA) or Allevi printers (Allevi, USA). Their prices range between £5,000 and £10,000. Alternatively, a conventional FFF printer can be modified and equipped with a paste extruder. There are paste extrusion modules like the Discov3ry (Structur3d Printing, Canada) which are easily integrated with an existing FFF printer. Alternatively, a custom print head can be built using one of several open-source paste extruder designs.[181–184] Another very common approach is the use of entirely custom-built printers consisting of a linear cartesian robot equipped with pressure driven extruders. In this design, the print head merely holds the material cartridge (typically a disposable syringe) which is connected to a digital pressure regulator to control the material flow. Both cartesian robots and digital pressure regulators are commercially available.

Single material prints with highly elastic hydrogels have been demonstrated with an Ultimaker 2+ and Discov3ry Complete paste extrusion module.[185] An SPS1000 Bioplotter (Korea Institute of Machinery and Material, Republic of Korea) has been used to print highly elastic, tough hydrogels[154] as well as strain sensors made from PDMS with hydrogel electrodes.[155] Multi-material PneuNet actuators (Figure 25A) made of low- and high-stiffness silicone have been printed with water-soluble support on a 3DDiscovery (regenHU Ltd., Switzerland).[186] The same printer has been used to make multi-material parts with controlled, anisotropic stiffness and swelling, generated by application of a magnetic field.[187] Multi-material printing of a valve made of active hydrogel has been demonstrated on an EnvisionTEC 3D-Bioplotter (EnvisionTEC, USA).[188] Various forms of custom-built 3D printers with pneumatic dispensers have been used to print a whole range of soft devices such as tactile sensors,[148,155] Li-ion batteries,[189] quantum-dot LEDs,[178] hydrogel capsules for programmable drug release[190] and even bending-mode DEAs with hydrogel electrodes.[156] A printer with a custom-designed mixing nozzle for two-component silicone was used to print PneuNet actuators (Figure 25B) that showed improved performance over comparable actuators made by casting of the same materials.[179] A custom printing setup using a Preeflow eco-PEN300 (ViscoTec, Germany) volumetric dispenser to print silicone rubber onto a rotating cylindrical mandrel was used to make contractile and torsional pneumatic

actuators.[186] Some experimental DIW printers even integrate other methods such as pick-and-place to make stretchable circuits with integrated electronic components (see Figures 25C-D),[122] or spray deposition to create layers of liquid metal microdroplets which are then mechanically sintered and encapsulated in printed material.[170] These examples show that DIW offers the capability to print soft, functional, multi-material structures including artificial muscles.

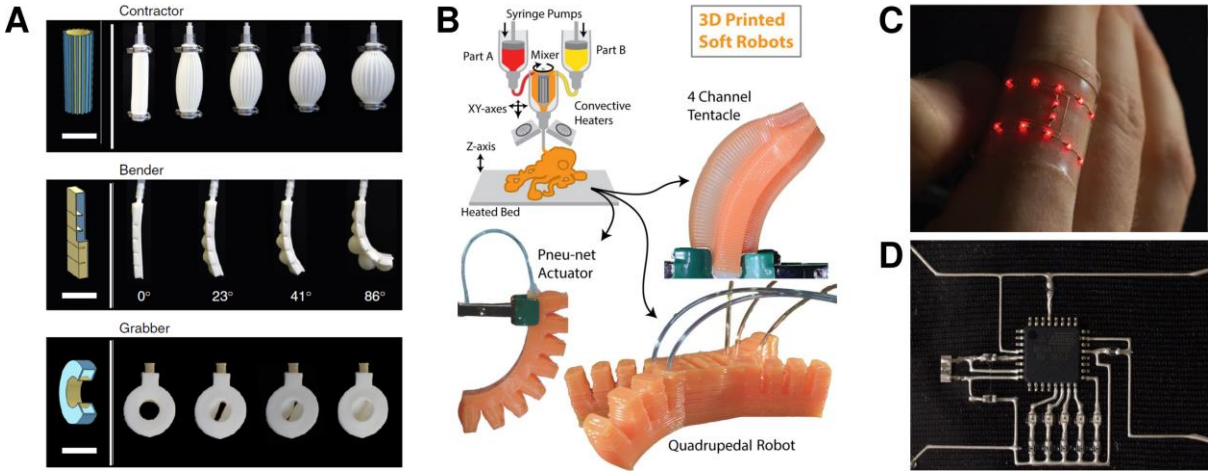

Figure 25. Soft actuators and devices made by direct ink writing. DIW-printed, multi-material, soft pneumatic actuators. The first image in each row shows the CAD model for the printed part, with stiff rubber in blue and soft rubber in yellow.[186] B) PneuNets made of two-component silicone rubber, printed with a custom-built DIW printer with mixing nozzle.[179] C-D) Stretchable circuits with printed interconnects and conventional SMD parts inserted through automated pick-and-place.[122]

For pneumatic actuators, printed structures can even match the performance of actuators made by conventional methods.[179] However, other devices such as DEAs, which demand high-performance materials and high-precision manufacturing in order to work effectively, cannot yet be printed with the same quality as those made by other manufacturing methods. One reason for this is limited resolution. Typical feature sizes are of the order of 100 µm and above. There is also only a limited selection of materials. Even though DIW is very accommodating in terms of the materials that can be processed, the optimal materials for a specific application are not always suitable for the printing process and compromises need to be made between material performance and processability. The examples given above highlight some of the amazing capabilities of DIW technology but also show that there is still much room for improvements, refining the printing process and developing new materials that are

well suited for both the 3D printing process and the respective application of the printed part.

2.5.3. Inkjet printing

Inkjet printing uses deposition of a spray or single droplets of a liquid ink (see Figure 23C). This technique is well-known from 2D office printers. These use a particular type of inkjet printing known as drop-on-demand (DoD), where individual microdroplets of a liquid ink are deposited at programmed locations to form a desired pattern. The same technique can be used for 3D printing, except that no paper substrate is used, and multiple layers of printed material are deposited on top of one another to form a 3D object. In the context of 3D printing, the process is also known as PolyJet, which is a trade name by Stratasys, Ltd. (USA), the largest manufacturer of inkjet 3D printers. DoD printers usually use piezo actuators to expel single droplets of ink. Droplet volumes are in the picolitre or even nanolitre range.[191] This allows printing of very thin layers and with very high lateral resolution. Layer height is typically of the order of 10 µm and lateral features of the order of 100 µm,[192,193] about an order of magnitude finer than typical FFF or DIW printing. DoD printers print with low-viscosity, photopolymerisable resins, very similar to the materials used in stereolithography (see Section 2.5.4). Low-viscosity inks must be used because highly viscous or viscoelastic materials do not easily form small droplets under the pressure exerted by a miniature piezo actuator. This limits the selection of materials that can be used in inkjet printing. Most elastomer precursors like liquid silicone are too viscous to be printed as-is and thinners or solvents must be used to print with these materials.[192] Some elastic materials exist that are suitable for inkjet printing, such as TangoPlus and Agilus30 which are sold by Stratasys for their range of PolyJet printers. Unfortunately, the properties of these materials are generally inferior to those of silicone and other "true" rubbers. For example, the elongation at break for TangoPlus and Agilus30 is around 200 %[193] whereas silicone rubber such as DragonSkin can withstand elongations up to 1000 %[94].

Fast photocuring is another important feature for inkjet materials. Because the inkjet-printed layers are so thin, many layers need to be printed to build up a macroscopic part. Each layer must therefore be cured in a matter of seconds upon UV light

exposure, if a centimetre-scale part (several thousand layers) is to be printed in a reasonable timeframe of several hours.

Multi-material printing is easily achievable on an inkjet printer. If microelectronic actuators are used for material dispensing, each nozzle can be made very small, and several nozzles can easily fit onto a print head side by side. Common 2D inkjet colour printers have at least four parallel nozzles to print in different colours. In the same way, 3D inkjet printers can print multiple materials. They can even create material blends with specific properties, the same way a 2D colour printer mixes colours. Such in-situ deposited material blends are referred to as "digital materials"[193] and they allow full-colour 3D printing as well as the creation of material gradients within a part, e.g., a gradual transition from rigid to flexible (see Figure 26A).[38]

The most well-known commercial inkjet 3D printers are from Stratasys' PolyJet family (Stratasys Ltd., USA), which includes the Objet Connex range of printers. Prices for these printers start at well above $100,000. They can print multiple materials, including elastic materials, with very high resolution. They also use soluble support material, giving almost infinite design freedom for printed parts. The Objet family printers are closed systems and only operate with proprietary materials. This makes them not only very expensive but also unsuitable for experimental use beyond the range of materials available from Stratasys. More open inkjet systems that are suitable for research applications are available from various manufacturers such as microdrop Technologies (Germany), Fujifilm Dimatix (USA), and MicroFab Technologies (USA). These all offer picolitre DoD inkjet dispensers as well as complete 3D printing systems. The jetlab® printers made by MicroFab are not actually true 3D printers as they are not designed to build full 3D objects, but they do allow multi-layer deposition. Printed structures as tall as 300 µm have been demonstrated.[194] All these platforms offer dispensing of arbitrary materials, although the material selection remains limited by the rheological properties of the ink formulation. Unfortunately, these commercial systems are all very expensive and not accessible to many researchers. Efforts have been made to repurpose cheap office inkjet printer with piezoelectric DoD technology for use with custom materials,[195,196] or to develop a low-cost, open-hardware DoD print

head,[191] but unlike with FFF and consequently DIW printing, no widespread, affordable DoD printing solution has emerged yet.

ACEO® is a new, proprietary 3D printing technology developed by Wacker Chemie AG (Germany) that allows DoD printing with silicone rubber.[197] They use Wacker's own UV-curable silicone rubber and have developed a DoD technology capable of printing "raw" liquid silicone rubber, despite its high viscosity, albeit at rather large layer heights of 0.4 mm.[198] Printing of PneuNet actuators and grippers has been demonstrated using this technology (see Figure 26D).[199] ACEO® has also demonstrated multi-material printing (see Figure 26E), including with conductive silicone composites.[200] However, their conductive material can currently only withstand up to 25 % strain. ACEO® printers or deposition systems are not currently for sale, but Wacker offers a print service to fabricate printed silicone rubber parts on demand. This limits the accessibility of their new DoD system. Nevertheless, the technology for inkjet printing with high-viscosity inks, and in particular with highly elastic silicone rubbers, has great potential for additive manufacturing of soft robotic devices and artificial muscles.

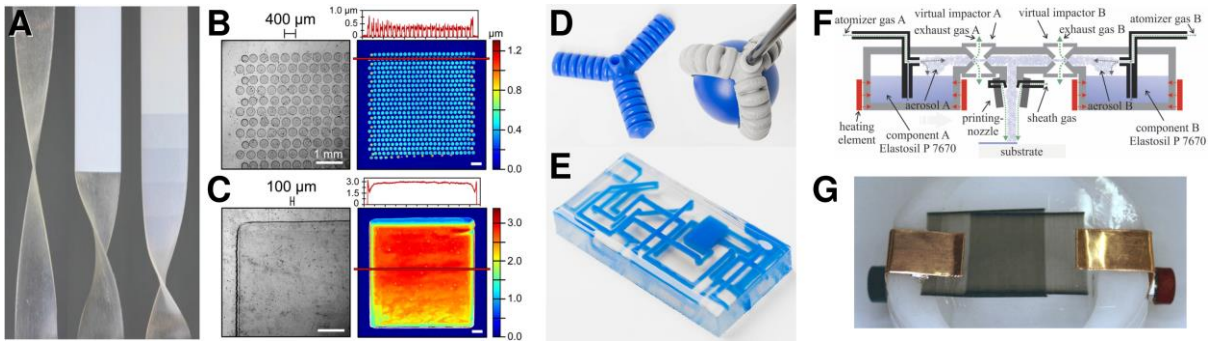

Figure 26. Inkjet-printed soft structures and devices. A) Inkjet-printed specimen of "digital materials": fully flexible (left), half rigid and half flexible (middle), and gradual transition from rigid to flexible over 9 discrete segments (right). All specimen were printed on a Connex500.[38] B-C) Inkjet-printed silicone films made of UV Electro 225-1. The process can produce individual droplets (B) or continuous films (C) with highly consistent thickness profile.[192] D-E) Inkjet-printed silicone part from ACEO®, demonstrating functional PneuNet grippers (D) and multi-material printing (E) of complex 3D structures (from ACEO). F) Schematic of aerosol jet system for printing of two-component silicone rubber.[201] G) Aerosol-jet-printed DEA.[201]

Several research groups have explored the use of inkjet printing for manufacturing of DEAs. A two-membrane antagonistic DEA assembly was 3D printed on an Objet Eden

printer back in 2009, however, the device still required manual assembly and application of electrodes.[109] More recently, Inkjet-printed silicone membranes and carbon black electrodes have been demonstrated using a jetlab® 4 platform.[130,192] High-quality, thin silicone layers of 2.3 µm thickness with only 0.06 µm (2.6 %) standard deviation were printed using UV-curable silicone rubber UV Electro 225-1 (see Figures 26B-C).[192] Electrode layers with thickness as low as 0.38 µm have been printed with carbon black ink.[130] The printed electrodes have been shown to have good cycle stability for over 10^7 cycles at 5 % strain.[129] For both inks, organic solvents are necessary to reduce their viscosity to the recommended level for the jetlab system between 0.5 mPa·s and 40 mPa·s. A high volume of solvent can help to achieve low layer thickness but it increases print time as solvents need to evaporate and it can also lead to thickness inconsistencies through the so-called coffee stain effect.[202] A fully printed DEA, including a rigid frame, elastic membrane, and electrodes, has been fabricated using this method.[203]

Aerosol jet printing has also been used to fabricate DEAs.[201,204] Aerosol jet printing is a different type of inkjet printing, where the ink is atomised to create an aerosol and then ejected by the flow of a carrier gas. The use of a sheath gas allows the formation of very tight aerosol jets to print micrometre-sized features with high precision. Aerosol jet printing has previously been used to make conductive traces from silver ink with ~20 µm feature size and ~3 µm thickness on flexible substrates.[205] The same technique was used to print silicone films as thin as 10 µm by using a mixing nozzle that mixes two aerosols of a two-component, thermal-cure silicone (Figure 26F).[204] The materials were heated to reduce viscosity below 1 Pa·s to allow atomisation. Using a third aerosol jet with an ink of reduced graphene oxide as electrode material, fully-printed single-layer DEAs were fabricated (Figure 26G).[201] A two-layer stacked DEA has also been printed, showing that multi-layer prints are fundamentally possible. Unfortunately, the process still suffers from large variations in layer thickness and fairly long print times per layer of several minutes, which is not suitable for multi-layer DEAs with hundreds of layers.

2.5.4. Stereolithography

Stereolithography (SLA, for stereolithography apparatus) is a 3D printing technique where a liquid polymer resin in a vat is photopolymerised layer by layer, either at the top or bottom of the vat, to form a solid part (see Figure 23D). The materials used are very similar to those used in inkjet 3D printing (see Section 2.5.3) because they also need to have low viscosity and photopolymerise quickly. However, instead of depositing the material layer by layer in the desired shape, the solid part is drawn form a vat of liquid resin. Layers are cured by shining light on the resin surface or through the bottom of the vat, depending on the process. The part, including the newly solidified layer, is then lowered (or raised) to allow a new layer of liquid resin to flow in and be photopolymerised to form the next layer of the 3D part.

A laser can be used as the light source to precisely trace the shape of each layer of the object. Alternatively, digital light processing (DLP) is used to produce dynamic masks and illuminate the entire surface of each layer at once. The latter is therefore also called DLP printing.

SLA/DLP printing has similar material requirements as inkjet printing. Low viscosity is required so uncured material can flow to form each new layer. A highly viscous resin would exert considerable shear forces on the printed part as it is lifted or lowered, which could lead to deformation and reduce dimensional precision of the print. As with inkjet printing, there are some elastic materials available for SLA printing, such as Spot-E from Spot-A Materials (Spain). Indeed, the same materials can be used for both processes. TangoPlus has been used to make printed PneuNet actuators on a custom-built DLP printer (Figure 27A).[111]

Multi-material printing with an SLA system is possible, but not very practical. The part needs to be transferred from a vat with one material to a second vat with another material, and back, for each layer. In between, the part needs to be washed to avoid contamination and mixing of the two materials. Such processes have been demonstrated but they are slow and wasteful due to the additional washing step between layers of different materials.[206] One interesting adaptation of the DLP process for multi-material printing, which has been developed recently, is called Solution Mask

Liquid Lithography (SMaLL). It uses a resin of two different polymers which are sensitive to different wavelengths. Selective exposure can cure either one or both components and make combined rigid and soft structures (see Figure 27E).[207]

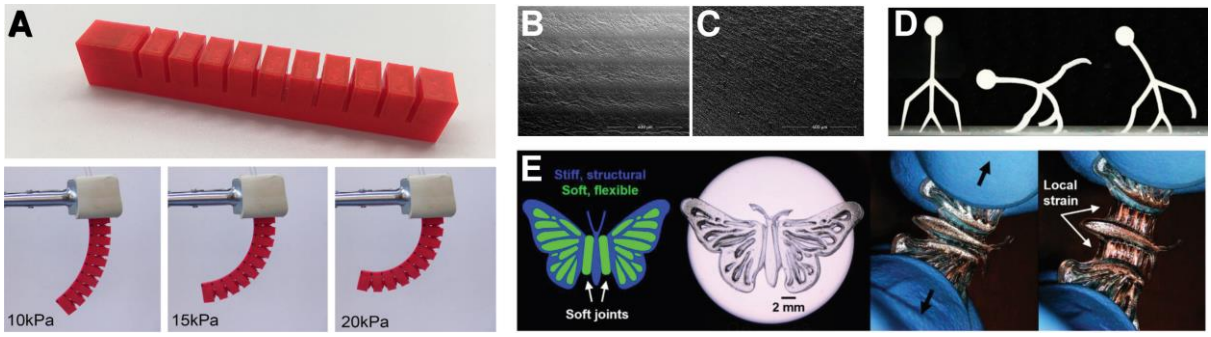

Figure 27. SLA-printed soft structures and devices. A) DLP-printed PneuNet actuator made of TangoPlus, shown at rest and under varying actuation pressure.[111] B-C) Micrographs comparing the surface of a conventional SLA part (B) showing visible layers with one made by the CLIP process (C) where no layers are discernible (from Carbon3D). D) DLP-printed figure made of electroactive hydrogel in three different deformation states which can be generated through application of an electric field.[208] E) Printed butterfly model using the SMaLL process which allows incorporation of soft and rigid regions.[207]

SLA printers are available from many different companies. EnvisionTEC (USA) are one of the largest manufacturers of professional SLA printers. They offer a range of DLP printers, both desktop-size and large-scale, with prices starting around £7000 for the small units. One of the most popular desktop SLA platforms is the Form 2 by Formlabs (USA) which offers high-quality desktop SLA printing for under £5000. A variation of the DLP printing process called continuous liquid interface production has been developed that can produce continuous parts with no discernible layers (see Figures 27B-C).[209] The technology has been commercialised by Carbon3D, Inc. (USA) and it allows their printers to print faster and produces parts with more isotropic mechanical properties. Carbon3D does not sell their printers but rather leases them on a yearly subscription. Each of the manufacturers offer their own range of materials. These also include some flexible and elastic materials, but commercial systems are generally not designed to work with custom-formulated materials. To the best of our knowledge, there are no commercial SLA printers that offer multi-material printing. Because of the relative simplicity of DLP printers, many researchers have used custom-built DLP systems to save costs and have full flexibility with the use of experimental

materials.[110,111,208] Examples of printed soft structures include more PneuNet-type actuators[110] as well as electroactive hydrogel actuators (see Figure 27D).[208] We are not aware of any attempts to print DEAs using a multi-material SLA process.

2.6. Laser-scribed materials

Laser treatment methods have been used on various materials to selectively induce changes in material properties. The term laser scribing will be used in the context of this thesis to describe any form of laser treatment with the purpose of modifying some characteristic of a material, as opposed to ablation or cutting, which is used to remove material. The ability to induce such material modifications locally makes laser scribing processes interesting for the mask-less production of arbitrary, high-detail geometries and patterns. In this section, several laser-scribed materials are presented that are relevant to our work regarding compliant electrode materials and fabrication.

2.6.1. Laser-scribed graphene oxide

Graphene oxide (GO) is a derivative of graphene with oxygen-containing functional groups attached to the basal plane and edges of the graphene sheets (see Figures 28A and B). These functional groups make GO water-soluble. They also decrease the inter-layer adhesion between GO sheets compared to graphene/graphite. This is important because it means that GO can be exfoliated into single-layer nanoparticles by light ultrasonication in water with no need for surfactants to stabilise the dispersion and prevent restacking of the sheets. GO can be produced from graphite powder by a chemical reaction with potassium permanganate in a mixture of nitric and sulfuric acid which is known as the Hummers method.[210] This process is easily scalable and opens a route to large-scale industrial production of graphene nanomaterials.

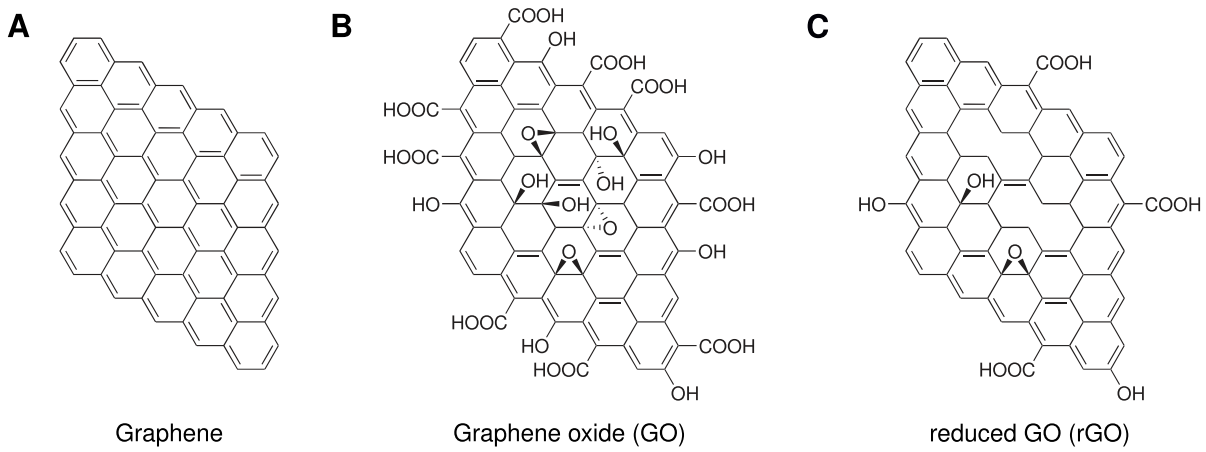

Figure 28. Structures of graphene, graphene oxide, and reduced graphene oxide. A) Graphene, a defect-free hexagonal lattice of carbon atoms. B) Graphene oxide, with various oxygen-containing hydroxyl, carboxy, and epoxy groups. C) Reduced graphene oxide with defects and some remaining side groups. (modified from Wikimedia Commons)

GO has far superior processability than graphene thanks to its water-solubility, however, it does not display many of the important characteristics of graphene that make it so desirable as an electrode material, most importantly, its conductivity. To restore the electrical conductivity, oxygen species on the basal plane of the GO sheets must be removed. This can be done by either chemical or (photo-) thermal reduction to yield reduced GO (rGO).[211] rGO is different from pristine graphene as it retains some amount of oxygen-containing side groups as well as defects introduced during oxidation (see Figure 28C). Because of this, the conductivity of rGO is usually on the order of 10^2 S/m or less,[211] compared to 10^6 S/m for nearly defect-free graphene made by carbon vapour deposition.[212] The properties of rGO vary greatly between different reduction methods.[213,214]

Direct laser scribing of GO has been found to be a facile method for producing precisely patterned rGO films. Effective laser reduction can be achieved under various conditions using different types of laser systems,[215–218] including a low-cost LightScribe™ DVD drive (see Figure 29).[219–221] Laser-scribed graphene oxide (LSGO) has been used to produce a whole range of electronic devices, many of them flexible.[219,221–228] Only in the last two years has LSGO been used on stretchable substrates, including human skin, to make truly soft devices.[228–232]

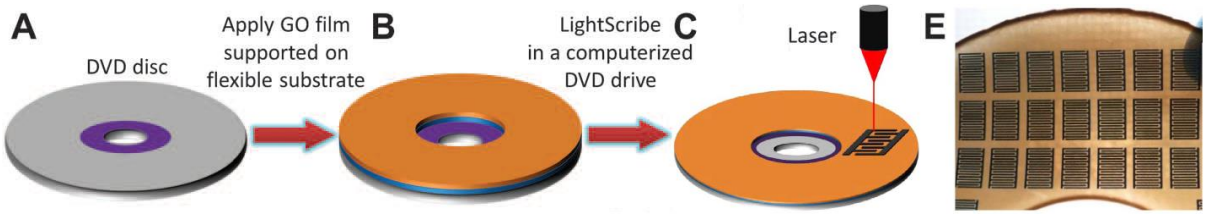

Figure 29. Laser scribing of GO using a LightScribe DVD drive. (modified from [219] and [220])

In Chapter 3 of this thesis, the use of LSGO as compliant electrodes for DEAs is explored. In-situ laser scribing of GO on soft substrates has only recently been demonstrated and to the best of our knowledge, the use of LSGO as an electrode material for DEAs has not been described in the published literature.

2.6.2. Laser-induced graphene

Direct laser scribing of polyimide (see Figure 30A) has been found to produce porous graphene films through carbonisation of the polymer material.[233] This is known as laser-induced graphene (LIG) and it shows good electrical conductivity as well as high effective surface area. LIG has been used for fabrication of flexible electronic components such as supercapacitors.[234] The fabrication of 3D LIG structures has also been demonstrated by stacking LIG layers and subsequent laser etching.[235] Soft LIG strain sensors have been fabricated by transferring LIG films to stretchable PDMS substrates (see Figure 30).[236]

Recently, it has been shown that LIG can be produced at ambient conditions on a wide variety of organic substrates other than polyimide, including various common polymers, wood, foods such as bread or potatoes, and even cotton fabric (see Figure 31A).[237] LIG is interesting because it offers a method to produce precise, conductive patterns on a wide variety of substrates using nothing but simple direct laser scribing. It has been shown that LIG films can be flexible and stretchable. LIG is therefore another promising candidate for stretchable electrode materials for DEAs and other soft electronics. Although the use of LIG as electrode material is not explored in this thesis, the fact that certain polymers can be converted to a conductive carbon material when laser scribed inspired our work on direct laser scribing of PDMS presented in Chapter 4.

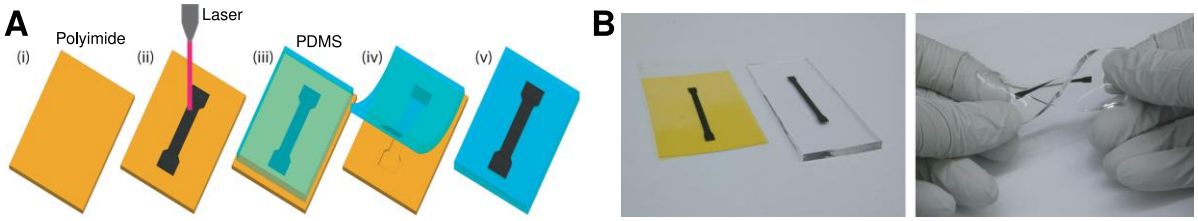

Figure 30. Laser-induced graphene (LIG) stretch sensor. A) LIG is produced by direct laser scribing of polyimide and transferred to PDMS. B) LIG pattern on polyimide film (left) and soft LIG sensor on PDMS (right). (modified from [236]).

2.6.3. Laser-scribed silicone rubber

Direct laser treatment of silicone rubber (PDMS) has been explored from as early as 1996 in order to produce superhydrophobic surfaces.[238] Various groups have since used laser scribing on PDMS for wettability modification or to prepare the surface for selective metallisation.[239–242] It has also been shown that surface modification of PDMS can be achieved using cheap, low-power diode lasers.[243–245] Due to the presence of silicon in the polymer, the materials formed by laser scribing of PDMS differ from LIG produced on silicon-free materials. The exact composition appears to vary greatly between different silicones and different laser scribing methods (see Table 5, Appendix, Section A1). The term laser-scribed silicone rubber (LSSR) will be used in the scope of this thesis to describe any material produced by this method, regardless of the exact chemical composition. Metallic silicon, silicon carbide, amorphous and graphitic carbon, carbon nanotubes, and silica have all been found in LSSR. Table 5 (Appendix, Section A1) shows an overview of previous reports of LSSR, including process parameters and chemical composition.

In March 2018, we reported for the first time that laser scribing of silicone rubber can be used to produce electrically conductive films.[246] None of the previous publications on LSSR mentioned electrical conductivity. Since then, an article reporting the fabrication of resistive strain sensors using based on LSSR has been published.[247] Therein, conductive patterns were produced by direct laser scribing of Ecoflex® 00-30 silicone rubber (see Figure 30E). The authors note that only a narrow range of process parameters leads to the formation of a conductive material (silicon carbide). If irradiation energy per area was too high, non-conductive silicon oxide (SiO_x) was

primarily formed. The reported LSSR strain sensors are functional up to 5 % linear strain.[247]

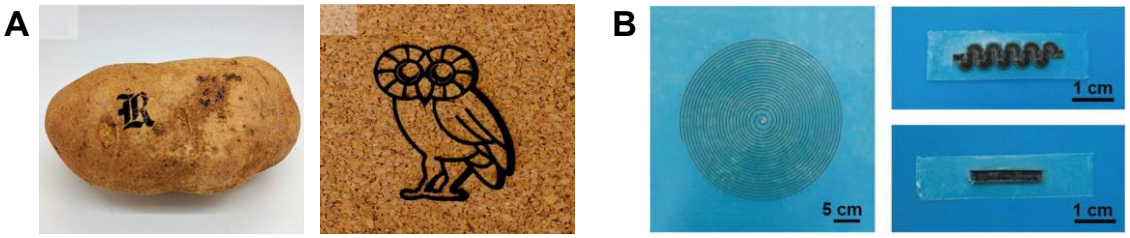

Figure 31. Laser scribing of different substrates. A) LIG produced on various organic substrates: potato and cork.[237] E) Conductive LSSR patterns made by direct laser scribing of PDMS.[247]

Because of the compelling simplicity of direct laser scribing, LSSR was investigated as a potential electrode material for DEAs as well as for other functions as part of the LAMDA printing process. This work is presented in Chapters 4 and 5.

2.7. Conclusion

As the field of soft robotics grows, there is an ever-greater need for powerful manufacturing methods for soft structures and devices. Particularly for soft actuators like DEAs, advancements are mainly restricted by limitations of our existing materials and manufacturing techniques (see Section 2.3). 3D printing has enabled the fabrication of completely new, complex structures with interesting functionality that could not be manufactured by other methods. Unfortunately, 3D printing with soft materials is still rather limited and printers capable of printing functional parts from soft materials are very expensive (see Section 2.4). Laser scribing has emerged in recent years as an intriguing new method for simple, low-cost fabrication of thin, conductive films with intricate patterns (see Section 2.6). We believe that this could be a very useful tool for manufacturing of artificial muscles and soft devices.

The following chapter investigates the use of laser scribing for the fabrication of DEA electrodes. Chapters 4 and 5 then explore the further integration of laser scribing and 3D printing which could pave the way to multi-material printing of functional soft devices and artificial muscles.

Chapter 3

Laser-scribed graphene oxide for compliant electrodes

The content of this chapter is based on the article "Laser-Scribed Graphene Oxide Electrodes for Soft Electroactive Devices" published in Advanced Materials Technologies Volume 4, Issue 2 in February 2019.[248] All text and figures from the article that are included in this thesis were written and created by Djen Kühnel.

3.1. Introduction

A major challenge for all soft, stretchable electronic devices is the need for compliant electrical conductors. DEs in particular rely on compliant electrodes that are able to expand in area during actuation. A range of different materials has been proposed for use as compliant electrodes, but all of these come with certain drawbacks (see Section 2.3.3). Conductive rubber composites based on graphite or carbon black are common, but they require high filler loading to achieve good conductivity, which has an adverse impact on their mechanical properties (see Section 2.3.3.3). Composites with nanofillers such as carbon nanotubes or silver nanowires have achieved high conductivity at low filler loadings, however, these tend to be more expensive and more difficult to prepare.

As DE devices become more sophisticated, there is also a growing need for precise patterning of the compliant electrodes.[69] Various methods have been proposed to fabricate compliant electrodes with complex patterns and high geometric detail.[68,130,145,146] However, these all have certain limitations such as high cost of the required equipment, reliance on prefabricated moulds or masks, or the use of transfer techniques which can introduce defects and alignment errors. Particularly for research

and prototyping of DE devices, adaptable fabrication methods are required that do not rely on prefabricated tools. Simple, low-cost methods are also desirable in order to make the exciting field of DEs more accessible to a wider community of researchers. To this day, the method of hand painting carbon grease electrodes (see Section 2.3.3.2) is still widely used in DE prototyping, despite its shortcomings. This method is so successful because it is simple, cheap, relatively quick, does not require expensive equipment and can produce arbitrary geometries, albeit with limited precision. An alternative method with similar characteristics but offering improved repeatability and resolution would be highly desirable.

In this chapter, the use of laser-scribed graphene oxide is explored as a simple, low-cost, semi-automated method to produce compliant electrodes for DEAs with arbitrary patterns and high detail.

3.1.1. Laser-scribed graphene oxide

Graphene oxide (GO) is a derivative of graphene that is produced by addition of polar, oxygen-containing functional groups to the graphene sheets (see Section 2.6.1). Unlike graphene, it can be produced economically at a large scale using current methods and is easily processable in water with no need for organic solvents. GO itself is not electrically conductive but it can be converted by various methods from GO to reduced GO (rGO), where some of the oxygen-containing functional groups have been removed and the electrical conductivity restored to a certain degree.[211] Laser scribing is one method that allows highly localised reduction of a GO film. The resulting material is commonly called laser-scribed graphene (LSG), although we prefer the term laser-scribed graphene oxide (LSGO) since LSGO is a type of rGO, which is chemically and structurally different from graphene (see Section 2.6.1, Figure 28). LSGO was first demonstrated by El-Kady et al. in 2012 using a LightScribe® DVD drive.[219] It has since been used to fabricate a variety of devices using different substrates and different laser systems.[215–232] However, to the best of our knowledge, we are the first to have demonstrated fabrication of compliant electrodes for DEAs using LSGO.

3.2. The laser-scribing process

Laser irradiation of a GO film induces local reduction, which causes a visible change in colour (see Figure 28A) and an increase in electrical conductivity by around five orders of magnitude.[218,220] Specific areas of the film can be irradiated selectively to produce a desired pattern. Areas that are not irradiated remain as non-conductive GO. 2D patterns are created by scanning the GO film line by line (see Figure 32B). The desired pattern is typically specified as a bitmap image, which the laser engraver software converts to a line pattern for laser scribing. Thin (≤1 µm) GO films can be produced by a simple drop casting method from aqueous GO dispersion (see Section 3.3.1.2). After laser scribing, excess GO can be removed by washing with water (see Section 3.3.1.4). The LSGO, which is more hydrophobic, remains in place. Washing with ethanol instead of water can be used to also remove LSGO. This technique was used to inspect the substrate for damage from the laser scribing process (see Section 3.2.1, Figure 37).

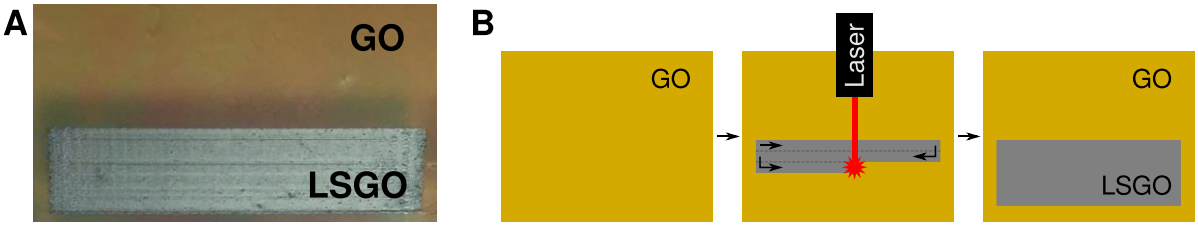

Figure 32. The laser scribing process for graphene oxide. A) Photograph of a section of GO and LSGO film. GO undergoes a visible change in colour during laser scribing. B) Schematic of the laser scribing process. 2D patterns are created line by line.

3.2.1. Laser engraver

El-Kady et al. used a LightScribe® DVD drive for LSGO production.[219] This method is very low cost as LightScribe®-capable DVD drives can be purchased for under £20. However, the use of such a drive limits the control over laser intensity and exposure. It also puts a limit on the size and possible substrates for the LSGO films since it must be carried on a LightScribe® DVD in order for the DVD drive to perform the laser scribing. In our work, a low-cost desktop laser engraver (generic, labelled "Benbox") was used instead, which was purchased on eBay for less than £100. The engraver is shown in Figure 33A. It consists of a motorized, two-axis cartesian gantry, driven by miniature stepper motors. A 405 nm, 250 mW violet-blue laser diode is mounted on

the gantry. The workspace of the engraver is 70 x 76 mm. Resolution of both axes is 0.1 mm. Maximum reliable operating speed is 1000 mm/min. At faster speeds, the motors may skip steps when accelerating since the firmware does not provide acceleration control. Laser power is controlled via pulse width modulation (PWM) with 8-bit resolution (0-255). A laser safety enclosure, shown in Figure 33B, was custom built from 3-mm-thick, orange-tint acrylic glass (0.3% transmittance at 405 nm, see Figure 81 in Section 5.3.3.2) to ensure safety of the user.

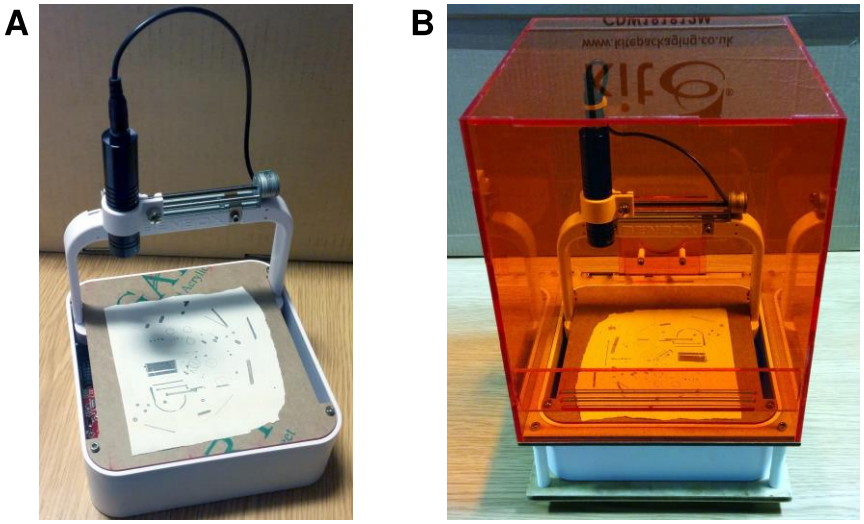

Figure 33. The laser engraver used for LSGO DEA fabrication. A) "Benbox" laser engraver. B) The laser engraver inside its custom-built safety enclosure.

Micrographs of LSGO samples produced using this laser engraver (Figures 34 and 37) reveal wavy rather than straight, parallel lines. This is an artefact caused by vibrations in the gantry mechanism and is one of the downsides of using such a very low-cost device. Nevertheless, we were able to produce uniform LSGO films using this engraver by adjusting the process parameters to ensure sufficient overlap between adjacent lines (see Section 3.2.2.2).

3.2.2. Process parameters

The laser scribing process is mainly controlled by three parameters: power, speed and focus. Their respective influence on the process and the properties of the resulting LSGO films is discussed in the following subsections.

3.2.2.1. Speed

In our work, movement speed of the laser was limited to 1000 mm/min by hardware constraints. At this speed, laser scribing of a small circular electrode with 40 mm diameter takes roughly 20 min. For a DEA, both sides need to be laser scribed resulting in 40 min process time per device. Although good reduction has also been observed when engraving at lower speeds, 1000 mm/min was chosen as the default speed to keep process time low.

3.2.2.2. Power

Higher laser power generally results in higher irradiation energy per area and thus in higher temperatures at the GO surface. Laser power must be high enough to achieve thermal reduction of GO, which occurs around 200 °C.[249] At the same time, it must be low enough to avoid ablation of the GO film.[218] Excessive power can also damage the substrate carrying the GO film. A trade-off must be found where a uniform, coherent LSGO film is produced without damaging the LSGO film or the substrate underneath.

Laser power is controlled via 8-bit PWM at 1 kHz. That means an integer value between 0 and 255 is used to set the duty cycle between 0 % and 100 %. The laser diode has a nominal power of 250 mW. The response of the laser diode to the PWM signal is not be perfectly linear due to finite rise and fall times. It is therefore difficult to determine actual radiant flux for any given setting. Because of this, laser power will generally be specified as a percentage (duty cycle), since this is the most practically relevant parameter.

Suitable laser power was determined empirically by laser scribing several sections of a GO sample at varying power and evaluating the quality of the resulting LSGO films. Figure 34 shows a range of LSGO samples laser scribed at powers between 31 % and 100 %, at a constant speed of 1000 mm/min. It can be seen that line thickness increases with laser power. At high laser power (86 % and 100 %), a bright line in the centre of each LSGO line indicates ablation of LSGO where laser intensity is highest. The micrographs where taken on an Olympus BX50 polarized light microscope (without a polarizing filter) using an Olympus C-5060 WZ digital camera (Olympus Corporation, Japan).

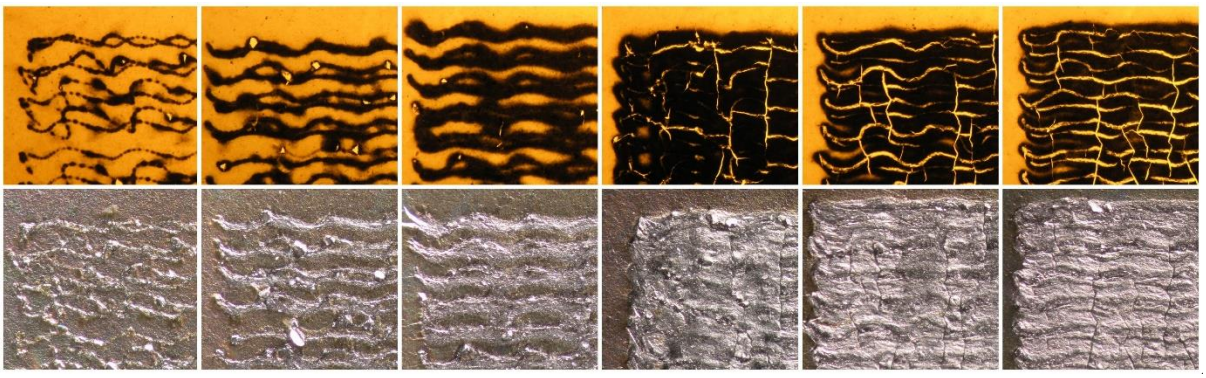

Figure 34. Micrographs of LSGO samples laser scribed at varying laser intensity. Samples were laser scribed at 1000 mm/min at varying relative laser power of 31 %, 45 %, 59 %, 73 %, 86 % and 100 %, respectively (left to right). The top row shows images lit from below. GO appears orange and LSGO appears black due to its high absorbance. The bottom row shows images of the same samples lit from above. GO appears brown-beige and LSGO appears silvery grey. The laser lines are wavy due to vibrations in the laser engraver. At the lowest power (far left), individual dots from the pulsing laser are visible. Each image shows an area of 1 mm^2.

3.2.2.3. Focus

Since line spacing is limited to 100 µm, line width must be at least 100 µm to produce uniform films. As shown in Section 3.2.2.2, power can be increased to increase line width. However, if the power is set too high, ablation of the GO film and damage to the substrate (see Figure 37) can occur. Instead, defocusing of the laser is used as a method to widen the beam at the point where it intersects the GO film, which results in wider lines and more uniform reduction. It was empirically determined that, for our engraver, focussing the laser 6 mm above the surface of the GO film resulted in the most uniform LSGO films with the highest conductivity.

3.2.2.4. Other factors

The results of laser scribing are influenced by several other factors that cannot be directly controlled during the laser scribing process. Film thickness plays an important role since thin GO films are translucent and thus thicker films will absorb more laser energy and reach higher temperatures. Therefore, thicker films require less laser power. The substrate material also has an effect. The thermal conductivity of the substrate will influence heating and cooling rates, which influence the reduction of GO.

Great variation was also found between LSGO films produced from different batches of GO that were purchased from different suppliers, as described in the following section.

3.2.1. Graphene oxide characterisation

Four different batches of graphene oxide were tested for laser scribing: two different batches of graphene oxide aqueous dispersion (4 mg/mL) purchased from Graphenea Inc. (USA) in 2014 and 2016, respectively, one batch of graphene oxide aqueous dispersion (4 mg/mL) purchased from Graphitene Ltd. (UK) in 2016, and one batch of GO prepared in-house by Alex Bell, a colleague otherwise not involved in this work. The latter batch was prepared using the Hummers method.[210] The four batches showed visible differences in colour, ranging from dark brown to bright orange-yellow, as shown in Figure 35B.

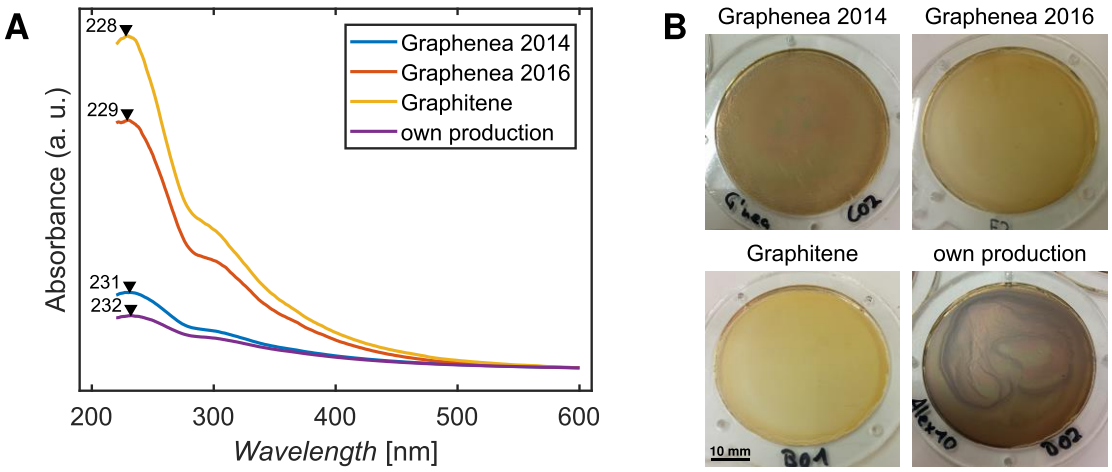

Figure 35. Visual appearance and UV-vis spectra of different batches of GO. A) UV-vis spectra of GO aqueous dispersion from four different batches. Spectra are normalised to the respective absorption at 600 nm which serves to highlight differences in the wavelength selectivity for lower wavelengths. B) Photographs of dry GO films made from the same four dispersions, showing visible differences in colour.

UV-vis absorbance spectra recorded on a Shimdazu UV-2700 Spectrophotometer (Shimdazu Corp., Japan) are shown in Figure 35A. Because of differences in sample concentration, the spectra were normalised to the respective absorbance at 600 nm. The spectra clearly show that the Graphitene and Graphenea 2016 batches show much higher absorbance at shorter wavelengths than at longer wavelengths. In contrast, the batches from Graphenea 2014 and from our own production show only a small

difference in absorbance between high and low wavelengths. This is consistent with the observed colour, since the former two batches have more of an orange-yellow colour (blue light absorbed selectively) whereas the latter two have more of a brown colour (broad absorption over the entire visible spectrum). Since reduced graphene oxide (in dispersion) appears black, these observations indicate that the Graphenea 2014 and Graphitene GO are more strongly oxidised than the other two batches.

Elemental analysis, performed on a Euro EA 3000 (EuroVector Srl, Italy) by the Microanalytical Laboratory at the University of Bristol, reveals the relative amounts of carbon, hydrogen and nitrogen in samples of the four different GO batches, as shown in Table 1. Oxygen cannot be directly measured by this method, but it can be assumed that the missing fraction in each sample is mostly oxygen, although small amounts of other contaminants such as sulphur may also have been present. These results seem to suggest that Graphenea 2014 is actually much more oxidised (lower carbon fraction) than the other batches and also contains more contaminants (nitrogen). The other three batches, particularly Graphitene and our own product, show remarkably similar elemental profiles. These observations are not consistent with the conclusions drawn from the UV-vis spectra and optical appearance of the materials.

Table 1. Elemental analysis of graphene oxide. The relative amounts (in percent) of nitrogen, carbon, and hydrogen are given for each batch of GO.

	Graphenea 2014	**Graphenea 2016**	**Graphitene**	**own production**
N	2.53	0.35	0.76	0.637
C	29.18	40.70	42.73	42.683
H	2.88	2.80	2.72	2.72

Raman spectroscopy of GO samples from different batches reveals only small differences (see Figure 36A). All samples show broad peaks corresponding to the D band (around 1350 cm^{-1}) and G band (around 1600 cm^{-1}) which are characteristic for GO.[213] The intensity ratios between the D and G peaks (I_D/I_G) are indicated for each sample in Figure 36A. This value is often used as a measure of the frequency of defects in carbon materials, with a higher ratio indicating fewer defects.[250] According to this parameter, the batches from Graphenea 2014 and from our own production have fewer defects which means a lower degree of oxidation. This is consistent with the

observations from UV-vis spectrometry (Figure 35). However, it should be noted that the reliability of the I_D/I_G metric for graphene oxide materials has been disputed.[251] An alternative method proposed by King et al.[251] relies on the position of the 2D' peak which can be observed around 3,200 cm^{-1}. Unfortunately, this peak lies outside the range of the recorded spectrum and thus we are unable to apply this improved metric to the GO materials used in our work.

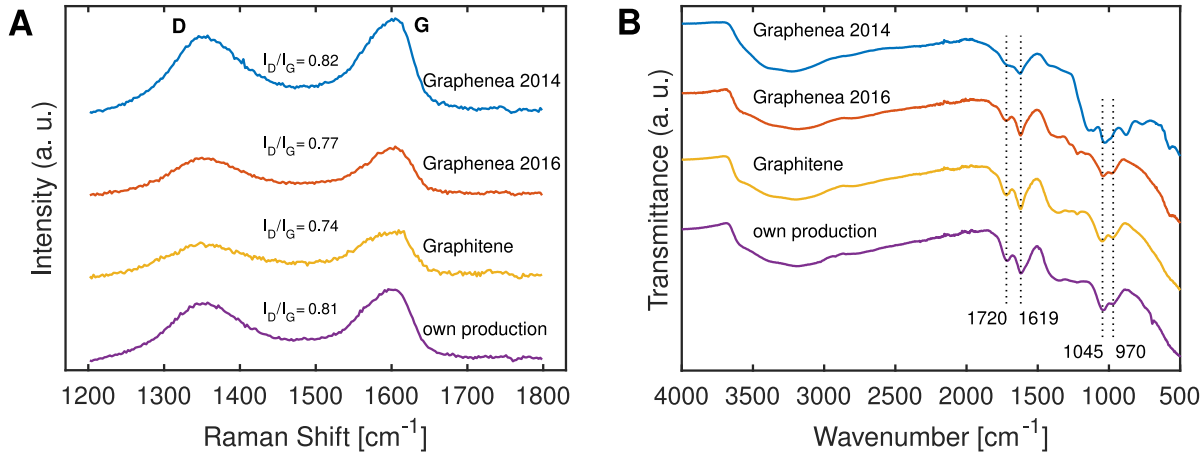

Figure 36. Raman and FTIR spectra of graphene oxide. A) Raman spectra showing characteristic peaks corresponding to the D and G bands. The intensity ratio of the peaks (I_D/I_G) is indicated for each sample. B) FTIR spectra of the different GO samples. Four peaks characteristic for GO are marked by the dotted lines.

Fourier-transform infrared spectroscopy (FTIR) was also used to characterise the GO materials. The transmittance spectra for all four batches are shown in Figure 36B. Only subtle differences are visible between the four samples. Each spectrum shows a very broad peak between 3000 cm^{-1} and 3600 cm^{-1} which can be attributed to hydroxyl groups in GO or remaining water in the sample. (FTIR samples were only dried for one day at ambient conditions so the presence of residual water is expected.) The peak at 1720 cm^{-1} is attributed to C=O stretching.[252] Another peak indicative of aromatic C=C would be expected at 1574 cm^{-1}, however, this is probably obscured by a larger peak at 1616 cm^{-1} due to water, resulting in a single peak seen at 1619 cm^{-1}.[252] The peak at 1045 cm^{-1} is indicative of out-of-plane epoxy groups and the peak at 970 cm^{-1} is attributed to skeletal C-O and C-C bonds.[213] These four peaks, which are indicated by the dotted lines in Figure 36B, appear consistently in all GO batches except Graphenea 2014. In the latter, the C=O peak at 1720 cm^{-1} is greatly reduced and there

are at least three distinct peaks visible below 1200 cm^{-1} which do not line up with the peaks seen in the other spectra.

One possible explanation for the additional peaks in the Graphenea 2014 sample is the presence of contaminants. Nitrogen and sulphur are commonly present in GO produced by the Hummers method where graphite reacts with potassium permanganate in sulfuric and nitric acid.[210] We were unable to attribute the peaks in the FTIR spectrum to any specific contaminant. However, the presence of larger quantities of contaminants in Graphenea 2014 compared to the other samples is also supported by the elemental analysis (see Table 1) which showed a much higher fraction of nitrogen than any other sample. Researchers at the Soft Materials and Colloids Lab at Monash University also found that the presence of contaminants can have a large impact on the properties of GO and that thorough purification by dialysis is necessary to obtain consistent results (personal communication, Rico Tabor, 13/07/2017). We therefore propose that the differences between the batches of GO arise from a combination of varying degrees of oxidation and varying amounts of contaminants. Flake size and the presence of aggregates might also have an impact on the properties of GO but these were not investigated.

The analysis presented here remains inconclusive as to the exact degree of oxidation or the specific nature of contaminants in the investigated GO samples. Unfortunately, a more thorough analysis was beyond the scope of this project. For the purpose of our work, it was found that all tested batches of GO were suitable for laser reduction after addition of L-ascorbic acid (see following section). Graphenea 2016 was therefore chosen arbitrarily and all further experiments were carried out with only this one material to ensure consistency.

3.2.2. Effects of L-ascorbic acid

L-ascorbic acid (LAA) can be used as a mild reducing agent for GO.[253] This reaction is very slow at room temperature. Complete reduction of GO takes more than 24 h at an LAA concentration of 1 mg/mL in a GO dispersion of 0.1 mg/mL.[253] We found that LAA can be used to aid laser reduction when added to the GO dispersion before drop casting. Because the reduction reaction is slow, no notable reduction will occur if a

very small amount of LAA (0.2 mg/mL) is added to the GO dispersion (1 mg/mL) right before drop casting. The resulting GO film is visually indistinguishable from a GO film with no LAA added. The GO film with LAA also does not show measurable electrical conductivity, which means that no significant reduction of GO has occurred at this stage. Reduction by LAA can only occur in a suitable solvent and no further reduction takes place once the films have dried. However, when laser-scribed, the GO films containing LAA produced LSGO with much higher conductivity. Without any LAA added, the minimum observed sheet resistance of any of our LSGO films was 70 kΩ/sq. With LAA added at 0.2 mg/mL, LSGO sheet resistance as low as 8 kΩ/sq was achieved.

With a higher LAA content of 5 mg/mL, sheet resistance of LSGO of 4 kΩ/sq was observed, but the resulting films were visibly thicker and stiffer because the they now contained five times as much LAA as GO (by weight). Hence, the LAA made a large contribution to the film's mechanical properties in this case. An LAA concentration of 0.2 mg/mL (in a 1 mg/mL GO dispersion) was determined as a good trade-off between electrical and mechanical properties. This concentration was therefore used for the fabrication of LSGO DEAs, as described in Section 3.3.1.

3.2.3. LSGO on soft substrates

The major challenge in producing LSGO on elastomer membranes suitable for DEAs arises from heat damage to the elastomer membrane caused during laser scribing. Thermal reduction of graphene oxide starts to occur around 200 °C.[249] The acrylic elastomer VHB 4905, which is commonly used as a dielectric membrane in DEAs, starts to degrade at temperatures above 149 °C, according to the manufacturer.[113] Because of the necessity to use elevated temperatures for GO reduction, this material was found to be unsuitable for the laser scribing process. Instead, ELASTOSIL® silicone films were used (see data sheet in Appendix Section A2.1). These operate up to 200 °C (long term)[105] and can endure short-term, localized heating to temperatures sufficient for GO reduction. However, even on the silicone films, laser damage can occur if laser power is too high. Figure 37 shows three LSGO samples on ELASTOSIL® membranes, laser-scribed at different power. It also shows the respective silicone membranes after LSGO was removed by washing with ethanol. The membrane that

was laser-scribed at 100 % power clearly shows damage caused by ablation of the silicone rubber. However, Figure 37 also shows that, at 60 % laser power, GO can be effectively reduced without visible ablation of the silicone substrate. It is still possible that laser scribing at this power still affects the elastomer, albeit in less visible ways, but the actuation tests (Section 3.3.3) show that there is at least no drastic degradation in mechanical or dielectric strength, as would be expected from a partially ablated membrane. Figure 37 shows three different LSGO samples on the same silicone membrane. The same trend was observed on three separate membranes with LSGO samples prepares in the same manner.

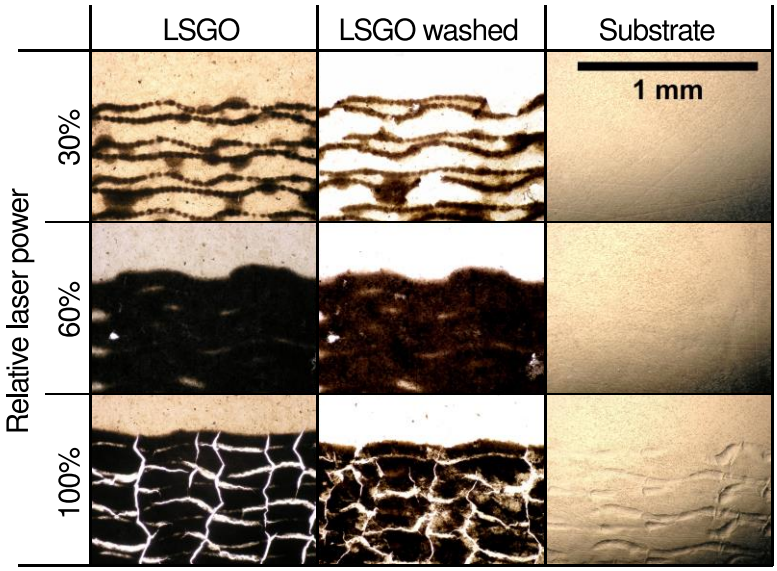

Figure 37. Micrographs of LSGO films on silicone substrates. The first column shows the films directly after laser scribing. LSGO appears black, unreduced GO appears beige. The second column shows the same LSGO films after unreduced GO was removed by washing with water. The third column shows the silicone substrates after completely removing GO and LSGO by washing with ethanol (the lighting was adjusted to highlight surface structure). At 100% laser power, damage to the membrane is clearly visible. All films were laser-scribed at 1000 mm/min.

3.2.4. Properties of LSGO

For use as compliant electrodes, both the mechanical and electrical properties of LSGO are important. Section 3.2.2.1 provides a qualitative review of the mechanical properties of LSGO, which helps to understand how the electrical properties change under strain, as described in Section 3.2.2.2.

3.2.4.1. Mechanical properties

The dried GO films, before laser scribing, are very brittle. They crack easily under small strain or even just slight bending. Careless handling can cause damage to the unreduced films. One LSGO film on a silicone membrane was accidentally dropped to the floor from about 1 m height before it was laser scribed. The cracks caused by the fall are clearly visible in the laser-scribed film, shown in Figure 38A. For comparison, Figure 38B shows a different LSGO film that was (intentionally) dropped in the same manner after it had been laser scribed. On this film, no cracks are visible. Figure 38C shows the same film after training (see Section 3.3.1.6) and actuation tests (see Section 3.3.3), where it was subjected to large out-of-plane strains. Still, there are no visible cracks in the surface. Cracks do appear in the LSGO surface while it is subjected to large strain, as shown in Figure 38D. However, these cracks close again when the membrane is relaxed. There are no visible signs of delamination from the silicone substrate during stretching.

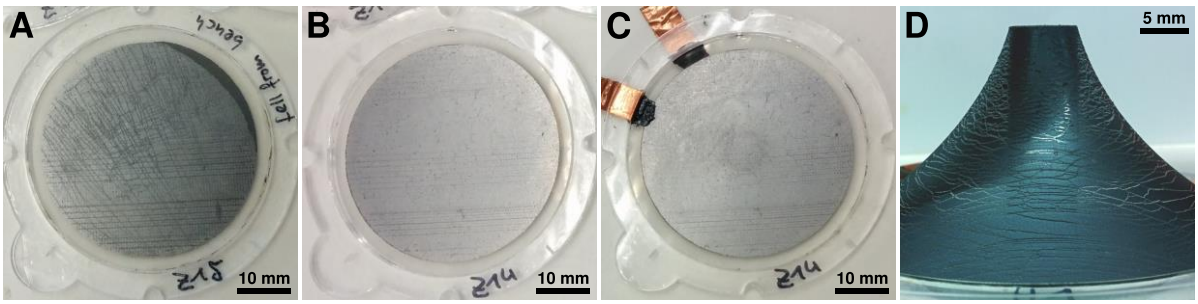

Figure 38. Mechanical properties of LSGO films on silicone substrates. A) LSGO sample that was accidentally dropped before it was laser scribed, resulting in visible cracks throughout the film. B) LSGO sample that was dropped in the same manner as (A) after it had been laser scribed, which did not result in visible cracks. C) The same membrane shown in (B) after actuation tests, where it was subject to large strain, similar to the membrane shown in (D). There are still no cracks visible. D) LSGO film being stretched out of plane. Large cracks are visible in the film, which close again when the membrane is relaxed. No delamination is evident.

The brittle nature of the unreduced GO films can be explained by the fact that the GO sheets in a drop cast film are closely stacked (see Figure 39A) and display strong interactions due to the presence of polar functional groups. This leads to a very stiff structure where cracks can easily propagate, as illustrated in Figure 39C. In contrast, LSGO has a sponge-like structure with greater distance between individual sheets (see Figure 39B). Interactions between sheets are also weaker because most of the polar

groups have been removed. The loosely stacked structure prevents crack propagation. When LSGO is stretched, the sheets separate in different locations, so that electrical contact can be maintained through adjacent layers. This is illustrated in Figure 39D. At large strain, sections of the LSGO film become completely separated, eventually resulting in loss of conductivity, as shown in Figure 39E.

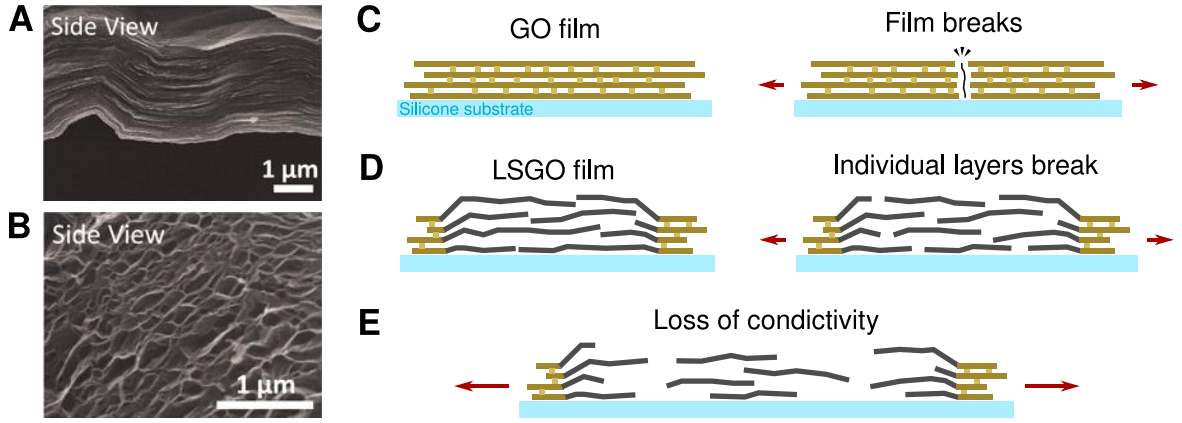

Figure 39. LSGO structure and behaviour under strain. A-B) Cross-section electron micrographs of GO (A) and LSGO (B).[219] C) Schematic of a GO film at rest and under small strain. The connections between the layers indicate strong interactions between polar functional groups in LSGO. D) Schematic of an LSGO film at rest and under small strain. E) Schematic of the LSGO film at large strain.

To better understand the mechanical properties of GO and LSGO films, stress-strain curves of laser-scribed and non-laser-scribed samples on silicone films in comparison with pristine silicone films could have provided valuable insights. ELASTOSIL silicone has a very low initial modulus around 0.5 MPa[105] and the drop cast GO films were on the order of 1 µm thickness, thus, expected forces during strain tests would be on the order of micronewtons. Unfortunately, a sufficiently sensitive load cell to record these features was not available. High strain characterisation of the silicone membranes (to determine elongation at break, which would have been possible with available equipment) were not carried out because the expected actuation strains (see Section 3.3.3) were well below the rated maximum elongation of 450 %.[105]

3.2.4.2. Electrical properties

The most important property of a compliant electrode material is its electrical conductivity, and how its conductivity changes under strain. Sheet resistance of LSGO films (prepared according to the procedures in Sections 3.3.1.1 to 3.3.1.3) at 0 % strain

is 7.2 kΩ/sq (n=3, σ=1.2 kΩ/sq). This was measured by a two-point method using a Fluke 77 IV digital multimeter (Fluke Corporation, USA). For a discussion of different measurement methods for sheet resistance, see Chapter 4, Section 4.6.4.

To measure resistance under strain, LSGO samples were prepared on unstretched silicone film, according to the procedure in Section 3.3.1.2. A rectangular area of 50 x 10 mm was laser scribed for each sample at 1000 mm/min and 60% laser power. Samples were tested on a custom strain rig (see Figure 40C) consisting of two metal clamps, one static and one mounted on a motorised linear stage (Zaber X-LSQ150B-E01, Zaber Technologies Inc., Canada). Resistance was measured between the clamps using a HA-151B Potentiostat/Galvanostat (Hokuto Denko Corporation, Japan). A small amount of CG was applied between the clamps and the LSGO sample to reduce contact resistance.

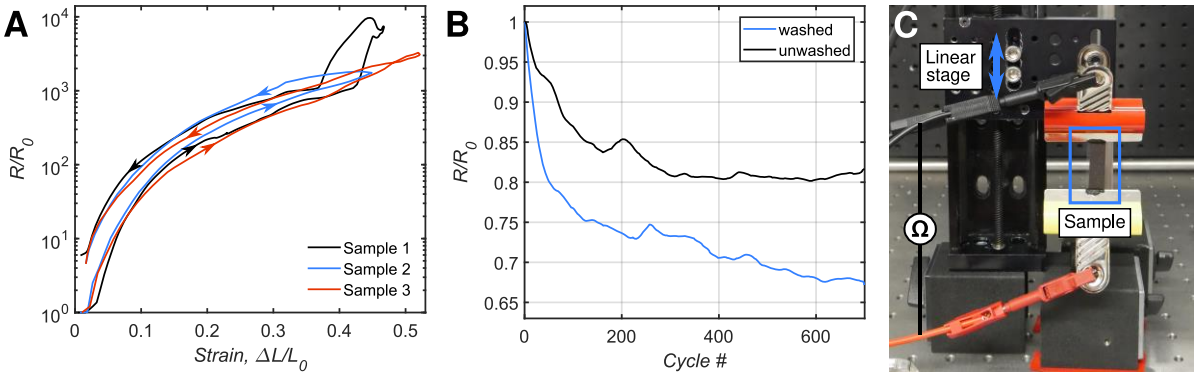

Figure 40. Resistance of LSGO films under strain. A) Relative resistance increase plotted against uniaxial strain for three LSGO samples. One full cycle is shown for each sample. B) Relative change in resistance at 33 % uniaxial strain over 700 strain cycles for one washed and one unwashed LSGO sample. C) Uniaxial strain rig used for measuring LSGO.

Figure 40A shows the relative change in resistance against uniaxial strain for three LSGO samples. Each sample was stretched until the measured resistance exceeded 50 MΩ, and then relaxed. It can be seen that all samples maintained measurable electrical conductivity up to 40 % linear strain, although resistance increased by three orders of magnitude. It can also be seen that there is a residual increase in resistance at 0 % strain after the first strain cycle. To determine the cycle stability of the LSGO films, samples were subjected to repeated strain up to 33 % for 700 cycles. Figure 40B shows the relative change in resistance against cycle number. Interestingly, it was found that resistance decreases with the number of strain cycles, steeply at first, before

seemingly approaching a constant value. A similar reduction in resistance over the first few hundred strain cycles, has also been documented for Inkjet-printed CB electrodes.[129,130] Resistance of these electrodes decreased at first, but started increasing again after 300 cycles at 50 % uniaxial strain. Judging by this example, it has to be assumed that the resistance of LSGO electrodes will also start increasing if subjected to a higher number of strain cycles. Still, the fact that resistance continued decreasing up to 700 cycles could be seen as an indication of good cycle stability. Strain tests with a much higher number of cycles will need to be carried out to fully determine the long-term stability of LSGO compliant electrodes.

Directly comparing the electrical conductivity of LSGO under strain to CG is difficult since the thickness of CG electrode, brushed on by hand, is not uniform and the exact amount of CG per area is not known. CG has a bulk conductivity around 1 S/m. [131] That means a CG film of the same thickness as GO (~1 µm) would have a sheet resistance of 1 MΩ/sq, more than two orders of magnitude higher than LSGO. However, CG is known to show only a small increase in conductivity under strain, less than one order of magnitude at 150 %.[254] Comparing this to the resistance increase observed in LSGO of three orders of magnitude at 40 % strain, it can be assumed that CG, even if applied at the same thickness as GO, will have lower resistance if strain exceeds 40 %. It should also be noted that this discussion is based on uniaxial strain tests, which are not necessarily representative of the performance of the same material subjected to biaxial strain.

3.3. LSGO DEAs

To show the suitability of LSGO as an electrode material for DEAs, several DEAs with different electrode geometries were fabricated and their performance evaluated in comparison with a control group of DEAs with CG electrodes.

3.3.1. LSGO DEA fabrication

The fabrication process for DEAs with LSGO electrodes is shown in the schematic in Figure 41. First, an aqueous GO dispersion is drop cast onto a pre-stretched elastic membrane. After drying, the drop casting process is repeated on the other side of the membrane. Laser scribing is used to reduce the GO film in the desired electrode

pattern, first on one side of the membrane, then on the reverse side. Unreduced GO is removed by washing with water, leaving only the LSGO pattern behind. The individual steps of the process are described in more detail in the following subsections.

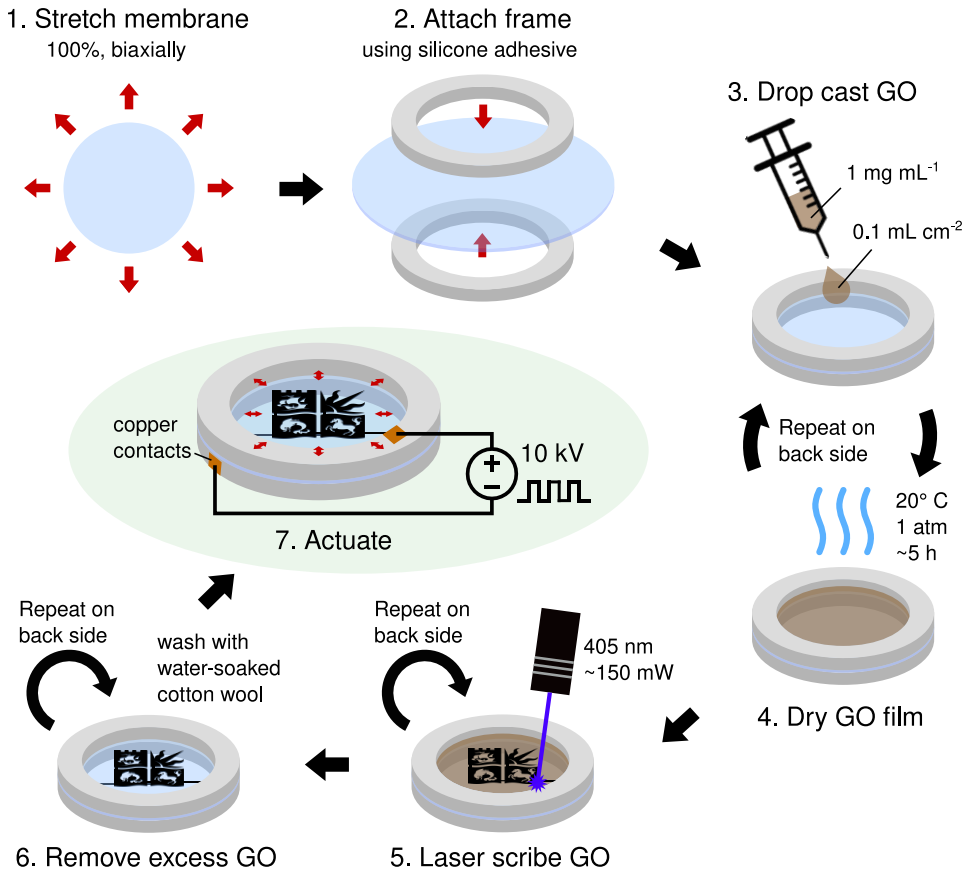

Figure 41. Diagram of the LSGO DEA fabrication process.

3.3.1.1. Membrane preparation

A 125 x 125 mm square piece of ELASTOSIL® silicone film of 0.2 mm thickness is pre-stretched 100 % biaxially. Stretching of the silicone membrane is done manually. Twelve marks are made on the unstretched film using a stencil, evenly spaced on a circle of 100 mm diameter. The membrane is then stretched over twelve rounded pins, arranged evenly spaced on a circle of 200 mm diameter, one pin at a time until all marks are aligned with the corresponding pins. Next, circular, laser-cut acrylic frames with an inner diameter of 45 mm are glued to the stretched membrane using SilPoxy® silicone adhesive. Frames are glued pairwise to either side of the membrane. One piece of pre-stretched membrane can fit seven frames. Positioning and alignment of the frames is done manually. Since the silicone membrane is transparent, it is easy to

accurately align frames on opposite sides of the membrane. After 5-10 minutes, the glue has cured, and the membranes can be cut out using a knife. This way, one piece of pre-stretched film yields 7 circular membranes of 45 mm diameter with acrylic frames on either side. The thickness of the pre-stretched membranes is 0.05 mm.

3.3.1.2. GO film preparation

For each batch of GO films, the desired quantity of GO dispersion (1 mg/mL) is measured and LAA is added at 0.2 mg/mL (see Section 3.2.2). The mixture is sonicated in an ultrasonic bath for about 10 minutes to ensure complete dissolution of LAA and dissociation of possible GO aggregates. Afterwards, the GO+LAA dispersion is drop cast onto the pre-stretched silicone membranes. The amount is chosen based on the surface area of the membrane in order to yield a coverage of 0.1 mL/cm^2. A long needle or similar tool is used to spread the dispersion on the surface. Once the liquid makes contact with the frame on all sides, surface tension ensures that complete wetting of the entire membrane surface is maintained. De-wetting has occurred during drying on very rare occasions. GO is dried at ambient conditions in a fume cupboard to ensure a constant, gentle air flow which accelerates drying. GO+LAA mixture is always freshly prepared, sonicated, and drop cast immediately because reduction by LAA causes GO to slowly lose its hydrophilicity and aggregate if left for long periods of time in solution.

3.3.1.3. Laser scribing

GO films are laser scribed as specified in Section 3.2. Scan speed was set to 1000 mm/min and laser power to 60%. The focal point of the laser is 6 mm above the GO surface to increase line width and ensure interconnection between adjacent lines (see Section 3.2.2.3). On the back side of the membrane, a mirror image of the pattern is laser scribed to match the electrode pattern on the front side (for non-symmetric patterns).

3.3.1.4. Washing

Because unreduced GO films are quite stiff (see Section 3.2.2.1), they can restrict the deformation of the elastic membrane. Depending on the electrode geometry, it may therefore be necessary to remove excess GO after laser scribing. To wash off unreduced

GO, the GO surface is first wetted with deionised (DI) water. A piece of cotton wool soaked with DI water is rubbed over the surface very gently until all GO is removed and the silicone membrane is visible underneath. Any remaining loose flakes of GO are removed from the surface by rinsing with DI water. To get a clean result, the washing procedure may need to be repeated with a clean piece of cotton wool.

LSGO will remain in place due to its hydrophobicity, however, rubbing with too much force can damage the LSGO film. Rubbing is necessary because GO, although it is relatively hydrophilic, will not dissociate in water without any additional mechanical stimulus. Ultrasonication is not feasible because it tends to remove a large portion of the LSGO along with the GO. Thus, rubbing very gently with wet cotton wool was found to be the most effective method.

3.3.1.5. Contacts

Electrical contacts to connect the LSGO DEA to the driving electronics are made using copper tape. Adhesive copper tape is attached to the frame, as close to the membrane as possible without touching it, to avoid damage. The gap between the LSGO electrode and the copper tape on the frame is bridged using carbon grease. On silicone membranes, silicone-free carbon grease is used (see Section 3.3.2).

3.3.1.6. Training

Initial stretching of an LSGO film causes is to break into individual flakes, as explained in Section 3.2.2.1. This process requires a higher stress than an LSGO DEA can exert through electrostatic actuation. Initial stretching of the film must therefore be done manually by application of an external force. We term this process "training", and it results in loosening of the LSGO film, as well as softening of the elastomer membrane through the Mullins effect (see Section 2.3.1). For effective training, the film must be exposed to a strain equal or higher than the intended actuation strain.

For LSGO DEAs, training was performed using the actuation test rig described in Section 4.3.3.1. By applying a downward force to the steel rod on the test rig, the centre of the membrane is stretched out of plane by 16 mm. The stretching is repeated three times per sample. During each cycle, the strain is held for approximately one second. It is known that strain softening through the Mullin's effect can continue to

occur over several cycles, although the most notable change always occurs during the first strain cycle.[72] It is possible that three cycles are not sufficient to reach a steady behaviour at this level of strain. However, the applied strain during training was chosen to be much larger than the maximum expected actuation strain (2 mm, see Section 3.3.3.1) so that it can be assumed with good confidence that no significant changes to the material properties due to the Mullins effect will occur during actuation. There was also no evidence of further softening of the actuator membranes during cyclic actuation tests (see Section 3.3.3.3).

To what degree ELASTOSIL silicone films experience the Mullins effect is not documented in the literature or the manufacturer's data sheets. However, the fact that there is a marked difference in actuation strain between trained and untrained CG DEAs (see Figure 46A) shows that softening of the films does occur. Since the CG electrodes would be unaffected by training, any changes in actuation strain must be due to softening of the silicone.

To show the effect of training on actuator performance, the actuation tests described in Section 3.3.3.1 were first performed on untrained LSGO DEAs up to an actuation voltage of 5 kV, before performing the full tests up to 10 kV on the same samples after training. Actuation stroke for each group of samples (washed and unwashed LSGO, as described in Section 3.3.3.1) is shown in Figure 42. Actuation stroke of the untrained samples is consistently less than half of that of the trained samples. For washed LSGO, it is even less than 10%. This large difference in performance highlights the importance of training for LSGO DEAs. For CG DEAs, untrained actuators have 46 % lower strain than trained actuators. The fact that the difference between trained and untrained actuators is lower for CG DEAs than for LSGO DEAs shows that softening of the LSGO electrodes also has a noticeable effect on actuator strain, and that the difference cannot be attributed only to the Mullins effect.

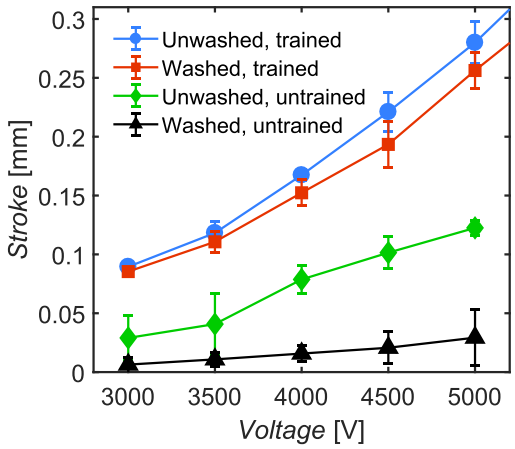

Figure 42. Actuation stroke of LSGO DEAs before and after training. (n = 6 for unwashed, n = 4 for washed, error bars show standard deviation)

3.3.2. Control group fabrication

DEAs with CG electrodes were fabricated as a control group to compare the LSGO DEAs against. ELASTOSIL silicone membranes were prepared in the same way as for LSGO DEAs (see Section 3.3.1.1). CG electrodes were applied by hand, using a laser-cut mask to ensure that electrode geometry is the same as the LSGO electrodes. CG controls were only fabricated for electrodes with simple, circular shapes.

It was found that conventional CG, which is based on silicone oil, is not compatible with the ELASTOSIL membranes because the oil can infiltrate the silicone membrane, swell and weaken it, while drying out the CG at the same time. Therefore, custom-made, silicone-free CG was used instead.

3.3.2.1. Silicone-free carbon grease

The silicone-free CG was made by mixing 1 g of carbon black powder (PRINTEX® XE2, Evonik Industries AG, Germany) with 3 g of castor oil (NOW Health Group, Inc., USA). The mixture was first carefully stirred by hand to achieve wetting of all carbon black powder, then blended with a household hand blender for approximately 20 s to achieve a homogenous dispersion.

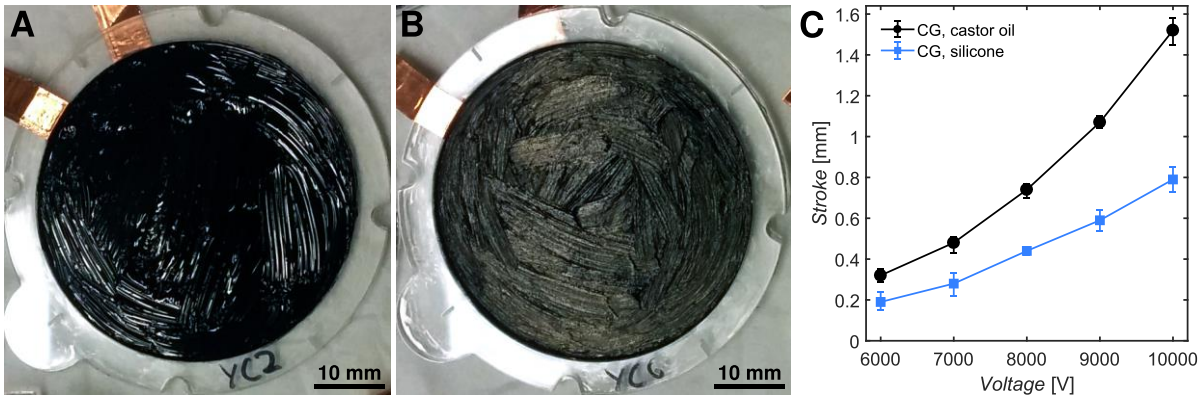

Figure 43. Interaction of carbon grease with silicone membranes. A-B) ELASTOSIL® silicone membranes coated with CG, one week after application. CG based on castor oil (A) underwent no visible changes. CG based on silicone oil (B) has changed to a matte grey colour indicative of a loss of the silicone oil, which has infiltrated the silicone membrane. C) Actuation performance of DEAs with castor oil and silicone CG electrodes. (n = 4 for castor oil, n = 3 for silicone, error bars show minimum and maximum values)

For comparison, DEAs were fabricated with both, silicone-based CG (Carbon Conductive Grease 846, MG Chemicals, Canada) and castor oil-based CG. Silicone CG became visibly dry and crumbly after several days and changed to a matte grey colour. Castor oil CG did not undergo any visibly changes, even after several weeks' time. Figures 43A and B show the two types of CG DEAs one week after fabrication. Freshly made, both types had been visually indistinguishable. Figure 43C shows the actuation performance of both types of CG DEAs, which was recorded according to the procedure described in Section 3.3.3.1.

3.3.3. Evaluation of LSGO DEAs

The quality of LSGO DEAs was evaluated through high-voltage actuation tests. DEAs with simple, circular electrodes were tested, as well as DEAs with more complex electrode patterns. The experimental conditions for the two types differ slightly.

3.3.3.1. Circular DEAs

To characterize the performance of LSGO DEAs, three groups of simple, circular actuators were compared. Group 1: LSGO electrodes, used as-is without washing (6 samples). Group 2: LSGO electrodes, washed to remove unreduced GO (4 samples). Group 3: castor oil CG electrodes as described in Section 3.3.2 (9 samples). CG is used as a baseline to compare LSGO electrodes against. Except for the electrode material, all actuators were made identical to eliminate other influencing factors. Each DEA

consists of a circular, 100% biaxially pre-strained silicone membrane (Ø45 mm) with matching circular electrodes (Ø40 mm) on either side. Figure 44 show one sample of each group.

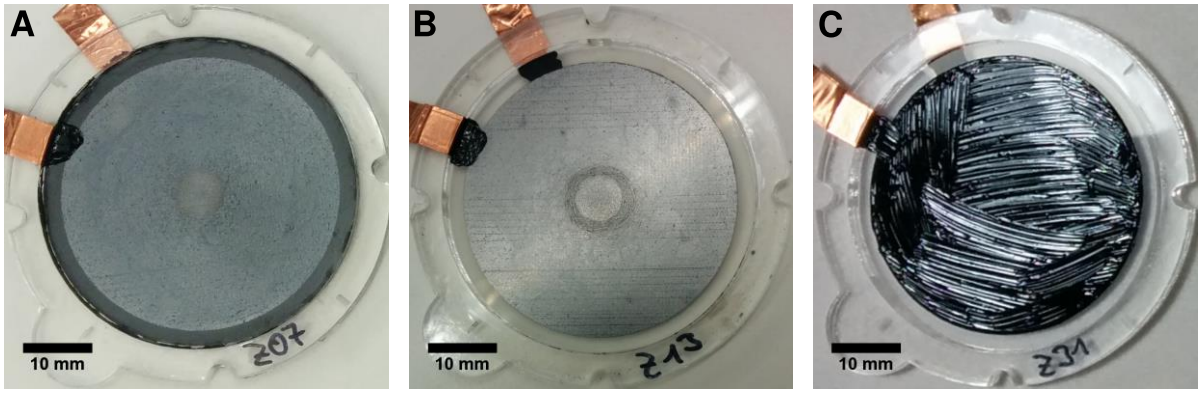

Figure 44. LSGO DEA samples for actuation tests. A) Unwashed LSGO DEA. B) Washed LSGO DEA. C) Castor oil CG DEA.

The electrode area was made slightly smaller than the membrane because earlier experiments had shown that breakdown of the membrane would always occur somewhere along the edge where the acrylic frame is attached. Therefore, the area closest to the frame was not covered by the electrodes in order to avoid premature breakdown.

Actuator stroke is measured on a custom test rig with a steel rod of mass 31.7 g suspended vertically above the horizontally mounted DEA, resting on the centre of the membrane. Actuation of the DEA causes the membrane to expand in area, which makes the rod to move up and down. Displacement of the rod was recorded using a Keyance LK-G152 laser displacement sensor (Keyence, Japan). A picture of the test setup is shown in Figure 45A. Two Ultravolt 5HVA24-BP1 HV amplifiers (Ultravolt, Inc., USA) were used to apply a maximum of 10 kV differential voltage (+5 kV and –5 kV, respectively) to the electrodes of the DEA. Figure 45B shows an example of the data recorded from a single test of three cycles at 10 kV for an unwashed, trained LSGO DEA. Stroke is defined as the average displacement of the rod between the relaxed and actuated state.

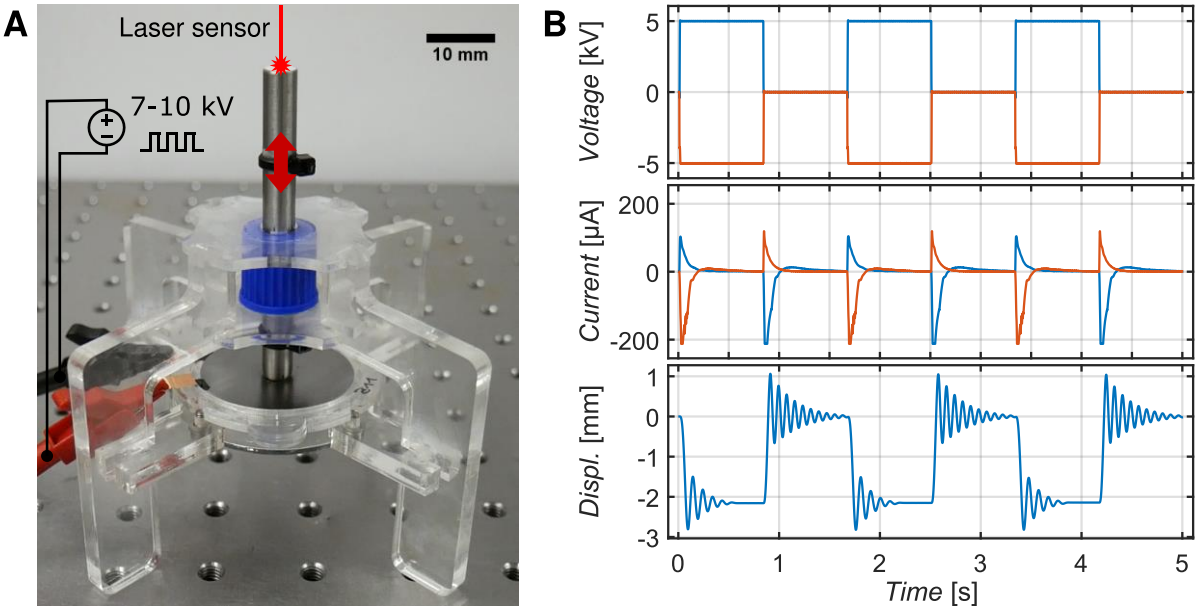

Figure 45. LSGO DEA actuation test setup. A) Photograph of the test setup. The vertical steel rod is moved up and down by membrane actuation. B) Example of recorded data (voltage, current and displacement) of an unwashed LSGO DEA during cyclic actuation at 10 kV. Current and voltage are recorded separately for each amplifier (blue and orange lines).

Figure 46A shows actuation stroke over voltage for LSGO actuators (washed and unwashed) and CG actuators (trained and untrained). Overall, unwashed LSGO DEAs showed the highest stroke of 1.94 mm at 10 kV. Washed LSGO produced a stroke of 1.40 mm at 10 kV. On average, the stroke of washed LSGO DEAs was 18% lower than for unwashed LSGO. This can be explained by two complementary effects. Firstly, washing might cause loose flakes of LSGO to be removed from the surface. These flakes help to maintain interconnection between domains of LSGO as the membrane is stretched. Without them, some areas of the electrode may become isolated and do not actuate, leading to reduced performance. Secondly, because the membrane is pre-stretched, the passive area of the membrane (i.e., the area along the edges that is not covered by the electrode) will contract when the DEA is actuated. This in-plain contraction absorbs part of the actuation strain and reduces the amplitude of out-of-plain motion. For the unwashed LSGO DEAs, the stiff GO film restricts the contraction of the passive area. This creates a slight advantage for the unwashed LSGO DEAs in this actuator configuration.

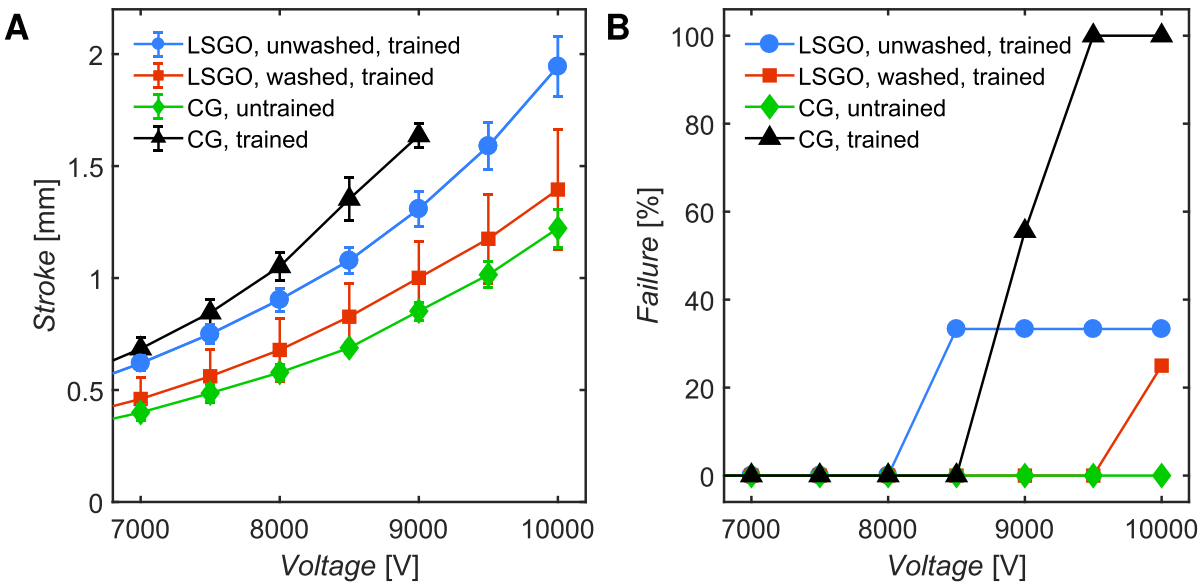

Figure 46. LSGO DEA actuation tests. A) Stroke of LSGO and CG DEAs against actuation voltage. B) Percentage of failed samples at given voltage in each group of DEAs. Untrained CG DEAs show systematic failure above 9 kV. (initial sample numbers n = 6 for unwashed LSGO, n = 4 for washed LSGO, n = 9 for CG, error bars show standard deviation)

Both unwashed and washed LSGO DEAs (trained) show larger stroke than untrained CG DEAs. This can be explained by softening of the elastomer membrane due to the Mullins effect (see Section 2.3.1). When the same training procedure was used on CG DEAs, their average stroke increased by 81%. Trained CG DEAs show the highest strain of the four tested groups for any given voltage. At 9 kV they produce an average stroke of 1.64 mm. At the same voltage, unwashed LSGO DEAs show 1.31 mm and washed LSGO DEAs show 1.00 mm stroke. However, all trained CG DEAs broke down above 9 kV while both groups of LSGO DEAs withstood 10 kV, which is the maximum voltage of the high-voltage drivers used in our experiments. Figure 46B shows the cumulative percentage of failed samples due to dielectric breakdown against applied voltage for each group of samples. While none of the untrained CG DEAs failed up to 10 kV, the trained CG DEA all failed above 9 kV. Three of the LSGO DEAs also failed at 8.5 kV and 10 kV respectively, but unlike trained CG DEAs, neither of the two LSGO groups showed systematic failure of all samples. This indicates that training can cause some form of damage to the membrane, leading to premature failure, but only in CG DEAs. The mechanism for this phenomenon is yet unknown, but it is an interesting observation that warrants further investigation. Diffusion of oil from CG into the silicone membrane is not a likely explanation since the castor oil-based CG

was used specifically to avoid this sort of interaction (see Section 3.3.2). Castor oil is not known to degrade ELASTOSIL® silicone rubber.[255]

3.3.3.2. Patterned DEAs

To demonstrate the patterning ability of the laser scribing process, a three-segment DEA was manufactured where the circular membrane surface is covered with three segments of LSGO electrodes of equal size (shown in Figure 47A). Actuating a segment results in area expansion of that segment as well as lateral displacement of the centre of the membrane, as the passive segments contract. To determine area strain of each segment, DEAs were filmed using a Lumix G7 digital camera (Panasonic, Japan) mounted at a fixed distance above the membrane. Strain was determined by pixel counts of LSGO in segmented images using MATLAB (MathWorks, Inc., USA). Figure 48 shows the average area strain in the actuated segment (one segment active at any one time) plotted against actuation voltage. At 10 kV, a strain of 8.8% is achieved. This is small compared to some previously reported DEAs with area strain near 150%,[256] but lies in the range that a contractile stack actuator might experience.[257]

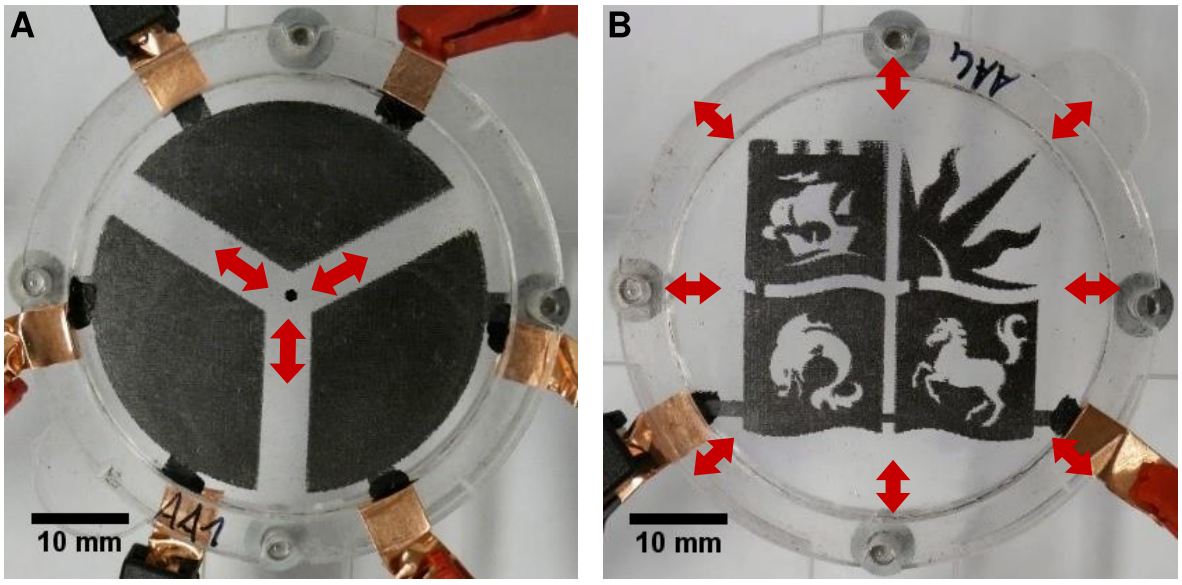

Figure 47. Patterned LSGO DEAs. A) LSGO DEA with three-segment electrode pattern, washed. B) LSGO DEA with University of Bristol logo pattern, washed.

The laser scribing method can produce electrode patterns with sub-millimetre details. The resolution is dictated by the laser engraver hardware and is limited to 0.1 mm (see Section 3.2.1). Even higher resolution could be achieved with a different engraver.

To showcase high-detail patterning, a DEA with electrodes in the shape of the University of Bristol (UoB) logo was laser scribed, which is shown in Figure 47B (after washing). The logo expands when actuated. Figure 48 shows the area strain in the electrode at actuation voltages from 5 kV to 10 kV. Because the shape of the logo is not well suited for DEA actuation, the observed strain is smaller than in the three-segment DEA, but it is still clearly visible by the eye. Effective in-plane actuation in DEAs requires interaction between active (actuated) and passive areas in the membrane. With interlaced active and passive areas covering most of the membrane surface in case of the logo, little effective strain in any particular direction is achieved.

A reduction of strain was observed in the UoB DEA over three actuation cycles, as shown in Figure 48. During actuation, electrical sparks were visible across some parts of the membrane at voltages above 6 kV as the membrane was charged. This did not lead to membrane failure but indicates that some areas of the electrode became disconnected as the membrane deformed. This is much more likely in an intricately patterned electrode, as many small areas are only connected by narrow pathways, which may break under strain. When the actuation voltage was sufficiently high, small gaps within the LSGO electrode were bridged by sparks. This leads to degradation of the electrode, which eventually results in isolation of certain areas and a decrease in the active electrode area. As can be seen in Figure 48, this gradual degradation counteracts the increasing voltage, leading to an overall decrease in actuation strain that is retained in subsequent cycles. For practical applications, it may be necessary to ensure that connecting traces of LSGO have a specific minimum width to avoid sparking and degradation.

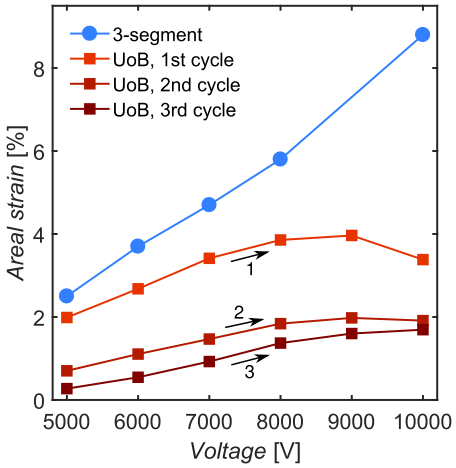

Figure 48. Actuation performance of patterned LSGO DEAs. The plot shows area strain against voltage for the three-segment and UoB DEAs (one sample each). Three actuation cycles from 5 kV to 10 kV were recorded for the UoB DEA.

For the DEAs with circular electrodes (see Section 3.3.3.1), which have no narrow connecting pathways, no degradation was observed during the actuation tests. To characterize their cycle stability, separate cyclic actuation tests were carried out, as described in the following section.

3.3.3.3. Cyclic actuation tests

Cyclic actuation tests were carried out on the same groups of samples and using the same test setup described in Section 3.3.3.1. Each sample was subjected to 120 actuation cycles at 2 Hz, at a voltage of 6 kV. All samples were trained. Actuation stroke of each actuator is plotted against cycle number in Figure 49A. Unwashed LSGO and CG show similar stroke around 0.7 mm. The measured stroke in washed LSGO samples is generally lower, around 0.5 mm. This is consistent with the actuation performance presented in Section 3.3.3.1, Figure 46A. The data shows a very slight reduction in stroke over the duration of the test for washed LSGO, from 0.512 mm to 0.497 mm on average (2.9 % reduction). Unwashed LSGO and CG show barely appreciable reduction of 0.5 % and 0.2 %, respectively. The given values are based on averages of the first and last ten cycles of each sample and averaged between the samples of each group.

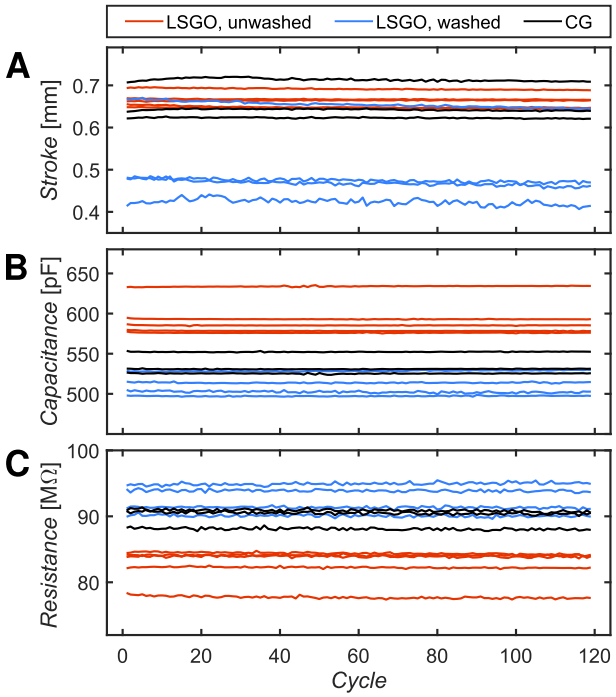

Figure 49. Cyclic actuation tests of LSGO DEAs. Stroke (A), capacitance (B), and resistance (C) are shown for several LSGO and CG DEAs under cyclic actuation at 6 kV over 120 cycles. Different lines of the same colour represent different samples from the same group. (n = 5 for unwashed LSGO, n = 4 for washed LSGO, n = 3 for CG)

Instantaneous voltage and current were also recorded during the cyclic test (same as actuation tests, see Figure 45B). Based on this data, total membrane charge was determined as the integral of measured current over the charging cycle (first half of a full actuation cycle). This is used to calculate the capacitance of the DEAs. The capacitance of each sample over the duration of the test is shown in Figure 49B. Changes in capacitance are below 0.03 % in all three groups and could be attributed to noise.

Series resistance of the actuators was estimated based on the maximum current measured during the charge cycle, given the known supply voltage of 6 kV. Resistance of each sample over the duration of the test is shown in Figure 49C. A very slight decrease in resistance of around 0.35 % is observed in all three groups. This trend may not be significant given the low number of samples in each group (between 3 and 5), but it would be consistent with the decrease in resistance previously observed in LSGO under uniaxial strain (see Section 3.2.2.2).

It is interesting to note that the slight reduction in stroke observed for washed LSGO electrodes over the duration of the test is not reflected in the capacitance. This would indicate an increase in stiffness of the washed LSGO film during actuation, which seems unlikely. Alternatively, it could be that, since washed LSGO produced overall lower stroke, other influences such as friction in the suspension of the steel rod (see Section 3.3.3.1) can have a greater effect on actuation performance, such that a slight reduction in stroke is not necessarily indicative of actuator degradation.

Future work will need to include a more thorough analysis of actuator performance over a much larger number of cycles and greater voltage range. Direct measurements of resistance and capacitance would yield more reliable data that can help to investigate potential causes of any observed degradation. In any case, the fact that the preliminary cyclic tests showed no drastic degradation in performance, neither electrical nor mechanical, over the course of 120 actuation cycles is a good indication that LSGO DEAs could potentially offer the long-term stability required for practical applications as long as interconnects are sufficiently wide to prevent arcing (see Section 3.3.3.2).

3.4. Conclusion and Outlook

We have shown that LSGO is a viable method for producing compliant electrodes with highly detailed patterns for DEAs and other soft devices. However, even though the unwashed LSGO DEAs displayed the highest stroke in our tests, their actuation performance still falls short of what simple, hand-made CG DEAs on VHB film can achieve. There are several reasons for this which have nothing to do with LSGO as an electrode material. For instance, the thickness of the silicone membranes was relatively high, and the applied pre-strain was probably too large, since the preparation protocol had originally been devised for more elastic VHB films. The fact that the laser engraver did not produce uniform, straight lines may also have had a detrimental influence. Another limiting factor is the drop casting method used to produce the GO films, which, although very simple, does not yield very uniform films. Very often, non-uniform drying reminiscent of the coffee ring effect[202] was observed. In addition, the choice of an out-of-plane actuator configuration with DEAs whose electrodes do not

cover the entire membrane area made it difficult to make a fair comparison between the different groups of DEAs, since this configuration favours the unwashed LSGO DEAs (as mentioned in Section 3.3.3.1). Because of all these limitations, our work so far should be seen as a proof of concept and a starting point for further research.

Many of the stated problems are easy to address and, in combination, could greatly increase the performance of the LSGO DEAs. ELASTOSIL® films with lower thickness are available and different levels of pre-strain could be tested to find an optimal value. A higher-quality laser engraver could provide more uniform laser irradiation and allow more complete, uniform reduction of GO without damaging the membrane. Prices for small laser engravers have decreased since the start of this project and an engraver with much better quality could currently be purchased for under £200, which can still be considered very low cost. There may even be ways to use the laser to assist the drying process and mitigate the coffee ring effect during drop casting.[258] This could allow more uniform GO films to be made, which could greatly improve the quality of the LSGO films and resulting devices.

For more reliable evaluation, the in-plane expanding circle configuration as recommended by Carpi et al.[72] should be used. The size of the circular electrodes would have to be reduced to no more than one third of the membrane diameter. Area expansion would be recorded using a digital video camera and image processing, as described for the patterned LSGO DEAs in Section 3.3.3.2. A more thorough analysis of the long-term stability would also be required to fully determine the potential of LSGO as compliant electrodes. In addition to greatly increasing the number of test cycles compared to our preliminary cyclic actuation tests (Section 3.3.3.3), the Novel Electrode Resistance Degradation (NERD) setup proposed by Rosset et al.[259] could be used to provide more reliable data and allow comparison with other electrode materials described in the literature.[129] The necessary electrode patterns for the NERD method are easily created using the laser scribing method.

By applying all the suggested improvements, the performance of LSGO DEAs could be greatly improved and a better understanding of their potentials and limitations could be gained. Even in its current form, the LSGO method has many advantages: it

is simple, green, low-cost and allows for intricate in-situ patterning of electrodes on a sub-millimetre scale. LSGO electrodes are much easier to handle during preparation and testing than (unencapsulated) CG electrodes since the electrodes do not rub off as easily. Of course, other stretchable electrode materials such as carbon silicone composites (see Section 2.3.3.3) also show good abrasion resistance. They are widely used in DEA applications[10] and have already been shown to have good long term cycle stability,[129] unlike LSGO, where rapid degradation was observed in electrodes with very small features (see Section 3.3.3.2). Currently, it does not appear that LSGO can match the performance of carbon silicone composites, although a direct experimental comparison has not been made. Nevertheless, LSGO offers an interesting new approach to fabricating electrodes with intricate patterns that does not require any expensive hardware. Considering the large potential for further improvements, as described above, we argue that further research into compliant LSGO electrodes is certainly warranted to develop this into a viable method for DEA fabrication and prototyping.

In recent years, LSGO has already been adopted for many interesting new applications including stretchable supercapacitors and temporary electronic tattoos on human skin.[228–232] We expect that this method will see even wider uptake for a range of different applications in the future, including DEAs and other soft devices. In addition to DEA electrodes, we have also successfully used the LSGO method to fabricate interdigitated electrodes on unstretched silicone film for soft, self-sensing electroadhesion (EA) pads. Figure 50 shows the LSGO electrode patterns of different EA pads with features as small as 0.2 mm. This work is part of an ongoing project and data on the performance of the EA devices is not yet available.

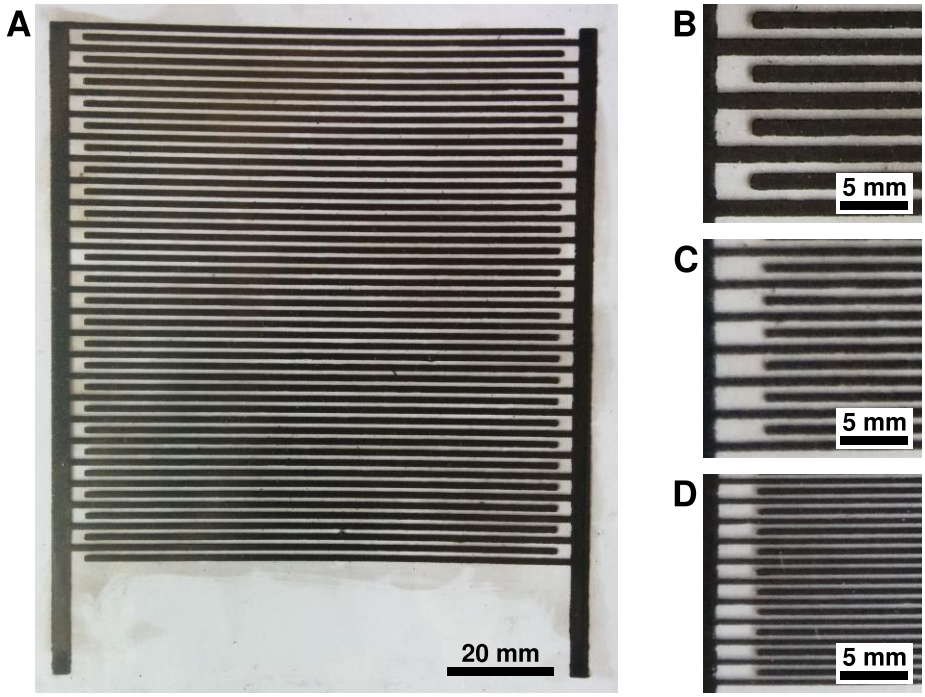

Figure 50. Interdigitated LSGO electrodes for electroadhesion. A) Photograph of a full LSGO electroadhesion pad with 1-mm-wide digits. B-D) Close-up views of the interdigitated patterns with feature width of 1 mm (A), 0.5 mm (B), and 0.2 mm (D).

The fact that laser scribing allows the fabrication of high-detail electrodes in situ makes it interesting for integration into a 3D printing process. It could enable incorporation of patterned electrodes on or in a printed part directly during printing. From a hardware perspective, integration of the 3D printing and laser scribing would be easy as they both rely on a simple cartesian robot. Although we were not able to develop a suitable method to integrate LSGO with 3D printing, our experience with LSGO inspired research into direct laser scribing of other materials and led to our discovery of conductive LSSR, which is described in Chapter 4.

Chapter 4

Laser-scribed silicone rubber for in-situ electrode fabrication

Some of the earlier results from the work described in this chapter were presented at the SPIE Electroactive Polymers and Devices (EAPAD) conference in March 2018 and are published in the conference proceedings.[246]

4.1. Introduction

Dielectric elastomers and other soft artificial muscles show great potential for a variety of applications in robotics and related fields. However, these technologies are still in a relatively early stage of development and a lot more research will be needed to develop market-ready products. It is therefore important to have materials and processes that allow fabrication of DEAs and soft devices with high quality while also offering the great flexibility of modern rapid prototyping methods. Chapter 3 introduced a facile, low-cost laser scribing process for the in-situ fabrication of compliant DEA electrodes on elastic silicone rubber substrates. This method can produce precisely patterned, high-detail electrodes. Unfortunately, the process still relies on a series of manual tasks including substrate preparation, drop casting of GO films, and removal of excess GO by washing. In addition, drop casting of aqueous GO dispersion requires very long drying times. This method would not be feasible for a fully automated prototyping process capable of producing functional soft devices, as outlined in Section 1.2.

In this chapter, we describe our discovery of electrically conductive laser-scribed silicone rubber, an intriguing new class of materials formed by direct laser treatment of a silicone substrate. We propose this as a simpler alternative to LSGO for the

fabrication of precisely patterned, conductive layers on soft substrates. In the following sections, the electrical and physical properties and composition of LSSR are investigated. Chapter 5 explores its use for the in-situ formation of compliant electrodes on silicone rubber surfaces as part of an integrated 3D printing process.

Throughout this thesis, "laser-scribed silicone rubber" (LSSR) is used as a collective term to refer to any material generated by laser scribing of a silicone substrate. We use this term because LSSR is a complex material consisting of a variety of different compounds (see Section 4.4 and 4.6.1). The exact composition and properties of LSSR also vary greatly between different processes (see Table 5, Appendix Section A1). We therefore believe it would be incorrect to refer to LSSR as any one of its constituent parts, such as silicon carbide, as has been done in some of the cited literature.

4.2. Discovery

As it became apparent that, despite great success in fabricating DEAs, the LSGO method was not suitable for integration into an automated 3D printing process, alternative solutions were explored. Initially, an attempt was made to apply the laser scribing method on a 3D-printable silicone rubber which incorporates GO as a filler material. The idea was that, after deposition and curing, the GO composite could be laser-scribed to reduce GO and make the composite electrically conductive. It was found, however, that incorporation of GO into UV-curable silicone rubber at concentrations over 0.05 wt% causes inhibition of the UV curing mechanism (see Section 4.5 for more details). In addition, GO was also found to trigger premature, partial curing of the silicone rubber without UV irradiation. This made the composite unsuitable for 3D printing. At lower GO concentrations, bulk conductivity would not be achievable even if laser reduction is successful, since the percolation threshold (reported as 0.1 wt% for graphene[140]) is not reached. This approach was hence abandoned, but while contemplating what alternative filler materials could be used for this purpose, the question was raised if perhaps pristine silicone rubber will yield a conductive material when laser scribed.

It is known from the literature that polyimide film and other organic materials can be directly laser scribed to convert them to laser-induced graphene (LIG), which is

electrically conductive (see Section 2.6.2). This approach has even been used to fabricate soft strain sensors by transferring LIG from polyimide to a PDMS substrate.[236] To achieve the same result but without the need for an additional transfer step, we investigated if silicone rubber itself can undergo a similar conversion as polyimide through direct laser treatment. Even our very first experiment showed that direct laser scribing of silicone rubber does indeed result in a chemical conversion of the silicone and that the resulting material shows electrical conductivity on the order of 100 kΩ/sq. The composition and properties of this LSSR material are discussed in detail in Section 4.4 and 4.6, respectively. Both vary for different silicone rubbers and different laser scribing conditions.

LSSR in itself is not a new discovery. Direct laser scribing of silicone rubber has been explored in several publications from as early has 1996.[238] Pulsed, high-power lasers like CO_2, Nd:YAG and KrF-excimer lasers have been used for surface treatment of PDMS with the purpose of modifying its wettability, either for subsequent metallisation[238–241] or to produce artificial skin with switchable hydrophobicity.[242] Laser scribing with a low-power diode laser has also been demonstrated as a cost-effective method to produce fluorescent nanoparticles and waveguides on PDMS substrates.[243–245] However, none of these publications mention the inherent conductive properties of LSSR. The reason for this may be that conductivity was not observed or reported because it wasn't relevant to the respective target applications. It is also possible that laser-scribing under the particular conditions applied in previous research produces non-conductive LSSR. In any case, to the best of our knowledge, ours is the first published account of an electrically-conductive material produced by direct laser scribing of silicone rubber.[246] Since then, one other article describing conductive LSSR has been published.[247] It presents resistive strain sensors based on LSSR. The scarcity of publications on the subject shows that direct laser scribing of silicone rubber to produce conductive materials is a novel, cutting-edge technique that has not yet been widely explored. Our work is, to the best of our knowledge, also the first to combine laser scribing with 3D printing for the production of soft actuators (see Chapter 5).

4.3. The laser scribing process

LSSR is generated by direct laser irradiation of silicone rubber. A silicone surface is scanned with a laser, line by line, same as traditional laser engraving. Where the laser is absorbed by the silicone material, it induces the chemical conversion of silicone rubber to LSSR. The conversion is locally restricted around the focal point of the laser. This allows selective conversion of particular areas to create arbitrary, complex 2D patterns, as shown in Figure 51A. The laser scribing process is similar to the production of LSGO described in Section 3.2, but a more powerful diode laser (1.6 W, 450 nm) was used because LSSR conversion requires more energy than GO reduction (see Section 4.4 for details on the conversion process). The laser was mounted on the same cartesian robot that was also used for 3D printing (see Section 5.3.3). This machine allows higher maximum speed and higher lateral resolution. It is also more rigid and less susceptible to vibrations than the laser engraver previously used (see Section 3.2.1).

The laser-scribing process for LSSR is mainly controlled by two parameters: scan speed and laser power. This is analogous to the LSGO process, as described in Section 3.2. Scan speed v is controlled by the cartesian robot and is typically specified in mm/min, which is the default unit used by the robot's firmware. Typical speeds for laser scribing range from 50 to 1000 mm/min (3 to 60 m/s). The power output of the laser is controlled using pulse width modulation (PWM) at a frequency of 5 kHz. Laser power is therefore specified via the duty cycle D. In the context of this thesis, the parameter D will be referred to as "laser power" or "relative laser power" even though it is not a quantity of power in the physical sense. We use this terminology anyway because, in practice, D is used to control the average power output of the laser. It is worth stressing that duty cycle is a relative measure. This means that $D = 100$ % in the LSSR process equates to 1.6 W, whereas, in the LSGO process, $D = 100$ % is equivalent to 250 mW.

Although the laser is technically operating in a pulsed mode due to the use of PWM control, the high PWM frequency of 5 kHz ensures that no individual dots are discernible. The process can therefore be considered to produce continuous lines. 2D patterns are constructed from parallel line segments rather than individual dots. The

lateral resolution is determined by the cartesian robot and is theoretically as low as 12.5 µm. However, minimum feature size depends on the width of an individual laser-scribed line. The line width varies depending on the process parameters (higher laser power results in wider lines). It is also influenced by the dot size of the laser which depends on the laser optics and how well it is focussed. In practice, resolution is typically of the order of 100 µm, similar to LSGO.

Laser scribing is done under ambient conditions, i.e. in the presence of atmospheric oxygen. Different silicone materials have been used for laser scribing. When using transparent materials such as UV Electro 225-1, absorbent particles are added to the silicone in order to make it absorb the laser wavelength. The suitability of different materials and the effects of absorbent fillers on the laser scribing process are discussed in Section 4.5.

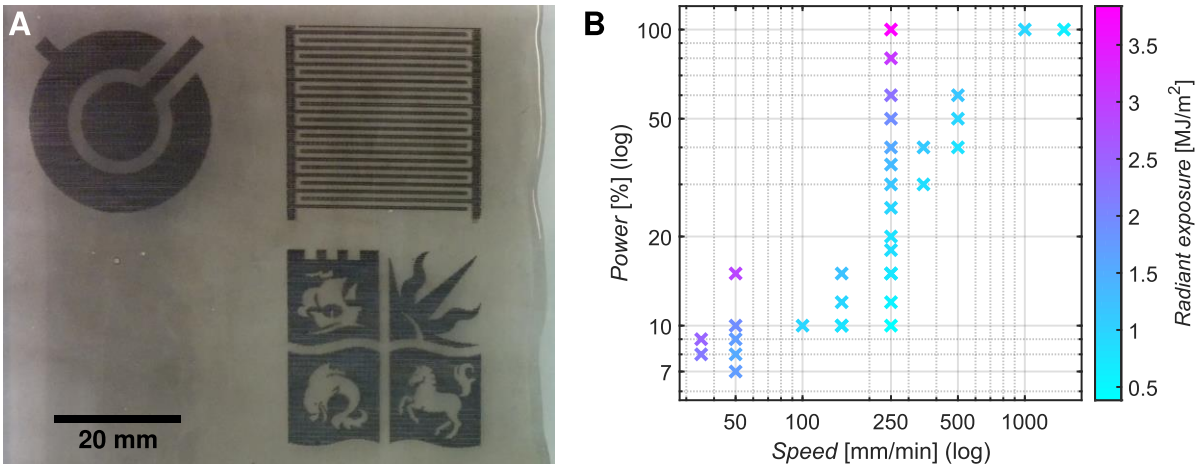

Figure 51. Laser-scribed silicone rubber. A) Laser-scribed patterns on a film of UV Electro 225-1 silicone rubber. A very thin layer of carbon black was applied to make the film absorbent. B) Plot of all parameter combinations (power and speed) at which successful laser scribing has been observed. The colour of each data point indicates the radiant exposure. Evidently, higher power is required at higher speeds. However, it can also be seen that this relationship is not linear and higher exposure is necessary at lower speeds.

As mentioned, the LSSR process is mainly controlled by the two parameters laser power (duty cycle) D and speed v. Figure 51B shows a plot of all the combinations of D and v which successfully produced LSSR. For each of these, an estimate of the radiant exposure H_e (the total incident optical energy per surface area) can be calculated according to Equation (2). To calculate H_e, the total energy output E of the laser is averaged over the laser-scribed area A. For a given area A, the total energy

E is determined by the laser power P and the total duration t of the laser scribing process, which can be calculated by dividing area A by the scan speed v and the line spacing s. Laser power P is the product of the nominal, continuous output power of the laser P_{max} and the duty cycle D. Nominal power P_{max} is 1.6 W. Line spacing s was set to 100 µm for most experiments.

$$H_e = \frac{E}{A} = \frac{Pt}{A} = \frac{P}{A} \cdot \frac{A}{sv} = \frac{P}{sv} = \frac{P_{max}D}{sv} = \frac{P_{max}}{s} \cdot \frac{D}{v} = \frac{1.6\,W}{10^{-4}\,m} \cdot \frac{D}{v} = 16\,\frac{kW}{m} \cdot \frac{D}{v} \qquad (2)$$

Exposure is proportional to laser power and inversely proportional to scan speed. This estimate of H_e disregards the absorption or reflectance of the laser-scribed material, as not all incident radiation will be absorbed. It also does not account for possible absorbance or scattering in the laser optics, which may lower the overall efficiency of the laser. The magnitude of these effects is not known. However, neither of these factors affects the general relationship of (inverse) proportionality between speed, power, and exposure.

The plot of viable parameter combinations in Figure 51B shows that laser scribing at higher speed requires higher power. This seems intuitive since higher power increases exposure, whereas higher speed reduces it. However, it can also be seen from the plot that LSSR conversion does not always occur at the same level of exposure. Laser scribing at low speed and power requires higher exposure than at higher speed and power. This is most likely the case because, at low power, heating rates are lower, and more heat can be dissipated within the material before the necessary temperature for LSSR conversion is reached. This trend is also evident in the literature (see Table 5, Appendix Section A1), where reported radiant exposure for LSSR conversion with high-power, pulsed lasers[238–241] is typically between 0.005 and 0.04 MJ/m^2, compared to 0.4 to 4 MJ/m^2 in our process. Gao et al.,[247] who use a laser with 0.4 to 0.8 W power, similar to ours, report exposures of 1.1 to 6.4 MJ/m^2. (These exposures were calculated from reported speed and laser power using Equation (2)). Laser scribing of PDMS using a low-power (~100 mW), near-infrared diode laser has been reported at exposures ranging from 0.16 to 43 MJ/m^2.[260]

4.4. Chemical formation of LSSR

Silicone rubbers consist of loosely crosslinked networks of polysiloxanes with high molecular weight. Polysiloxanes are a class of polymers consisting of a backbone of alternating Si and O atoms with organic side groups attached to the Si. The simplest and also the most commonly used polysiloxane is PDMS. It forms the basis of most commercial silicone rubbers. The chemical structure of PDMS is shown in the inset in Figure 52B.

During laser scribing, the laser beam is absorbed at the surface of the silicone rubber and causes localised heating. If sufficiently high temperatures are reached, the silicone rubber will start to decompose. LSSR is the residue of decomposition products that remains on the surface after laser scribing.

The end products of complete thermal decomposition of PDMS in the presence of oxygen are silica (SiO_2), CO_2, and water.[261] Carbon and hydrogen in the methyl groups react with oxygen to form CO_2, and water. The Si contained in the polymer backbone reacts with oxygen to form silica, which is the only solid residue left after complete decomposition of PDMS in air.[261] In the presence of oxygen, decomposition of PDMS starts to occur at temperatures above 290 °C.[261] However, at high heating rates (50-100 °C/min), degradation occurs at much higher temperatures around 500 °C and the difference between decomposition in air and in inert atmosphere is smaller (compare Figures 52A and B). This is because diffusion of oxygen through PDMS is relatively slow and if heating rates are high, decomposition mostly occurs under low-oxygen conditions. At heating rates of 50 °C/min and above, conductive silicon carbide (SiC) and silicon oxycarbide (SiOC) can form.[261]

Crosslinked PDMS can be used as a polymeric precursor for SiOC glass.[262] At temperatures between 600 °C and 1000 °C in inert atmosphere, PDMS decomposes and forms vitreous SiOC. However, the resulting material is electrically insulating.[262] At temperatures above 1000 °C, phases of graphitic carbon and SiC can evolve from SiOC, forming a multi-phase glass ceramic consisting of segregated carbon and SiC in a SiO_2 matrix in varying proportions.[262] The resulting material has semiconducting properties which arise from the SiC and carbon phases. Electrical conductivity at room

temperature can be as high as 700 S/m.[263] SiOC ceramics generally appear black and opaque due to the presence of segregated carbon.[262]

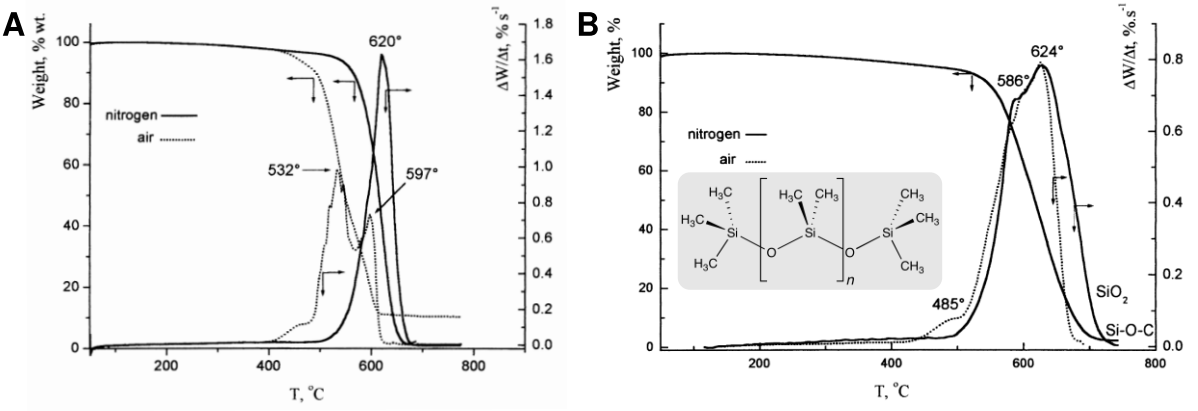

Figure 52. Thermal decomposition of polydimethylsiloxane (PDMS). A) Thermogravimetry (TG) and differential TG of PDMS in air and nitrogen at a heating rate of 50 °C/min. B) TG and differential TG of PDMS at a heating rate of 100 °C/min (from [261]). Inset: chemical structure of PDMS (Wikimedia Commons).

During laser scribing, heating rates are extremely high. Effective dwell time of the laser is below 1 second, even at very low speed, and surface temperatures must reach at least 500 °C for decomposition to take place. This indicates that heating rates must be well above 30,000 °C/min. It can therefore be assumed that decomposition mostly takes place in low-oxygen conditions, despite the presence of atmospheric oxygen. This allows SiOC, SiC and various carbon species to form. However, it can be expected that their composition varies greatly with the specific heating rates and peak temperature that the material experiences. Because the laser irradiation is highly focused, there is a strong spatial gradient in the local heating- and cooling rates and peak temperatures within the material. This leads to the formation of a highly heterogeneous residue with complex chemical composition.

The different phases that form depend on the specific parameters of the laser scribing process. For instance, the formation of SiC and even metallic silicon has been observed after laser scribing PDMS with a pulsed Nd:YAG laser.[240] In contrast, LSSR produced with a low-power (<100 mW) diode laser has been reported to consist mostly of silica and various carbon allotropes.[243–245] Formation of metallic silicon and silicon carbide has not been observed under these conditions. However, our laser scribing process more closely resembles that reported by Gao et al.,[247] who identified SiC as the main

constituent and source of electrical conductivity of the LSSR residue. Regardless of the exact composition, it can be assumed that silica will predominantly form at the surface where oxygen is available. Carbon, SiC or SiOC are expected to form in oxygen-depleted regions below the surface. This assumption is supported by observations of the structure and appearance of LSSR films presented in Section 4.6.2.

4.5. Materials for laser scribing

4.5.1. Silicone rubber

Formation of LSSR on a large variety of silicone materials has been documented in the literature (see Table 5, Appendix Section A1). In our work, five different silicone rubbers have been tested: UV Electro 225-1 (Momentive Performance Materials, USA), CFS RTV25 (CFS Fibreglass, UK), DragonSkin 10 (Smooth-On, USA), Ecoflex 00-20 (Smooth-On, USA), and ELASTOSIL prefabricated films (Wacker Chemie AG, Germany). Data sheets for all materials are included in the Appendix Section A2. On all five, LSSR was successfully produced. Some qualitative differences in the properties of the LSSR were observed. For example, on CFS RTV25 the LSSR film could easily be brushed off the silicone substrate, demonstrating lower adhesion to the silicone than other LSSR samples. In contrast, LSSR made on ELASTOSIL silicone films showed very good adhesion to the substrate. Even when the rubber film was strained, the LSSR did not peel off, although large cracks appeared in its surface. In a quick, single-step strain test, sheet resistance of ELASTOSIL LSSR increased from 20 kΩ/sq at rest to 10 MΩ/sq at 5 % uniaxial strain, which is somewhat higher but on a similar order as LSSR made on UV Electro (see Section 4.6.5). A comprehensive, comparative characterisation of LSSR formed on different silicone substrates is beyond the scope of this thesis. Since only minor differences between the different silicone material were observed in initial tests, UV Electro 225-1 was chosen for use in all further experiments because it is the most suitable for 3D printing due to its UV curing mechanism (see Section 5.3.2.4 for a discussion of different curing mechanisms).

4.5.2. Absorbent fillers

As has been noted in the literature, laser-scribing with visible or near-infrared lasers has no effect on pristine PDMS, which is transparent at these wavelengths.[243–245] In

order to be laser-scribable, a material must absorb the laser wavelength to a sufficient degree that the temperatures necessary for PDMS decomposition (>500 °C)[261] are reached at the surface. If using a laser that is not readily absorbed by PDMS, absorption can be achieved by addition of absorbent fillers. In the literature, this has been done with various carbon particles (carbon nanopowder, single- and multi-wall CNTs, fullerene C_{60}).[243–245] It has also been reported that surface coating with the absorbent filler leads to higher surface temperatures during laser scribing than embedding the filler within the polymer matrix.[243]

In our work, using a 450 nm laser, we found that laser scribing on clear UV Electro without additives had no visible effect on the silicone in most instances. This is the case because a typical UV Electro film has almost 90 % transmittance at 450 nm, as can be seen from the transmittance spectrum in Figure 53E. The small amount of laser radiation that is absorbed is not enough to heat the material sufficiently for LSSR conversion. Occasionally, LSSR would be produced even on clear silicone. In those cases, the process was most likely initiated through a dust particle at the surface of the silicone which helped to absorb the laser. Because the LSSR residue itself is absorbent, the laser scribing process is self-sustaining to a certain degree. Once LSSR conversion has initiated, it usually continues until the end of the current line (at which point the laser is turned off briefly before the next line is laser scribed). However, without the addition of absorbent particles, initiation of LSSR conversion was unreliable.

To improve process reliability, absorbent fillers were added to the silicone rubber. Four different materials were investigated as absorbent fillers for UV Electro. These are listed in Table 2, along with their respective influence on laser scribing and UV curing. Sheet resistances of LSSR samples generated from composites with the respective fillers are also given.

CB was found to be very effective when used as a surface coating on pre-cured silicone films. Laser scribing works reliably even with very thin CB films that are barely visible to the eye and don't have measurable surface conductivity by themselves. However, as reported in the literature,[243] when CB is dispersed in the silicone matrix, it is much

less effective at initiating LSSR conversion during laser scribing. We found that UV Electro with CB filler up to 0.1 wt% did not respond to laser scribing at all. At the same time, UV curing of the composite was significantly slowed due to the CB absorbing much of the UV light.

GO at concentrations of 0.05 or 0.1 wt% made composites that could be laser scribed, but relatively high laser power was required to initiate LSSR conversion. Unfortunately, at 0.1 wt%, GO caused premature curing of UV Electro, even without UV irradiation. At the same time, UV curing was inhibited so that the material could not be fully cured under UV light. GO was therefore deemed unsuitable as a filler material.

Table 2. Suitability of absorbent filler materials for LSSR. UV Electro 225-1 is used as the matrix material in all cases. The sheet resistance R_s is the minimum value observed in LSSR made from each respective starting material and the samples were not all laser-scribed under the same conditions.

Filler material	**Filler loading**	**Laser-scribable**	**UV-curable**	R_s **[kΩ/sq]**
Carbon black	thin film on surface	yes	(not applicable)	16
	dispersed, 0.02 wt%	no	yes	-
	dispersed, 0.1 wt%	no	yes, very slow	-
Graphite	dispersed, 0.03 wt%	yes, unreliable	yes	30
	dispersed, 0.1 wt%	yes, unreliable	yes	13
	dispersed, 2 wt%	yes	yes, slow	1.3
Graphene oxide	dispersed, 0.05 wt%	yes, at high power	yes	100
	dispersed, 0.1 wt%	yes, at high power	no, partially cured without UV	-
Tartrazine	dispersed, 2 wt%	yes	yes, slow	0.4

Graphite powder showed good performance as an absorbent filler. Even at 0.03 wt%, LSSR could be generated using relatively low laser power, but initiation was not reliable. At higher loading of 2 wt%, LSSR conversion initiated reliably. Figure 53A shows LSSR samples on a UV Electro film with graphite fillers. At 2 wt% graphite loading, the composite remained UV-curable, albeit slightly slowed, taking about twice the UV exposure to fully cure as unfilled UV Electro. That still allows thin films to be cured in a matter of seconds. Three different grades of graphite powder were tested with very similar results.

Tartrazine, a yellow organic dye used as food colouring, was also tested as filler in an effort to find selectively absorbent materials that have no detrimental impact on UV curing. Although tartrazine does not show the desired selective absorbance (see Section 4.8.3.1), it was found that a composite of UV Electro with tartrazine at 2 wt% was UV-curable and allowed effective laser scribing under generally the same conditions as composites with graphite. The filler loading of 2 wt% was chosen based on the experience with graphite filler and to allow direct comparison to the graphite composite with equal filler loading. Since this formulation yielded a material suitable for both UV curing and laser scribing, no other concentrations were tested. Figure 53B shows LSSR samples on a UV Electro film with tartrazine fillers. This material was investigated as an alternative to graphite that is not electrically conductive. Conductive fillers are known to reduce the dielectric strength of a material, although they also increase permittivity.[10] It was therefore expected that capacitive devices made from graphite composites have higher capacitance but those made from tartrazine composites would have a higher breakdown voltage. These hypotheses are tested in Chapter 5, Sections 5.4.3.4 and 5.4.3.5.

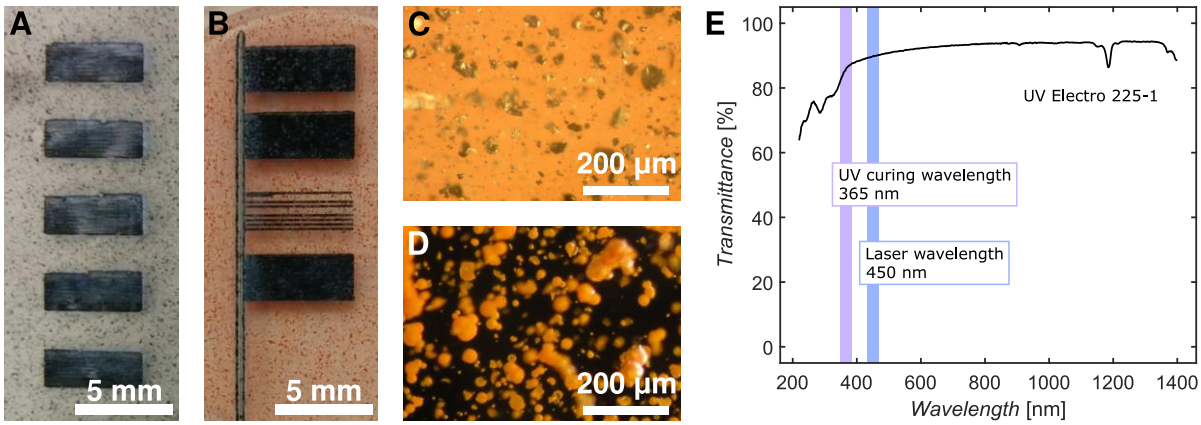

Figure 53. Silicone materials for laser scribing. LSSR samples on UV Electro225-1 silicone rubber films containing absorbent fillers: A) graphite, B) tartrazine. The samples were laser scribed at different laser power and speed. The micrographs (C-D) show particles of graphite (C) and tartrazine (D) dispersed in the clear silicone matrix. The difference in background colour is due to different lighting conditions in order to enhance contrast with the filler particles. E) Transmittance spectrum of UV Electro 225-1 silicone rubber. The wavelengths used for laser-scribing (450 nm) and UV curing (365 nm) are indicated. Transmittance at the laser wavelength is around 90%.

There are clear differences between the materials with carbon black fillers and graphite or tartrazine, as can be seen from Table 2. The reason for this is assumed to lie in the

size and distribution of absorbent particles in the silicone matrix. These affect how the laser beam gets absorbed by the material, as illustrated in Figure 54. Carbon black particles are very small, ranging from 15 nm to 320 nm.[126] In contrast, the graphite powders used here consist of plate-like particles with lateral dimensions between 40 µm and 100 µm. Tartrazine consists of mostly spherical particles around 20 µm, with some aggregates up to 100 µm. Micrographs of graphite and tartrazine in UV Electro can be seen in Figures 53C and D, respectively. Having fewer, larger particles is assumed to lead to more localised absorption and thus higher local temperatures when a particle is hit by the laser beam. For smaller particles, light gets absorbed gradually as it penetrates the material. Thus, the induced heat is spread throughout the depth of the material and is therefore less concentrated. However, if small particles are applied to the surface, rather than dispersed in the silicone, heating is again concentrated right at the surface. In addition, the presence of oxygen at the surface might cause combustion of the carbon particles which leads to further heating. It has also been shown that oxygen catalyses decomposition reactions in silicone rubber.[261] It is possible that lower temperatures are necessary to initiate thermal decomposition if these temperatures are generated right at the surface where oxygen is present.

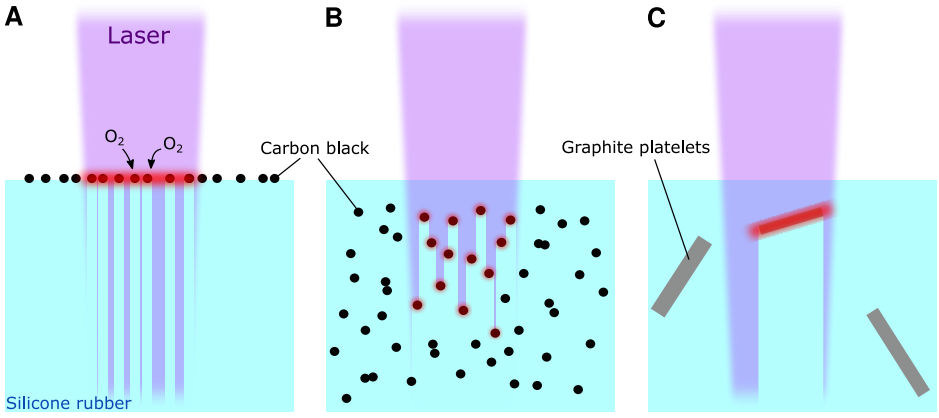

Figure 54. Effect of particle size and distribution on laser absorption. A) Carbon black applied to the surface generates concentrated heat at the surface layer. The presence of oxygen at the surface reduces the temperatures necessary for decomposition. Interference with the UV curing process is impossible since carbon black is added after curing. B) With dispersed carbon black, heat generation is more distributed, and the critical decomposition temperature is not reached. At the same time, UV curing is inhibited because UV light does not reach the full depth of the silicone film. C) Large, dispersed particles such as graphite platelets can generate high, concentrated heat from a single particle being hit by the laser. Because particles are sparse, UV curing is not inhibited as light can penetrate between particles.

The suitability of different fillers also needs to be evaluated from a practical perspective. Applying CG to the surface was found to be very effective, however, it requires an additional step in the fabrication process to be performed on each layer after curing. Implementing this as part of a 3D printing process increases the complexity of the printer. Although less effective, it is preferable to use fillers dispersed in the silicone rubber as these can be added prior to the printing process. Graphite and tartrazine are both supplied as powders that are easily mixed with uncured silicone by manual stirring or other methods. Therefore, composites of UV Electro with graphite or tartrazine at 2 wt% were chosen as the most effective materials for laser scribing, while also being UV-curable.

4.6. Properties of laser-scribed silicone rubber

In the following sections, several properties of LSSR are investigated, which are important for understanding the capabilities and limitations of this material and informing potential future optimisation of the laser scribing process.

4.6.1. Material structure

This section analyses the structure of LSSR and how it depends on different process parameters. An understanding of the material structure is important because it can greatly influence other physical properties such as the electrical conductivity. Several different methods were applied to investigate the structure and formation of LSSR.

4.6.1.1. Micrographs

Visual inspection of LSSR samples reveals that there are considerable differences in the surface structure of samples laser-scribed under different conditions. Figures 55, 58, and 59 show micrographs of nine different LSSR samples that were laser-scribed at different speeds v and laser power D, as specified in each subfigure. The parameters were selected arbitrarily to cover a broad section of the available parameter space (see Figure 51B).

The sample in Figure 55A was laser-scribed at $D = 8$ %, $v = 50$ mm/min. Under these conditions, LSSR conversion was not reliable and only the lines laser-scribed in left-to-right direction were converted. The reason for this is that a vertical line had been laser scribed on the left edge of the sample (not visible in Figure 55A but similar to

Figure 60B) which acted as a seed for LSSR conversion. On the right edge, there was no such seed, and because laser power was too low to self-seed the conversion, lines laser-scribed right to left did not get converted. Since only every second line was converted to LSSR, the silicone substrate with tartrazine particles can be seen between the LSSR traces. Besides this anomaly, the LSSR also shows a very different surface structure compared to the other samples. The material appears uniformly black with a glassy surface that has semi-circular ridges at slightly irregular intervals of the order of tens of micrometres, giving it a scale-like structure. Along the edges of each line, the material is transparent. Based on its appearance, the LSSR sample most likely consists of glassy SiOC which appears black due to the presence of carbon and SiC domains (as described in Section 4.4). There may be an outer transparent layer of silica which formed due to the presence atmospheric oxygen. Evaluation of the overall surface quality is difficult because only individual lines were converted, but this sample is the only one that does not show cracks or bubbles in the LSSR.

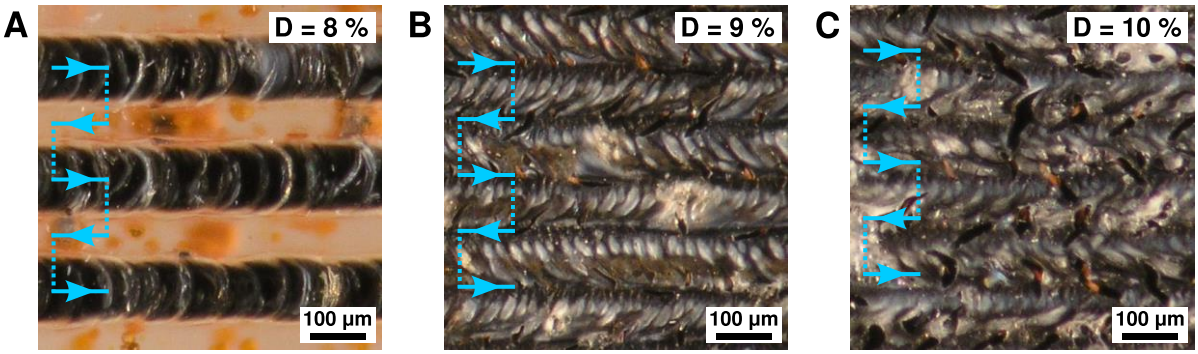

Figure 55. Micrographs of LSSR samples laser-scribed at $v = 50$ mm/min. Laser power D is specified in each image. The blue arrows indicate the path of the laser.

It is interesting to note that the scale-like surface is somewhat reminiscent of a weld seam, however, the curved ridges are actually pointing in the direction of the laser (left to right in Figure 55A), rather than the opposite direction, as they would for a weld. The difference is illustrated in Figure 56. The ridges on a seam weld are created as the melt pool cools after the arc moved past. Thus, the trailing edge remains visible in the cooled weld. In LSSR, the leading edge remains visible. This indicates that LSSR does not form by cooling from a liquid, molten phase. Instead, it appears to directly form a solid phase at the leading edge of the laser beam and retain its shape as the laser passes over it. This is plausible since PDMS decomposition occurs around 500 °C[261] while the

products, silica and SiC, melt or decompose at 1700 °C and 2830 °C, respectively.[264,265] If the surface temperature falls somewhere between these margins, LSSR evolves directly from the solid phase and does not get melted by the laser.

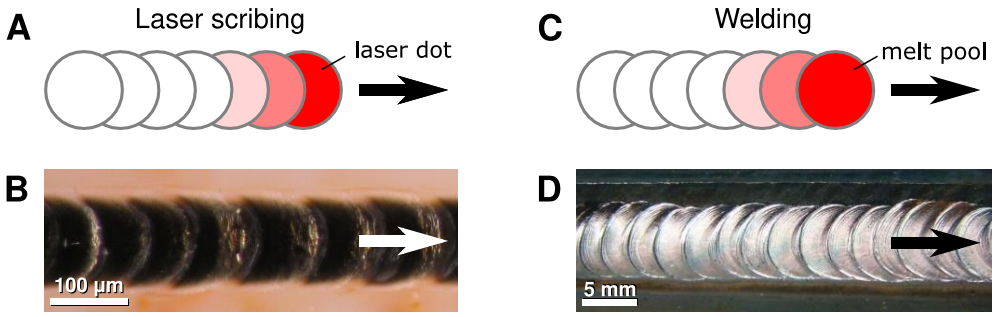

Figure 56. Schematic of LSSR surface pattern compared to a weld seam. A) During laser scribing, LSSR forms at the leading edge of the laser dot. Once formed, it remains solid. Therefore, the leading edges remain visible, forming a scale-like pattern that curves towards the direction of the laser path. B) Micrograph of a single line of LSSR (D = 8 %, v = 50 mm/min), showing the same scale-like pattern as the schematic in (A). C) During arc welding, metal is melted by the arc and solidifies at the trailing edge. Therefore, the trailing edges remain visible, forming a scale-like pattern that curves away from the direction of the weld path. D) Picture of a weld seam, showing the same scale-like pattern as the schematic in (B) (www.fabricatingandmetalworking.com).

The sample in Figure 55B was laser-scribed at D = 9 %, v = 50 mm/min. Here, LSSR conversion took place reliably and a closed surface is formed. The material has a similar black, glassy appearance and is assumed to consist of SiC and SiOC. The surface, again, has a scaly texture, although the spatial frequency of ridges is much higher. It should be noted that the average distance between ridges (25 µm) is two orders of magnitude higher than the distance that the laser travels between pulses (0.167 µm at v = 50 mm/min), which means that these ridges do not result from the pulsing of the laser. The ridges are also not semi-circular, like in sample 55A, but rather appear to be quarter circles. This structure probably arises from overlapping of adjacent lines of LSSR, as is illustrated in Figure 57. It can already be seen in sample 55A that the gaps between lines of LSSR are slightly narrower than the lines themselves. As laser power increases, so does the width of individual lines. In sample B, individual lines are almost twice as wide as the line spacing, causing adjacent lines to overlap by about 50 %. As discussed above, LSSR does not get melted by the laser. Therefore, existing LSSR stays intact as the laser (partially) passes over it again, and with each pass of

the laser, another half of a line is added to the LSSR film. This gives rise to the quarter-circle ridges visible in sample 55B.

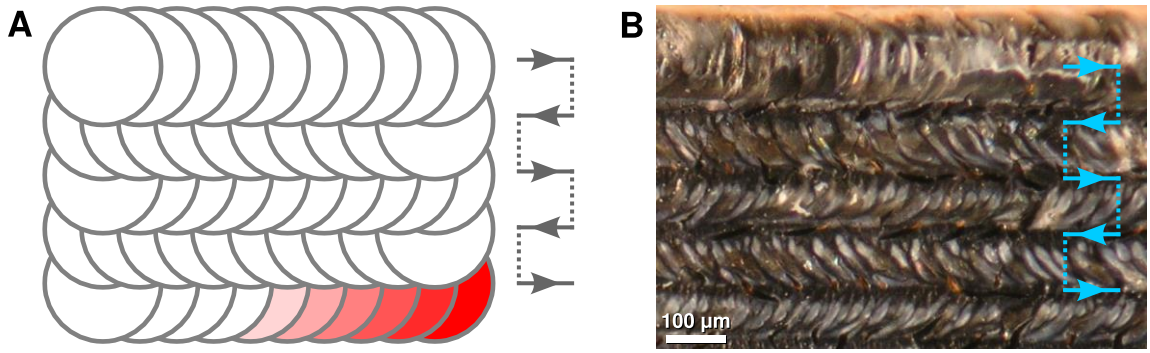

Figure 57. Schematic of LSSR multiline pattern formation. A) Adjacent lines of LSSR, which each form the scale-like pattern described in Figure 56A, overlap by about half their line width. This leads to the formation of a pattern of quarter-circles, which closely resembles the surface structure of the LSSR sample shown in (B). B) Micrograph of an LSSR sample (D = 8 %, v = 50 mm/min, same sample as Figure 55B) showing the same surface structure described in (A). The line at the top of the image is the first line of that sample and shows the semi-circular pattern described in Figure 56A. The arrows indicate the laser path.

The sample shown in Figure 55C was laser scribed at D = 10 %, v = 50 mm/min. It shows a similar structure to sample 55B except for a much larger number of small cracks and gaps in the film. These are most likely the result of higher thermal stresses resulting from increased heating by the laser. Another contributing factor could be the development of gases. At higher temperatures, gaseous by-products may develop at a faster rate and deeper beneath the surface, limiting their ability to escape via diffusion. This leads to a build-up of pressure beneath the surface which causes cracks through which the gas can escape. It has been noted in the literature that high heating rates can lead to cracking in SiOC ceramics formed from PDMS precursors.[262]

The samples in Figure 58 were all laser scribed at v = 250 mm/min. The surface of these samples appears dull and grey, rather than black and glossy like those in Figure 55. This is probably caused by gas bubbles trapped in the surface layer of the material. As heating rates increase, so does the development of gases. These get trapped in the surface layer of silica, forming a highly porous silica foam. Although bulk silica is transparent, the highly porous silica foam appears white and mostly opaque. With black SiC and carbon underneath, the resulting material has a dull grey appearance.

As laser power increases, the surface becomes increasingly white as the layer of porous silica grows thicker.

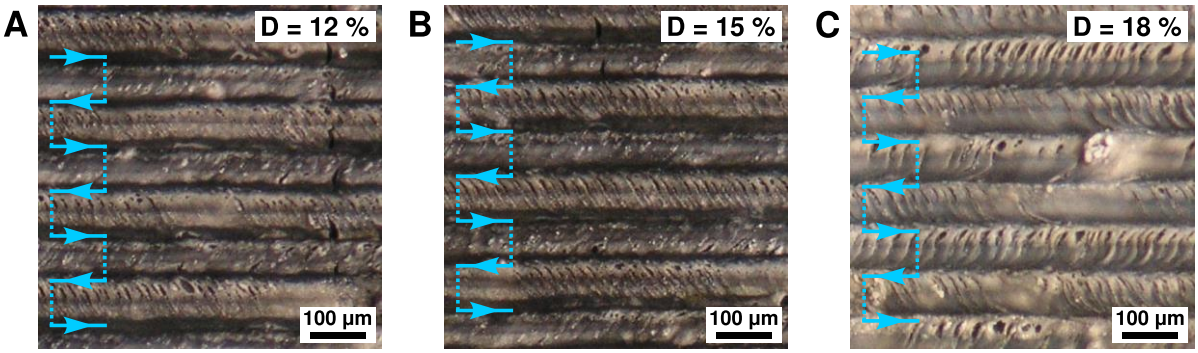

Figure 58. Micrographs of LSSR samples laser-scribed at $v = 250$ mm/min. Laser power D is specified in each image. The blue arrows indicate the path of the laser.

The samples in Figure 59 were all laser scribed at $v = 500$ mm/min. Laser power had to be increased accordingly to ensure reliable LSSR conversion. Here, the top surface is almost white, with black material underneath, visible through increasingly large holes in the top layer. These are probably the results of a further increase in the evolution of gases which break the layer of silica at the surface, exposing the carbonaceous material underneath. LSSR lines have also become increasingly wide to the point where two adjacent lines fully merge and become indistinguishable. The surface also no longer resembles the scaly pattern described in Figure 57. From the general appearance of the surface and the fact that adjacent lines have completely merged, we conclude that, at such high laser power, the silica layer at the surface does get melted during laser scribing.

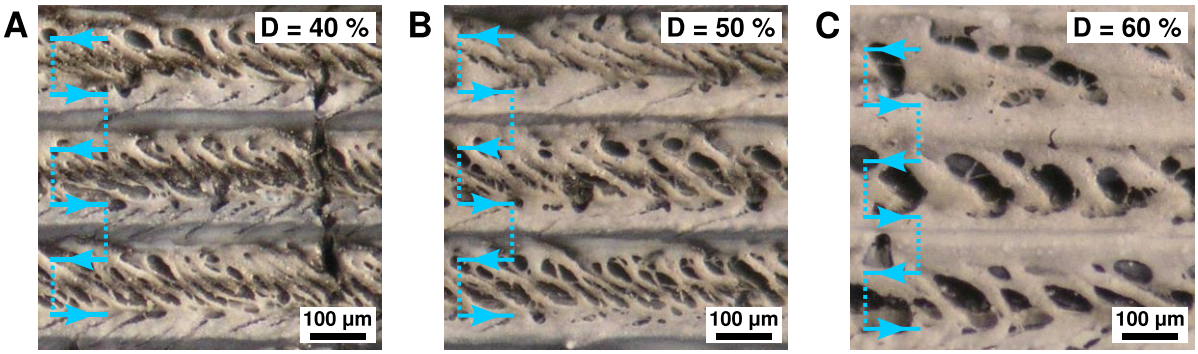

Figure 59. Micrographs of LSSR samples laser-scribed at $v = 500$ mm/min. Laser power D is specified in each image. The blue arrows indicate the path of the laser.

An interesting observation was made after electrical resistance measurements were performed on the LSSR films. During the measurements, contact with the resistance probe (see Section 4.6.4.1, Figure 69A) had removed the top layer of porous silica and revealed the black, carbonaceous material underneath, as shown in Figure 60A. Indeed, it was observed during resistance measurements (see Section 4.6.4) that LSSR samples often showed a (sometimes drastic) decrease in resistance when the measurement was repeated several times. This is likely due to the removal of the insulating top layer of silica, allowing better contact with the conductive material underneath.

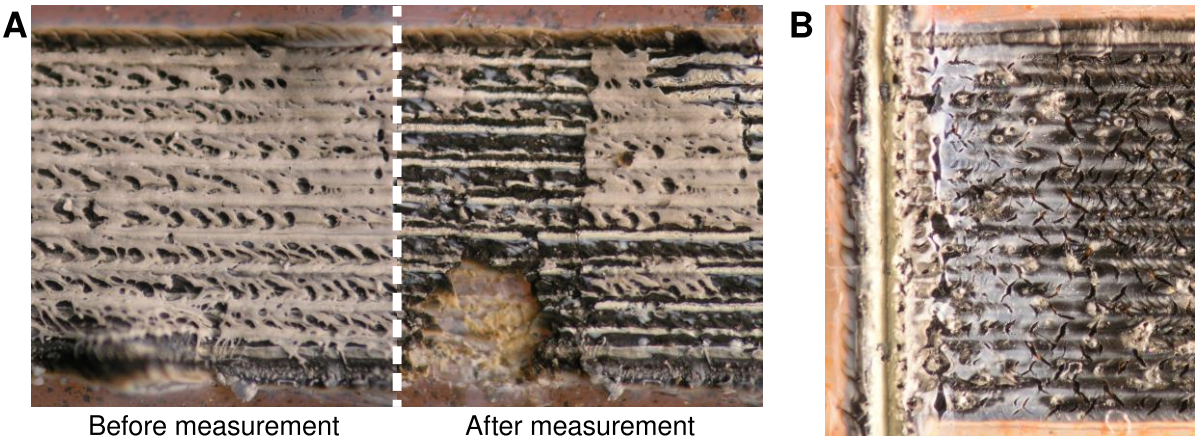

Figure 60. Different forms of silica surface layers on LSSR films. A) LSSR sample (D = 60 %, v = 500 mm/min, same as Figure 59C) before and after resistance measurements. Contact with the probe removed most of the silica surface layer. B) LSSR sample, where a vertical line was laser-scribed at maximum laser power (D=100%, 1.6 W) before the horizontal lines were scribed at D = 9 %, v = 50 mm/min (same as Figure 55B). A white film is visible on the surface, which appears to originate from the vertical line. The white film did not get removed during laser scribing of the horizontal lines, and LSSR formed underneath.

Finally, Figure 55N shows an LSSR sample that was produced in two steps. First, the vertical line on the left side of the image was laser scribed at D = 100 %, v = 1000 mm/min, which was arbitrarily chosen as a combination that is certain to generate LSSR. This line was used as a seed for the rectangular area laser scribed in a horizontal pattern at D = 10 %, v = 50 mm/min, because laser scribing at these parameters is not fully reliable otherwise. The surface structure of the film looks very similar to the one shown in Figure 55C, except for a white film on the surface which appears to originate at the vertical line and fades with increasing distance from it. This white film consists of silica which condensed from the gas phase onto the surrounding

silicone surface when the vertical line was laser scribed. It is known that volatile silicon monoxide (SiO) can form from silicone at a temperature of 1500 °C (and possibly also at lower temperatures).[262] SiO will promptly oxidise to SiO_2 in the presence of atmospheric oxygen and re-condense onto nearby surfaces. Indeed, after repeated laser scribing, particularly at high power, the same white film was evident on the inside walls of the laser safety enclosure, more than 20 cm away from the laser-scribed samples. This serves as additional evidence that the silica originates from the gas phase rather than solid particles ejected during laser scribing. It is interesting to note that, during laser scribing of the horizontal lines (in Figure 60B), LSSR formed underneath the silica layer and the white silica remained intact. Since the white colour results from the structure of the material (bulk silica is optically clear), the fact that the silica remains white after laser scribing indicates that it was not re-melted by the laser. This is evidence that surface temperatures, under these particular conditions at low laser power, remained below the melting point of SiO_2 around 1700 °C.[265]

4.6.1.2. SEM

Scanning electron microscopy (SEM) images of LSSR films were taken on a JEOL JSM-IT300 (JEOL Ltd., Japan) to further investigate their structure. These SEM samples were prepared during the early stages of our work with LSSR, where most of the procedures and materials described in this thesis had not yet been developed. Therefore, the material and laser scribing conditions differ from the samples investigated in Section 4.6.1.1, and the observed structures are not directly comparable. Nevertheless, some interesting observations can be made from the SEM images. The sample for SEM were made on clear UV Electro silicone films with a very thin layer of carbon black applied to the surface. They were laser-scribed at $D = 100$ %, $v = 2000$ mm/min.

Figure 61A shows a low-magnification view of an LSSR film. The laser scan lines are clearly distinguishable. Along each line, a scale- or rib-like structure can be observed. This rib-like structure is even more evident in the magnified view of the bottom-most line, shown in Figure 61B. Some loose, stringy debris can be seen on the surface, most likely consisting of strands of silica that formed along the ridges between scan lines.

However, there is no evidence of a solid surface cover of silica as seen in the micrographs in the previous section.

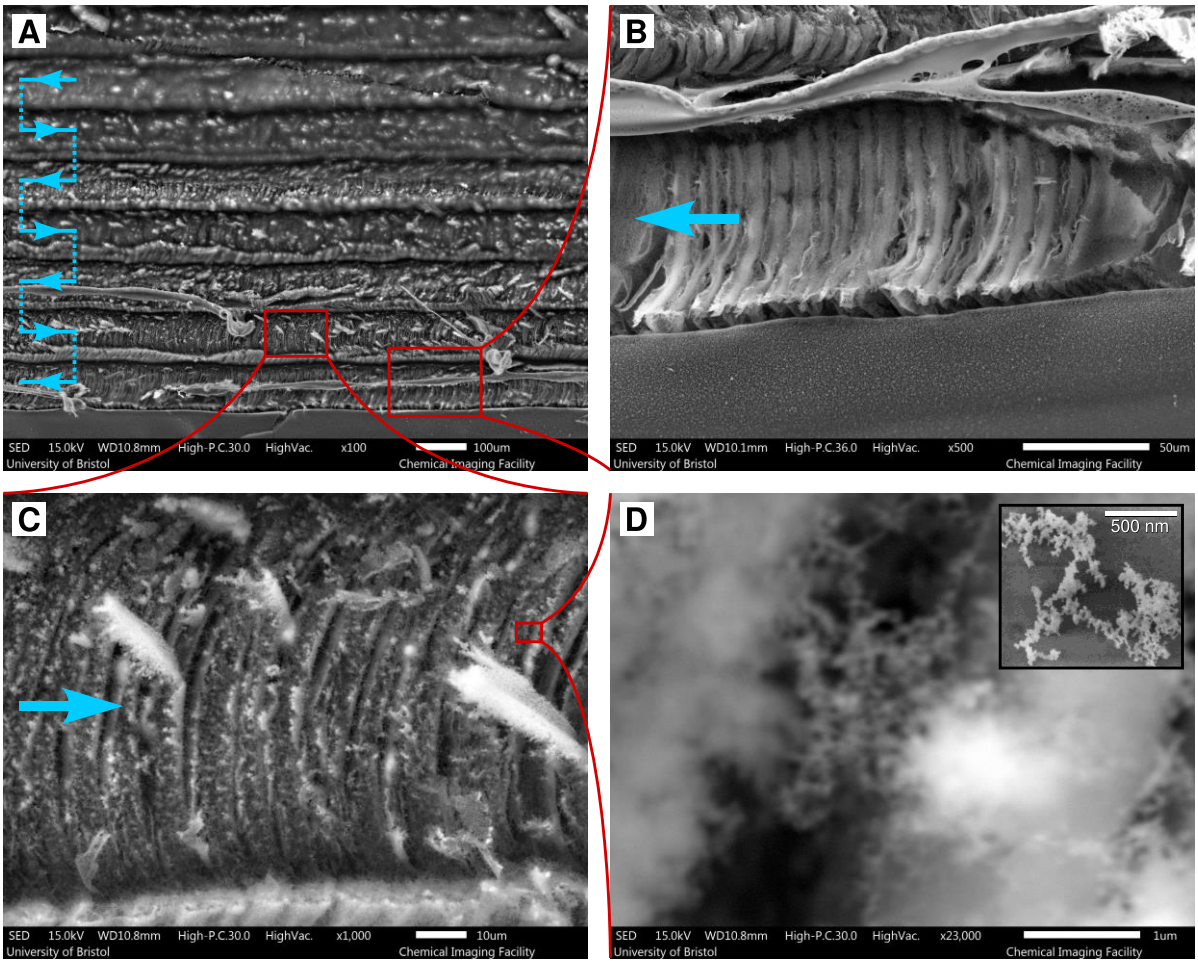

Figure 61. SEM images of LSSR. A) Low-magnification image of LSSR sample spanning several lines. B) Magnified view of a single LSSR line showing the scale-like structure. C) Feather-like silica structures on LSSR growing more than 30 µm in length. D) High-magnification image of silica particle on the LSSR surface, revealing a highly intricate, branched structure with features as small as 50 nm. Inset: SEM image of fumed silica.[266] The blue arrows indicate the direction of the laser path. The red rectangles show which regions the magnified images (B) to (D) where taken of. For (B), the exact region is not included in (A), but it is on the same line and shows the same kinds of features as the marked region.

One very interesting observation is that, near the top of Figure 61A, the image appears blurry, as if it were out of focus. The image is not, in fact, out of focus, and some features can be seen to be in sharp focus even near the top edge of the image. Instead, the surface is covered by the same thin layer of silica that was seen as a white film on the LSSR surface in Figure 60B. This phenomenon is only visible near the top of the image because the sample was laser-scribed top to bottom, i.e. lines near the top were

laser-scribed earlier than the lines near the bottom. Since the silica condenses from the gas phase during laser scribing, it builds up on older lines. On the line that was laser-scribed last (at the bottom of the image), no silica could deposit since no subsequent laser scribing took place. Hence, this line appears sharp in the image.

Figure 61C shows a magnified view of the second to last line of the LSSR film. Here, fine feather-like structures up to 30 µm tall are evident on the surface. Their intricate structure and height, combined with the observation that no such structures are evident on the LSSR in Figure 61B (last line), provide strong evidence that these are made of silica grown from the gas phase. Figure 61D also shows a high-magnification view of this silica film on an older LSSR surface, revealing particles with a highly intricate, branched structure with feature sizes as low as 50 nm. The observed structure is highly reminiscent of fumed silica (see the inset in Figure 61D) which is produced by condensing silica from the gas phase,[266] providing further evidence towards the origin of this hazy surface layer. The presence of fumed silica on the surface of LSSR might play a role in the surface properties of LSSR such as its wettability, discussed in Section 4.6.6.

4.6.1.3. EDX

Energy-dispersive X-ray spectroscopy (EDX) was used to investigate the chemical composition of LSSR. X-ray spectra were recorded on the JEOL JSM-IT300 (JEOL Ltd., Japan) SEM using an X-Max 80 mm^2 X-ray detector (Oxford Instruments, UK). Figure 62A shows an SEM image of the analysed sample which includes laser-scribed and non-laser-scribed regions of silicone film. The red boxes specify regions of interest (ROIs) that were analysed to compare their elemental composition. LSSR lines are investigated separately in order to show the influence of an increasing surface layer of fumed silica on older lines (towards the top of the image). Figure 62B shows the map sum spectrum (sum over the entire sample region). The spectrum shows characteristic peaks for oxygen (O), carbon (C), and silicon (Si). No other elements are present in detectable amounts (hydrogen is not detectable by EDX).

Spatial maps of signal intensity for each element are shown in Figure 62D, E, and F, respectively. These were analysed to investigate spatial differences in the elemental

composition of the LSSR sample. Relative concentrations of the different elements were calculated by averaging image brightness over each ROI indicated in Figure 62A. The resulting concentrations for each ROI are shown in Figure 62C. Each value is normalised to the concentration in ROI 1 (the non-laser-scribed region), which is arbitrarily defined as the baseline. EDX does not allow quantitative elemental analysis unless careful calibration using samples of known elemental composition has been carried out.[267] Therefore, direct comparison between the measured intensities for different elements is not valid and no useful information is lost by normalising the values to an arbitrary baseline.

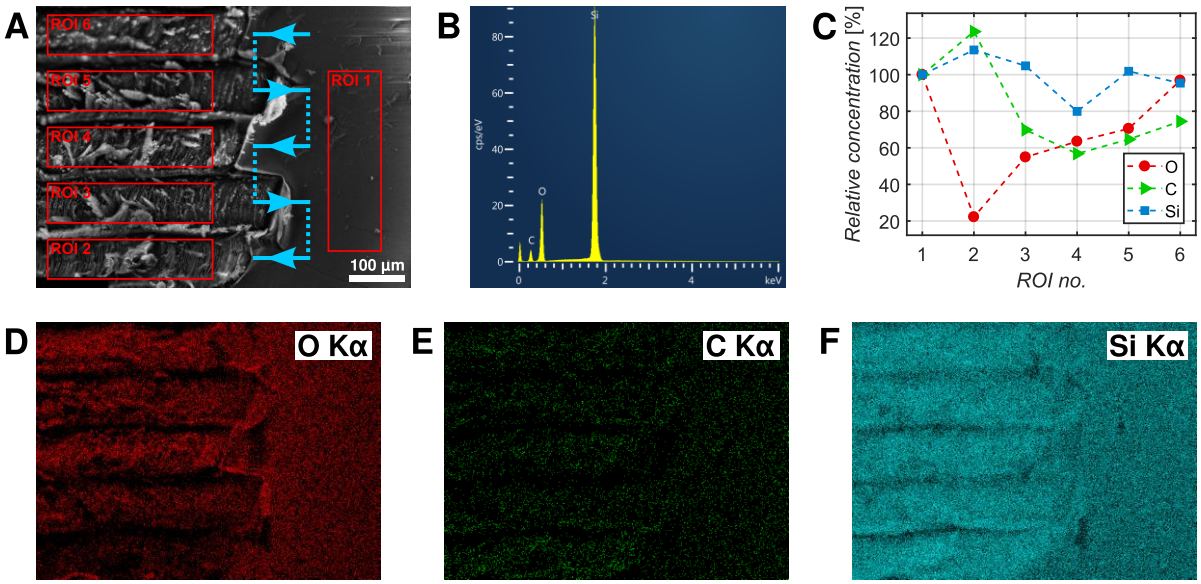

Figure 62. EDX analysis of LSSR. A) SEM image of the analysed sample. The sample includes laser-scribed and non-laser-scribed regions of silicone film. The red boxes specify the different regions of interest (ROIs) that were analysed individually. The blue arrows indicate the laser path B) EDX spectrum over the entire area of the sample shown in (A). Characteristic peaks for oxygen (O), carbon (C), and silicon (Si) are visible and no other elements were detected. C) Relative concentrations of O, C, and Si for each ROI indicated in (A). Displayed values are averages over each region. ROI 1 is arbitrarily defined as the baseline concentration (100 %) for each element. D-F) EDX spatial maps showing relative concentrations of O, C, and Si, respectively, for the region of film shown in (A).

X-ray intensity also varies with sample topology and a non-uniform surface (as in the present sample) can greatly impact the measurement.[267] To partially correct for this influence, brightness of the SEM image is used as a predictor of expected X-ray emission intensity. Since it can be assumed that a higher number of secondary electron emissions also coincides with higher X-ray emissions, brighter regions in the SEM

image (due to surface topology) will also appear brighter in the EDX maps, regardless of elemental composition. This trend is evident in the EDX maps presented in Figures 62D-F. The relative difference in brightness in the SEM image between the ROIs was therefore subtracted from the relative variations in element concentrations. This is a very crude method of correction and cannot be expected to fully compensate for effects from the irregular surface topology. The reliability of the EDX data is therefore very limited. Nevertheless, some general trends are evident from the data displayed in Figure 62C. ROI 2, the bottom-most LSSR line presumed to have the least silica on the surface, shows the highest relative concentration of carbon and a significantly reduced concentration of oxygen. This supports the assumption that LSSR is rich in carbon and most likely consists of SiC or graphitic carbon in a matrix of silica or SiOC (as discussed in Section 4.4). For the other lines (ROI 3 to 6), which where laser scribed before ROI 2, carbon is greatly reduced and oxygen concentration increases. This is consistent with the observation that an increasingly thick layer of silica builds up on the LSSR surface during subsequent lasers scribing of adjacent lines. The concentration of silicone is relatively constant between all ROIs. This is expected since all materials assumed to be present in the sample (PDMS, silica, SiC, SiOC) are rich in silicon. It should be noted that the baseline (ROI 1) cannot be assumed to represent pristine silicone rubber since the surface is adjacent to the laser-scribed region and will also have accumulated a surface layer of fumed silica. It is therefore unsurprising that the measured composition of the oldest line (ROI 6) approaches that of ROI 1, because in both regions the predominant constituent is most likely silica.

4.6.2. Layer thickness

Thickness of LSSR layers was determined by comparing pairs of two adjacent, square (5 by 5 mm) samples of LSSR made in direct sequence in the same process and using the same process parameters. From one sample in each pair, LSSR was removed by gentle scraping with a metal spatula and brushing off any remaining debris with a dry paint brush. This exposes the silicone rubber underneath. The surface topology of both samples was then measured using an Alicona Infinity Focus Microscope. From this data, the height of the LSSR film relative to the surrounding silicone could be determined. From the sample where LSSR had been removed, it could be determined

how far the LSSR film reached into the depth of the silicone material. The difference in height between the two samples of each pair corresponds to the overall thickness of the LSSR layer. Figures 63A-D show micrographs and corresponding heightmaps of one pair of LSSR samples, as recorded by the Alicona microscope.

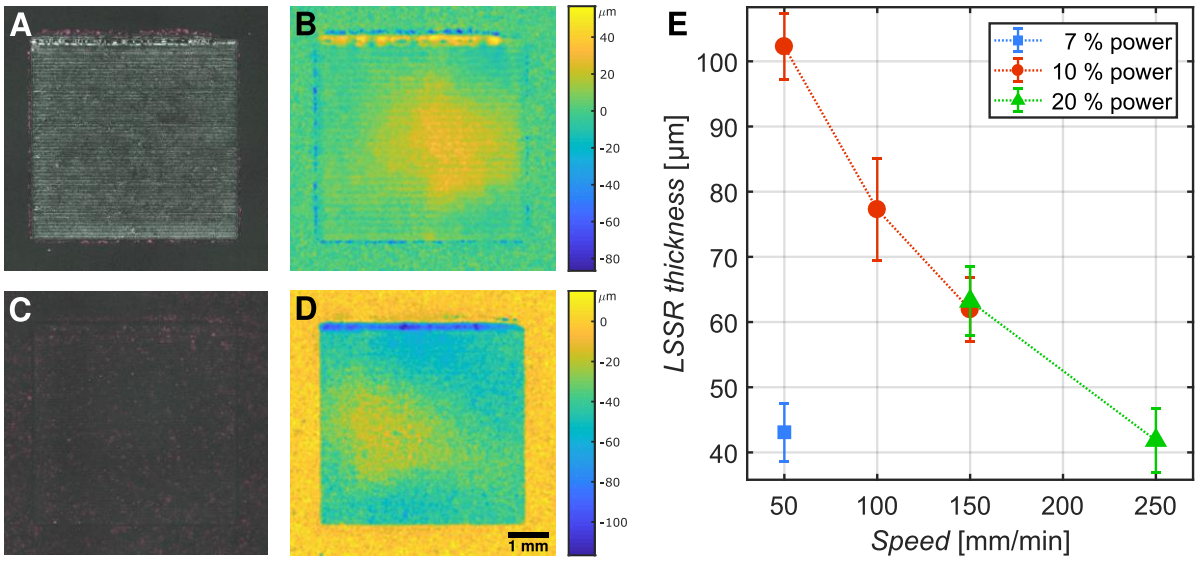

Figure 63. LSSR layer thickness. A) Micrograph of the LSSR sample. B) Heightmap of the LSSR sample. C) Micrograph of the corresponding identical sample with LSSR removed. D) Heightmap of the sample with LSSR removed. In (B) and (D), the height of the surrounding silicone rubber has been subtracted to only show the relative height of the LSSR film. E) Plot of LSSR thickness determined from the heightmaps for various samples laser-scribed under different conditions (speed and laser power). On each pair of samples, four separate regions were measured, as indicated in Figure 64C. The plot shows mean values standard deviation between the four regions. For the samples at 7 % power, the region at the top edge of the sample is excluded, i.e. n = 3 for power = 7 %; n = 4 for power > 7 %.

The Alicona microscope creates heightmaps of a sample by recording several micrographs while gradually shifting the focal plane through the depth of the sample. Image processing software is then used to determine which areas of each image are in focus. The depth of the corresponding focal plane is then assigned to those regions. Because this method relies on visual features, it is not suitable for transparent or semi-transparent surfaces. In order for the microscope to accurately recognise the surface of our semi-transparent silicone material, CB was brushed onto the surface of all samples and the surrounding silicone with a soft, dry paint brush. CB particles are of the order of a few hundred nanometres and a thin layer of CB is not expected to contribute notably to the thickness of the LSSR or silicone layer. The use of a soft brush ensures

that LSSR is not damaged in the application process. CB adheres well to the slightly tacky silicone surface. In the micrographs in Figures 63A and C, the samples can be seen to have an almost entirely black surface. The grey texture of the LSSR film remains visible because CB adheres less well to its dry, glassy surface. This is unproblematic because LSSR is opaque by itself. The sample with LSSR removed is almost entirely black from the CB on the surface. In both samples, some orange tartrazine particles can be seen shining through the CB layer, especially around the edges of the intact LSSR sample. This is likely due to silica deposited on the silicone surface from the gas phase during laser scribing. This reduces adhesion of CB to the surface, making it more translucent. This effect is less pronounced where LSSR was removed, probably because the removal of LSSR also removes the deposited silica from the surrounding area. It can be seen that visible tartrazine particles (orange spots in Figure 63A) often correspond with valleys in the heightmap (blue spots in Figure 63B). This is because the tartrazine particles, embedded in the silicone below the surface, get falsely recognised as the sample surface by the image process software that creates the heightmap. This shows that even after application of CB, the Alicona microscope's ability to accurately measure the surface topology of the semi-transparent silicone remains limited. It appears that the overall height is accurately represented. However, the lack of a fully opaque surface introduces small, local errors. This is particularly important for measurements of surface roughness (Section 4.6.3 and 5.4.3.1), since some of the recorded roughness will be due to measurement errors. To determine layer thickness, surface height was averaged over a larger area, reducing the impact of these measurement errors. Nevertheless, because the errors tend to be negative (particles below the surface that are falsely recognised as part of the surface), the median height of each sampled area was used (rather than the arithmetic mean) as a representative measure that is less sensitive to this one-sided bias.

LSSR layer thickness was determined by subtracting the height of one sample with LSSR removed from the height of an identical sample with LSSR intact. Unfortunately, although the process parameters for laser scribing both samples were identical, the topology of the underlying silicone film is not uniform over the sample area (see Figure 64A) and differs between samples. To correct for these differences, the height of the

surrounding silicone film was subtracted from each sample. Biharmonic spline interpolation in MATLAB was used to estimate the topology of the original silicone film over the area of the LSSR sample, based on the surrounding area. An example of estimated background topology is shown in Figure 64B. This estimate of the original surface diverges from the true surface topology as the distance from the edges increases. This can be seen in the heightmaps in Figure 64C as well as Figures 63B and D, which all show a broad, shallow peak inside the laser-scribed area. Because the estimate gets less accurate with increasing distance from the edges of the laser-scribed area, only the narrow areas near the edges are used to calculate the thickness of the layer. The extent of these area is indicated in Figure 64C. Each area includes 12,300 data points.

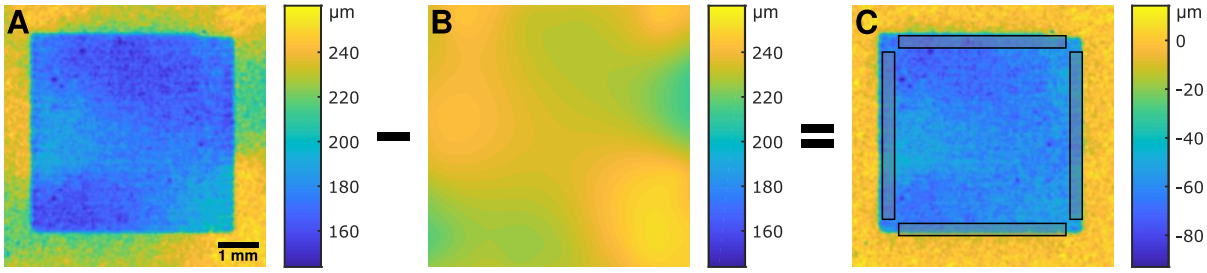

Figure 64. LSSR thickness evaluation from surface heightmap. A) Original heightmap of one LSSR sample, as recorded by the Alicona Infinity Focus microscope. B) Interpolated background profile to be subtracted from the raw data. C) Corrected heightmap of the LSSR film which is gained by subtracting (B) from (A). Now, the surrounding silicone film is at 0 µm height. The sample shown above had the LSSR film removed and shows the depth to which the LSSR reached below the surface of the silicone rubber. To determine overall LSSR thickness, the median height values in the four rectangular areas highlighted in (C) are averaged and subtracted from the height of the corresponding sample with LSSR intact. Each area includes 12,300 data points.

Figure 63B and D both show a large divergence from the overall height of the LSSR sample at the top edge of the laser-scribed area. This is the case because the first line was laser scribed at a higher laser power in order to reliably seed the LSSR conversion. It is therefore expected that the LSSR film at the top edge is much thicker than average. The sample shown in Figure 64 was laser scribed at an overall higher laser power and did not require seeding at increased laser power. Hence the top edge does not differ from the other edges. For samples where seeding was used, the top edge is excluded from the calculation of layer thickness.

Figure 63E shows a plot of the layer thickness for six LSSR samples laser-scribed under different conditions. Overall, thickness ranges between 41 µm and 103 µm. Unsurprisingly, it can be seen that thickness generally increases with increasing laser power and decreases with increasing speed. However, the increase from 7 % to 10 % power at $v = 50$ mm/min has a much more drastic effect on layer thickness than the increase from 10 % to 20 % power at $v = 150$ mm/min, where the increase in thickness could be considered negligible. It appears that the sensitivity of the laser scribing process to one parameter is dependent on the other. It should also be noted that these results may have limited reliability due to the low sample number (only one pair of samples was measured for each combination of parameters). All data shown in Figure 63E is from tartrazine LSSR samples. One graphite LSSR sample ($v = 50$ mm/min, $D = 7$ %) was also measured but showed no discernible difference to the comparable tartrazine LSSR sample.

4.6.3. Surface roughness

The surface roughness of the LSSR layers is of great importance if they are to be used as DEA electrodes in printed, soft actuators. As mentioned in Section 2.2.3, DEA electrodes as well as dielectric layers, need to be as uniform as possible to maximise their performance. In a printed DEA with LSSR electrodes, variation in LSSR thickness also leads to variation in dielectric layer thickness since the printed silicone conforms to the topology of the previous layer. Local peaks in electrode layer thickness will cause the dielectric layer to be thinner in those places. Due to the quadratic relationship between dielectric layer thickness and actuation pressure, this will lead to stress concentrations and greatly reduce the breakdown voltage of the actuator. In other applications such as pneumatic actuators (as described in Section 5.4.3.8), thickness variation is similarly important since the minimum local wall thickness of the rubber will determine maximum inflation pressure and local variations can lead to non-uniform inflation.

To quantify the surface roughness of LSSR layers, the same topology data from the Alicona microscope (see Section 4.6.2) was used. From each 5 x 5 mm LSSR sample (and of the corresponding sample with LSSR removed), a 4 x 4 mm region in the centre of the sample was analysed (see Figure 65A). The height profiles were high-pass filtered

to contain only the small-scale features with lateral dimensions under 400 µm. Since LSSR lines are around 100-200 µm wide (see Section 4.6.1.1), surface roughness of LSSR cannot be larger than this. Larger surface features are more likely to originate from thickness variations in the silicone film (see Section 5.4.3.3) and should therefore be excluded. High-pass filtering was achieved by first smoothing the profiles using biharmonic spline interpolation in MATLAB, and then subtracting the smoothed profiles from the originals, as shown in Figure 65. The resulting flattened profiles were used to determine roughness.

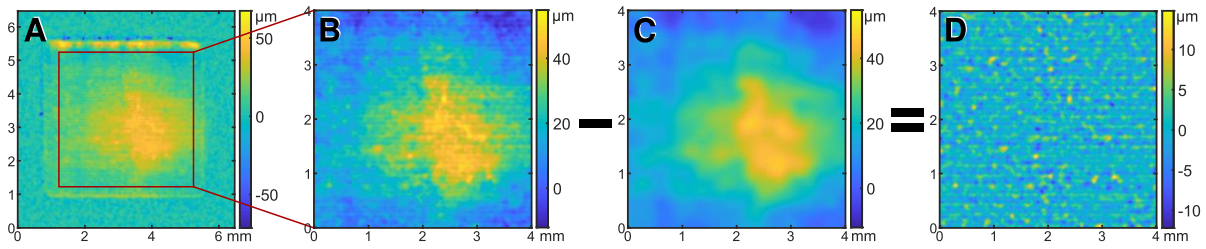

Figure 65. LSSR surface profiles for roughness analysis. A) LSSR surface profile, as used in Section 4.6.2 (see Figure 63B). The red rectangle indicates the region used for roughness analysis. B) 4 x 4 mm region of (A) used for roughness analysis. C) Smoothed version of (B). D) High-pass filtered profile obtained by subtracting (C) from (B) where only features with lateral dimensions smaller than 400 µm remain.

Several different descriptors for surface roughness are commonly used. Arithmetic mean deviation or root mean square (RMS) deviation (equivalent to the standard deviation of the height distribution) are widely used to quantify roughness, mainly because of their simplicity.[268] However, these measures are insensitive to infrequent, large peaks or valleys.[268] Because these large peaks are particularly important in actuator applications, these descriptors were deemed unsuitable. Maximum profile height R_z, defined as the difference between the highest peak and lowest valley in the sample, is another common descriptor that captures these extreme values. However, R_z is subject to large random variation between samples.[268] Also, in the case of DEA electrodes, peaks are more important than valleys. A local peak in LSSR thickness can drastically reduce the breakdown voltage, whereas a local valley only results in an area with slightly reduced actuation pressure. With these considerations in mind, the roughness parameter R_{P5} was introduced, defined as the 95th percentile of peak height, i.e., the maximum peak height above the average, but disregarding the highest 5 % of

peaks. A descriptor like R_{p5} offers an acceptable measure of extreme values while also being more robust to random variation than R_z.[268]

Roughness R_{p5} for different LSSR samples, recorded over a sample area of 4 by 4 mm, is shown in Figure 66A. Both the top surface of the LSSR film and the bottom surface (top surface of the underlying silicone rubber after LSSR was removed) were measured. The bottom surface was inverted because valleys in the silicone surface represent peaks in the LSSR surface. Interestingly, samples with higher roughness on the top surface tended to have lower roughness on the bottom surface. The bottom graph in Figure 66A shows the sum of the R_{p5} roughness for the top and bottom surfaces. This corresponds to the maximum expected positive deviation of the LSSR layer from its mean thickness. The total roughness tends to decrease with increasing speed, starting around 21 µm at 50 mm/min and approaching a value around 18 µm as speed is increased to 250 mm/min. Laser power seems to have a much smaller impact on surface roughness. Overall, total positive thickness deviation is of the order of 20 µm for all samples. Unfortunately, this is quite large for electrode layers that are between 40 µm and 100 µm thick. It should be noted that the measured surface roughness may be subject to substantial measurement errors. As mentioned above, large peaks in the bottom surface can be caused by filler particles visible through the clear silicone despite the CB coating, which is not perfectly opaque. The measured values should therefore be considered as upper bounds on thickness deviation. It should also be noted that, due to time constraints, only one single sample per set of parameters could be analysed. Visual inspection of larger sets of LSSR samples, such as the sheet resistance samples with $6 \leq n \leq 9$ (see Section 4.6.4.2), showed very consistent surface quality between samples laser scribed under the same conditions. This gives us reason to believe that the results presented in Figure 66 should give a good indication of the general surface properties of LSSR. Nevertheless, a more thorough evaluation of surface quality on a larger set of samples will need to be carried out in the future to reliably characterise the surface roughness of LSSR and how it depends on the process parameters.

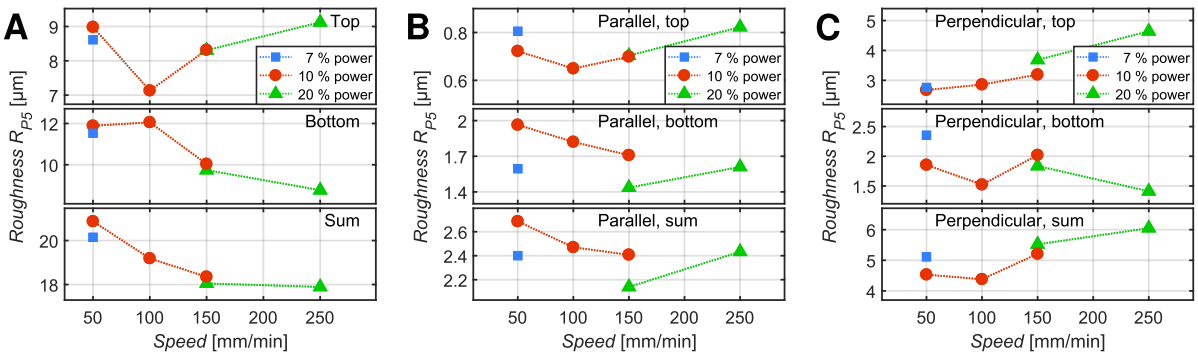

Figure 66. Surface roughness of LSSR samples. A) Surface roughness R_{P5} over the entire sample. B) Surface roughness R_{P5} parallel to the direction of laser lines, averaged over the width of each sample. C) Surface roughness R_{P5} perpendicular to the direction of laser lines, averaged over the length of each sample. In each subfigure, the top graph shows the top surface of the LSSR film and the middle graph shows the bottom surface, i.e., the inverted surface of the underlying silicone rubber. The bottom graph shows the sum of top and bottom which is the maximum expected positive deviation from the mean thickness of the LSSR film.

Because laser scribing occurs in discrete, parallel lines, the surface topology of the resulting LSSR films is dependent on the direction of the laser scanning. The parallel-line structure is clearly evident in the heightmap shown in Figure 67A. To better characterise this anisotropy, surface roughness was evaluated separately along both principle axes of the laser-scribed pattern (parallel and perpendicular to the laser lines). For this purpose, the surface profile was averaged along either axis to yield an average cross-section profile. Examples of averaged cross-section profiles parallel and perpendicular to the laser direction are shown in Figures 67B and C, respectively. The perpendicular cross-section clearly shows a periodic, wavy surface pattern. The averaging reduces the influence of random deviations and exposes systematic topology features that are an inherent consequence of the laser scribing process. By filtering out random deviations, errors caused by the semi-transparent sample surface should be greatly reduced. On the other hand, there may be real, local, random fluctuations in the surface profile which also get removed from the data. Therefore, roughness values extracted from the averaged profiles can be interpreted as lower bounds on the real surface roughness. For consistency, R_{P5} is also used as roughness descriptor for the averaged profiles.

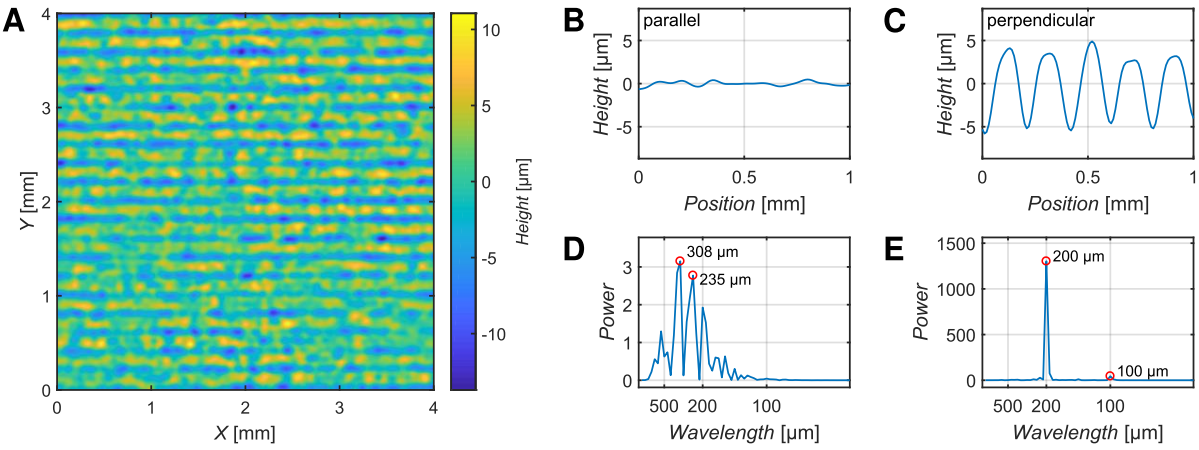

Figure 67. Surface topology of LSSR. A) Heightmap of LSSR top surface (background subtracted), clearly showing a pattern of parallel lines generated by the laser scribing process. B-C) Averaged cross-section profiles parallel (B) and perpendicular (C) to the laser direction. D-E) Power spectra from the Fourier transforms of the profiles in (B) and (C), respectively. Power is plotted over wavelength rather than spatial frequency to be directly relatable to topological features of a certain length scale. The two most prominent peaks in each spectrum are highlighted. All data is taken from the same sample (D = 20 %, v = 250 mm/min, UV Electro 225-1 with tartrazine).

The R_{P5} roughness for the averaged profiles perpendicular and parallel to the direction of the laser lines are shown in Figures 66B and C, respectively. The bottom surface shows similar roughness in both directions (on average 1.66 µm parallel and 1.86 µm perpendicular) with no obvious trends over the explored parameter space. In contrast, the top surface shows very little roughness in the parallel direction (0.75 µm on average) but very large roughness in the perpendicular direction (3.26 µm on average). This is clear evidence of an anisotropic surface topology that results from the scribing of discrete, parallel lines. The plot in Figure 66C (top) also shows a consistent trend towards higher roughness at higher speeds. This could be explained by the fact that higher speeds, which lead to lower exposure, result in narrower lines and less overlap between adjacent lines. Wider lines with more overlap can be expected to merge into a more uniform surface.

The periodicity of the surface variations in either direction was characterised by analysing the power spectrum (square magnitude of the Fourier transform) of the averaged cross-sections. Prominent peaks in the power spectrum show dominant frequencies in the surface structure. The power spectra for one LSSR sample (D = 20 %, v = 250 mm/min) are shown in Figures 67D and E (parallel and

perpendicular, respectively). As expected, the power spectrum of the parallel profile shows multiple peaks of similar and overall very low magnitude. In contrast, the highly periodic perpendicular profile is reflected by a single, very prominent peak in the power spectrum. Interestingly, the most prominent peak occurs at 200 µm wavelength, which is twice the line spacing of the laser lines. This was observed in all recorded LSSR surface profiles. The second largest peak coincides with the line spacing of 100 µm. However, this peak generally has less than 10 % of the magnitude of the first. This indicates that every second pass of the laser produces much more prominent surface features than the lines in between. An explanation for this phenomenon is illustrated in Figure 68. This explanation assumes that the width of a single line of LSSR is more than twice the laser line spacing (see Figure 68A), which was arbitrarily set to 100 µm. If this is the case, then the second line that is laser scribed will hit the LSSR from the previous line rather than the silicone substrate. Because the heat is now generated on the LSSR surface instead of the silicone, it can be dissipated within the LSSR and only a small amount of silicone rubber, if any, is exposed to sufficiently high temperatures to generate new LSSR. Because little new LSSR is formed, it does not extend to the next laser line (Figure 68B). The next pass off the laser will hit pristine silicone rubber again and cause conversion of a new line of LSSR (Figure 68C). This way, a line of LSSR is formed every second pass of the laser, which explains the measured cross-section profile (Figure 67C and E). This phenomenon is also evident in the micrographs in Figure 59, where LSSR lines appear about twice as wide as the line spacing. This shows that the width of individual lines should be more thoroughly investigated in the future and that line spacing might be an important parameter to influence the surface structure and roughness of LSSR.

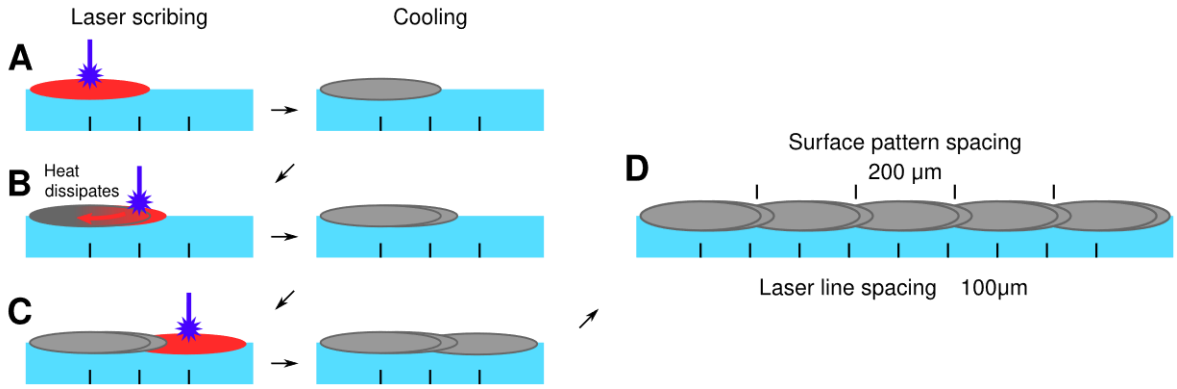

Figure 68. LSSR surface pattern forming at twice the laser line spacing. Each schematic shows a cross-section view (perpendicular to the laser lines) of a silicone film during laser scribing. The tick marks at the bottom indicate the laser line spacing. A) The first pass of the laser generates a line of LSSR that is more than twice the width of the line spacing. B) The next pass of the laser hits the LSSR of the previous line, which can dissipate much of the heat so that only a small amount of new LSSR is formed. The newly formed LSSR does not reach to the next laser line. C) On the third pass, the laser hits the silicone rubber again, creating a full new line of LSSR. D) Since every second pass generates only a small amount of LSSR, the resulting cross-section pattern has slightly broadened peaks at twice the line spacing, same as the cross-section profile shown in Figure 67C.

4.6.4. Sheet resistance

Since LSSR is intended to be used as an electrode material in soft devices, the electrical conductivity is one of the most important properties. This was characterised by measuring sheet resistance of different LSSR films. Because several different methods were used to measure the same LSSR samples, these methods are first presented in Section 4.6.4.1 before discussing and comparing the results in Section 4.6.4.2.

4.6.4.1. Methods

Sheet resistance of LSSR films was measured by three different methods. The simplest method takes two-point measurements with a Fluke 77 IV digital multimeter (Fluke Corporation, USA). The probe consists of two parallel copper contacts which are placed on an LSSR sample so that they enclose a rectangular section of known width w (the width of the sample) and length l (distance between the contacts). Resistance R is measured between the contacts. Because the resistance of the copper is negligible compared to the resistance of the sample, parallel current flow can be assumed. In this case, the sheet resistance can be calculated very simply according to Equation (3).[269] For a square area ($w = l$), the measured resistance is equal to the sheet resistance. Typically, rectangular areas of 2 x 5 mm were laser-scribed for sheet resistance

measurements and the copper contacts were placed 2 mm apart such that a square 2 x 2 mm area of the LSSR film was measured. A schematic of the probe is shown in Figure 69A.

$$R_S = \frac{Rw}{l} \tag{3}$$

The resistance values measured by this method include contact resistance, which may not be negligible. It was found that repeated measurements of the same sample with this method yielded greatly varying results. Generally, the first measurement of each sample showed much higher resistance than subsequent measurements. This can be attributed to non-conductive silica at the surface layer which is (partially) removed through contact with the probe, as was shown in Figure 55M (Section 4.6.1.1). On subsequent measurements, the probe is in better contact with the conductive material and therefore contact resistance is reduced. It was also found that the measured resistance varied greatly with contact pressure. Increasing the pressure with which the copper contacts are pressed onto the LSSR sample generally decreased measured resistance. For a typical measurement, a downward force of around 50 N was applied to the probe which was placed on top of the LSSR sample resting on a hard, flat surface. This force was applied manually and given values are estimates. Increasing the contact pressure is assumed to help break the porous top layer of silica and improve electrical contact with LSSR. However, in some cases the pressure can also cause damage to the conductive phase of the LSSR film and lead to a permanent increase in resistance. Since measured resistance generally decreased with repeated measurements but measurements may also cause damage to the sample and increase resistance, each sample was measured three times and the minimum measured value was selected. Because of the various uncertainties associated with this measurement method (contact resistance, contact pressure, sample damage), two other methods were also used to measure the sheet resistance and determine the validity of the first method.

The second method is similar to the first but uses CG to improve the electrical contact between the LSSR film and the probe (see schematic in Figure 69B). As in the first method, sheet resistance was calculated according to Equation (3).

The third method uses a four-point probe in linear configuration which consists of four equally spaced metal pins in contact with the sample (see schematic in Figure 69C). A small current is sourced through the outer pins and voltage is measured between the inner pins. This setup greatly reduces the influence of contact resistance.[270] In the four-point method, sheet resistance is calculated using Equation (4), where I is the applied current between the outer probes, V is the measured voltage between the inner probes, and C is a geometric correction factor to account for the specific sample dimensions, given in ref.[271]

$$R_S = C \frac{\pi}{\ln(2)} \frac{V}{I} \tag{4}$$

For methods two and three, larger samples of 12 x 4 mm were used to reduce susceptibility to local variations within each sample and to fit the dimensions of the four-point probe. The measurements were performed using a Keithley 2400 SourceMeter (Keithley Instruments, USA), which is more sensitive and precise than the handheld multimeter used in the first method. It also allows resistance measurements over a range of applied currents or voltages to generate multiple data points per sample and show possible non-ohmic behaviour. The three measurement methods will be referred to as 2-point, 2-point CG, and 4-point, respectively.

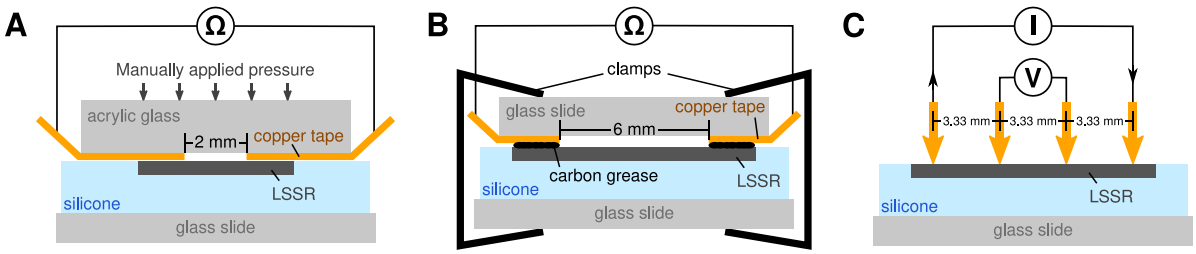

Figure 69. Sheet resistance probes. A) Two-point probe with dry, flat copper contacts (2-point method). Pressure is applied manually to improve contact between the probe and sample. B) Two-point probe with flat copper contacts and carbon grease to reduce contact resistance between the probe and sample (2-point CG method). The probe is held on by clamps that exert a small and constant amount of pressure. C) Four-point probe with four pins in co-linear configuration (4-point method). A current is sourced between the outer pins and voltage is measured between the inner pins.

4.6.4.2. Results

Using the 2-point method, various samples of LSSR films made from UV Electro 225-1 with tartrazine (2 wt.%) were measured to investigate the dependency of sheet

resistance on the two primary process parameters (speed v and relative laser power D). The results are shown in Figure 70.

Figure 70A shows sheet resistance over speed for samples laser-scribed at $D = 10$ %, while Figure 70B shows sheet resistance over laser power for samples laser-scribed at $v = 250$ mm/min. Between the two, laser power appears to have a greater influence on sheet resistance than speed. Mean R_S differs by about a factor of two between $v = 50$ and $v = 250$ (for $D = 10$ %). Meanwhile, R_S changes by about a factor of ten between $D = 15$ % and $D = 50$ % (for $v = 250$).

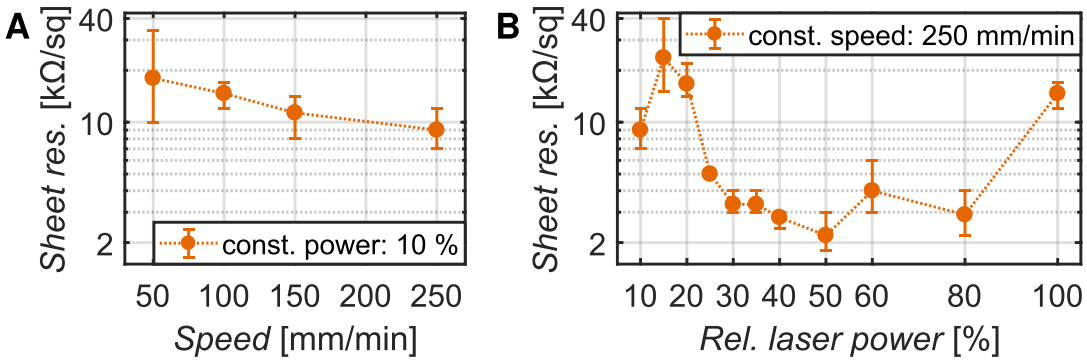

Figure 70. LSSR sheet resistance. A) Mean sheet resistance (log scale) over speed for samples laser scribed at 10 % laser power. B) Mean sheet resistance (log scale) over laser power for samples laser-scribed at 250 mm/min speed. All samples were made from UV Electro 225-1 with tartrazine filler. Error bars show min and max values (n = 3).

Figure 70A shows that sheet resistance reduces with increasing speed. This is somewhat unexpected since it has been shown previously that higher speed leads to a reduction in film thickness (see Section 4.6.2) which would cause an increase in sheet resistance if the bulk resistance of the material were to remain constant. We can therefore conclude a change in material composition that counteracts the differences in film thickness. The most likely explanation is that lower speed, which leads to higher exposure, causes a thicker layer of non-conductive silica to form at the surface. We showed in Section 4.6.1.1 that higher exposure tends to result in more silica forming at the surface. The presence of non-conductive silica at the surface impedes a good electrical contact with the conducting material underneath. Therefore, measured resistance would high, even if the conducting layer were thicker and should thus be more conductive. That would mean that the decrease in resistance with increasing speed is an artefact of the measurement method rather than a real property of the

LSSR film. Nevertheless, if a thick layer of silica at the surface makes it difficult to achieve a good electrical contact with the material, this is an important consideration for practical applications.

According to the data shown in Figure 70B, R_S is lowest for $v = 250$, $D = 50$ %. Both lower and higher laser power lead to higher resistance. This behaviour can be attributed to the same two counteracting phenomena described above: Higher power leads to a thicker LSSR layer with overall lower resistance but also produces a thicker top layer of non-conductive silica that increases contact resistance. Among the samples presented here, $D = 50$ % offers the best trade-off between these tendencies. It is interesting to see that, at the very lowest power ($D = 10$ %), sheet resistance reduces again. This may be result of an abrupt decrease in the amount of surface silica at very low power. The micrographs in Section 4.6.1.1 show almost no visible silica at the surface of LSSR scribed at very low laser power.

Figure 71 shows a comparison of the three measurement methods described in Section 4.6.4.1 for four different LSSR samples. As expected, the 2-point method generally yields much higher resistance values than the other two since the use of CG or a four-point probe should greatly reduce the influence of contact resistance. The 2-point CG and 4-point methods appear to be in good agreement (for all but the first sample). This is a good indication that the measured values are close to the ground truth.

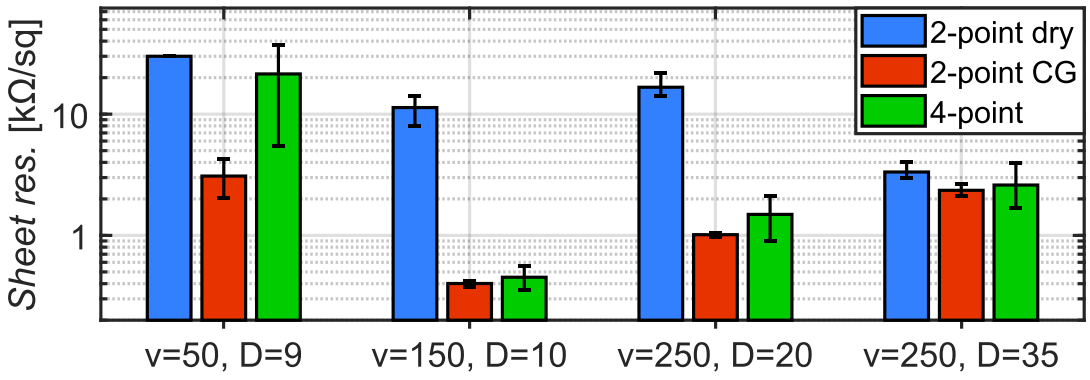

Figure 71. Comparison of sheet resistance measurement methods. The mean sheet resistance of several tartrazine LSSR samples measured using three different methods is shown. Error bars show min and max values. Sample sizes are between 1 and 5. For each group of samples, the parameters v (speed in mm/min) and D (duty cycle in %) are given.

The reason that the two methods diverge on the first sample ($v = 50$ mm/min, $D = 9$ %) may have to do with the anisotropic nature of LSSR. Since LSSR consists of discrete, parallel lines, conductivity along the lines is different from the conductivity across lines. The more the lines overlap, the less anisotropic behaviour would be expected. For very low laser power, line width and thus overlap are much lower than for high power. This was shown in Section 4.6.1.1. Sheet resistance measurements were all carried out parallel to the laser lines. That means that all four pins of the four-point probe were placed on the same line. Theoretically, in the extreme case that the individual lines are completely separated, the 4-point method would only measure the resistance of a single line. This is bound to be much higher than the resistance of the whole sample. The copper contacts of the two-point probe cover the entire width of the sample and are therefore guaranteed to measure the whole sample even if the individual lines were separate. In reality, the sample in question is not composed of separate lines. Nevertheless, the reduced overlap between lines at low laser power will lead to increased anisotropy which can explain the increased resistance measured by the 4-point method. Indeed, it was found during use of the four-point probe that the measurements are highly sensitive to sample placement. If the sample was not perfectly parallel with the probe (or deliberately placed diagonally), the measurement would be noisier and the measured resistance generally higher than for the same sample after realignment. This indicates that electrical conductivity in LSSR is indeed anisotropic but that the effect is more relevant in samples laser-scribed at very low power.

Another interesting observation was made when measuring resistance at different probe voltages. Figure 72A shows representative current-voltage (I-V) curves of a single LSSR sample measured using the 2-point CG and 4-point methods. With each method, multiple voltage sweeps were recorded. For the 2-point CG method, two sweeps (one low-to-high, and one high-to-low) are shown. For the 4-point method, six sweeps (three low-to-high, and three high-to-low) are shown. The data points form the different sweeps line up so well as to be indistinguishable in the plot in Figure 71A. This shows that the measured behaviour is highly consistent.

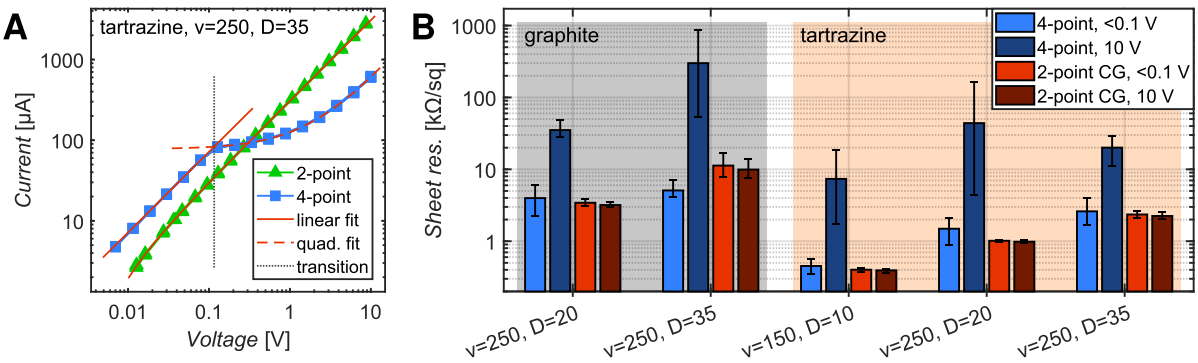

Figure 72. Influence of probe voltage on sheet resistance measurements. A) Representative I-V curves of an LSSR sample measured using the 4-point method (showing six voltage sweeps, three up and three down) and 2-point CG method (showing two voltage sweeps, one up and one down). B) Mean sheet resistance of graphite and tartrazine LSSR measured at low (< 0.1 V) or high (~10 V) probe voltage using the 4-point or 2-point CG method ($3 \leq n \leq 5$, error bars show min and max values).

The I-V curve from the 2-point CG method shows almost perfect ohmic behaviour, as indicated by the linear fit ($R^2 = 0.9976$) superimposed in the plot. In contrast, the I-V curve from the 4-point method shows a distinct non-linearity and an abrupt transition between a linear region at low voltages and a non-linear region at higher voltages. In the linear region, measurements are indeed almost perfectly linear ($R^2 = 0.9999$). The non-linear region very consistently follows a quadratic trend ($R^2 = 0.9997$). Most, but not all samples showed this non-linearity when measured with the 4-point method. The transition voltage is generally of the order of 100 mV but varies greatly, even between identical samples. Transition voltages between 3 mV and 2 V have been observed. For any one particular sample, the transition is highly consistent and independent of the direction of the sweep.

We do not, at this point, have a satisfactory explanation for this non-linear behaviour observed in the 4-point measurements. The phenomenon does not seem to be caused by thermal effects (Joule heating at higher currents) since we would then expect to see a hysteresis between the up and down sweep. In addition, heating would mainly occur near the outer pins where the current is sourced and should not influence the voltage measurement at the inner pins. An alternative explanation could be the semiconducting nature of LSSR. Together with the metal pins of the probe, the LSSR might form a metal-semiconductor junction which can have a non-ohmic I-V characteristic.[272] However, we are not familiar with any metal-semiconductor junction

that has an I-V characteristic reminiscent of that shown in Figure 72A. Further investigation of the electrical properties of LSSR is certainly warranted, given this curious observation. Unfortunately, such an investigation is beyond the scope of this thesis.

In Figure 72B, the influence of probe voltage on the measured resistance for five different LSSR samples is shown. For the 4-point method, resistances measured at low voltage (in the linear region, generally below 100 mV) are roughly one order of magnitude lower than at 10 V (in the non-linear region). For the 2-point CG method, there is no appreciable difference between measurements at 100 mV and 10 V.

Overall, the 2-point CG method seems to have greater robustness to sample positioning and probe voltage while showing similarly low susceptibility to contact resistance as the 4-point method. We therefore determine the 2-point CG method as the preferred method for measuring LSSR sheet resistance.

From the data shown in Figure 72B it can also be seen that tartrazine LSSR has lower sheet resistance than graphite LSSR for the two matching samples that are presented. This is somewhat surprising since one might expect that the presence of conductive particles in the silicone matrix might aid overall electrical conductivity. However, the differences between tartrazine and graphite LSSR probably stem from differences in absorption of the two fillers. Graphite is generally more absorbent, leading to different reaction conditions during laser scribing even when the process parameters are the same.

The overall lowest sheet resistance of 401 Ω/sq (σ = 24 Ω/sq, n = 3) was measured for tartrazine LSSR laser-scribed at v = 150, D = 10 %. At these parameters, LSSR has a thickness of 62 µm (see Section 4.6.2). Accordingly, the bulk resistivity of LSSR in this sample is 2.5 × 10^{-2} Ω · m (conductivity 40 S/m). This is very high compared to some other common DEA electrode materials such as CG (see Section 2.3.3).

4.6.5. Resistance under strain

Resistance under uniaxial strain was measured on 5 samples of LSSR made from UV Electro 225-1 with tartrazine (2 wt.%). Laser-scribed samples were made on printed

silicone membranes of 0.3 mm thickness and covered with a second layer of printed silicone (see Section 5.4 for details on the printing process). The top layer has an H-shape (see Figure 73C) that exposes a region of the LSSR layer on either side and leaves space to attach copper strips as contacts. A small amount of CG is applied to reduce contact resistance between the copper strips and the LSSR. The copper contacts are glued in place using SilPoxy silicone glue. Figures 73A and B show the resistance samples before and after the copper contacts were attached. The LSSR area between the contacts is 6 x 6 mm. The samples were laser scribed at $v = 150$ mm/min and $D = 10$ %.

The resistance samples were tested on a manually driven, uniaxial strain rig shown in Figure 73C. Resistance was measured between the copper contacts using the Fluke 77 IV digital multimeter. Strain was determined by filming the sample with a digital camera and measuring clamp spacing in individual video frames using subpixel edge detection[273] in MATLAB.

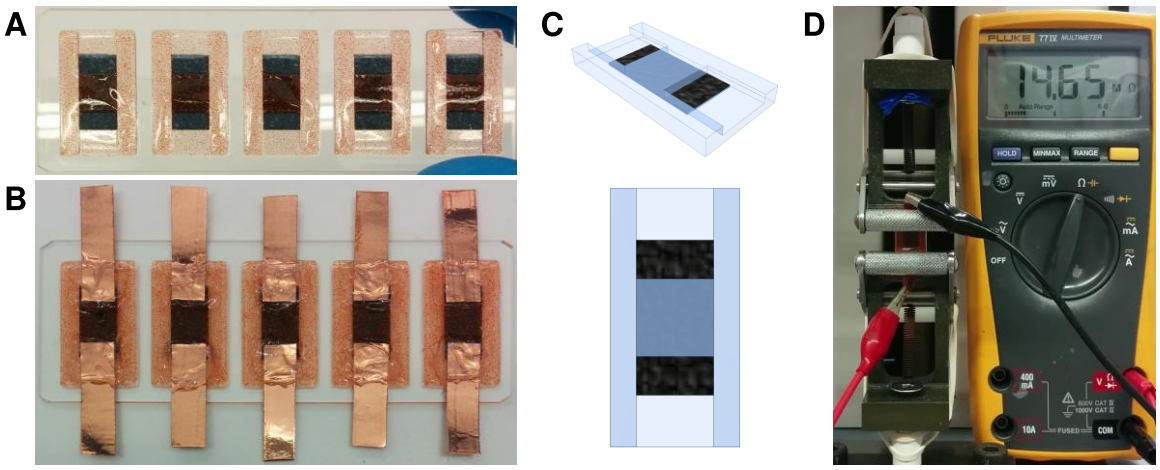

Figure 73. LSSR conductivity samples for strain testing, as-printed (A) and after attaching copper contacts (B). Carbon grease was applied to the exposed areas of the LSSR film to enhance electrical contact with the copper strips. The strips are fixed in place with silicone glue. C) Rendering of the conductivity samples, perspective and top view, showing the geometry of the top layer. D) Uniaxial strain rig and multimeter used for resistance measurements under strain.

Figure 74A shows the measured resistance plotted against sample strain. Negative strain indicated that the clamp spacing was reduced below its initial value, leading to buckling of the sheet-like sample and hence corresponding to a bending load. Resistance can be seen to increase exponentially under both positive and negative

strain (note the logarithmic scale of the y-axis). All samples were stretched at least until the point where the sample's resistance exceeded the measurement range of the multimeter (up to 50 MΩ). Some samples were subjected to higher strains beyond this point to investigate the effects of the maximum strain that a sample has experienced. Table 3 lists several characteristics of each LSSR sample, including the maximum strain the sample was subjected to as well as the maximum strain at which the sample showed measurable conductivity. Table 3 also lists the initial resistance and residual increase in resistance after stretching. Initial resistance was measured directly after attaching the copper contacts and before mounting the sample in the strain rig because peeling the sample off the glass substrate on which it was prepared subjects the sample to some strain and causes a permanent increase in electrical resistance. The residual resistance increase is specified relative to this pre-test resistance.

Table 3. Characteristics of LSSR resistance samples tested under uniaxial strain. Sample 5 is considered an outlier and excluded from the calculation of mean and standard deviation. The maximum experienced strain is a test parameter that was chosen arbitrarily for each sample.

Sample	**Initial resistance [kΩ]**	**Residual relative resistance increase**	**Maximum strain experienced**	**Max strain before loss of conductivity (R < 50 MΩ)**
1	18.7	33.0 %	15.8 %	15.7 %
2	22.3	87.6 %	56.0 %	27.9 %
3	22.6	107.7 %	69.5 %	26.0 %
4	23.5	47.5 %	28.5 %	19.8 %
5	60.1	62.6 %	25.9 %	18.4 %
Mean:	**21.8**			**22.3 %**
Stdev.:	2.1			5.6 %

Both the initial resistance (μ=21.8 kΩ, σ=2.1 kΩ, n=4) and the maximum strain (μ=22.3 %, σ=5.6 %, n=4) at which LSSR remains measurably conductive (R<50 MΩ) are fairly consistent between samples 1 to 4. Sample 5 is considered an outlier because its initial resistance deviates from the mean by more than 18 standard deviations.

The maximum strain determined in our experiments is much larger than the maximum measurable strain described by Gao et al. for their LSSR strain sensors.[247] They report

a maximum measurable strain up to 5 % compared to an average 22.3 % in our samples. On the other hand, behaviour under strain of our LSSR samples was found to be highly inconsistent, noisy, hysteretic and varying greatly between samples. These inconsistencies make our LSSR films poor strain sensors, despite the fact that they can sense over a broader range of strains. The strain sensors reported by Gao et al. appear to show more consistent behaviour.

During the very first strain cycle, samples 1 and 2 showed a very steep increase in resistance, exceeding 50 MΩ at strains below 10 % (seeFigure 74A). In subsequent cycles, conductivity was maintained up to higher strains. This indicates a sort of "training" effect where the sample needs to be stretched to its maximum intended strain at least once in order to reach steady performance. This is similar to the training of DEAs described in Section 3.2.4. The reason that this effect was only observed in two samples could be that samples were subject to varying (unspecified) amounts of strain during sample preparation such that the "training" might already have occurred in the other samples before the recorded measurements were started.

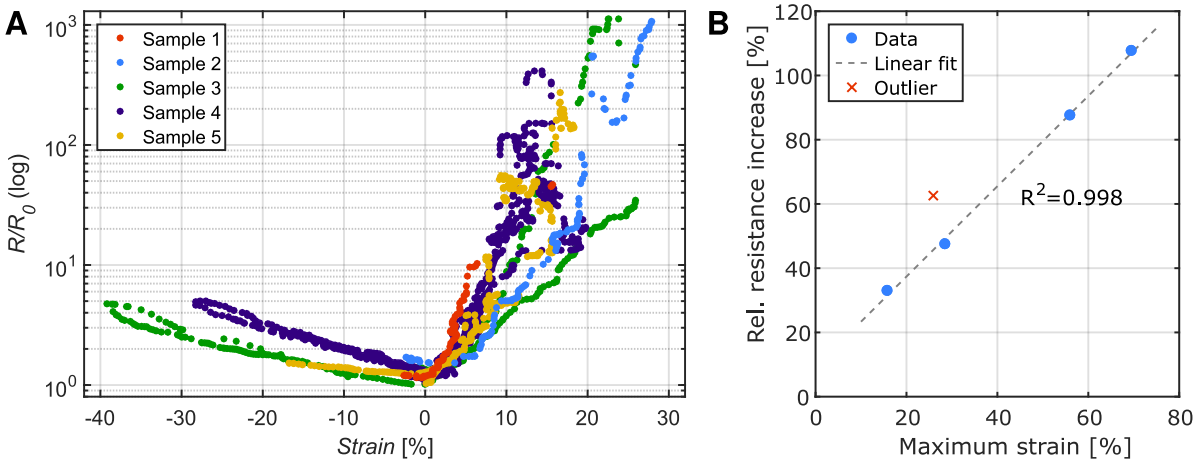

Figure 74. LSSR resistance under strain. A) Relative resistance changes in LSSR samples under positive and negative strain. Negative strain corresponds to out-of-plane buckling of the LSSR films. B) The residual resistance increase after strain testing shows a very strong linear relationship with the maximum strain that the sample had been subjected to. Sample 5 is classified as an outlier because of its very high initial resistance (see Table 3).

Another interesting observation from our measurements is that despite great variation in the resistance/strain profiles between samples, there appears to be a very consistent linear relationship between a sample's residual resistance increase and the maximum

strain it experienced. Figure 74B shows the permanent increase in resistance of each sample at the end of the strain test (as a percentage relative to the initial resistance before testing) plotted against the maximum strain that the sample experienced during testing (both of these values are also listed in Table 3). A linear fit of the data is also plotted. Sample 5 is excluded from the fit since it has been classified as an outlier based on its initial resistance. Although 4 is a very small population size and further testing is necessary to verfiy this behaviour, these results point towards potential applications of LSSR in strain sensors used for measuring maximum experienced strain. Such sensors could be useful for monitoring of structural parts in civil engineering to detect potential damage if a part has been subjected to strains higher than its rated maximum. The sensor could be probed at sporadic intevals and would reveal the maximum strain that the part has experienced in its lifetime.

4.6.6. Wettability

Laser treatment has been documented in the literature as a method to modify the wettability of PDMS.[238–242] We therefore investigated what influence our laser scribing process has on the wettability of the resulting LSSR films. Contact angles were determined visually from the profiles of water droplets resting on a flat LSSR surface. Seven different LSSR samples were tested and two or three droplets were measured on each sample. The results are presented in Figure 75A. Figure 75E shows an example of a droplet profile image used for contact angle measurements. The silicone rubber with graphite or tartrazine fillers, without laser scribing, is very slightly hydrophobic, with contact angles of 95° and 92°, respectively. In contrast, all investigated LSSR samples are very hydrophobic and most of them verge on superhydrophobic (contact angle $> 150°$). Water droplets can sit on, slide across, or bounce off the surface without wetting it (see photographs in Figures 75C and D). Interestingly, the hydrophobicity of the LSSR surface only arises several hours or days after laser scribing. It was found that freshly laser scribed LSSR films are superhydrophilic. A water droplet placed on the LSSR film quickly spreads out across the surface, leaving no discernible droplet behind (i.e. contact angle 0°). This is shown in the image sequence in Figure 75B. After several days of storage at ambient conditions, the same LSSR sample displays superhydrophobic properties. All contact angle measurements were carried out on

samples that were more than one week old. Previous work by Wang et al.[242] describes the superhydrophobic nature of laser-scribed PDMS but the authors make no mention of any changes in the surface behaviour over time.

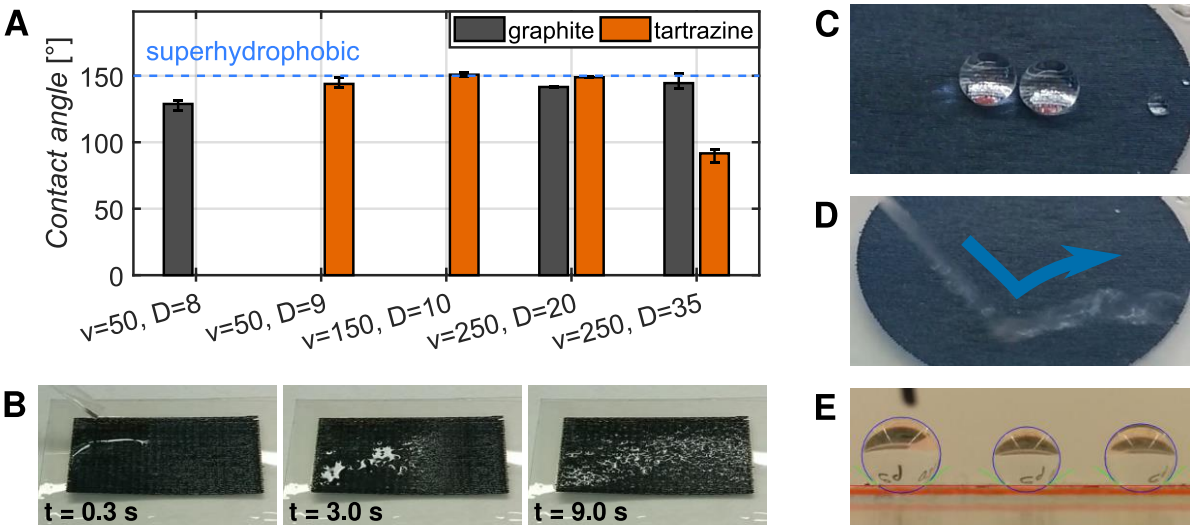

Figure 75. Wettability of LSSR films. A) Measured contact angles of various LSSR samples, some of which show superhydrophobic behaviour. Error bars show min and max values ($2 \leq n \leq 3$). B) Superhydrophilic behaviour of a freshly laser scribed LSSR sample. The water droplet deposited on the surface spreads across the whole sample, leaving no discernible droplet (contact angle 0°). C) Water droplets sitting on a hydrophobic LSSR surface. D) Water jet bouncing off a hydrophobic LSSR surface. E) Profile of water droplets on tartrazine LSSR ($v = 50$, $D = 9$ %) used for contact angle measurements. The blue ellipses are fitted to the edges of the droplets. The green line segments indicate the measured angles.

A gradual change from hydrophilic to hydrophobic behaviour, as we have observed on LSSR, is also known to occur on PDMS surfaces after oxygen plasma treatment.[274,275] The plasma treatment temporarily increases the wettability of PDMS by forming a thin layer of silica at the surface.[275] However, this increase in wettability is not permanent and usually returns to near its original value over the course of several hours or days in a process known as hydrophobic recovery. For plasma-treated PDMS, hydrophobic recovery has been attributed to mobile, hydrophobic polymer chains migrating to the surface and covering the hydrophilic silica layer that was formed by the plasma.[275] The same phenomenon could be occurring in LSSR. We have established that a surface layer of silica is present on LSSR, which could give it hydrophilic properties immediately after laser scribing. Migration of mobile polymer chains from the silicone underneath could also be a plausible explanation for the hydrophobic

recovery in LSSR, even though LSSR layers are much thicker than the silica layers formed by plasma treatment (8-10 nm).[275] The fact that LSSR layers typically have a cracked and porous structure (see Section 4.6.1.1) means that migration is fundamentally possible. The rough surface structure of LSSR also contributes to its hydrophobic behaviour.[242]

4.6.7. Layer adhesion

LSSR has relatively low adhesion to the silicone substrate compared to the internal cohesive strength of the silicone. Adhesive forces between LSSR and silicone were not measured, but on all samples used for measurements of layer thickness in Section 4.6.2, LSSR could be easily removed by scarping with a metal spatula. The process caused no visible damage to the underlying silicone surface. This property allows LSSR to be used as a separation layer between layers of silicone rubber. In a 3D printing process, this can be very useful for separating support structures from the printed part. The ability to create layer separations also enables the fabrication of pneumatic or fluidic actuators by incorporating internal cavities and channels into rubber parts. Using this approach, a pneumatic actuator can be 3D printed in a collapsed state and then inflated into its desired shape after the print is complete. This method is explored in Chapter 5, Section 5.4.3.8.

4.7. Conclusion

In this chapter, we introduced direct laser scribing of silicone rubber as a novel method for making conductive patterns on soft silicone substrates. The LSSR process was developed as part of our effort to design a simple, low-cost 3D printing platform for soft functional structures and actuators. We believe that its great simplicity makes this process uniquely suited for integration with 3D printing. The direct laser scribing of printed materials to produce a secondary material with different properties is an intriguing new concept that allows multi-material parts to be printed without the added complexity of multi-material deposition. The combination of laser scribing with the 3D printing in a single integrated process is described in Chapter 5.

We have established that LSSR has a complex material structure, which we propose consists of SiC, SiOC, and graphitic carbon, with a porous surface layer of silica. The

composition and material properties greatly depend on several process parameter. The main parameters used to control the process are scan speed v and laser power, represented as the duty cycle D of the PWM-modulated laser signal. Both indirectly control the temperature and heating rate experienced by the laser-scribed material which ultimately determine the result.

LSSR films range in thickness between 41 µm and 103 µm. The thickness variation, which is of great importance for applications as high-voltage electrodes in DEAs, could not be determined with certainty due to limitations in the measuring process (see Section 4.6.3) but was narrowed down to a range between 5 µm and 20 µm. Both the overall thickness and thickness variation are quite large for application as DEA electrodes. Future work should focus on reducing these in order to produce more effective actuators. Nevertheless, when used in conjunction with a DIW-based 3D printing process, where typical layer thickness is between 200 and 300 µm, the thickness of LSSR layers may be sufficiently small to produce working DEA devices (for practical results, see Chapter 5, Section 5.4.3.7).

Sheet resistance of LSSR is typically of the order of 1 to 10 kΩ/sq, but values as low as 401 Ω/sq have been measured, translating to a bulk conductivity of 40 S/m for these samples. This is much higher than CG and other common DEA electrode materials (see Section 2.3.3). Despite its brittle nature, LSSR enclosed in silicone rubber was found to remain measurably conductive ($R \leq 50$ MΩ) up to uniaxial strains around 20 % (see Section 4.6.5, Figure 74A). Although resistance increased by two or three orders of magnitude at these strains, the material remains sufficiently conductive for application as DEA electrodes. The great increase in resistance under strain may also be useful for sensor applications.

Two other interesting properties of LSSR have also been documented:

1) Its wettability, which changes from superhydrophilic right after laser scribing to superhydrophobic after several days' storage at ambient conditions. The former is potentially useful to temporarily increase wettability of silicone rubber for subsequent processing (as has been done in the past[239–241]). The latter has been used to produce switchable wettability surfaces[242] and may be useful for fluidics applications.

2) Its ability to form layer separations between silicone layers. This property can be very useful when integrated into a 3D printing process to separate parts from support material or create internal cavities for fluidic devices. This application is explored in Chapter 5, Section 5.4.3.8.

LSSR made from UV Electro 225-1 with tartrazine filler (2 wt.%) at $v = 150$, $D = 10$ % stands out in several characteristics. It has a mid-range thickness of 62 µm but has the lowest observed sheet resistance of 401 Ω/sq and was the most hydrophobic of all tested samples. However, the entire parameter space for the LSSR process has not been exhaustively explored and further optimisation is expected. It should also be noted that not all the same sets of parameters were tested on both tartrazine and graphite materials. Therefore, it cannot be concluded that tartrazine is inherently superior, even though our best results have mostly been obtained with tartrazine. Furthermore, different applications may require a different set of specific properties. More research into the properties of LSSR and their dependencies on different process parameters is certainly needed to be able to effectively produce LSSR for specific applications. In addition, several improvements can be made to the laser scribing process to further improve the desired properties of the resulting materials. These are discussed in the following section.

4.8. Outlook

LSSR is a new, exciting type of laser-scribed materials, similar to LSGO and LIG, but with its own unique properties. Further work is still required to fully characterise this material and optimise the laser scribing process.

4.8.1. Characterisation

First of all, a more thorough chemical and structural analysis of LSSR needs to be carried out to better understand the chemical composition and formation process. Such analysis is difficult since LSSR is a highly inhomogeneous material consisting of multiple phases of varying composition, forming very complex structures. In addition, the great disparity in stiffness between LSSR and the silicone rubber substrate makes it very difficult to prepare samples for analysis that preserve the structure of the material. Attempts to cut cross-sections of LSSR in order to measure layer thickness under the microscope were abandoned because it was found that the preparation

process altered the samples to such a degree that they could no longer be assumed to be representative of the original LSSR film. Perhaps cooling of the sample below the glass transition temperature of the silicone rubber will make the mechanical properties of the two adjacent materials sufficiently similar to allow cutting of clean cross-sections. These could then be analysed using electron microscopy and spatially resolved analysis techniques such as Raman spectroscopy, energy-dispersive X-ray spectroscopy, or X-ray photoelectron spectroscopy. Better knowledge of the composition of LSSR could lead to a better understanding of its formation and a more informed optimisation of the laser scribing process.

Furthermore, the electrical and mechanical properties of LSSR need to be characterised more thoroughly to determine the suitability of this material for applications in electronic devices. We have so far only described the mechanical properties of LSSR in empirical, qualitative terms. Measurements of elastic modulus and tensile strength, for example, could help build models of LSSR and composite structures of silicone rubber with embedded LSSR to predict their mechanical behaviour. Characterisation of the electrical properties of LSSR can also be expanded. Resistivity under strain has only been measured in uniaxial strain tests. It has been proposed that these are not generally representative of applications in dielectric elastomers, which are typically subject to biaxial strain.[72] Biaxial strain tests should therefore be carried out to understand the behaviour of this material in the intended application. Finally, the semiconducting properties of LSSR could be explored, which may perhaps open entirely new applications and also help to explain the curious non-linear I-V characteristic encountered during sheet resistance measurements using the four-point probe (Section 4.6.4.2).

4.8.2. Laser scribing process

So far, only a small section of the available parameter space for the laser scribing method has been explored. Only a few combinations of parameters have been tested and of those, not all have been thoroughly analysed using all the available methods. Further exploring this space may yield LSSR with improved properties in several aspects such as electrical conductivity, layer thickness and uniformity. Furthermore, the parameter space can be expanded by several additional parameters. Laser focus

has so far not been considered in the context of LSSR. Chyan et al.[237] have found that a defocussed laser worked better at producing LIG from organic substrates and also produced thinner layers of LIG. Similarly, our work on LSGO has shown that a defocussed laser can achieve better reduction of GO without damaging the substrate underneath (see Chapter 3, Section 3.2.2.3). Perhaps the same will be true for LSSR and thinner layers or otherwise improved properties can be achieved by altering the laser focus.

Line spacing is another parameter that can be easily adjusted and may have profound effects on the resulting LSSR but has not been fully investigated. We have determined that the true line width is often much wider than the set line spacing (see Section 4.6.3). Adjusting spacing in accordance with the actual line width might produce very different results. Laser wavelength, type (pulsed or continuous wave), and pulse frequency are yet more parameters that have not been explored systematically. Previous reports of LSSR in the literature show that LSSR produced by different lasers can have vastly different properties.[238–245,247]

Another factor limiting the accessible parameter space is process reliability. It was often found that certain combinations of parameters would only generate LSSR intermittently (see example in Figure 55A, Section 4.6.1) if power was set too low or speed was set too high. This makes these parameter combinations impractical, which is unfortunate because some of the best results were achieved with combinations of relatively high speeds and very low laser power (e.g., $v = 150$ mm/min, $D = 10$ %). If reliability can be improved, the accessible parameter space will be expanded, and more favourable parameter combinations may be found. The crucial factor for reliability of the laser scribing process is the initiation of LSSR conversion. Once initiated, the conversion is fairly self-sustaining.

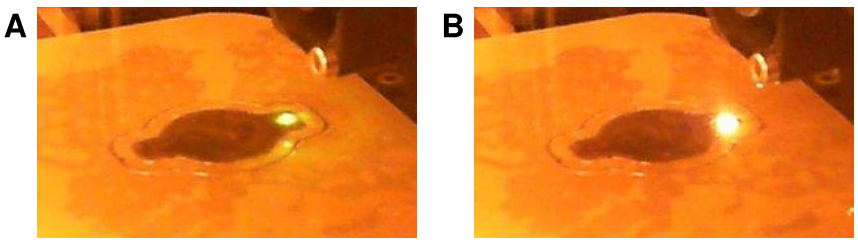

Figure 76. Incandescence of the LSSR conversion reaction. A) Printed sample of UV Electro 225-1 with graphite filler that is being laser scribed. The laser was just switched on and LSSR conversion has not yet initiated. A bright spot from the scattered laser beam is visible at the surface of the silicone. B) The same sample half a second later. LSSR conversion has initiated and a very bright spot is visible at the surface of the silicone rubber due to incandescence produced by the conversion reaction. This incandescence is easily distinguishable from the scattered laser beam visible in (A) and could be utilised for closed loop control of the laser scribing process. The images are taken through a high-pass filter with a cut-off wavelength around 550 nm which blocks most of the light from the laser.

One possible mechanism to ensure reliable initiation would be to start laser scribing each line with high laser intensity and then immediately reduce intensity once initiation has occurred. There is a visible difference between laser scribing with and without LSSR conversion due to the incandescence resulting from the conversion reaction (compare images in Figures 76A and B). The difference in brightness and spectrum could easily be detected using a low-cost camera and basic image processing. Such data could serve as feedback for closed-loop control of laser power to ensure reliability of the process. This would allow laser scribing at overall lower laser power than is possible with the current feed-forward control.

4.8.3. Materials

4.8.3.1. Selectively absorbent fillers

Another way to improve LSSR properties and reliability of the process is to modify the material formulation to achieve better absorption of the laser. Since our goal is to incorporate the LSSR method into a 3D printing process, the material must also be UV-curable (see Chapter 5, Section 5.3.1). That means that it must be absorbent at the wavelength of the laser, but at the same time translucent at the wavelength used for curing. Currently, we use particulate fillers to achieve this (see Section 4.5.2). The disadvantage of this approach is that LSSR conversion will only initiate when a particle near the surface is hit by the laser, making the initiation probabilistic. If instead of absorbent particles, a selectively absorbent pigment could be used that makes the

silicone material fully opaque at the laser wavelength, reliable initiation could be guaranteed. With the current materials, absorbance of the laser increases during laser scribing because the product (LSSR) is more absorbent than the starting material. This makes control of process conditions like the actual surface temperature during laser scribing more difficult. If the starting material was highly absorbent to begin with, laser scribing would be more consistent. This might even eliminate the need for feedback control to ensure reliable initiation of LSSR conversion, as proposed in Section 4.8.2.

A suitable pigment or dye will need to be highly absorbent at 450 nm and mostly transparent at 365 nm. Tartrazine was used as a pigment in silicone rubber for much of our work, however, despite its orange colour, it does not show the desired selective absorbance. Absorbance spectra for tartrazine dissolved in water and dispersed in UV Electro 225-1 silicone are shown in Figure 77A. It can be seen that the peaks and valleys in the absorbance spectrum of dissolved tartrazine do not line up well with the laser and UV curing wavelengths. More importantly, when tartrazine is dispersed in UV Electro, its absorbance is constant over the relevant range of wavelengths. Tartrazine was found to work well in our lasers scribing and 3D printing processes as a non-conductive alternative to graphite (see Section 5.4.3.5) but it cannot be considered a selective pigment for our purposes.

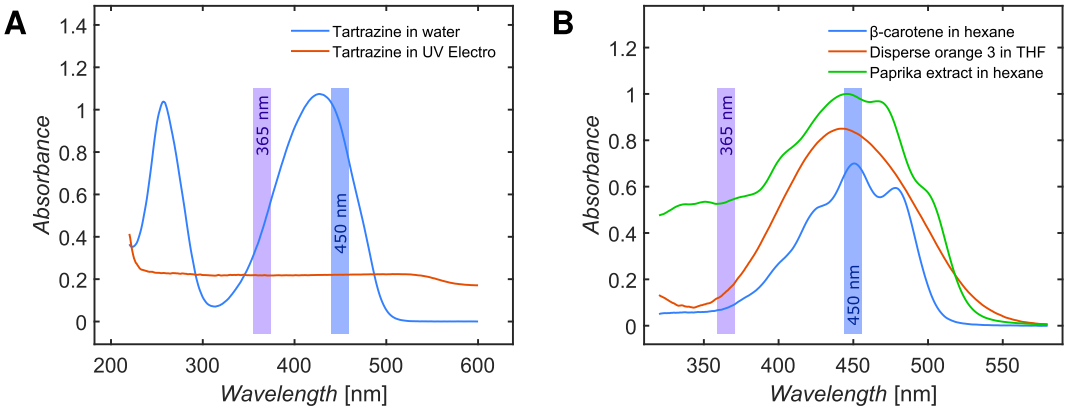

Figure 77. Absorbance spectra of various orange dyes. A) UV-vis absorbance spectra of β-carotene, disperse orange 3, and paprika extract in organic solvents. B) UV-vis absorbance spectra of tartrazine dissolved in water and dispersed in UV Electro silicone. The UV curing and laser wavelengths (365 nm and 450 nm, respectively) are indicated by the vertical bars.

Several organic dyes were briefly investigated for selective absorption. Figure 77B shows absorbance spectra of disperse orange 3 (4-(4-Nitrophenylazo)aniline), β-carotene, and paprika extract (which gains its colour from various carotenoids[276]) in organic solvents. All three show an absorbance peak near 450 nm with up to 10 times higher absorbance than at 365 nm. This fits our requirements for selective absorption very well. However, several additional factors need to be considered when formulating composite materials with such dyes. Firstly, as seen in tartrazine (Figure 77A), absorbance of such dyes changes when they are dispersed in silicone rubber instead of a suitable solvent. All dyes that were tested showed lower selectivity in silicone than in the respective solvents. Secondly, the dyes can interfere with the UV curing mechanism of the silicone rubber. For example, β-carotene was found to completely inhibit UV curing of UV Electro 225-1, even at a mass fraction of less than 0.1 wt%. Lastly, UV stability of the dyes needs to be considered. UV stability β-carotene is very poor, and it was found to lose all visible colour after several minutes of UV exposure. So not only does β-carotene inhibit curing, it also loses its selective absorbance after UV exposure, making it completely unsuitable as a selective dye. This shows that chemical compatibility and UV stability are important requirements for such a dye.

Covalent functionalisation of polysiloxanes with azo dyes could be a potential route to selectively absorbent silicone rubber. For example, functionalisation of silicones with Disperse Red 1 (N-Ethyl-N-(2-hydroxyethyl)-4-(4-nitrophenylazo)aniline) has been demonstrated.[277] Disperse red 1 has good UV stability.[278] In addition, the functionalised silicone has increased dielectric permittivity,[277] which could be highly beneficial for DEA applications. If a similar material could be formulated with the desired absorption profile, it could increase the reliability of the LSSR process and greatly improve the performance of devices made using the LAMDA 3D printing process described in Chapter 5.

4.8.3.2. Silicone-free materials

A suitable dye may improve the reliability of the laser scribing process, but there is a more fundamental problem with LSSR as a material. Although it provides an interesting, novel approach to fabricating conductive films on rubber substrates, it does not have very favourable properties for soft devices. Most importantly, LSSR

itself is not inherently elastic and breaks even under very small strain, thereby reducing its electrical conductivity (see Section 4.6.5). Although we expect to improve the properties of LSSR by optimising the process parameters, laser scribing of silicone rubber will inevitably produce silicon compounds such as silica or silicon carbide which are extremely brittle materials. In order to avoid this, silicon-free starting materials could be used. It has been shown that laser-induced graphene (see Section 2.6.2) can be generated on a variety of organic materials, including some soft materials like cotton fabric and white bread.[237] Perhaps a silicon-free elastomer can be found that, when laser scribed, generates a conductive material that is less brittle than LSSR. Unfortunately, preliminary experiments with TangoPlus-FLX930 (Stratasys, Ltd., USA) and HydroMed™ D3 polyurethane (AdvanSource Biomaterials Corp., USA) yielded no favourable results. Laser scribing of both materials led to clean ablation without any visible residue. Interestingly, when fumed silica was added to TangoPlus-FLX930, laser scribing did produce a black residue, which also showed electrical conductivity. Although the addition of silica might, again, cause the resulting material to become brittle, the observation that a filler material can trigger the formation of a conductive residue indicates that it may be possible to formulate a soft, 3D-printable, and silicon-free material that can be laser scribed to generate electrically conductive films which are less brittle than LSSR.

Although improvements to the LSSR process and materials will be necessary to enable the fabrication of truly soft devices, the fundamental concept of using laser scribing to produce conductive materials from elastic substrates offers a great range of interesting opportunities. The simplicity of the process makes the LSSR method uniquely suitable for integration with a 3D printing process to produce conductive patterns in-situ during printing. This idea, its potential uses, and challenges are explored in Chapter 5.

Chapter 5

3D printing soft devices: the LAMDA process

Some of the work presented in this chapter was presented at the SPIE Electroactive Polymers and Devices (EAPAD) conference in March 2018 and is published in the conference proceedings.[246]

5.1. Introduction

As the field of soft robotics is growing (see Section 2.1), there is an increasing need for new materials and processing techniques to manufacture soft, functional structures. In particular, the fabrication of artificial muscles to power soft robots remains challenging (Section 2.2). Traditionally, soft parts are mostly being manufactured by casting or moulding processes which greatly limit the possible complexity of the parts, as discussed in Section 2.4. In contrast, novel fabrication techniques like 3D printing can offer almost limitless design flexibility. Our goal is to develop a 3D printing process capable of fabricating soft, functional multi-material structures with complex geometry in a fully automated fashion. Such a process could greatly accelerate innovation in soft robotics and related fields.

Various 3D printing techniques have already been used to fabricate soft, functional structures but all of these techniques suffer from certain limitations (see Section 2.4). Existing 3D printing platforms that are capable of printing soft, functional, multi-material structures are also highly expensive (see examples in Section 2.4) which greatly limits their accessibility. The development of FDM-type 3D printers over the last decade has shown the impact that such manufacturing technology can have once it becomes affordable enough to be adopted in great numbers by research laboratories,

small companies and even private individuals. If a similarly accessible platform can be developed that is capable of 3D printing functional, soft, electroactive structures, this will greatly boost research and development in soft robotics and other soft devices.

Our research is therefore focused on developing a 3D printing platform for soft, functional structures that is affordable and built from low-cost, easily accessible hardware. In this chapter we present a novel 3D printing process that combines direct-write 3D printing of soft materials with the LSSR process escribed in Chapter 4. The combined process has been named Laser-Assisted, Multi-material Direct-write Assembly (LAMDA). The LAMDA printer is a self-contained desktop-size unit that is built entirely from low-cost, readily available components. We demonstrate the fabrication of soft capacitors and simple pneumatic actuators. We also show a first demonstration of a LAMDA-printed object with complex 3D geometry and embedded pneumatic structures. The LAMDA process is simple, safe and environmentally friendly as it uses no organic solvents and operates at room temperature. Some practical challenges still need to be overcome to print fully functional devices such as DEAs, but the LAMDA printer shows great potential as an accessible prototyping platform for soft devices that can enable new advances in soft robotics and artificial muscle technology.

5.2. The LAMDA process: combining laser scribing and 3D printing

3D printing with soft materials, including high-performance rubbers such as silicones, has been demonstrated many times before, even on printers based on low-cost, open-source designs (see Section 2.5.2). However, printing with multiple soft materials, particularly with a combination of insulating and conductive materials, remains a challenge. For low-cost DIW printers, multi-material extrusion adds a great amount of complexity since it is prone to suffer from seemingly small technical difficulties such as oozing and cross-contamination between the different extruders which can be difficult to resolve in practise (see Sections 5.3.3.2 and 5.3.3.3).

To overcome this challenge, we introduce the use of laser scribing as a method to convert the first, soft material into a second, conductive material, as has been

demonstrated in the LSSR process in Chapter 5. Based on this idea, we developed the new process of Laser-Assisted, Multi-material Direct-write Assembly (LAMDA). LAMDA uses direct-write 3D printing of silicone rubber in combination with laser scribing to produce complex, multi-material structures. The novelty of this process lies in the fact that, rather than depositing multiple materials with different properties, only a single material is deposited. Laser irradiation is then used to induce a chemical change in the deposited material to alter its physical properties. That way, multi-material structures can be produced without the need for deposition of multiple materials. To the best of our knowledge, such a process has not been demonstrated before.

The great advantage of laser scribing is that it is very easily integrated into the 3D printing process without greatly increasing the complexity of the required hardware. These days, small, low-cost laser engravers are available that use compact, self-contained laser diode modules. Such a module can easily be added to a 3D printer. In fact, several commercial 3D printers offer the capability to exchange the extruder for a laser module to allow both 3D printing and laser engraving/cutting on the same machine.[279,280] However, none of these printers make use of both processes in conjunction.

The LAMDA process makes use of the fact that laser scribing capability can easily be added to a 3D printer while avoiding many of the problems encountered in multi-material deposition. It is therefore uniquely suited to enabling printing of functional, multi-material soft structures while keeping the cost and complexity of the printer hardware as low as possible.

5.3. 3D printer development

Development of the LAMDA platform took place in several stages. The overall goal was to build a 3D printer capable of fabricating soft structures of layered conductive and non-conductive material to produce dielectric elastomer actuators and other soft electroactive devices. In each development stage, different mechanisms for material deposition and curing and other accessories were explored and evaluated in order to

determine their suitability. The process and hardware were upgraded iteratively in this way until an effective configuration had been found.

5.3.1. Requirements

Actuators like DEAs or other functional structures will typically consist of at least two different materials with different properties that can interact to produce a meaningful function. For DEs, alternating layers of electrically conductive and non-conductive layers are required. Even in a simple fluidic actuator that consists of only a single material, actuation arises from interaction with another material, the fluid. That means, that the original structure must contain the fluid or another material that can be replaced by the fluid after manufacturing. Specifically, in the case of a 3D printed fluidic actuator, deposition of a support or filler material is necessary to create hollow or inflatable structures. In any case, the basic requirements for a 3D printing process for functional structures is to produce structures of at least two different materials. For the specific case of DEs, those must be two elastic materials of which one is electrically conductive, and one is insulating.

Since the goal is to produce soft structures, the 3D printer must be capable of depositing soft materials. These materials must be deposited with high precision to be able to make useful functional structures. For DEs, layer thickness and uniformity are very important factors. To match the quality of commercial silicone films made for DEA applications, the thickness of 3D printed layers should be 200 µm or lower with a tolerance of ±5 %.[105] Lateral feature size is less critical but should be below 1 mm to allow for intricate electrode geometries such as interdigitated electrodes for electroadhesion (like the ones shown in Figure 50, Section 3.4).

For a 3D printing process, it is also important that the deposited materials can be cured or hardened quickly and selectively. This is crucial to ensure that deposited layers maintain their shape as subsequent layers are deposited on top. At the same time, undeposited materials must remain processable for the duration of the print, which can be up to several hours or even days for large, complex models.

Lastly, accessibility and affordability of the printing platform is an important factor with regard to the impact this technology can have. In order to provide a useful tool

for researchers and enthusiasts to accelerate development in soft actuator technology, the printing platform should be easily accessible. For accessibility of a technology, cost is generally the most important factor. The 3D printing revolution has shown the impact that a technology like FFF printing can have once its price drops and it becomes accessible to researchers, small businesses, and consumers. Therefore, in order to amplify potential impact, the 3D printer should preferably be built from low-cost and easily accessible hardware. In addition, development of the 3D printer was constrained by the project budget, which allocated roughly £3,500 for materials and consumables. Assuming that several hardware iterations would be necessary to develop a working printer, we aimed to limit the total hardware cost for one unit to around £1000 (€1130, $1270).

To ensure accessibility, the process should also be safe to use without professional training. That means it should not use any hazardous substances like organic solvents. It also should not rely on external facilities such as an extraction or air purifying system. Such a reliance would limit accessibility, especially for private individuals who do not have such facilities available and would have to purchase them along with the printer. This would greatly increase the overall cost of the system.

To summarise, the 3D printing platform for soft, active structures envisioned here must fulfil at least the following requirements. Essential properties are the minimum capabilities necessary for 3D printing functional devices. Desirable properties are non-essential to the basic function of the printer but will help to ensure accessibility and improve the potential impact of this technology.

Essential properties:

- Fabrication of structures of at least two different materials
- Deposition of soft materials
- Fast, selective curing/drying/hardening of deposited materials
- Layer thickness of 200 µm or lower and ±10 µm tolerance
- Lateral feature size below 1 mm
- Good repeatability (less than 10 % chance of print failure or a printed device being faulty, printed devices should have consistent properties)

Desirable properties:

- Low-cost (~£1000) and easily accessible hardware
- Safe to use without special training (safety mechanisms, no harmful substances)
- No reliance on external facilities (e.g., air purifier or extraction system)
- Environmentally friendly (low energy consumption, no harmful substances)

Although the idea of reconfigurable materials was considered from the beginning, the above requirements were set before the LAMDA process was conceived. They were therefore formulated in such a way that they make minimal assumptions about the specific nature of the printing process to be used. This avoided restricting the design process and allowed novel, creative solutions like the LAMDA process to emerge.

5.3.2. Design considerations

5.3.2.1. 3D printer type

The constrained budget of £1000 limits the choice of 3D printer to base our platform on. Currently, only FFF- and DLP-type printers are commercially available for under £1000. DLP printers are generally not capable of fabricating multi-material structures. That leaves FFF printers as the only option that offers multi-material deposition at an acceptable price. The design of our printer is therefore based on the Prusa i3 model. The Prusa i3 is of the latest generation of open-source FFF printers. It has found widespread adoption in the hobby and consumer market, as well as research environments. The platform combines low cost and easy assembly with good print quality. It is also easily reconfigurable to specific applications. Prusa i3 kits are available from various manufacturers in the price range from £300 to £3000 depending on features and quality of the parts. The Prusa i3 is intended to use one or more thermoplastic extruders but can be easily reconfigured to use paste extruders instead, which are capable of depositing arbitrary, paste-like materials. This gives great flexibility in the choice of materials. Several paste extruders are available for use with the Prusa i3 or similar printers, both open-source and commercial.

FFF printers generally have relatively low resolution compared to other 3D printers (SLA, inkjet, powder), but a typical Prusa i3 supports printing at 100 µm layer

thickness or lower, with 50 µm lateral positioning resolution and 0.5 mm lateral feature size. This is sufficient to meet our requirements.

5.3.2.2. Soft materials for 3D printing

Most commonly, 3D printers today use either thermoplastics (FFF) or liquid polymer resins (SLA/DLP, inkjet, DIW). Thermoplastics are supplied in solid form, as a filament or powder, and are melted for processing. Polymer resins are supplied in liquid form and selectively cured in situ after deposition. In both of those categories, some elastic materials are available.

Filaments made from TPU are the most common elastic material for FFF printing. Unfortunately, their high modulus and low elongation make them unsuitable for DE applications (see Section 2.3.2.4).

Resins of acrylate- or urethane-based monomers and oligomers are available that form soft, elastic materials after polymerisation and crosslinking. A photopolymerisable formulation of three different acrylic oligomer resins has been used with great effect in dielectric elastomer actuators.[76] This proves their feasibility for DE applications. The liquid precursors are easily deposited using a paste extruder. Photopolymerisation offers a fast, selective curing mechanism. The combination of these properties makes photopolymerisable acrylate rubber a promising candidate for 3D printing soft devices.

Some of the most versatile elastic materials available today are silicone rubbers. They are widely used in the fabrication of DEs and other soft actuators due to their superior mechanical properties (see Section 2.3.2.1). Silicone rubbers are usually supplied as one- or two-component liquid precursors with varying viscosity. In this state, they can easily be deposited using a paste extruder. They can use different curing mechanisms such as UV light, moisture, heat or the addition of a catalyst.

Both silicone and acrylate rubbers are generally suitable for 3D printing and have been used successfully to fabricate DEAs and soft actuators. Thermoplastic rubbers, although easily 3D-printable, are deemed unsuitable for DEA fabrication due to their mechanical properties.

5.3.2.3. Deposition mechanism

Since thermoplastic elastomers have been ruled out, either acrylate- or silicone-based rubbers will be used. Both of these come as liquids or pastes of varying viscosity in their uncured form. The specific rheological properties of the material determine the types of extruders that can be used. There are two common types of deposition systems for liquids and pastes: inkjet and DIW. Both of these are presented in Section 2.4.

DIW systems extrude a continuous bead of material. There are various types of DIW extruders that differ in the mechanism used to exert pressure on the fluid to force it through the nozzle. The range of processable materials depends on the specific mechanism but DIW can generally work over a very large range of material viscosities, from watery liquids (~1 mPa · s) to clay (~100,000 Pa · s).[182,184,281] Resolution, layer thickness and minimum size of printed features for a paste extruder is mainly dependent on the nozzle that is being used. A common nozzle size is 400 µm. This allows layer thickness between 100 µm and 300 µm and lateral feature sizes down to 500 µm. This size of nozzle offers a good trade-off between resolution and print speed. For finer detail, smaller nozzles can be used.

Inkjet systems deposit material as individual droplets (DoD) or a stream of droplets dispersed in a gas (aerosol jet). An aerosol jet system has been successfully used to print silicone rubber, but the required hardware is very expensive.[204] Low-cost, open-hardware DoD systems are available.[191] Modified office printers, which are cheaply available, have also been used to print a range of liquids and gels.[195,196] The downside of choosing a DoD deposition system is that this puts an upper limit on material viscosity at 25-40 mPa · s.[192,196] The resolution of a DoD system is typically somewhat higher than that of a direct-write extruder. Layer thickness of 2 µm has been achieved, with a lateral feature size around 350 µm.[192]

Liquid silicone rubber typically has viscosities between 3 Pa · s and 100 Pa · s. Even the lowest-viscosity silicone rubber is therefore not suitable for inkjet printing. It is possible to reduce the viscosity of silicones by dilution with organic solvents,[192] but the use of solvents should be avoided if alternative solutions are available. Acrylate rubber resins generally have low viscosity and can be used in either inkjet or DIW systems.

Overall, a paste extruder offers greater versatility and will be able to dispense most silicone rubbers without modification. Although inkjet printing offers lower layer thickness than DIW, both systems fulfil the requirements on layer thickness and feature size defined in Section 5.3.1. Since the printing platform developed here is experimental in nature and aimed at researchers to explore new methods and materials for fabrication of soft devices, it is desirable that the extrusion mechanism can handle a wide range of materials. With this in mind, DIW was determined as the preferred choice of deposition system.

DIW can use various types of extrusion mechanism. For industrial dispensing applications, pneumatic extruders are often used where pressurised air pushes the fluid through the nozzle. Pneumatic systems are very versatile and can, in principle, process any type of paste or liquid. Pressure can be applied and released almost instantaneously. This allows material flow to be started and stopped very quickly. However, precise pressure control is required to achieve specific flow rates as the pressure must be carefully calibrated to the viscosity of the material. Negative pressure might be necessary to prevent oozing, especially for low-viscosity materials. Unfortunately, digital pneumatic controllers with these capabilities are too expensive to be considered for this project.

The most common type of DIW extruder uses a syringe pump design where a motor is used to push the piston of a syringe and exert pressure on the fluid inside. Since it is driven by a motor, it can easily replace the filament extruder in a standard FFF printer, with no other hardware or software modifications required. Several open-hardware and commercial syringe pump extruders are available to retrofit FFF printers.[281,282] We initially chose this approach for our printer due to its great simplicity and low cost. It was found, however, that a syringe pump extruder does not allow sufficiently precise control of material flow rates, particularly for high-viscosity silicone rubber. This is due to a large delay between flow rate and motor turn rate, as shown in Section 5.3.3.1.

An auger extruder provides a possible alternative to the syringe pump design. Here, a feed screw (auger) that sits in the material path is used to exert shear force on the

fluid. The flow rate can be controlled by the turn rate of the feed screw. Because the feed screw sits in the material path right above the nozzle, flow rate responds very fast to changes in turn rate, allowing for precise control. This type of extruder can also be driven by a stepper motor, so integration with the 3D printer hardware is simple. The downside of an auger extruder is that the extrusion mechanism is in direct contact with the material which can be difficult to clean and may cause contamination when switching materials. Disposable auger extruders solve this problem (see Section 5.3.3.2). They are commercially available at an affordable price around £20 per piece. Auger extruders do not work very well with low-viscosity liquids. These can flow around the feed screw and out the nozzle even when the screw is not turning. Our experience has shown that a material needs to have a viscosity of at least 50 Pa · s for the auger extruder to work reliably.

A progressive cavity pump (PCP) would offer even better control over material flow rate. This type of pump consists of a rotor and a stator, similar to an auger pump, but the two parts form discrete cavities that travel along the rotation axis as the pump rotates.[283] A PCP expels a constant volume of liquid per rotation regardless of viscosity so it does not require calibration. It also produces a constant flow, unlike other pumps such as peristaltic pumps where flow is intermittent. Commercial PCP dispensing solutions exist,[284] but prices start around £3,000. Unfortunately, no low-cost PCPs comparable to the disposable auger extruders are available. Attempts to fabricate a small Moineau pump using 3D printing also failed because the 3D printed parts do not have sufficient precision to create a good seal between the rotor and the stator, leading to leakage and inconsistent flow rates. The Moineau pump is also mechanically more complex than an auger pump because it does not have a static rotation axis.

Since PCPs are not compatible with our budget constraints, disposable auger extruders were used in our printer from generation 2 (see Section 5.3.3.2). They were found to work well in the viscosity range of liquid silicone rubber. However, to achieve good control over material extrusion rates and meet the precision requirements, the auger extruders required additional pressurisation. The final extrusion system is therefore a hybrid pneumatic auger extruder.

5.3.2.4. Curing mechanism

Polymerisation or curing of elastomer precursors often requires mixing of two or more compounds. This is difficult during the printing process. Mixing nozzles can be used but these are problematic when material flow is discontinuous since the material can cure inside the nozzle. It is more desirable to use pre-mixed compounds where polymerisation or crosslinking can be triggered by a physical stimulus. Most commonly, UV light or heat are used as the stimulus to induce curing/polymerisation. Moisture cure is another mechanism that is commonly used in silicone sealants.

Moisture cure is slow because it relies on the diffusion of water vapour through the polymer. Exposure to moisture is also difficult to control locally and over time. It is therefore not a suitable mechanism for selective curing in a 3D printing process.

Heat-induced curing is a feasible mechanism. Non-contact heating with a heat lamp has been used to cure thin layers of silicone rubber for DEA fabrication.[77] By heating the deposited material to 100 °C or higher, curing is accelerated drastically such that deposited material is cured within a few minutes while undeposited material (shielded from high temperatures) can remain processable for hours. The disadvantage of using heat is that it requires many printer components like the print bed and other parts in the vicinity of the heat source to be heat resistant or shielded. This adds cost and complexity. Heating also consumes a lot of energy, making the process less energy efficient and possibly requiring an additional or larger power supply, again increasing cost. A powerful heating unit also poses a significant fire risk and can cause injuries. Additionally, heat treatment can have an influence on the material properties of the cured rubber and heating must be precisely controlled to avoid degrading the material by exposure to excessive heat.

UV light is arguably the most practical curing mechanism for a 3D printing process. Light is easy to apply selectively and keep away from undeposited material. Other printer components do not get exposed to high temperatures. That way, cheap plastic materials and 3D-printed parts can be used, reducing the overall cost of the printer. Relatively cheap, high-power UV LEDs are available, providing a convenient, efficient source of UV light. UV curing can also be very fast, taking only seconds to cure a thin

layer of material. Many commercial printing systems like Stratasys' Objet and most SLA/DLP printers use photocuring for this reason. UV light is typically used rather than visible light so that the material can be handled under ambient light without curing. Materials that cure in visible light would have to be shielded at all times, making material preparation more complicated.

The downside of using UV light is that it can be harmful to human skin and eyes. A UV-blocking safety enclosure is therefore necessary to protect the user from harmful radiation. UV light was chosen nonetheless because it is fast and easy to use, and a UV-blocking enclosure is neither difficult nor expensive to make. If a laser is used as part of the printing process (see Section 5.2), a safety enclosure is indispensable anyway, regardless of the curing mechanism. Compared to heat curing, a UV curing process also poses a much lower risk of fire or injury through burns. Overall, UV curing was selected as the most suitable curing mechanism for the 3D printing process.

5.3.2.5. Material selection

Given the choice of a direct-write paste extruder and UV light for curing, suitable materials can be selected. The materials must be UV curable and have relatively high viscosity of 50 Pa · s or higher.

A UV-curable silicone rubber, UV Electro 225-1, was kindly supplied free of charge by the manufacturer, Momentive Performance Materials, Inc. (USA). This material is specifically formulated for high-voltage applications. It has already been used in inkjet printing of dielectric elastomer membranes[192] and was found to be highly suited for printing thanks to the fast UV curing mechanism. Only a few other manufacturers currently offer UV-curable silicone rubbers. Wacker Chemie AG (Germany) and Shin-Etsu Chemical Co., Ltd (Japan) both offer products in this category. However, because UV Electro was procured easily and found to be very well suited for 3D printing, no other UV-curable silicone rubbers were tested.

The photopolymerisable acrylic oligomer resins used by Duduta et al.[285] appear to be suitable for 3D printing and have been proven to be adequate for DE applications. They might be an interesting alternative to UV-curable silicone rubber. Unfortunately, it was not possible to procure these materials as the manufacturer (Arkema, France)

only supplies these specific materials for the US market. The suitability of these materials for 3D printing could therefore not be tested at this point.

Despite ruling out moisture cure silicone in the previous section, silicone sealant was used in our early 3D printing tests. It was used for testing because of its very low cost (less than £10/kg) and great accessibility. Because silicone sealant is a high-viscosity paste when uncured, printed layers hold their shape against gravity and few-layer parts can be printed without the need for selective curing.

In addition to the primary elastomer material, a secondary conductive material is also required that can serve as electrodes in printed soft devices. Before the discovery of LSSR, attempts were made to use composites of UV-curable silicone with conductive fillers like CB or graphite (see Section 5.3.3.2 and 5.3.3.3). Unfortunately, the addition of such fillers above the percolation threshold impedes UV curing, so the materials were no longer suitable for printing.

Once the LAMDA process was invented, the material requirements changed slightly. Now, a single material was required that is UV-curable and can be laser scribed. For this purpose, composites of UV Electro 225-1 with 2 wt% of an absorbent filler, either graphite or tartrazine, were formulated, as described in Chapter 4, Section 4.5.2.

5.3.3. Printer hardware

Designing and building the printer was an iterative process. It can generally be divided into four generations between which important changes to the hardware were made.

5.3.3.1. First generation

A Prusa i3 kit (single sheet frame design) was purchased for £350 from Semi-Utilitronic Industries (UK). The kit included a RAMPS 1.4 controller board which supports two extruders. The printer was first built in its original configuration with a single thermoplastic extruder to test components and get familiar with the hardware, software and electronics.

A simple syringe pump extruder was built based on an open-source model. The design was modified to reduce the footprint of the extruder. This allowed two extruders to be mounted side by side on the print head for multi-material printing. A 10-mL disposable

syringe holding the material can snap into a bracket at the front of the extruder. A stepper motor is used to turn a lead screw which drives the carriage that attaches to the syringe plunger. A locking mechanism was introduced that allows decoupling of the carriage from the lead screw. This is useful when inserting a syringe, so the carriage can be moved to the desired location by hand and then locked in place by engaging the lead screw. This is much quicker than moving the carriage using the motor. The 3D printer with two syringe pump extruders can be seen in Figures 78A and B.

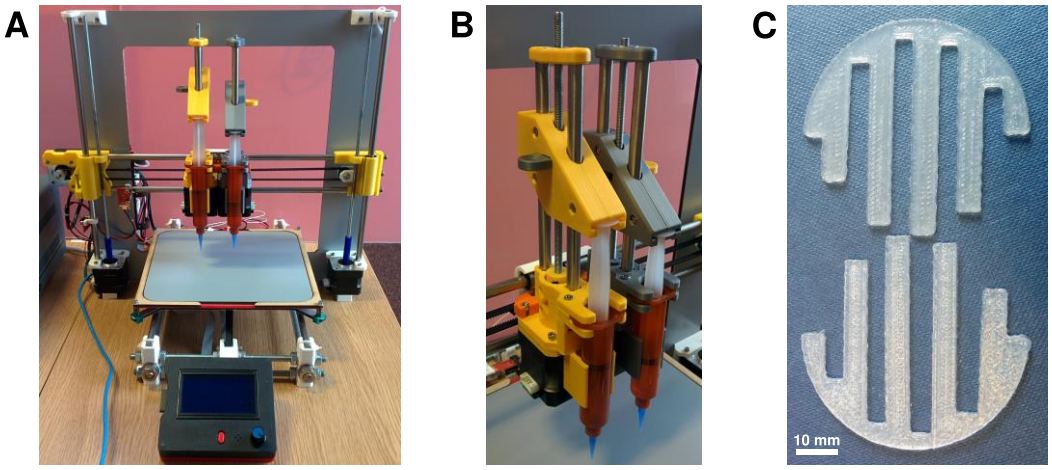

Figure 78. First-generation 3D printer with two syringe pump extruders. A) The 3D printer based on a Prusa i3 kit with modified print head. B) Close-up view of the print head with two syringe pump extruders. C) Single-material test pieces printed with silicone sealant. The geometry was designed to test specific feature sizes and does not serve any practical function.

Print tests using silicone sealant, which has a very high viscosity, immediately highlighted a significant shortcoming of the extruders. Because there is some elasticity in the mechanism and the pressure required to extrude the viscous sealant is relatively high, the flow rate response to input from the motor was greatly delayed. As the motor starts to drive the syringe plunger, pressure builds up slowly. A constant flow rate is not reached until several seconds after the motor started turning. When the motor stops, the syringe is still under pressure and material keeps flowing until all the pressure is released. Priming and retraction, i.e. turning the motor faster initially to quickly build up the desired pressure and turning backwards to release pressure quickly, can help reduce the delay in the response but they are not sufficient to eliminate the problem.

Simple single-material test prints actually showed fair results despite the poor flow rate control. Two test pieces printed with silicone sealant are shown in Figure 78C. However, this could only be achieved by printing continuously with very short travel moves between extrusions so that flow rate was kept almost constant throughout the entire print. This method is clearly not suitable for multi-material printing where material flow is highly intermittent as the printer alternates between the two extruders. The use of syringe pump extruders was therefore abandoned.

5.3.3.2. Second generation

In the second-generation printer, which is shown in Figure 80, the print head was upgraded to use disposable auger extruders instead of the syringe pumps. These allowed much more direct control over material flow rate with very little delay. The auger valves were purchased from Adhesive Dispensing Ltd. (UK). They consist of a small feed screw inside the material path just above the nozzle. Material from a syringe barrel is fed in from the side. Rotation of the screw pushes material out through the nozzle. The nozzle and syringe barrel are attached via standard Luer lock fittings. Figure 79A shows an exploded view of the auger extruder assembly. The valves are meant to be disposable, but they can also be cleaned and reused. They are sold as packs of 10 for around £200 per pack. The valve assembly does not include the syringe barrel and nozzle. These were purchased separately from the same supplier. UV-blocking syringe barrels were chosen to prevent curing inside the barrel.

Each extruder consists of an auger valve, a syringe barrel, a nozzle, a stepper motor, a small adapter to couple the motor shaft with the feed screw, and a 3D-printed mounting bracket that attaches the valve, motor, and barrel to the print head. Figure 79B shows the fully assembled print head with two auger extruders.

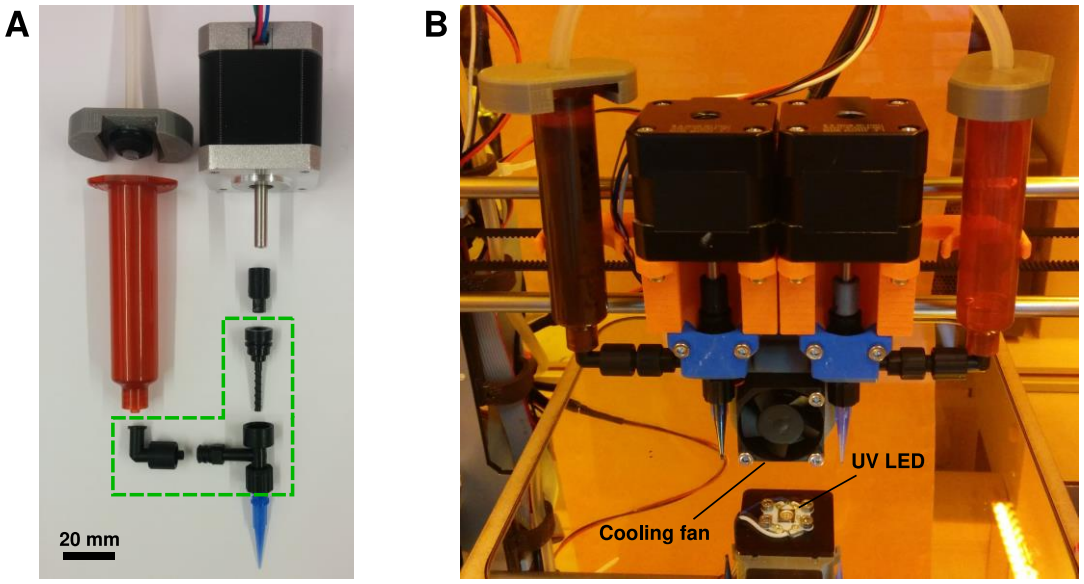

Figure 79. Auger extruder print head. A) Exploded view of the auger extruder. The parts of the disposable auger valve are highlighted by the green frame. B) Print head with dual auger extruders and a UV LED for curing. The LED can be seen in the reflection on the mirror surface of the print bed.

The print head was also equipped with a UV light to allow the use of UV-curable silicone rubber (UV Electro 225-1). A 3.8-W UV LED with a peak wavelength of 365 nm was mounted underneath the extruders, 2 mm above the tips of the extruder nozzles so as not to obstruct material deposition. The LED is actively cooled using a heat sink and a fan to avoid overheating during continuous operation. A 3023 BuckPuck constant-current LED driver (LEDdynamics, Inc., USA) is used to power the LED. Because the LED requires more than 12 V (which is the supply voltage for the 3D printer), a step-up converter (generic, purchased on eBay) is used to generate a 24 V supply for the LED driver. Power to the LED is controlled through one of the heater ports on the RAMPS 1.4 controller board. In Figure 79B and Figure 80, the cooling fan for the UV LED can be seen between the two nozzles. The LED itself is visible in Figure 79B through its reflection in the mirror surface of the print bed below.

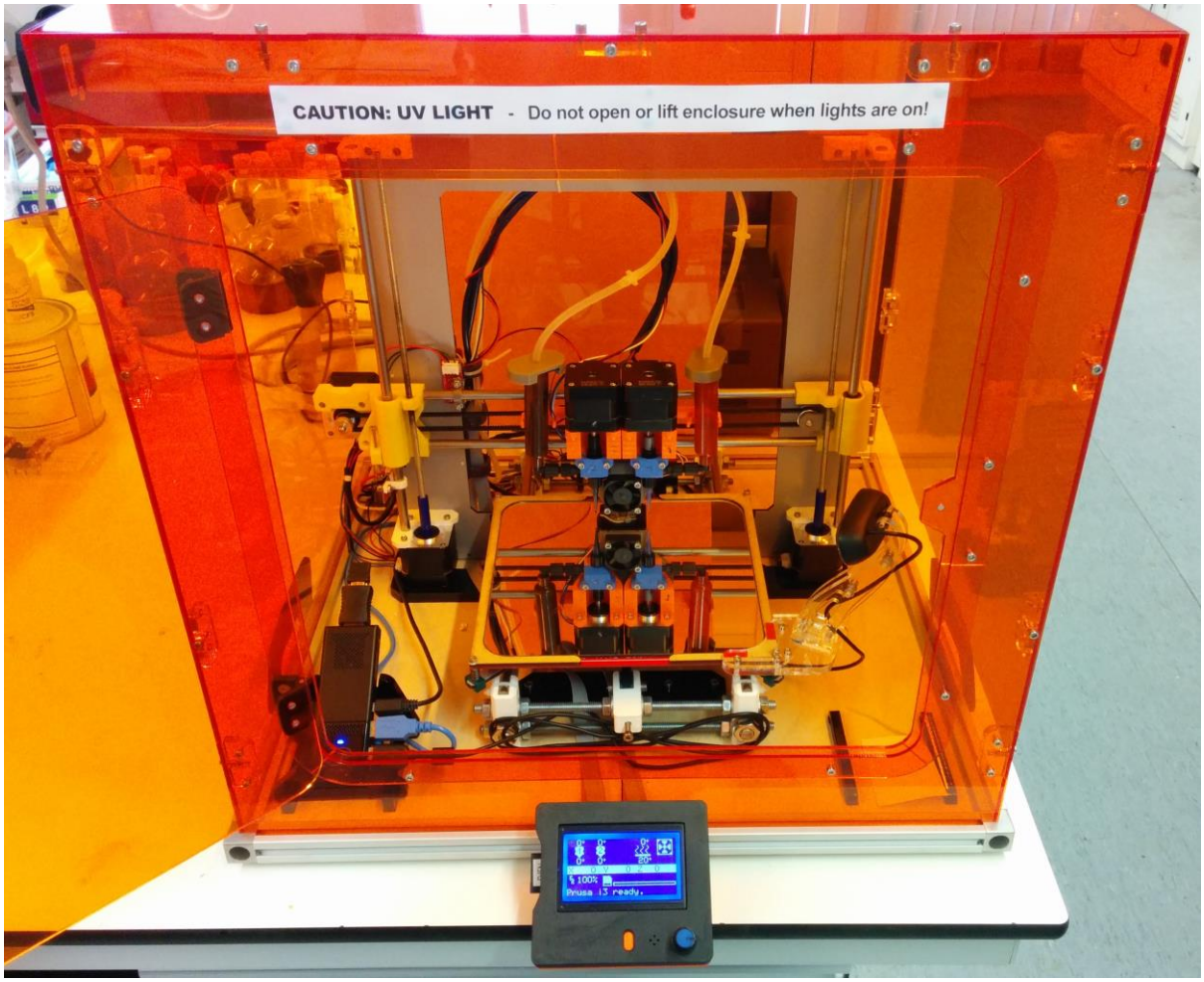

Figure 80. The second-generation 3D printer inside its safety enclosure made of UV-blocking acrylic glass.

The addition of a UV light made it necessary to build a UV-blocking safety enclosure. This was constructed from 3-mm-thick orange-tint acrylic glass. The safety enclosure with the printer inside is shown in Figure 80. A technical drawing of the enclosure can be found in Appendix Section A3.2. The acrylic glass used is not certified to be UV-safe. To ensure safety, the material was tested using UV-vis spectroscopy and found to have under 0.5 % transmittance at wavelengths between 220 nm and 500 nm, as shown in Figure 81. That is sufficiently low transmittance over a wide range around 365 nm that no harmful amount of UV radiation from the LED will be able to leave the enclosure.

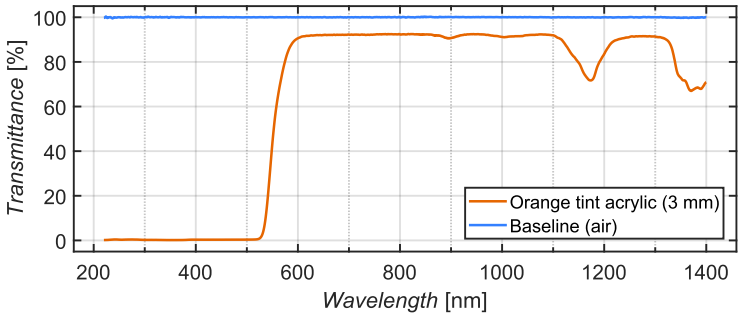

Figure 81. UV-vis-IR transmittance spectrum of orange-tint acrylic glass, which was used to construct the safety enclosure for the 3D printer. Transmittance is less than 0.5 % between 220 nm and 500 nm

Although the auger extruders use feed screws, they also require the material cartridge to be pressurised for effective extrusion, depending on the viscosity. The feed screw can only exert a limited amount of shear force on the fluid. This is not always enough to draw the desired amount of material out of the syringe, through the feed path, and out through the nozzle. The pressure should be adjusted to just below the point where the material starts flowing on its own around the static feed screw. Then, even a small amount of shear from the screw will cause material to flow. This makes the extruder more responsive and allows overall higher flow rates. To pressurise the material, a 3D-printed cap is fitted to the syringe barrel that seals it and connects to a pressurised gas supply. The nitrogen gas line available in the lab where the printer is located is used for this purpose. To adjust the pressure, a Shako URPL4-02 manual pressure regulator valve (SHAKO Co., Ltd., Taiwan) is used. This type of valve can produce regulated output pressures between 10 kPa and 400 kPa with a sensitivity and repeatability of ±0.5 %. The advantage of using the auger extruder with a pressurised syringe compared to a purely pneumatic system is that the material flow is not directly controlled by the pressure and therefore the pneumatic pressure can be constant. No expensive digitally controlled pressure regulator is necessary. The manual regulator was purchased for £75. The nitrogen gas line was used as pressurised gas supply for convenience, even though it violates the requirement to not be reliant on external facilities. However, since the required pressure is static, a variety of different sources could be used instead, such as a small, low-cost CO_2 canister for use in bike pumps. For materials with lower viscosity, pre-pressure would not be required.

Test prints were performed with both UV Electro 225-1 and silicone sealant. Both materials work well after suitable values for pressure and extruder turn rate were found for each material. UV curing of UV Electro is performed by scanning across the surface of the deposited layer with the UV LED at full intensity held 5 mm above the surface. For a 200 µm layer, curing takes roughly 5 s/cm^2, resulting in cure times of under one minute per layer for small models.

Figure 82. Surface quality of printed layers. A) Test piece printed with silicone sealant. B) The same piece printed with UV Electro. Because of UV Electro's ability to flow and settle, the surface quality is much better than in (A), but the edges are less precise. C) The same part printed with UV Electro and separately cured perimeters. The outline of the model is sharper than in (B).

There is a visible difference in the surface quality between models printed with UV Electro and models printed with silicone sealant (see Figure 82). Because silicone sealant is very viscous, it retains any surface irregularities introduced during deposition. Since the material is deposited in parallel adjacent lines, the surface shows a distinct line pattern similar to FFF-printed parts (Figure 82A). UV Electro has lower viscosity, which allows small surface irregularities to even out if the material is given a few seconds to settle before UV curing. The result is a very smooth surface as can be seen in Figures 82B and C. This is a highly useful property since uniform layers are very important for DEA fabrication. The downside is that the outlines are less well defined since the material forming the perimeter of the model can also flow out of shape. To avoid this, the UV curing routine was changed so that perimeters are cured separately. First, each perimeter is printed and cured as quickly as possible by retracing it with the UV LED. Then the infill is printed and given a few seconds time to settle before curing the entire layer. This gives the material of the perimeters less time to flow and increases dimensional accuracy. The result can be seen in Figure 82C.

Two-material test prints were also performed. Unfortunately, the results were poor. A composite made of UV Electro and CB, intended to serve as electrode material, was found to be too opaque to be UV-curable. Printing with this material was attempted nevertheless, in the hopes that uncurable electrode layers could be encapsulated in cured silicone rubber. Unfortunately, the electrode material mixed with the clear UV Electro and smeared across the entire surface during printing of the next layer. The results are shown in Figure 83. It is evident that printing on top of an uncured layer is not feasible and that carbon composites with UV Electro are not viable if they can't be made UV-curable.

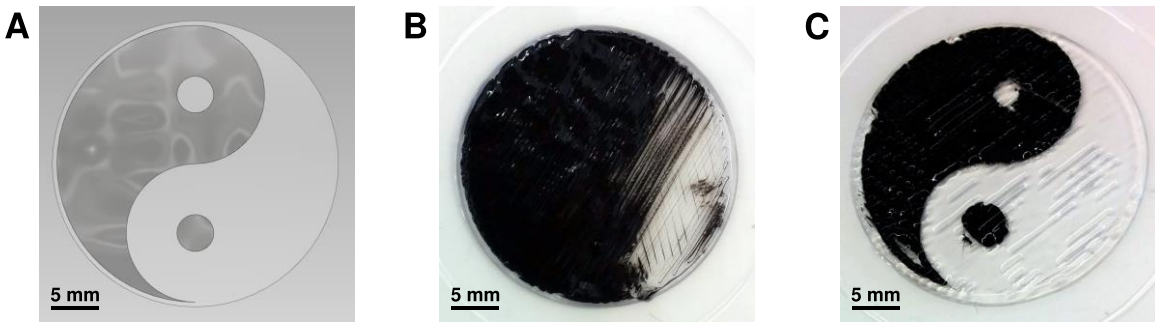

Figure 83. Results of two-material printing test. Silicone with carbon black filler is used as secondary material. A) CAD model of the two-material part. A single layer of black silicone is embedded between layers of clear silicone. The part was designed to have a recognisable shape with varying levels of detail. B) Result of the first test print. Smearing and cross-contamination between layers makes the printed shape unrecognisable. C) Result of the second test print with reduced extrusion rate. The printed shape is recognisable but cross-contamination is still evident and electrode layers are not fully encapsulated.

Another problem with multi-material extrusion also became apparent. Since both nozzles are at the same height, the inactive nozzle can come into contact with the freshly printed layer and contaminate it. This is especially problematic if insulating layers get contaminated with conductive material as this can cause short circuits between electrode layers, rendering the printed device unusable.

5.3.3.3. Third generation

In this iteration, the basic functionality of the printer was not changed but several technical improvements were implemented with the aim to improve overall print quality. The frame of the printer was upgraded from the original DIBOND® frame (a laminate material made of two thin aluminium sheets with a polyethylene core) to a P3Steel frame (purchased from Orballo Printing, Spain). This frame is made entirely

of sheet metal with no printed parts. It is easier to assemble and offers much higher rigidity. This reduces vibrations and generally improves print quality as the precision of print head moves is increased. The 3D printer with upgraded frame is shown in Figure 84. A drawing of the frame can be seen in Appendix Section A3.1. The enclosure was not altered.

The controller board was upgraded to a DuetWiFi with a Duex5 expansion board (Think3DPrint3D Ltd., UK). The DuetWiFi board is an advanced controller board for 3D printers and CNC machines. It uses a 32-bit processor (opposed to the 8-bit Arduino Mega on the RAMPS 1.4 board used previously) and improved stepper motor drivers. This allows quieter operation and more precise positioning of the print head. With the Duex5 expansion board, the DuetWiFi supports up to 7 extruders. More importantly, the board has various high-power and low-power PWM outputs for extra periphery such as LEDs, servos and lasers. The DuetWiFi, as the name suggests, also offers wireless connectivity via Wi-Fi and can be accessed through a web interface hosted on the printer itself. This helps to reduce wiring and can also be useful for remote access to the printer.

In addition to the frame and electronics upgrade, the print head was redesigned to feature two lifting nozzles to eliminate layer contamination from the inactive nozzle. In this design, each extruder is mounted on a slider and can be lifted or lowered using a miniature servo motor. This allows lifting of the inactive nozzle during printing to prevent contamination. This version of the print head is also built entirely of laser-cut acrylic glass sheets, rather than 3D printed parts, in order to accelerate the prototyping process. The new print head design is shown in Figure 85A.

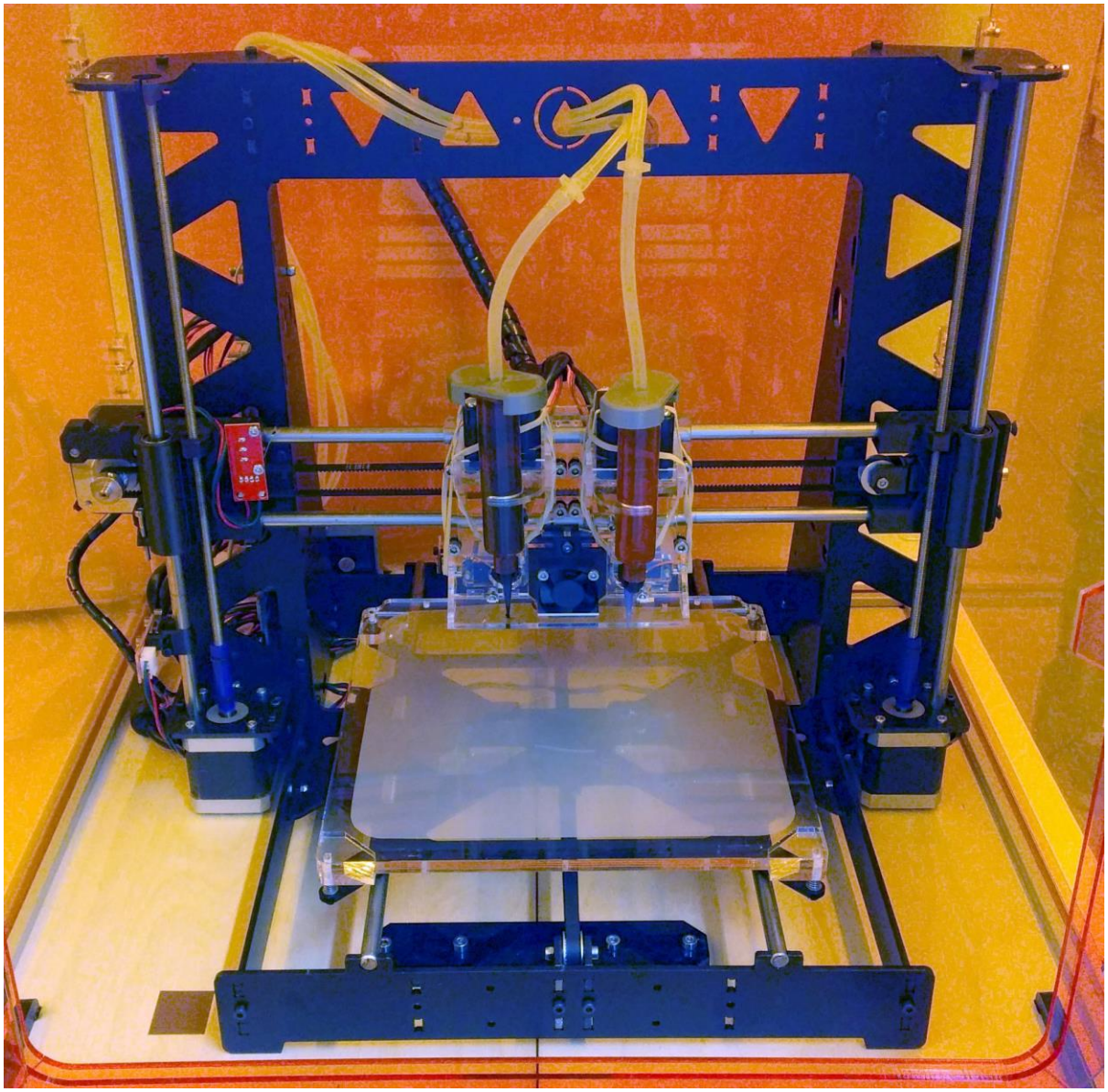

Figure 84. Third-generation 3D printer with new frame and print head. The frame is entirely made of steel sheets and the print head features two lifting nozzles and a UV LED.

With the upgraded printer, very successful single-material prints were made using clear UV Electro silicone. To test and showcase the capability of precise 3D printing with elastic materials, a model of an octopus[286] was printed. The printed octopus was 60 mm in diameter and 16 mm tall. It was printed at 200 µm layer thickness with a print speed of 25 mm/s. Total print time was 80 min, which equates to an average of 1 min/layer, including curing. It must be noted that print time for the bottom layers of the model was much longer than average, because they include more detail and cover a much larger area. The top layers, which form the head of the octopus, took far less than 1 min/layer. The octopus print is the first demonstration of a truly 3-

dimensional object printed out of silicone on this 3D printing platform. The printed octopus is shown in Figures 85B and C.

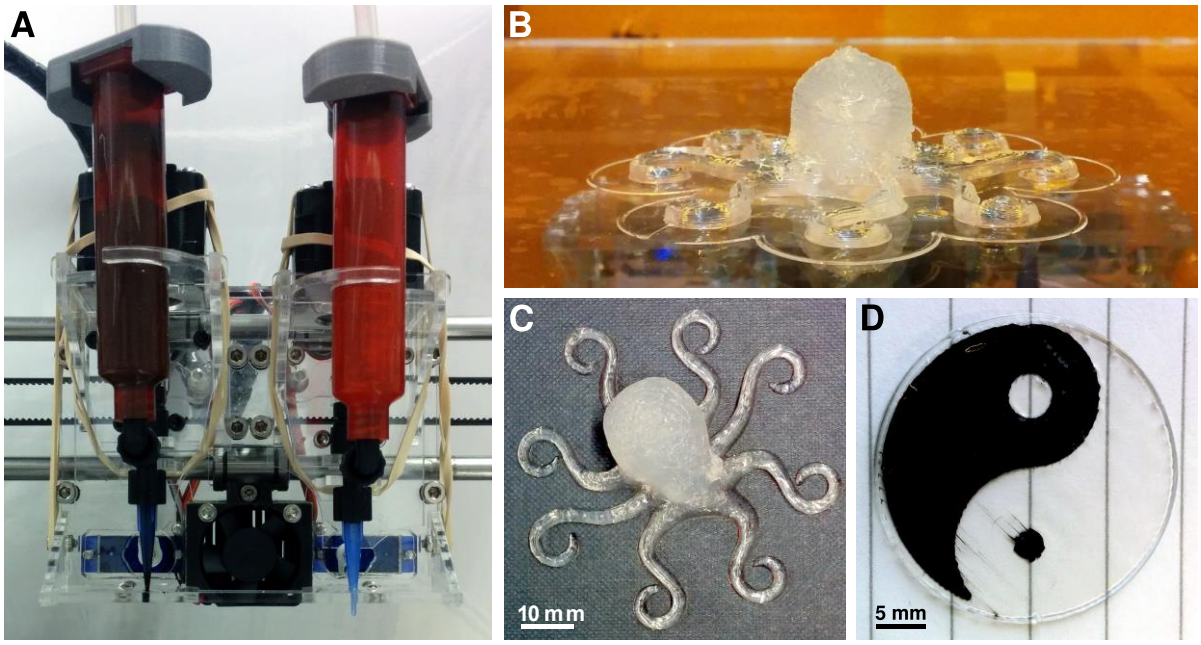

Figure 85. Print head and printed parts from the third-generation printer. A) The redesigned print head with two lifting nozzles. The UV LED, fan and heat sink are still mounted between the extruder nozzles, same as in the previous print head design. The servo motors used to lift the extruders are visible through the acrylic glass on either side of the LED fan. B) Printed octopus on the print bed. C) Top view of the octopus after removing it from the printer. D) Two-material test print with clear and black UV Electro.

Despite great success with single-material parts, multi-material prints remained unsuccessful. The lifting nozzles do eliminate contamination from the inactive extruder but that does not solve the persisting problem that conductive silicone composites with CB are not UV-curable. If layers of electrode material cannot be cured, silicone layers need to be printed on top of uncured material. Because material exits the nozzle with a certain amount of pressure, the material being deposited displaces the uncured material underneath. The electrode material then wells up between lines of printed silicone and penetrates the insulating layer. Electrode material can also get picked up by the active nozzle and get dragged along, mixing with freshly deposited materials and resulting in layer contamination. Figure 85D shows a two-material test print with clear silicone and CB composite. The quality of the printed part has improved compared to the previous test prints shown in Figure 83, but there are still visible

smears along the print lines where CB contaminates the clear layer. While this problem persists, printing of DEAs is not feasible.

The obvious way to overcome the problem of layer contamination is the use of an electrode material that is UV-curable. Ionic gels are a potential candidate for a soft, conductive, transparent material that can be made UV curable (see Section 2.3.3.5). However, after the discovery of LSSR, the search for printable electrode materials was abandoned in favour of exploring the possibility of laser scribing as a substitute for multi-material deposition.

5.3.3.4. Fourth generation

Once LSSR was discovered as a potential electrode material and a fabrication method that is easily integrated into a 3D printing process, the printer capabilities were adapted to fit the requirements of the LAMDA process. LAMDA printing uses only a single UV-curable material. Laser scribing is then used to convert this material into conductive layers. Accordingly, the LAMDA print head has only a single extruder, a UV LED for curing, and a compact diode laser module for laser scribing.

No lifting mechanism for the extruder nozzle is required because there is no second nozzle that it could interfere with. Both the laser and UV LED are non-contact tools, which means that the entire print head can be lifted while the extruder is inactive. This configuration is much simpler and cheaper than the previous design. It requires no servo motors and the only moving parts on the entire print head are two cooling fans and one extruder rotor. Figure 86 shows the final configuration of the LAMDA printer and the reconfigured print head. Figure 87A-C shows each of the three tools in operation. A technical drawing showing the arrangement of the tools and general dimensions of the print head can be found in Appendix Section A3.3.

The laser module is the same that was previously used for LSSR experiments (see Section 4.3). It houses a 450 nm, 1.6 W laser diode. The module was included in a DIY laser engraver kit that was purchased for £150. The module can also be purchased separately for around £60. Blue lasers (445-450 nm) are the most widely available and most affordable high-power (1 W or more) laser diodes currently on the market and were chosen mainly for their wide availability.

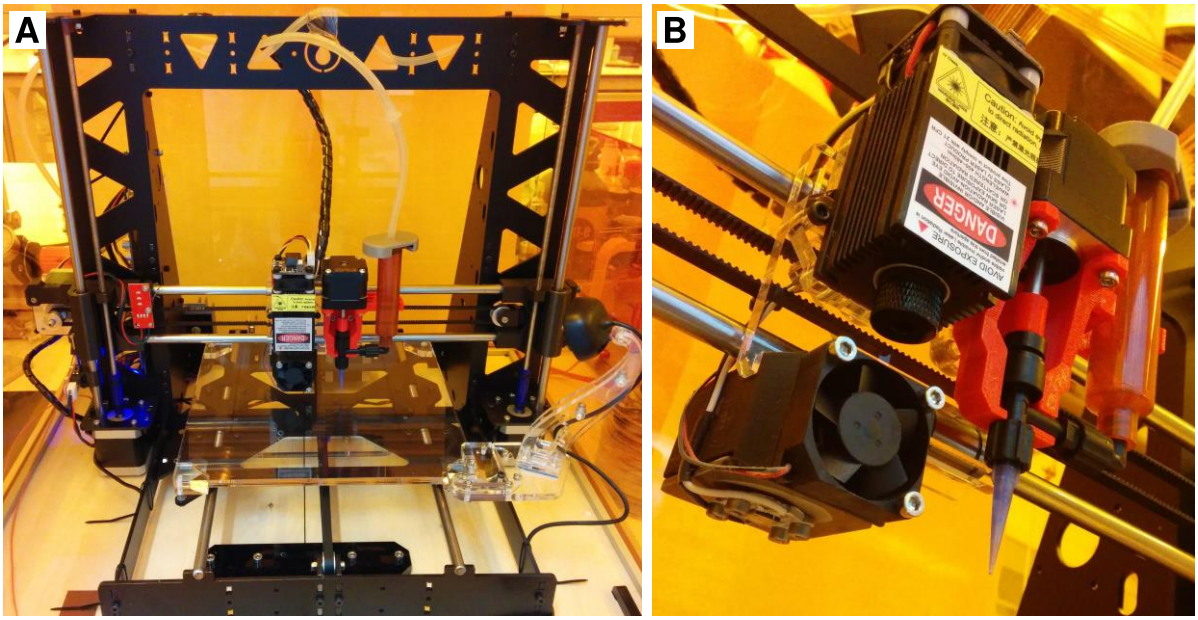

Figure 86. Final configuration of the LAMDA printer. A) LAMDA printer with revised print head design and a webcam mounted on the print bed to monitor and document the printing process. B) Close view of the print head which now incorporates a single paste extruder, a UV LED and a laser module.

The existing UV safety enclosure also blocks the laser wavelength and was found sufficient for safe operation of the laser. As an extra precaution, a microswitch was installed on the door of the enclosure that will cut power to the laser module if the door is opened during operation. This ensures that the laser cannot be accidentally switched on if the door is open or the enclosure has been lifted.

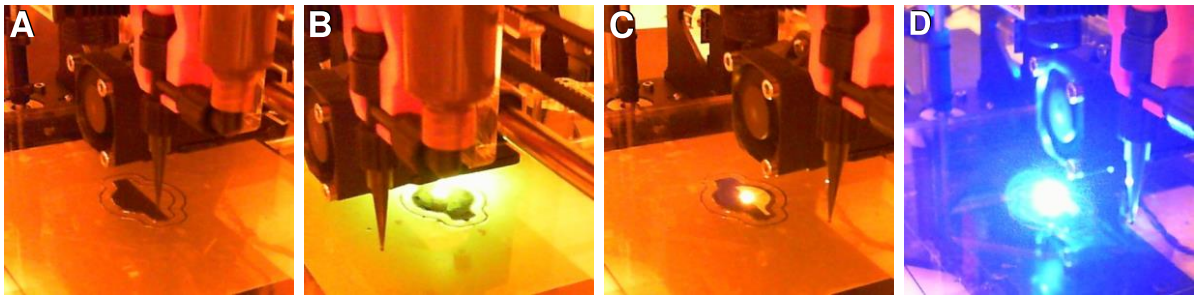

Figure 87. The LAMDA process in action. A) Deposition of siliconce composite. B) UV curing. C-D) Laser scribing. The image in (D) is taken without a colour filter. All images are taken with the webcam installed on the print bed. It can be seen that the use of a colour filter greatly improves visibility.

A webcam (LifeCam HD 3000, Microsoft, USA) was also fitted on the printer to record images and videos of the printing process. Because the print bed moves along the Y-axis during printing, the camera was mounted on the corner of the print bed. This

ensures that the camera is static with respect to the printed part during the printing process. Figure 87 shows images of the LAMDA process in action, recorded using the webcam. A small piece of orange-tint acrylic glass (the same that was used to build the safety enclosure) was attached to the webcam in front of the lens to act as a colour filter. This avoids over-exposure from the very bright light of the LED or laser, which would otherwise white out most of the part during printing, as shown in Figure 87D.

Table 4. Cost of LAMDA printer hardware. Costs are estimated and include reasonable margins for VAT and shipping. Actual cost will vary depending on the specific parts, suppliers and availability.

Part	**Approx. cost in £**
Prusa i3 kit, incl. electronics	500
UV LED, 365 nm, 3.8 W (incl. LED driver, step-up converter, heat sink, fan)	100
Laser module, 450 nm, 1.6 W	60
Printed/laser-cut parts for custom LAMDA print head	30
Safety enclosure (orange tint acrylic, aluminium profiles, plywood, etc.)	150
Pressure regulator	80
Pneumatic fittings and tubing	20
Pressurised gas source (e.g. CO_2 bike pump)	30
Webcam (optional)	30
Total:	**1000**
Consumables (can also be reused)	
Auger valve extruders (pack of 10)	250
UV-block syringe barrels (pack of 50)	20
Syringe tips (pack of 50)	20
Total:	**290**

Table 4 lists all the parts necessary to build a LAMDA printer with the same specs as the one described in this section. Estimated costs are given for each part. These are not necessarily the exact parts that were used here to build the LAMDA printer since this printer was developed iteratively through successive upgrades and modifications. For example, a Prusa i3 kit, frame upgrade and DuetWiFi electronics board would not need to be purchased separately. For around £500, a good-quality 3D printer kit can be purchased with all the necessary capabilities to be transformed into a LAMDA printer. Cost estimates include VAT and a reasonable margin for shipping costs. For

custom parts, the listed costs are material costs only. Access to prototyping tools such as a 3D printer for plastic parts and a laser cutter or CNC mill to cut acrylic glass sheets is assumed.

5.3.4. Software

5.3.4.1. Printer firmware

The DuetWiFi controller board runs the open-source RepRap Firmware. This firmware uses standard G-code for printer commands. It also supports a number of custom commands for controlling peripherals like servo motors. The firmware offers separate FFF, laser and CNC modes to operate a 3D printer, laser cutter/engraver or CNC mill. The mode can be switched during printing via a G-code command. This is useful for the LAMDA process as both 3D printing and laser scribing are used. Other 3D printer firmware like Marlin does not have these modes but can also be configured to use a laser tool.

5.3.4.2. G-code generator

A G-code generator, also called a slicer, is a piece of software that takes a 3D model, typically in STL file format, as input along with a range of print parameters and generates a G-code file that can be interpreted by the printer to carry out the print operation. Several free and commercial G-code generators are available with varying capabilities and features.

G-code is a human-readable code used to control CNC machines. It consists of lines of commands which are executed sequentially. A typical G-code command specifies target coordinates (X, Y and Z) for the next move, feed rate (movement speed) and a tool parameter such as laser power, spindle speed or amount of material to extrude. There is a range of other commands with different parameters for specific functions which vary by printer and firmware.

Generally, a G-code generator segments the 3D model into horizontal slices which represent the printed layers. Each slice is then broken down into individual linear print moves. For each print move, a G-code line is written to tell the printer how to execute the move. Additional G-code commands may be inserted to set certain print parameters.

Simplify3D (S3D) was chosen as the most suitable G-code generator software for this project because of its great flexibility and multi-material support. S3D offers a multi-material printing wizard that helps to align models and set printing parameters for multi-material prints. More importantly, multiple processes with different tools and different parameters can be defined and assigned to different parts of the model.

S3D does not inherently support UV curing or laser scribing. However, due to the great flexibility it offers in defining different process parameters for different parts of the model, laser-scribed parts can be "printed" with parameters adequate for laser scribing. This way, minimal post-processing of the G-code is required to implement laser scribing as part of the 3D printing process. S3D can also be configured to automatically execute another piece of software to post-process its G-code output. This helps to accelerate the 3D printing workflow.

S3D is commercial software. A single-user license for up to two PCs can be purchased for $150, which needs to be factored into the cost of the printer but is not prohibitively expensive.

5.3.4.3. G-code post-processing

UV curing is not supported by S3D as a standard feature. Therefore, custom software was developed to analyse the G-code produced by S3D and add the commands for a UV curing routine in the appropriate places. This software first determines the extent of each printed layer. Then it generates a raster pattern to cover the entire layer. This raster pattern is converted to G-code and inserted into the original G-code file after each layer. There is an option for curing the perimeter of each layer separately (see Section 5.3.3.2). This is done by copying the print moves used to deposit the perimeter of each layer but removing the extrusion commands, changing movement speed, and setting the UV LED as the active tool. The printer will then trace the same trajectory with the UV LED and quickly cure the deposited material. Several parameters such as speed, spacing of the raster and distance from the model can be specified by the user.

Laser scribing is also not inherently supported by S3D. G-code for laser-scribed layers can be generated with S3D by treating it like a standard 3D-printed layer. These layers

are set in S3D to be “printed” at very narrow line width (100 µm) to match the width of LSSR lines. Another piece of custom software is then used to post-process the laser G-code. This software analyses the G-code from S3D to find sections where the laser tool is active and replaces extrusion commands with laser commands. It also removes perimeters as it is not necessary to laser-scribe the perimeter of the LSSR pattern.

The effects of the post-processing can be seen in Figure 88, which shows G-code visualisations of a simple LAMDA part before and after post-processing. It can be seen that a path for the UV tool is added which covers the area of the print in a rectangular pattern. It can also be seen that the UV tool traces the printed perimeter. The perimeter of the laser-scribed area has been removed. The fact that extrusion commands have been replaced by on/off commands for the laser tool is not evident from the visualisation since the tool path remains unchanged.

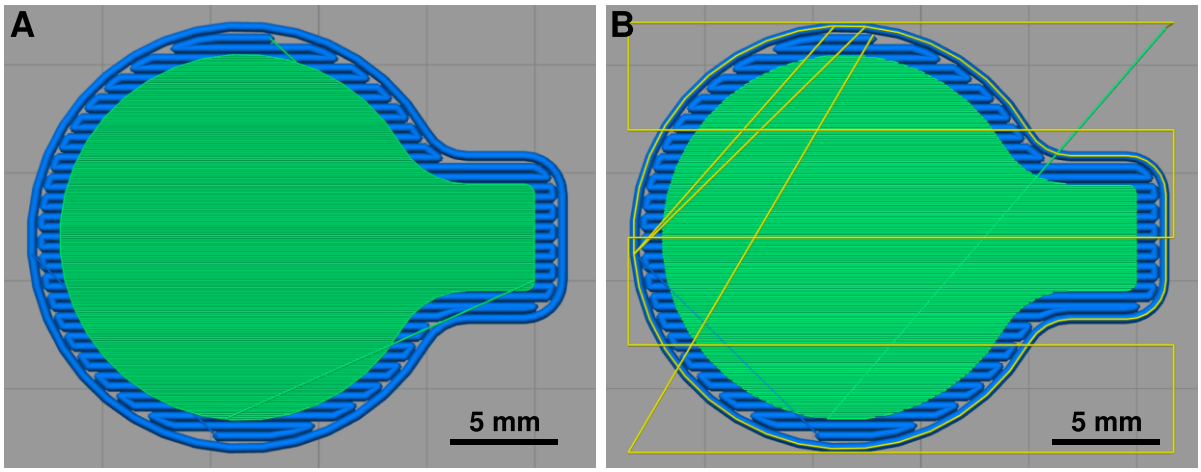

Figure 88. G-code post-processing. G-code visualisations of a simple LAMDA part are shown before (A) and after processing (B). Blue lines indicate printed features, green lines indicate laser scribing and yellow lines represent the UV curing tool.

Currently, the software does not modulate laser power with the current speed of the print head. Laser exposure will therefore be higher at the beginning and end of each line, where the print head accelerates and decelerates. This could potentially lead to non-uniform properties of LSSR throughout the layer. However, since laser scribing is generally done at very low speeds, acceleration is effectively instantaneous. No notable variation near the edges of the LSSR layers has been observed (see Section 4.6.3).

As mentioned in the previous section, UV curing and laser toolpath generation can be integrated into the S3D toolchain. When saving a G-code file, the custom software gets executed automatically to perform necessary post-processing.

5.4. 3D printing soft devices

The LAMDA printer allows alternating deposition of material, UV curing, and laser scribing. With these three tools, layered structures of silicone rubber and LSSR can be built. Several simple devices were printed to evaluate the quality and properties of LAMDA-printed parts.

5.4.1. Design

5.4.1.1. Capacitive devices

The simplest DEA consists of two electrode layers with one dielectric layer between them. The first layer of a LAMDA-printed structure must always be silicone since it forms the substrate for the first LSSR layer. The top layer should also be silicone so as not to expose the high-voltage electrode and also protect the LSSR layer from damage during handling. Thus, the simplest LAMDA DEA is a structure of three printed layers with two laser-scribed layers between them (5 layers in total). For actuation tests, circular DEAs with 20 mm diameter (16 mm electrode diameter) were designed. This design is shown in Figures 89A and B.

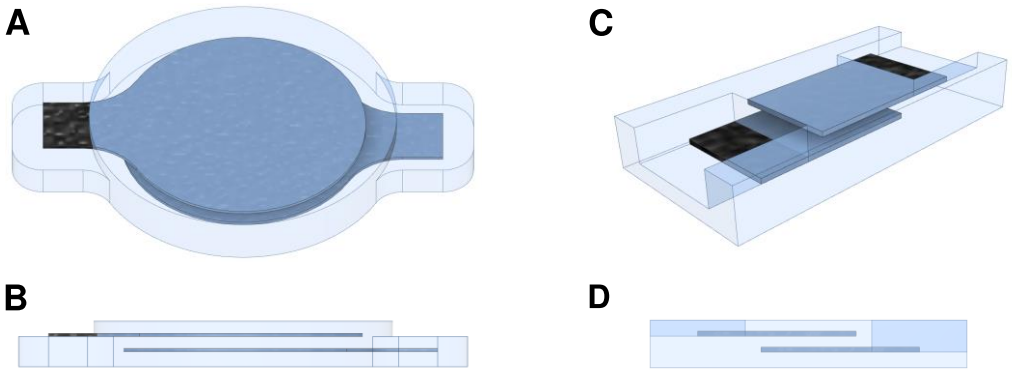

Figure 89. CAD models of simple LAMDA devices. A) Circular LAMDA DEA with three printed and two laser-scribed layers. The outer diameter is 20 mm, electrode diameter is 16 mm. B) Half-section view of the LAMDA DEA. C) Rectangular LAMDA capacitor, 10x20 mm. Active electrode area is 6x6 mm. Silicone is depicted blue translucent, electrodes are black. The models were scaled in z-direction to 1 mm layer height for improved visibility. True layer thickness is 0.3 mm. D) Half-section view of the rectangular LAMDA capacitor.

For characterisation of capacitance and breakdown voltage, rectangular capacitors of 20x10 mm with 6x6 mm active electrode area were designed. This design is not suited for actuation, but it is more compact and allows more samples to be printed at once in a single print. The rectangular capacitor design is shown in Figures 89C and D. On both models, parts of the electrode layers are exposed to allow electrical interfacing with each electrode. In the circular design, the bottom electrode layer is fully enclosed in silicone. This creates a closed cavity and allows inflation of the DEA to impart pre-strain, as explained in Section 5.4.3.7.

Each CAD model consists of two separate bodies. The first body describes the shape in which the silicone rubber is to be printed. The second body represents the LSSR layers. LSSR is placed on top of each silicone layer rather than sunken into it, as would be more realistic. This is done because the LSSR layers are treated like printed layers by the G-code generator and it must be ensured that they are "printed" after the corresponding silicone layer.

Actuation of the circular DEAs is evaluated in Section 5.4.3.7. Capacitance and dielectric breakdown of the rectangular capacitors are examined in Section 5.4.3.4 and 5.4.3.5, respectively. Capacitive deformation sensing with these devices is also explored. This is described in Section 5.4.3.6.

5.4.1.2. Pneumatic devices

As discussed in Section 4.6.7, LSSR can also be used for layer separations to create inflatable cavities for fluidic devices. To demonstrate this, two simple pneumatic actuators were fabricated. The first is a circular balloon, similar to the LAMDA DEA (Section 5.4.1.1) but with only one LSSR layer and two silicone layers to either side of it. A rendering and G-code visualisation of this model are shown in Figure 90A, C and D. The second design is a PneuNet-type bending actuator. It has a series of four discrete inflatable chambers. There are two layers of silicone below the LSSR and four layers on top. This asymmetry leads to bending motion when the actuator is inflated. Visualisations of this design are shown in Figure 90B and E-G. The behaviour and performance of both pneumatic actuators is evaluated in Section 5.4.3.8.

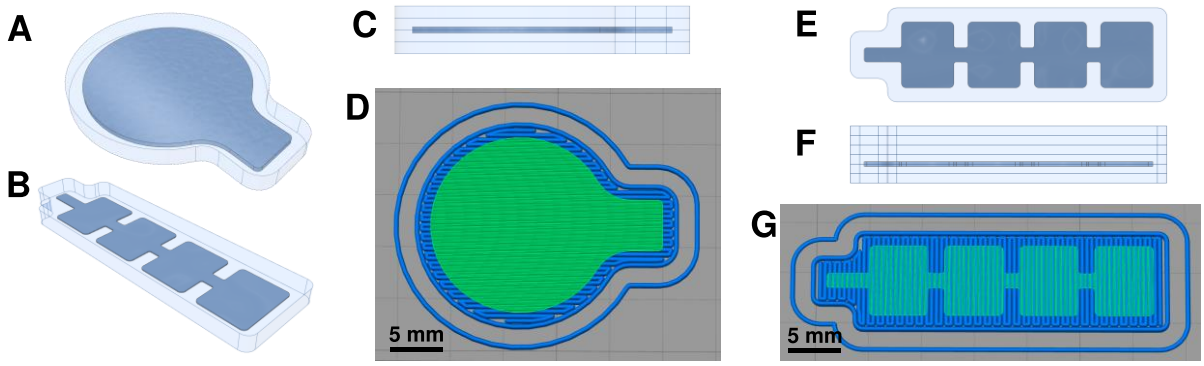

Figure 90. Pneumatic actuator designs. A) Rendering of the balloon design (20 mm diameter). B) Rendering of the PneuNet actuator design (30 x 10 mm). C) Side view of the balloon, showing four printed and one laser-scribed layer. D) G-code visualisation of the balloon, showing the second layer. E) Top view of the PneuNet design, showing the four discrete cavities. F) Side view of the PneuNet design, showing six printed and one laser-scribed layer. G) G-code visualisation of the PneuNet actuator, showing the second layer. In (D) and (G), printed layers are shown in blue, laser scribed layers are shown in green. (C) and (F) were scaled to 1 mm layer height for visibility; true layer height is 0.3 mm.

5.4.2. Fabrication process

5.4.2.1. Material preparation

The material used for LAMDA printing is a composite of UV Electro 225-1 with an absorbent filler, either graphite or tartrazine. UV Electro 225-1 is supplied as two components: a base and a catalyst. These two are to be mixed in a ratio of 100:2. The composite is usually prepared in batches based on 10 g UV Electro base since this is the capacity of the disposable syringes used as material cartridges. To 10 g UV Electro base, 0.2 g catalyst and 0.2 g absorbent filler (graphite or tartrazine, as dry powder) are added in a small glass beaker. The components are mixed by thorough stirring with a spatula for several minutes. Exposure of UV Electro to ambient light is not a concern as it requires strong UV radiation to induce curing. After stirring, the beaker is placed into a vacuum chamber for 30 min to degas the material. It is then filled into a UV-blocking syringe and centrifuged lightly at 2000 rpm for 1 min to remove air bubbles introduced while transferring the material. This light centrifugation does not lead to a visible sedimentation of the filler particles. The material is then ready for use in the LAMDA printer.

5.4.2.2. G-code preparation

In S3D, the two-part CAD model is loaded, and each part is assigned a different process which uses the appropriate tool (extruder or laser). In each process, relevant parameters such as print speed and layer height are defined. For printed layers, layer height is typically set to 0.3 mm and print speed is set to 500 mm/min. Laser speed is set to 150 mm/min. Laser power and the duration of UV curing is defined separately in the custom software used to post-process the G-code (see Section 5.3.4.3). Laser power is typically 10 % and UV curing is done at 150 mm/min and 8 mm line spacing of the scan pattern. Post processing is performed automatically when the G-code is saved to a file from within S3D.

5.4.2.3. Print setup

The syringe holding the silicone composite is loaded onto the print head and connected to the inlet of the auger extruder. The top of the syringe is sealed with the air-tight cap connected to the pressure supply. UV Electro has relatively low viscosity and only needs minimal overpressure. Typically, a pressure of 200 mbar is applied.

Different materials can be used as print substrates. Mostly, glass microscope slides (75x25x1 mm) or thin PET sheets were used. Directly printing on the acrylic glass print bed is also possible but if a substrate is used, the part can be removed from the printer along with the substrate without having to peel it off. Substrates were attached to the print bed by applying a very small amount of water to the bed, pressing the substrate onto the bed's surface and sliding it into the desired place. It is then held there by surface tension. This method was found to effectively attach the substrate for the duration of the print, although it could prove problematic for very large prints where adhesion might be lost after a few hours as the water evaporates. Once the substrate is in place, the origin of the z-axis is adjusted to coincide with the surface of the substrate.

Before starting the print, the extruder is primed by extruding some amount of material until a steady flow out of the tip of the nozzle is observed. This step is repeated even if the extruder was already primed from a previous print in order to flush the nozzle and ensure unobstructed flow. The material extruded during this step is collected on

a paper tissue and discarded. The controls for moving the printer and running the extruder are available through the web interface of the RepRap firmware.

5.4.2.4. Printing process

After preparation is complete, the G-code file is uploaded to the printer and executed by the firmware. The printing process is fully automated and, if set up correctly, does not require any intervention. The printing process can be recorded via the webcam installed on the print bed. It was typically set to record an image every three seconds. These images could later be combined into a time-lapse video of the printing process.

5.4.2.5. Post-processing

After printing is finished, the part can be removed from the print bed together with the substrate. Where possible, printed samples were measured without removing them from the substrate to avoid causing damage and altering their properties. Inflatable devices, which cannot stay attached to the substrate for testing, are peeled off carefully by hand. Copper strips are attached to the exposed areas of the LSSR layers to serve as electrical contacts. A small amount of CG is applied between the LSSR and the copper to improve the electrical contact between the materials. The copper strips are fixed in place using Sil-Poxy silicone glue (Smooth-On, USA). For inflatable devices, a short hypodermic needle is inserted into the silicone at the LSSR layer as an air inlet. A small amount of Sil-Poxy glue is applied around the needle where it enters the silicone rubber to fix it in place and ensure an air-tight seal. For the circular LAMDA DEAs, the stainless-steel needle also serves as electrical contact (see Section 5.4.3.7).

5.4.3. Evaluation

Several characteristics of LAMDA-printed devices were investigated to understand the capabilities and limitations of the process. The following sections describe both the methodology and results of the various tests that were performed.

5.4.3.1. Print quality

This section examines qualitative observations of print quality. A quantitative analysis of the accuracy of individual printed layers is presented in Sections 5.4.3.2 and 5.4.3.3.

Deposition of silicone rubber and UV curing work very well. The addition of fillers does not have a visible adverse effect on print quality. To demonstrate this, the same octopus model shown in Figure 85 was printed again using UV Electro composite with tartrazine. The result is shown in Figure 91A. All features are very well defined, including the arms which are 1.5 mm wide at the tips. Printed layers are smooth and do not show a visible line pattern. The sides of printed objects show the characteristic roughness caused by printing of discrete layers. There are no air bubbles or other visible defects in the printed silicone.

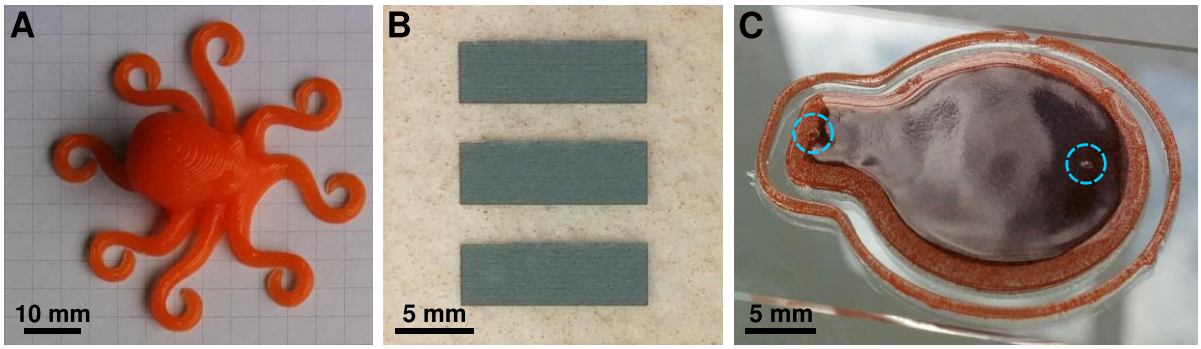

Figure 91. Quality of LAMDA-printed parts. A) Octopus printed with tartrazine composite. B) Rectangular LSSR patches on tartrazine composite. C) LAMDA-printed balloon showing bubbles in the silicone layer printed on top of LSSR (marked with blue circles).

Laser scribing works reliably if laser power is at least 10 %. LSSR conversion is highly localised and creates very sharp patterns (see Figure 91B). When printing a silicone layer on top of an LSSR layer, air bubbles sometimes appear in the silicone. This probably occurs because the porous surface of the LSSR layer contains some amount of air. If the surface is covered with silicone, this air becomes trapped and, as the silicone settles, the air is displaced and forms bubbles that rise through the silicone. The likelihood of bubbles forming greatly increases with the extent of the laser-scribed layers. Small parts like the rectangular LAMDA capacitors (see Section 5.4.1.1) are printed reliably without bubbles. Among 20 printed samples, not a single bubble was visible. However, on larger parts such as the circular DEAs or balloons, bubbles appeared frequently. Figure 91C shows an example of a LAMDA balloon with two visible bubbles in the top silicone layer. More than 50 % of the LAMDA-printed DEAs and balloons had to be discarded because they contained bubbles. The exact failure

rate cannot be determined with certainty because print parameters were adjusted in an attempt to prevent the formation of bubbles. Therefore, no more than two DEAs were ever printed using the exact same parameters. It is very important that a solution is found to reduce the occurrence of bubbles. Possible solutions are discussed in Section 5.4.3.9 and Section 5.6.2.

5.4.3.2. Layer thickness

The quality of printed silicone layers with regard to thickness and consistency was investigated by measuring surface profiles using an Alicona Infinity Focus Microscope. The method used here is the same described in Section 5.6.2 and 5.6.3 for surface analysis of LSSR samples. Because of the semi-transparent nature of the silicone composites used for LAMDA printing, the samples were covered in a thin layer of carbon black to make them opaque.

Figure 92A shows the heightmap of a printed sample made of UV Electro 225-1 with tartrazine (2 wt%). The sample consists of three layers in a step shape such that an equal area of each layer is visible. Above the heightmap, a cross-section of the sample is plotted. The three layers are clearly distinguishable by a step change in sample height. It can also be seen that the surface of each layer is relatively flat but slopes downwards near the edges. Because of this, a margin of 2 mm from the edges is excluded from the analysis of layer thickness and surface roughness.

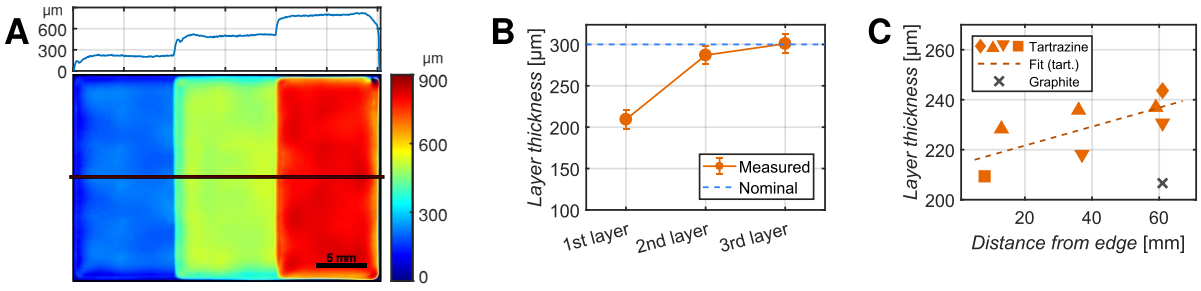

Figure 92. Thickness of printed silicone layers. A) Heightmap of a three-layer printed silicone sample. The plot at the top shows the cross-section at the position indicated by the red bar. B) Mean thickness of the three layers of the sample (n = 1) shown in (A). Error bars show standard deviation over the surface of each layer (122 mm^2, 1.22 × 10^6 data points). C) Layer thickness of the first layer of 8 printed samples, plotted over the position on the print bed at which the respective sample was printed (distance from the right edge). Samples with the same marker were printed in the same print and on the same substrate.

The mean layer thickness (height above the previous layer) of each of the layers is shown in Figure 92B. The thickness of the first layer is only 209.4 µm but thickness increases with successive layers. The third layer, at 300.9 µm, matches the nominal layer thickness of 300 µm almost perfectly. The large deviation in the first and, to a lesser extent, in the second layer is probably due to poor bed levelling. To print the correct layer thickness, the printer nozzle needs to be at the right height above the print bed. If the zero-point of the z-axis is set slightly below the level of the print bed, the height of the nozzle will be too low on the first layer. Because the extrusion is pressure-controlled (rather than flow rate- or volume-controlled), a reduction of the nozzle height above the surface leads to an increase in pressure at the tip of the nozzle, which causes a reduction in flow rate. The resulting layer is therefore thinner. This means that, on the next layer, the error in the z-position of the nozzle relative to the surface of the first layer is reduced. Thus, the initial error in z-height is corrected over several layers. We can see from the plot in Figure 92B that this happens very quickly and that the error has been fully corrected on the third layer.

Seven single-layer samples were also recorded, 6 made with tartrazine and one made with graphite. All of these samples were printed on glass slides placed on the print bed. It was established during the evaluation of LAMDA-printed capacitors (presented in Section 5.4.3.4) that glass slides placed very close to the edge of the printer's workspace will not lie perfectly flat on the bed. This causes the height of the print substrate to change with the distance from the bed's edge. This effect is explained and illustrated in more detail in Section 5.4.3.4. Observation of this phenomenon prompted an investigation into whether variations in layer thickness of the samples presented in this section might also be caused by variations in substrate height. Figure 92C shows a plot of layer thickness against the position on the print bed at which the respective sample was printed. More specifically, the distance of the sample from the right edge of the printer's workspace is specified to describe the location. There is a fairly clear overall trend of higher thickness with increasing distance from the edge among the tartrazine samples. It has to be noted that not all samples were printed on the same glass slide. After each print, the glass slide was removed with the printed samples and a new slide was placed on the print bed. Since the slides are placed manually, their

exact placement, including their height and slope, varies. Therefore, the relation between layer thickness and distance from the edge will differ slightly between prints. In Figure 92C, different prints among the tartrazine samples are indicated by different markers. Samples with the same marker were printed on the same glass slide. The linear fit that is shown indicates the general trend of all tartrazine samples together. The fit has a root mean square error (RMSE) of 8.9 µm. This includes the error introduced by the variation in positioning of the glass substrates. The true standard deviation of printed layer thickness is probably much lower than this but unfortunately the exact value cannot be determined from the available data. If we consider the RMSE of the fit as an upper bound on the standard deviation, we can state that the coefficient of variation (relative standard deviation) of layer thickness is less than 3.9 %.

The graphite sample has the overall lowest thickness (215 µm) despite being among the furthest from the edge. Since there is no reason to assume that the graphite material is affected differently from tartrazine by the substrate height, it seems likely that the low thickness is indeed caused by the material. This indicates that the graphite composite has slightly higher viscosity than the tartrazine composite. Higher viscosity causes lower extrusion rates and results in thinner printed layers. Since only a single graphite sample was recorded, no robust statistical analysis is possible and more experimental data is necessary to confirm this result.

5.4.3.3. Layer uniformity

For DEA applications, the uniformity of layers is of great importance. We therefore used the data recorded on the Alicona Infinity Focus microscope to also quantify the variation in thickness of printed silicone layers. First, to eliminate both the constant offset and any possible influence from the non-flat print substrate, a planar fit is subtracted from the surface profile. The resulting profile shows only the deviation from an ideal plane. Such a profile of a representative single-layer sample is shown in Figure 93A. The profile clearly shows two different kinds of variation. Firstly, there are several broad peaks and valleys, a few millimetres apart and 10s of micrometres tall/deep. Secondly, there is small-scale surface roughness. The latter may be cause by filler particles at the surface, but it may also be measurement noise and artefacts caused by the fact that the sample surface is not perfectly opaque. The broader peaks, on the

other hand, cannot be attributed to noise or any material property and must therefore have been caused by the printing process.

Root mean square (RMS) roughness R_q is used as a simple metric to quantify overall surface variation. It will mainly capture the broad peaks since those are more prominent. R_q of printed silicone samples (both single- and multi-layer) is shown in Figure 93B plotted against layer thickness. For the multi-layer sample, R_q of all three layers is between 10.5 µm and 11.0 µm. This shows that the roughness does not compound over multiple printed layers. Variation in R_q among the single-layer tartrazine samples is slightly larger, with values ranging from 10.6 µm to 14.0 µm. The data does not show a significant correlation between roughness and layer thickness. At 15.2 µm, the graphite sample has the highest R_q of all samples. Again, the single sample is not sufficient to prove a significant difference between graphite and tartrazine. However, the observation is consistent with the idea, established in the previous section (5.4.3.1), that the graphite composite has higher viscosity than the tartrazine composite. If the material is more viscous, it will flow more slowly and not be able to equalise as well as a less viscous material in the same amount of time.

Among the tartrazine samples, the average roughness R_q is 12.0 µm. Since R_q can be considered equivalent to the standard deviation σ, a range of $\pm 3\ \sigma$ around the mean could be expected to contain 99.7 % of all points on a printed silicone surface. Thus, for practical applications, we can consider the layer thickness to be accurate to ±36 µm. This is very large for a 300-µm-thick layer and efforts should be made to reduce this variation.

To investigate the cause of these large thickness variations, averaged cross-sections of the printed samples were analysed. By averaging the surface profile along either of the principle axes, random variations are reduced, and periodic variations along the axes are highlighted. The same method was also used in Section 4.6.3 to analyse the surface of LSSR samples. Figure 93D and E show the averaged cross-section profiles of the sample shown in Figure 93A parallel and perpendicular to the print direction. Analysis of the corresponding power spectra (shown in Figures 93F and G) confirms what is already evident from the cross-sections: there is large periodic variation along both

axes with a spatial wavelength of 5.5 mm in the parallel direction and 4 mm in the perpendicular direction. It is interesting to note that there are no visible remnants of the individual extrusion lines, which are 0.46 mm wide. This is consistent with qualitative observations of the surface of printed samples, such as the one shown in Figure 93C. The reflections on the surface in the photograph reveal both small-scale roughness and large-scale thickness variations, similar to the heightmap in Figure 93A. However, there is no evidence of the characteristic line pattern that is often seen in extrusion-printed parts. We can conclude that the practise of letting the extruded material settle for a few seconds before curing (see Section 5.3.3.2) effectively eliminates any surface patterns caused by the deposition of individual lines. However, some other phenomenon is causing local variations in thickness that are far enough apart that they do not equalise under gravity within a few seconds.

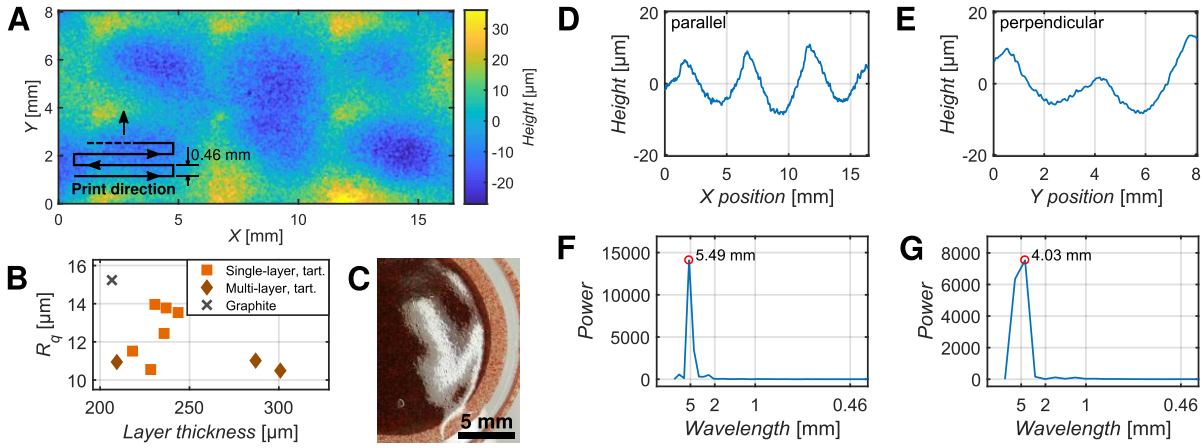

Figure 93. Surface variation of printed silicone layers. A) Heightmap of a printed silicone layer showing deviation from an ideal plane. B) RMS roughness (R_q) of various LAMDA-printed silicone samples plotted against layer thickness. The data shows no significant correlation between R_q and layer thickness. C) Close-up photograph of a LAMDA-printed sample (not the same as (A)). The light reflected off the surface reveals both large- and small-scale surface variations. D-E) Averaged cross-section profiles of the height profile shown in (A) along the principle axes. F-G) Corresponding power spectra of the averaged cross-sections revealing periodic variation at a spatial wavelength around 5 mm along both axes.

One possible cause of the uneven distribution of material during layer deposition is oscillation of the nozzle due to misalignment between the extruder and the stepper motor. Because the two components are connected by a rigid plastic part, slight misalignment between the rotation axis of the motor and the feed screw of the extruder

causes the tip of the extruder nozzle to oscillate with each rotation of the motor. This oscillation is small but visible, particularly at high rotational speed (e.g. when loading or purging the extruder). The exact amplitude has not been measured but is estimated to be of the order of 0.1 mm. During printing, rotational speed of the extruder is relatively low, typically around 1 Hz or 60 rpm. Assuming, for simplicity, a rotational speed of 50 rpm and a print speed of 500 mm/min, the resulting spatial wavelength of the oscillation is 10 mm per revolution along the print path. The effect of such oscillations on layer thickness were investigated using a simple simulation created in MATLAB. The print path, as specified by the G-code used to print the single-layer thickness samples, was divided into 10-µm steps. A sine wave with a frequency of 0.0983 mm^{-1} (10.173 mm wavelength) and an amplitude of ±0.1 mm (0.2 mm peak to peak), was added to the y-coordinates of the path. A corresponding cosine wave was added to the x-coordinates. The original print path is shown in Figure 94A. The print path with added oscillations is shown in Figure 94B. From this path, a simulated heightmap is created that shows the average local density of the print lines. The image is produced by taking a grayscale image of the plotted print path with oscillation (as shown in Figure 94B, without the red rectangle), filtering the image ten times using a Gaussian filter with σ=0.345 mm, and then mapping the brightness values to the colour spectrum used for the heightmaps of printed samples. The resulting image is shown in Figure 94C. It can be understood as an approximation of the average local concentration of deposited material. A higher concentration of extruded material is naturally assumed to result in higher layer thickness. The simulation does not contain a physical model of how the deposited material would flow. This is probably the reason why the resulting pattern does not fully match the pattern seen in the real, measured surface profiles, as shown in Figure 94D for comparison. Nevertheless, the simulation shows that even small oscillations of the nozzle at a low frequency can generate periodic features at the same length scale as the ones observed on the surfaces of printed silicone layers. From this, we conclude with reasonable confidence that the large-scale variations in layer thickness are indeed caused (at least to a large extent) by oscillations of the extruder nozzle. This means that they are not a necessary feature of

the printing process and can be eliminated, or at least reduced, by improvements to the extrusion mechanism.

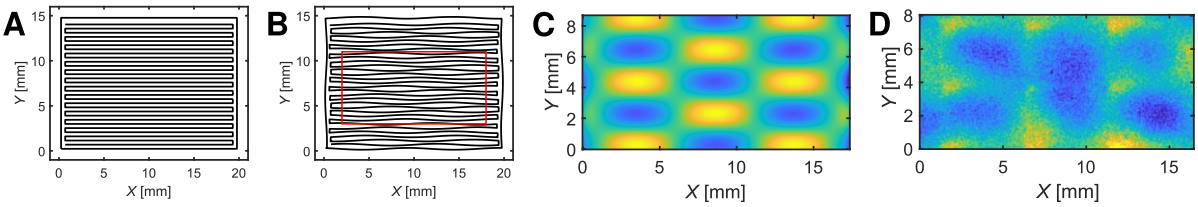

Figure 94. Simulation of extruder oscillations which cause variation in layer thickness. A) Original print path for a single-layer silicone sample, as specified in the G-code. B) Print path with added oscillations to approximate the real path of the nozzle. The red rectangle specifies the area of the heightmap shown in (C). C) Simulated height map showing the average local density of the print lines. D) Measured heightmap of a single-layer printed silicone sample, for comparison.

As mentioned at the beginning of this section, the measured profiles also show small-scale surface roughness. To quantify this, the large-scale, low-frequency surface variations had to be removed. This was achieved by creating a biharmonic spline fit of a down-sampled version of the surface profile, thus eliminating the high-frequency noise, and then subtracting this from the original profile so only the high-frequency variations remain. An example of this is shown in Figures 95A and B. Figure 95A shows the original surface profile at the top and the biharmonic spline fit at the bottom. It can be seen that the latter only contains the large-scale variations. Figure 95B shows a section of the difference between the two profiles in A. It can be seen that the profile in B is flat except for some small, unstructured deviations of the order of ±10 µm. To quantify the lateral dimensions of these small peaks and valleys, the width at half prominence of each peak was evaluated. Figure 95D shows the histogram of peak width for the sample shown in A and B. It can be seen that most peaks are around 50 µm wide and very few (less than 5 %) are above 300 µm. Figure 95D shows box plots of the peak width distributions for the different samples. All samples show an almost identical distribution, except for two of the single-layer samples (one tartrazine and one graphite). These samples differ from the others in the lateral resolution of the height profiles. The Alicona Infinity Focus software specifies the effective lateral resolution of these two samples as 22 µm, compared to 30 µm for all the other samples. The fact that the two samples with higher lateral resolution show lower peak widths indicates that the measurement of peak width is limited by the resolution of the data

and that the distribution gathered from the higher-resolution data is closer to the ground truth. The two high-resolution samples show a median peak width of 73 µm on average. Since the peak width distributions are very consistent between all samples, except for the difference in resolution, we can conclude that this value applies to all other samples as well and that the true value may be even lower than that. This matches quite well with the size of the filler particles in the silicone composites. These are generally between 20 µm and 100 µm in diameter for both graphite and tartrazine (see Section 4.5.2). This leads to the conclusion that the surface roughness is caused by the presence of filler particles at or near the silicone surface. This is further supported by the fact that there is visible surface roughness on samples printed with silicone composites but not on samples printed with pristine silicone rubber (compare Figure 93C and Figure 82C).

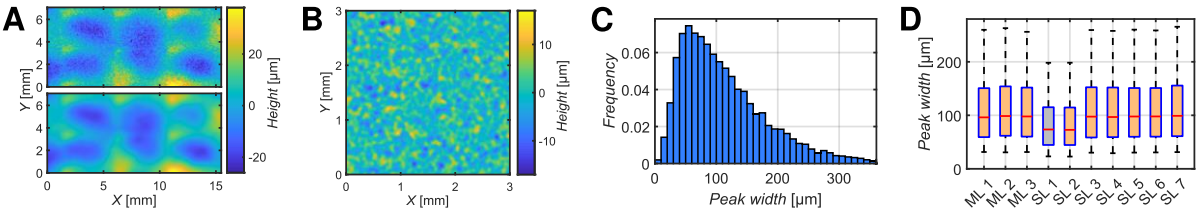

Figure 95. Surface roughness of printed silicone layer. A) Original surface profile (top) and a biharmonic spline fit of the surface that removes all high-frequency variations (under 1 mm lateral dimensions). B) Difference between the two profiles in (A), showing only the high-frequency variations. C) Peak width distribution of the sample shown in (B). D) Box plots of peak width distributions for all recorded samples. Whiskers indicate the 5th and 95th percentile, respectively. The multi-layer samples are indicated as "ML" and the single-layer samples as "SL". SL1 is the graphite sample, as also indicated by the box colour. All other samples are tartrazine.

To quantify the magnitude of surface deviation, the descriptor R_{T5} is used. Analogous to R_{P5}, which was introduced in Section 4.6.3, this descriptor is defined as the range between the 5th and 95th percentile of peak height (including valleys as negative peaks). This metric is used to eliminate outliers caused by dust particles on the surface or filler particles below the surface that are visible through the carbon black layer. R_{T5} of the flattened surface profiles is 20.9 µm on average (σ = 1.4 µm, n = 10). Rounding up, we can specify the tolerance of the flattened profiles as ±11 µm.

In conclusion, we have shown that the printed samples show long-range surface variations with a magnitude of ±36 µm, caused by oscillations of the extruder nozzle,

as well as short-range variations with a magnitude of ±11 µm, caused by the presence of filler particles. Both are very large for application as DEA membranes, where good layer consistency is critical. The former can most likely be eliminated by improvements to the extruder hardware (discussed in Section 5.6.1.2) while reduction of the latter will require changes to the material formulation (as proposed in Section 4.8.3.1).

5.4.3.4. Capacitance

Twenty rectangular, single-layer soft capacitors (design shown in Figure 89C) were printed using the LAMDA method to evaluate their electrical properties. Each capacitor consists of three silicone layers with two LSSR electrode layers between them. Thus, each device has one active layer between the two electrodes. The active area (where the two electrodes overlap) is 6x6 mm. A photograph of the finished, printed capacitors is shown in Figure 96A. Figure 96B is a visualisation of the G-code, which shows the arrangement of the samples on the print bed and the order in which they were printed. After printing, copper strips were attached to the exposed areas of each LSSR layer with a small amount of carbon grease to ensure good electrical contact. The strips were fixed in place with silicone glue. The samples were printed in four batches (A to D) of five capacitors each. The samples were printed on glass slides, with each batch printed on a different slide. Batches A and B were printed together at the same time. They are made from UV Electro 225-1 with tartrazine (2 wt%). Batches C and D were also printed together. They are made from UV Electro with graphite filler (2 wt%).

Capacitance C of the LAMDA capacitors was measured using two different methods: first with a VICHY VC6013 handheld capacitance metre and second with a Keysight E4980AL LCR Metre in parallel circuit mode (Cp-Rp) at 1 kHz. The measurements from both methods are in good agreement, with no measurement diverging more than 7 % between the two for the same sample. Hence, only the values recorded with the Keysight LCR Meter are used for further analysis, since these can be assumed to be more precise. The measured capacitance of all 20 samples is shown in Figure 96C.

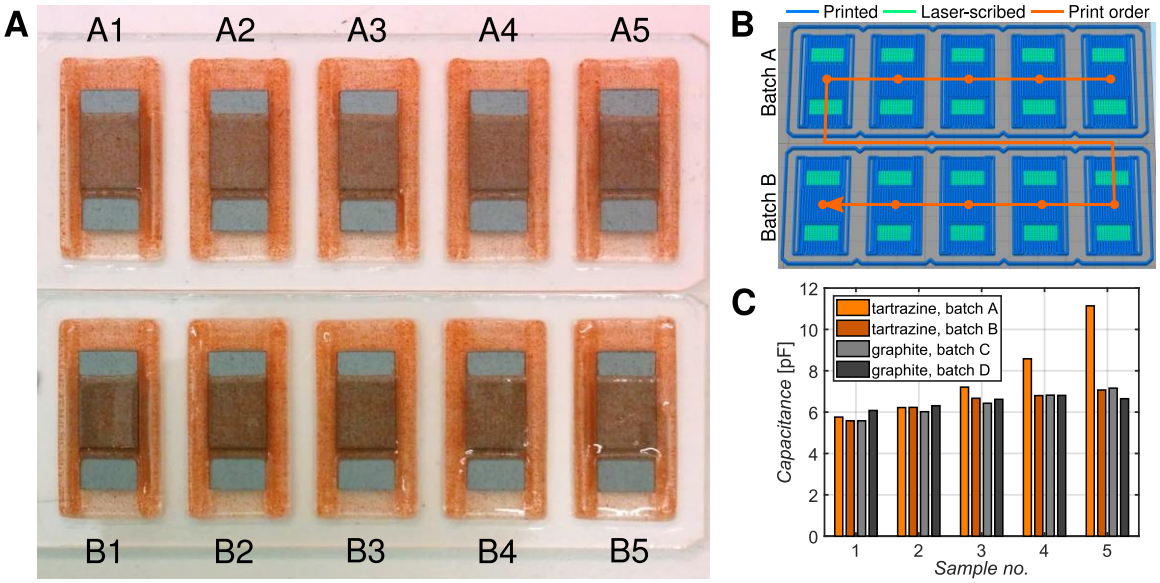

Figure 96. Capacitance of printed LAMDA capacitors. A) Photograph of as-printed LAMDA capacitors made from UV Electro/tartrazine composite. B) G-code visualisation of the two batches of 6 x 6 mm LAMDA capacitors. The image shows the arrangement of samples on the print bed, which is the same order as in (A). Batches A and B were printed in parallel, starting with the first layer of all samples, in the order specified by the orange arrow, then the second layer of all samples, etc. Batches C and D were printed in the same way. C) Capacitance for each capacitor in the four printed batches.

It is immediately noticeable that batch A shows a large, steady increase in capacitance from sample A1 to A5. The other three batches all show very similar results with a slight upward trend. Overall, the median capacitance is 6.79 pF with $\sigma = 1.23$ pF ($n = 20$). With batch A excluded, the median capacitance is 6.46 pF with $\sigma = 0.49$ pF ($n = 15$). This shows that most of the variation is contained in batch A.

Since batches A and B are made from the same material and have the same general geometry, the only possible difference between them causing variation in capacitance is the thickness of the dielectric layer (see Equation (5)). It therefore appears that layer thickness decreases from sample 1 to 5 in each batch, with batch A showing the largest decrease.

The samples are numbered according to their placement on the print bed (see Figure 96B) and the trend of increasing capacitance follows this order. This indicates that the variation in layer thickness could be caused by variations in the height of the print bed. Where the print bed is higher, the nozzle will be closer to the bed's surface during printing. This increases the pressure at the tip of the nozzle as material is extruded.

Since the extrusion pressure applied to the material cartridge is constant, an increase in pressure at the outlet results in reduced flow rates, creating thinner layers.

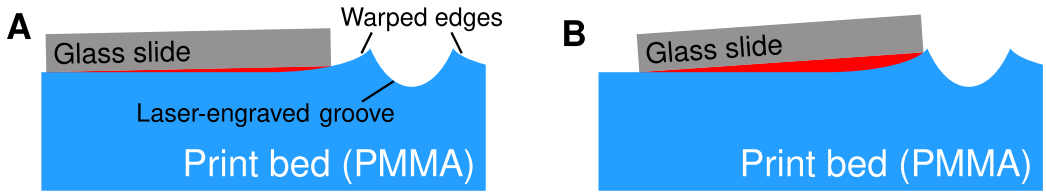

Figure 97. Schematic of an engraved edge resulting in a non-flat print substrate. A) Cross section of a laser-engraved groove on PMMA. Along the groove, material has been ablated by the laser. At the edges of the groove, the heat from the engraving caused the surface to warp upwards. A glass slide placed near the engraved groove does not lie perfectly flat due to the warped surface. B) If the glass slide is placed closer to the edge of the groove, the deviation from the flat surface increases, as indicated by the larger red area underneath the slide. Groove and glass slide are not to scale.

The samples were printed near the front right corner of the print bed. It appears that the samples printed closest to the edge of the print bed on the right side tend to have the highest capacitance and must therefore have the lowest layer thickness. Interestingly, Batch C does not show the same degree of variation as batch A, even though it was printed in the same location. This leads to the suggestion that the variation is not caused by the print bed itself. Instead, it is most likely caused by the glass slides on which the samples were printed. Thickness variation in the slides themselves could be to blame. Tolerances for the specific slides used here could not be found but other manufacturers specify thickness tolerances around 50 µm[287,288] which could make a noticeable difference in a 300 µm thick printed layer. Another possible explanation has to do with a specific feature of the print bed. The bed is made of a 10-mm-thick sheet of acrylic glass (PMMA). Because the bed is larger than the workspace of the printer (the area that all three tools can reach), the laser was used to engrave the outline of the workspace into the surface of the print bed as a visual aid. Engraving of PMMA creates a groove through ablation of the material, but it also results in warping of the surface at the edges of the groove. If a glass slide is placed near the engraved line, it will not lie perfectly flat due to the warped surface, as shown in Figure 97A. Most likely, this is the case in all four batches of LAMDA capacitors and is the reason for the slight increase in capacitance observed in each batch. The glass slide for batch A was possibly placed slightly closer to the engraved line, causing

it to have a steeper angle (see Figure 97B) and thus leading to a larger decrease in layer thickness with proximity to the right edge.

The theoretical capacitance C of a parallel-plate capacitor is given by Equation (5). It depends on the electrode area A, the thickness d and relative permittivity k of the dielectric, and the permittivity of vacuum $\varepsilon_0 = 8.854$ pF/m.[10] The nominal layer thickness of the printed capacitors is 300 µm. The electrodes were laser-scribed at speed $v = 150$ mm/min and power $D = 10$ % which results in an electrode thickness of 62 µm (see Section 4.6.2) and thus a theoretical dielectric layer thickness of $d = 238$ µm. Homing of the z-axis (to set the height of the print surface) was done near the centre of the glass slide that was closer to the front edge of the print bed. Therefore, the layer thicknesses of samples B2 to B4 and D2 to D4, which were printed in this area, are likely to be closest to the theoretical value. These samples have a capacitance of 6.57 pF (batch B) and 6.58 pF (batch D) on average. From these values, assuming $d = 238$ µm, we can calculate that the relative permittivity k of the dielectric materials is 4.90 for tartrazine and 4.91 for graphite. The permittivity of pristine UV Electro 225-1 is 3.13.[289] This shows that both fillers affect k in approximately the same way. It cannot be concluded with certainty that the fillers increased k since the given estimate of layer thickness could be inaccurate. For graphite, an increase in k would be expected since it is known that conductive fillers increase the permittivity of polymer composites.[10] For tartrazine, no previous reports were known. We were not able to find values of k for tartrazine or tartrazine composites in the literature. For a different azo dye (4-Acetaminophenol-[2-(4-Azo)]-4-amino diphenyl sulfone), a value of $k = 50$ at 1 kHz has been reported.[290] Although a generalisation to other azo dyes may be tenuous, it would seem plausible that tartrazine has a higher permittivity than the silicone rubber and thus also increases k of the composite.

$$C = \frac{k\varepsilon_0 A}{d} \tag{5}$$

Assuming a permittivity $k = 4.9$ for all samples, the measured variation in capacitance indicates that thickness varies between +42 µm and -98 µm from the nominal value of 238 µm (+18 % / -41 %).

5.4.3.5. Dielectric breakdown

The same 6x6-mm LAMDA capacitors described in section 5.4.3.4 were subjected to high voltage to determine their dielectric strength. Using an Ultravolt 5HVA24-BP1 HV amplifiers (Ultravolt, Inc., USA), an increasing test voltage V_t was applied to each capacitor. V_t was increased in discrete steps of 50 V. At each voltage, a square input signal between V_t and -V_t at 2 Hz was applied to the capacitor for three cycles before increasing V_t by another step. Current and voltage at the amplifier output were monitored to detect dielectric breakdown. When breakdown occurs, the series resistance of the capacitor decreases drastically. This causes the output current to rise sharply, accompanied by a decrease in voltage due to the Ultravolt amplifier's built-in current limiting (see Figures 98B and C). The voltage V_t at which breakdown occurs is determined as the breakdown voltage V_{break} of the capacitor.

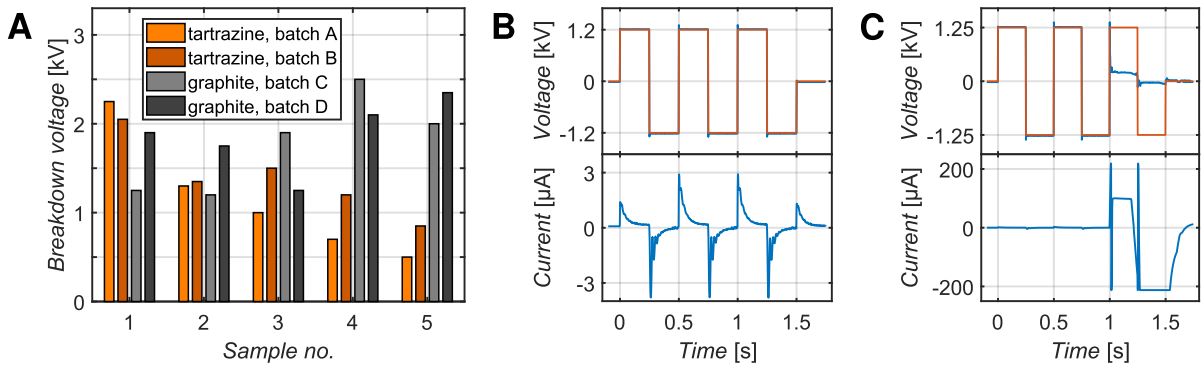

Figure 98. Dielectric breakdown of LAMDA capacitors. A) Breakdown voltage for each capacitor in the four printed batches. B-C) Voltage and current profiles from the breakdown test of sample C1. No breakdown occurs at V_t = 1.2 kV (B). At V_t = 1.25 kV, breakdown occurs during the 3rd cycle, as is evident from the difference in desired voltage (orange) and actual, measured voltage (blue). Note how the maximum current increases from under 4 µA to over 200 µA (the nominal current limit of the HV amplifier).

Figure 98A shows V_{break} for each of the LAMDA capacitors. In batch A, there is a strong downward trend in V_{break} with increasing sample number. This is effectively the inverse of the trend seen in the capacitance for this batch. Batch B also shows a downward trend, albeit less steep and with sample B2 falling somewhat below the trend. Overall, the tartrazine samples (batches A and B) have an average breakdown voltage of 1270 V (σ = 558 V). The graphite samples (batches C and D) don't show any clear trends. They have an average breakdown voltage of 1820 V (σ = 460 V) which is much higher than the tartrazine samples, and with lower overall variation.

However, the variation in the tartrazine samples appears to be systematic to a large degree, whereas the variation between the graphite samples appears mostly random.

V_{break} for an ideal parallel-plate capacitor can be calculated according to Equation (6) from the thickness d and the breakdown strength E_{break} of the dielectric. E_{break} is a material property and should not, in theory, vary between samples. Capacitance C of the same capacitor also depends on the thickness d, as described by Equation (5). Thus, since V_{break} is proportional to d, and C is inversely proportional to d, V_{break} should be inversely proportional to C. In a real capacitor, V_{break} is also strongly influenced by the layer quality and random defects of the dielectric. Nevertheless, a general trend of inverse proportionality between C and V_{break} can be expected.

$$E_{break} = \frac{V_{break}}{d} \quad \rightarrow \quad V_{break} = d \cdot E_{break} \tag{6}$$

Figure 99 shows breakdown voltage plotted against capacitance for all 20 LAMDA capacitors. The tartrazine samples (batch A and B) do indeed show an inverse trend between the two variables. For this group, the experimental data is best described by a rational fit (compared to a polynomial, exponential, or power fit in terms of adjusted R^2), as shown in Figure 99. Interestingly, the graphite samples (batches C and D) do not follow this trend at all. The data from this group is best described by a linear fit (see Figure 99) which indicates a positive correlation but fits the data very poorly. For tartrazine, the RMSE of the rational fit is 193 V. For graphite, the RMSE of the linear fit is 375 V. This shows that the variation among the tartrazine samples can largely be explained by variations in thickness of the dielectric layers, since these variations are also reflected in the capacitance. Among the graphite samples, there is comparatively little variation in capacitance. Despite this, there is large variation in breakdown voltage in this group. This might be caused by the random distribution of relatively large (compared to the layer thickness) conductive graphite particles in the composite. If several of these particles line up vertically, they can drastically reduce the effective thickness of the dielectric. Such local variation would have very little influence on the overall capacitance of the device but can greatly reduce its dielectric strength since breakdown will always occur at the weakest point and a single breakdown event causes catastrophic failure. For tartrazine, because the filler particles

are not electrically conductive, their distribution has little effect on the breakdown strength of the dielectric layer. Instead, the variation observed in this group is mainly due to the differences in layer thickness which were identified in Section 5.4.3.4.

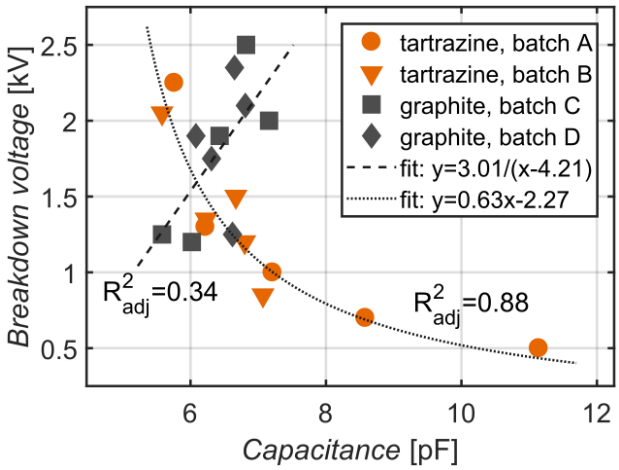

Figure 99. Correlation between capacitance and breakdown strength for 6x6 mm LAMDA capacitors. The lines show the respective best possible fit with respect to adjusted R^2 (R^2_{adj}). Note that R^2_{adj} penalises the number of degrees of freedom of the model, therefore a more complex model does not necessarily yield a better fit to the data even if the residuals are lower.

5.4.3.6. Capacitive sensing

The capacitance of a DE changes under mechanical deformation, which allows it to be used as a deformation sensor.[10] For example, compression of a DE results in an increase in the membrane area and a decrease in its thickness, which in turn leads to an increase in its capacitance. To test the sensing capabilities of LAMDA-printed DEs, three square LAMDA DEs with 6x6 mm^2 active area were subjected to a compressive force while monitoring their capacitance. The test setup is shown in Figure 100A. A plastic rod with a slightly rounded tip of 5 mm diameter compresses the sample. An IMADA DPS-110 (Imada, Inc., USA) digital force gauge is used to measure the applied force. The capacitance is measured simultaneously using a VICHY VC6013 handheld capacitance metre. The measured capacitance under varying compressive force is shown in Figure 100B. All three samples show a distinct and sudden decrease in capacitance as a certain amount of force is applied. The behaviour varies between samples as well as between test cycles of the same sample, but overall, the transition always occurrs between 6.8 N and 19.4 N. Before and after the transition, capacitance remains relatively constant. Before the transition, most samples show a slight increase

in capacitance with increasing force. All samples returned to their original capacitance once the force was removed.

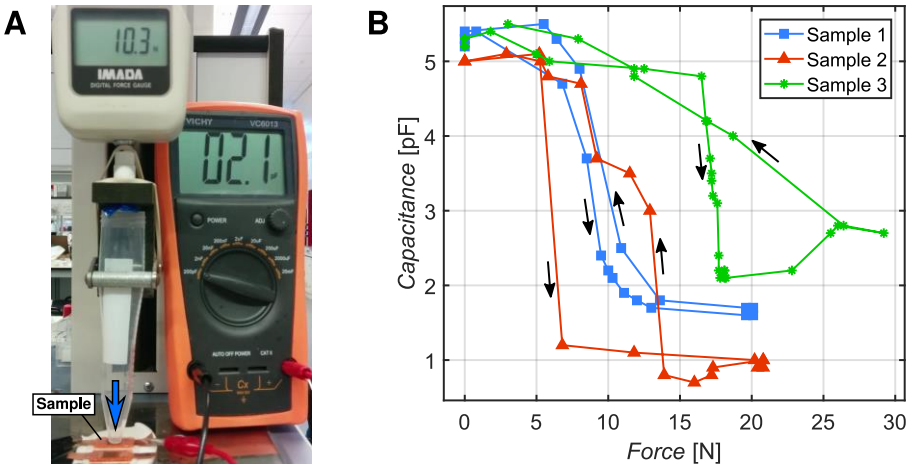

Figure 100. Force sensing behaviour of LAMDA-printed capacitors. A) Picture of the test setup. B) Measured capacitance over compression force for 3 LAMDA capacitors. A distinct reduction in capacitance under compression is evident in all samples.

Theoretically, an increase of capacitance with increasing compressive force would be expected, as this leads to a decrease in thickness and an increase in area of the soft capacitor (see Equation (5)). In reality, all samples show a sharp reduction in capacitance by at least 45 %. This can be attributed to cracking of the LSSR electrodes which causes some areas to become electrically insulated and thus reduces the effective area of the capacitor. This explanation is consistent with the known property of LSSR to lose conductivity under relatively small deformations, as shown in Section 4.6.5. We can conclude that LSSR is not a suitable material for this type of capacitance sensor. However, the large increase in resistance due to cracking could be utilised in resistive strain sensors, as has already been demonstrated.[247]

5.4.3.7. Electrostatic actuation

One of the overarching goals of our work is the fabrication of soft, 3D-printed actuators. To test if DEAs made using the LAMDA process are functional, several circular, single-layer DEAs as described in Section 5.4.1, Figure 89A were printed, three each of tartrazine and graphite composite. Each actuator consists of three silicone layers and two laser-scribed electrode layers. Only the middle silicone layer is active in this configuration. Because it is not possible to pre-strain the DEA membranes during the printing process, a variation of the diaphragm configuration recommended

for testing of low-pre-strain DEAs[72] is used. Instead of fixing the DEA to the opening of a pressurised chamber, air is injected directly into the DEA at the bottom LSSR layer. As mentioned in Section 4.6.7, the printed silicone membranes readily separate at the LSSR layer, forming a balloon with one silicone layer at the bottom and the other two, including the active layer, at the top. Figures 101B and C show schematics of an inflated DEA. When separating printed layers in such a way, the LSSR will mostly stick to the top layer (this is shown in Section 5.4.3.8), so the active DEA membrane remains enclosed by the two LSSR layers. When a voltage is applied between the electrodes, the active membrane contracts in thickness and expands in area. This reduces the elastic force of the membrane that counteracts the internal air pressure, therefore causing the internal volume to expand. This mechanism is shown in the schematic in Figure 101C.

The experimental setup for actuation testing is shown in Figure 101A. The needle inserted into the bottom LSSR layer serves as an air inlet and as an electrical contact at the same time. A copper strip is connected to the exposed part of the upper LSSR layer using carbon grease and fixed in place using silicone glue. Voltage is applied using two Ultravolt 5HVA24-BP1 HV amplifiers (Ultravolt, Inc., USA) which are connected to the needle and the copper strip, respectively. The internal air pressure of the DEA is held constant at 100 mbar using a Shako URPL4-02 manual pressure regulator valve (SHAKO Co., Ltd., Taiwan). These valves are self-relieving, which means they can release air when there is excess pressure at the outlet to always keep pressure constant. However, on some occasions, slight oscillations of the output presser have been observed, which might be contributing to noise in the recorded displacement. The displacement is measured using a Keyance LK-G152 laser displacement sensor (Keyence, Japan) mounted above, which records changes in the thickness of the actuator. During each test sequence, the applied voltage switches between off (0 V) and the test voltage (500 – 1500 V) for five cycles at 0.5 Hz. Test voltage is set to 500 V initially for each sample. For each following sequence, the test voltage was increased by 500 V until breakdown of the sample. Before the first test sequence, a baseline sequence at 0 V (constantly off) was recorded for each sample.

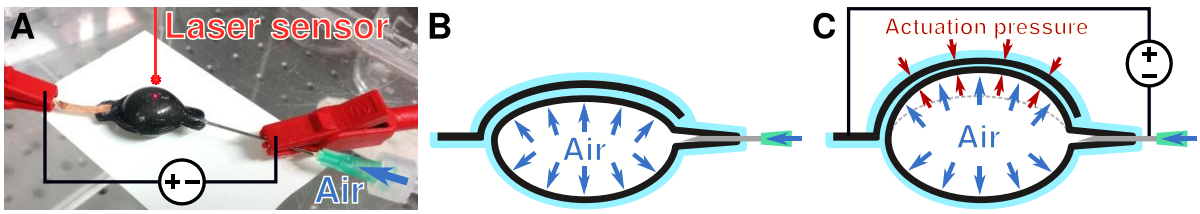

Figure 101. LAMDA DEA actuation testing. A) Test setup for actuation testing. Air is injected through the needle and held at a constant pressure of 100 mbar. Voltage is applied between the needle and the copper strip which connect to the LSSR electrodes. A laser displacement sensor above measures the vertical displacement of the actuator surface. B) Schematic cross-sections of the inflated LAMDA DEA before voltage is applied. C) Schematic cross-sections of the LAMDA DEA when a voltage is applied. The actuation pressure causes the active membrane to contract in thickness and expand in area, resulting in a volume increase.

Unfortunately, in two of the graphite DEAs and one tartrazine DEA, dielectric breakdown occurred immediately during the first test sequence at 500 V. No sample withstood more than 1000 V. This is problematic because, at relatively low voltages of 500 V or 1000 V, actuation strain is very low and hard to distinguish from noise. Figure 102A shows the recorded data from a baseline sequence. Applied voltage and current are 0, but the recorded displacement varies randomly over a range of 3 µm. The largest measured stroke (displacement between the on- and off-state) was 1.7 µm on average, measured on a graphite DEA at 500 V. The corresponding data sequence is shown in Figure 102B. In the displacement plot, the on- and off-phases are highlighted in green and orange, respectively. The measured displacement is consistently higher during the on-phase than the off-phase, despite considerable drift over the duration of the test. It also remains high for the duration of the on-phase. This is a good indication that the displacement is indeed caused by electrostatic actuation. Figure 102C shows the data sequence of the same sample at 1000 V. Here, with the exception of the first cycle, displacement appears to increase abruptly every time the voltage switches, regardless of whether it switches on or off. That indicates that the deformation is not caused by the applied voltage but rather by the flow of current, which spikes every time the voltage is switched. It is possible that resistive losses in the electrodes produce sufficient heat to raise the internal pressure and cause a measurable volume increase. It could also be that arcing occurs between disjointed areas of the LSSR electrodes during charging and discharging. This produces heat and possibly also gaseous combustion products that increase the internal volume.

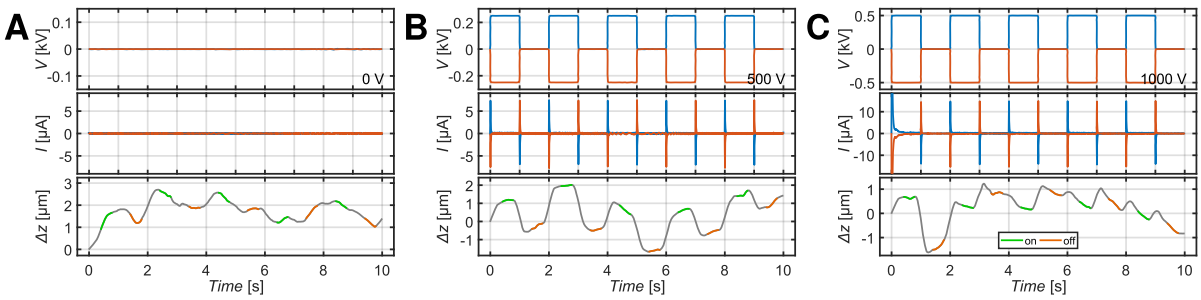

Figure 102. Recorded actuation of an inflated LAMDA DEA. Each graph shows the applied voltage (top) the output current (middle) and measured vertical displacement (bottom) over one test sequence of 5 cycles at 0.5 Hz. A) Baseline sequence with no voltage applied. The displacement is subject to substantial noise. B) Test sequence at 500 V. Positive vertical displacement is measured while voltage is applied. C) Test sequence at 1000 V. After the first cycle, displacement seems to follow current rather than voltage.

Because the displacement from electrostatic actuation is on the same order of magnitude as the recorded noise and other effects such as Joule heating and arcing, it is difficult to accurately determine actuation stroke of the LAMDA-printed DEAs. Perhaps pressurisation with a head of water instead of the mechanical regulator valve would ensure a more constant pressure and eliminate some of the noise. However, the focus of future work should rather be increasing actuation strain to macroscopic levels. Unfortunately, we have to conclude that the LAMDA DEAs are not currently capable of producing useful, macroscopic actuation. One major factor that limits the achievable actuation strain is the low breakdown voltage of the devices. DEAs typically require very high voltages of several kilovolts to exhibit macroscopic strain. To increase strain of the LAMDA DEAs, their breakdown strength needs to be improved.

The low breakdown strength can be attributed to inconsistencies in layer thickness, as described in Section 5.4.3.1 to 5.4.3.5. The absorbent filler, particularly graphite, may also be a cause of reduced breakdown strength. The theoretical layer thickness of the active membrane in the LAMDA DEAs is 300 µm – 60 µm = 240 µm (printed layer minus LSSR layer). A pristine, consistent silicone film of this thickness should be able to withstand 5.8 kV in theory (dielectric strength of UV Electro225-1 is 24 kV/mm[289]). Efforts need to be made to improve both the layer consistency and material formulation.

There are several additional factors which may be limiting the actuation strain of the LAMDA DEAs:

- The printed DEAs consist of three silicone layers of which only one is active. That leaves two passive silicone layers. In the inflated configuration, the top membrane, which expands during actuation, consists of two silicone layers, one active and one passive. The passive silicone layer restricts the deformation of the active layer.
- Inflation pressure during testing was much higher than the recommended pressure of 300 Pa (3 mbar) for the diaphragm test configuration.[72] The pressure of 100 mbar was chosen arbitrarily as a relatively low value at which clear macroscopic inflation was evident. Perhaps at lower inflation pressure, electrostatic actuation would be increased.
- The displacement measurement was very noisy, making it difficult to measure or even detect actuation. Perhaps a better pressure regulator or other source of constant pressure could reduce the noise.
- It has been shown that the resistance of LSSR increases sharply, even under small strain (see Section 4.6.5). It is possible that the applied pre-strain is enough to restrict charge distribution across the electrode surface. If this is the case, only a subsection of the active membrane area will indeed be active.

Further improvements to the LAMDA process are clearly necessary to enable it to produce functional DEAs. It may also be that LSSR is not a suitable electrode material due to its brittle nature. Testing of DEAs with LSSR electrodes made on pre-fabricated films would enable study of LSSR in more detail, independent of the performance of the 3D printing process.

5.4.3.8. Pneumatic actuation

Two different types of LAMDA-printed pneumatic actuators were tested: a simple balloon, and a PneuNet-type bending actuator, as described in Section 5.4.1.2, Figure 90B. Both actuators were injected with air at varying pressure. The pressure was monitored using a digital pressure sensor. Videos of the actuators were recorded to characterise the deformation. Since the pressure sensor only updates every 330 ms, the pressure values were interpolated to match the video frames.

Figure 103A shows an image sequence of the LAMDA balloon at different pressures. Figure 103C shows the corresponding pressure-deformation plot. It shows the

horizontal radius (long axis) and vertical radius (short axis) of an ellipse fitted to the outline of the balloon. The plot only shows pressures above 35 mbar since the balloon is not well approximated by an ellipse when it is completely flat. It can be seen that, initially, the vertical radius increases almost linearly while the horizontal radius stays constant and even reduces slightly. This is because the balloon starts out as a flat, circular shape and in the first phase of inflation, an increase in thickness causes a slight radial contraction. Once the balloon approaches a spherical shape, both radii grow proportionally. The plot in Figure 103C also clearly shows that elastic instability occurs as the pressure reaches 300 mbar. At this point, the pressure had to be reduced manually to keep the balloon from bursting. After reducing the pressure back to 227 mbar, a stable state was reached. From there, pressure was increased again until the balloon burst at 271 mbar. The image sequence in Figure 103A shows the balloon before inflation (0 mbar), shortly before the instability occurred (270 mbar), after instability occurred and pressure was reduced to 227 mbar, and right before bursting at 271 mbar.

One other interesting observation from the images in Figure 103A is that the LSSR almost entirely sticks to the top half of the balloon. This clearly shows that silicone deposited on the LSSR layer in liquid form and then cured, bonds to the LSSR much stronger than the adhesion of the LSSR to the cured silicone below. This is not surprising since the liquid silicone is able to conform to the rough, porous surface of the LSSR layer. On the other hand, we have previously shown that the adhesion between LSSR and the silicone substrate beneath is relatively weak (see Section 4.6.7).

Figure 103B shows an image sequence of the LAMDA-printed PneuNet actuator during actuation. Both the outline of the actuator (used to determine strain) and the bending angle are highlighted in the images. Figures 103D and E show the relationship between pressure and strain or bending angle for the PneuNet actuator, respectively. When deflated (pressure $\leq$ 0 mbar), the actuator is limp and bends under gravity. Initially, as pressure is increased, strain increases but bending angle decreases because the internal overpressure causes an increase in stiffness. However, above 300 mbar, both area strain and bending angle show a steep increase. Elastic instability is also observed in this actuator, albeit less severe than in the balloon actuator. Pressure was not

increased until failure. The deflation cycle shows relatively large hysteresis. This is not due to permanent relaxation of the material (i.e. Mullins effect). The actuator had been inflated prior to the measurements and the measured behaviour was consistent over three cycles.

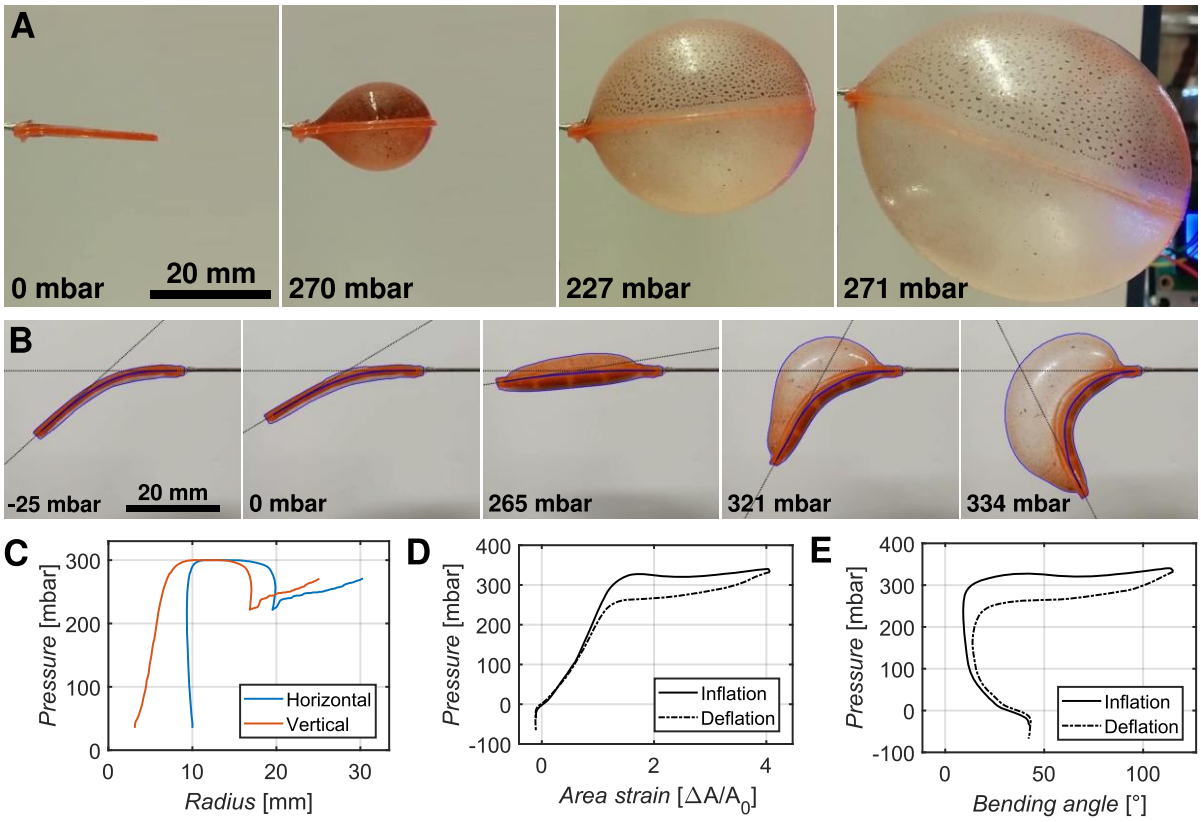

Figure 103. Pneumatic actuators fabricated using LAMDA printing. A) Balloon-type actuator undergoing large, uniform inflation. B) PneuNet-type actuator displaying bending action as well as large volumetric inflation. C) Pressure-deformation plot of the balloon actuator. Deformation is measured by the horizontal and vertical radius of an ellipse fitted to the outline of the balloon. D) Plot of pressure against area strain for the PneuNet actuator. Area strain is the increase in cross-section area as seen in (B), marked by the blue outline. E) Plot of pressure against bending angle of the PneuNet actuator. Bending angle is the angle between the two black lines in the images in (B).

From the images in Figure 103B it is evident that the PneuNet actuator does not, in fact, consist of the four discrete inflatable chambers shown in the renderings and visualisation in Figure 90 (Section 5.4.1). Instead, the actuator can be seen to inflate into a single, large volume. That is because, upon first inflation of the printed actuator, the top and bottom silicone layers detached at the separations between the chambers, thus combining them into a single, large chamber. The same phenomenon was also observed in other inflatable LAMDA-printed structures, whereby adhesion of a printed

layer to the silicone layer below is very weak in the vicinity of a laser-scribed region. This is probably due to silica that deposited on the silicone surface during laser scribing, as has been shown in Chapter 4, Section 4.6.1. The layer of silica is thickest very close to where the laser scribing took place, which is why those areas show the weakest adhesion. Usually, silicone adheres very well to previously printed layers of silicone. This is evident from the large inflation that both pneumatic actuators were able to withstand. In the case of the balloon actuator, the margin around the LSSR layer where silicone is exposed was 2 mm. When the balloon burst, the tear happened in the top surface, not at the interface between layers. This shows that interfacial bonding between silicone layers is generally good, even on layers where laser scribing occurred. For the PneuNet actuator, the margin around the LSSR was 1.5 mm, both around the edges and between the chambers. Since the PneuNet actuator was able to withstand even higher pressure than the balloon, silicone adhesion around the edges of the PneuNet must still have been good. Only between the chambers did the silicone layers detach. The difference here is that these separations were surrounded on both sides by LSSR, so the maximum distance from any laser-scribed region was only 0.75 mm. We can therefore conclude that there is a margin around any laser-scribed area where adhesion between silicone layers is weakened. We can narrow down the width of this margin to between 0.75 mm and 1.5 mm. The width may also change with the laser scribing conditions (speed and power). This margin needs to be respected when designing inflatable structures for LAMDA printing.

In addition to the balloon and PneuNet actuator, an octopus model with integrated pneumatic actuators was printed to showcase the ability to integrate pneumatic structures into parts with complex geometry. The model incorporates two separate channels from the back to the front of the model where two small inflatable chambers are placed at the base of two arms. Figure 104A shows a visualisation of the G-code for the pneumatic octopus. Figure 104B shows a visualisation of only the second layer, which contains the laser-scribed areas. In Figure 104C, the laser-scribed pattern is visible through the bottom of the printed part. Figure 104D shows the octopus with two needles inserted into the laser-scribed air ducts at the back of the model. These can be connected to a pressured air supply to inject air into the inflatable chambers.

As each chamber inflates, it bulges out and pushes the respective arm upwards. This is shown in Figures 104E and F.

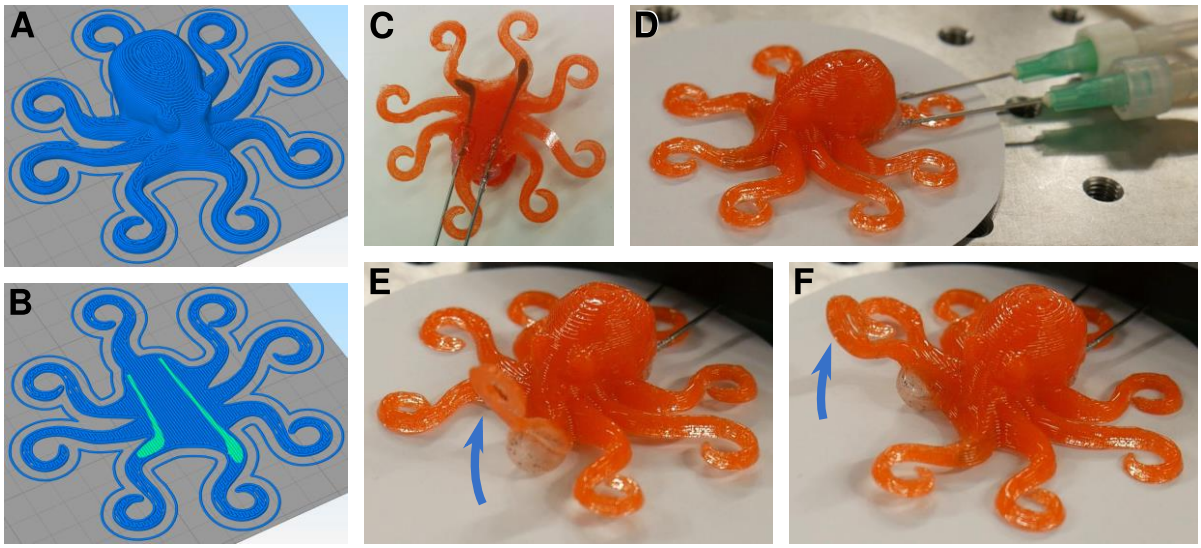

Figure 104. LAMDA-printed, pneumatically actuated octopus model. A) G-code visualisation of the octopus model. B) G-code visualisation of the first two layers of the octopus model, showing the areas to be laser scribed on the second layer. C) Underside of the printed octopus. The LSSR pattern is visible through the bottom silicone layers. D) The printed octopus model with needles inserted into the air channels and connected to a pressured air supply. E) Octopus lifting its left arm. F) Octopus lifting its right arm. Injection of air causes the laser-scribed air chambers to expand and form bubbles, pushing the respective arm upwards.

The first time that air was injected into the channels, the printed layers had to separate at the laser-scribed layer to open the channels and allow airflow. It was found that, for the narrow channels of 1 mm width, a relatively large pressure was required to separate the layers. Great care had to be taken to open the channels without immediately bursting the inflatable chambers as soon as the channels were open. This happened with the first printed octopus. On the second attempt, greater care was taken, and the channels were successfully opened. To do so, air was injected manually using a syringe which allowed the pressure to be reduced quickly whenever the channel started to open up further. To avoid this difficulty in the future, pneumatic structures should be designed with sufficiently thick walls to withstand the pressure necessary for layer separation. In the pneumatic octopus, the channels were laser scribed on the second printed layer (layer thickness 300 µm). The side walls of the inflatable chambers were as thin as 1.3 mm in the narrowest place. Considering the margin of low layer

adhesion around laser-scribed areas, as discussed above, this was too thin to make a robust pneumatic actuator. The channels could also be made wider to reduce the pressure necessary for opening them.

The pneumatic octopus successfully demonstrates that the LAMDA process can be used to fabricate soft parts with complex geometry and embedded pneumatic actuators. The experience shows that a channel width of 1 mm and a wall thickness of 1.5 mm are the minimum values required to make robust pneumatic structures. To allow sub-millimetre fluidic channels, a better method for opening the channels needs to be found, such as injecting an incompressible fluid instead of air or perhaps using a solvent that reduces adhesion between silicone and LSSR. Such techniques have so far not been explored.

The ability to produce fluidic channels and make inflatable structures is not unique to the LAMDA process. 3D printing of pneumatic actuators has been demonstrated before e.g., using SLA,[111] DIW,[179] and FFF printing,[121] or by printing a sacrificial material inside a vat of uncured silicone.[44] Many of these methods actually have advantages over the LAMDA process with regard to pneumatic structures since they allow fabrication of varying sizes of channels and cavities whereas LAMDA printing only allows separations between printed layers. It may be possible to generate larger volumes of LSSR inside a LAMDA-printed part but removing the LSSR from the part to create a cavity will be difficult. Assuming that LSSR largely consists of silicon carbide, it is not soluble in any known solvent or otherwise processable at temperatures that the silicone rubber could withstand.[264] It can therefore not be used in the same way as other sacrificial materials that can be cleanly removed after printing. This means that, for fabrication of purely pneumatic structures, other printing methods are more suitable. However, LAMDA printing has the advantage that it can also generate conductive structures inside the same part. This offers the potential to print hybrid devices that use fluidic and dielectric structures similar to HASEL actuators (see Section 2.2.3.1). The examples of pneumatic actuators shown in this section serve to demonstrate that this additional functionality is possible within the LAMDA process. Unique applications could arise when pneumatic structures are combined with DE actuators or sensors that cannot easily be fabricated by other 3D printing methods.

5.4.3.9. Repeatability

For the LAMDA process to be a useful research and prototyping tool, it must have good repeatability so that users can be certain that two parts produced from the same design will have the same properties. Among all the samples presented in Section 5.4.3, there was distinct variation with respect to different characteristics.

Between the 6 single-layer printed silicone samples made of tartrazine composite, standard deviation of layer thickness was only 8.7 µm or 3.8 %. Much of this variation can be attributed to fact that the samples were printed on different substrates and in different positions, which was shown to have an impact on layer thickness (see Section 5.4.3.4). We could also show that a large amount of surface variation is caused by oscillations of the extruder nozzle (see Section 5.4.3.3), which could be eliminated through minor hardware changes. This means that much lower variation is probably achievable with only a few minor improvements to the process.

Among a batch of 10 LAMDA-printed capacitors, standard deviation of capacitance was 23.1 % of the mean for tartrazine and 7.2 % for graphite. However, we could show that the variation is most likely the result of large differences in layer thickness between the samples (see Section 5.4.3.4). After correcting for these differences, standard deviation of the residuals could be as low as 2.5 % of the overall mean for tartrazine and 1.7 % for graphite.

The breakdown voltage of the LAMDA capacitors showed a relative standard deviation of 43.9 % for tartrazine and 25.3 % for graphite. After correcting for the variation in layer height, standard deviation of the residuals could be reduced to 15.0 % for tartrazine. The graphite samples did not follow the expected trend in layer thickness, and we can therefore not assume any correlation between thickness and breakdown voltage for the tested samples (see Section 5.4.3.5). Breakdown voltage naturally has relatively high variation because it can be greatly influenced by small, random defects.

Overall, the printed devices showed a large amount of variation. However, much of this variation could be attributed to inconsistencies in layer thickness and we have identified two very simple fixes that can be expected to significantly improve layer

consistency. Our data also indicates that the tartrazine composite produces more consistent results than the graphite composite.

One other major source of inconsistency is the sporadic inclusion of air bubbles in silicone layers that are printed on top of LSSR layers, as described in Section 5.3.4.1. It may be possible to eliminate these, or at least reduce their frequency, by adjusting several process parameters (see Section 5.6.2). These improvements should be the main focus of further development of the LAMDA process since good repeatability is essential to make LAMDA printing a useful and practical tool for soft robotics research.

5.5. Conclusion

The LAMDA process is a new technique for manufacturing soft actuators and devices. The discovery of LSSR and its use as an electrode material open up new ways to fabricate thin layers of conductive materials on soft substrates using a very simple method that is easily integrated into the 3D printing process. The combined process allows fabrication of multi-material structures while circumventing many of the difficulties often encountered with traditional multi-material deposition.

Many but not all of the initial requirements (see Section 5.3.1) have been met:

- Multi-material printing: Structures made of two different materials with very different properties can be fabricated (silicone rubber and LSSR). (met)
- Printing with soft materials: The base material is a silicone rubber composite with high elasticity, allowing the fabrication of soft, deformable parts. (met)
- Fast curing: The use of UV-curable silicone rubber allows curing within seconds and enables high print speed of the order of only a few minutes per layer (depending on part size). (met)
- 200 µm layers with ±10 µm tolerance: The printer is capable of printing 200 µm thick layers. However, due to large variation in layer height, devices were typically printed at 300 µm layer thickness to improve consistency. If tolerance can be reduced, 200 µm layers will become feasible. Layer thickness tolerance is currently ±36 µm, far exceeding the target of ±10 µm, but small improvements to the extruder hardware (see Section 5.6.1.2) could significantly improve layer uniformity. Surface roughness due to the incorporation of filler particles in the silicone material is within a range of ±11 µm. This is close to the target of

10 µm but changes to the material formulation will probably be necessary to meet the requirement for thickness tolerance. (almost met)

- Lateral feature size below 1 mm: Features as small as 0.84 mm were printed consistently using a 0.41 mm nozzle. A smaller nozzle would enable even smaller features at the cost of print speed. LSSR features can be as small as 0.1 mm. For pneumatic structures, a wall thickness margin of 1.5 mm needs to be respected, reducing effective feature size to roughly 4 mm (see Section 5.4.3.8). (almost met)
- Good repeatability: Small parts print very reliably. 20 out of 20 capacitors (6 x 6 mm) printed successfully and were functional. Their properties (capacity and breakdown voltage) varied rather widely, but this has, to a large extent, been attributed to the placement of the print substrate. We expect that capacitance variation of 2.5 % from the mean is achievable. Parts with large LSSR surfaces print less reliably. Circular DEAs with 20 mm diameter had roughly a 50 % chance of being faulty (having a short circuit or extremely low breakdown voltage under 500 V) due to the formation of air bubbles in the silicone layer. This can probably be improved by adjusting process parameters (see Section 5.6.2), but at the cost of print speed. (not met)

Desirable properties:

- Low-cost hardware: The hardware required for the LAMDA printer is just within the target budget of £1000. However, this excludes consumables and materials costs, so the overall cost of the system is slightly above £1000. Nevertheless, the cost is far lower than any comparable alternative (see Section 2.4). (almost met)
- Safe to use: The safety enclosure with interlock switches ensures user safety during normal operation. The uncured silicone material is suspected of damaging human fertility and should be handled with appropriate care, but the material does not pose any acute health hazards. The filler materials tartrazine and graphite are not known to be harmful. Very small amounts of hazardous gases may be produced during laser scribing. In a well-ventilated area, these do not pose any significant health risk. (met)
- No reliance on external facilities: The extruder currently relies on an external source of pressurised gas. Where this is not available, a low-cost substitute such as a small compressor or gas cartridge could be used. Material preparation also requires a vacuum chamber and a centrifuge, although the latter is not essential. (almost met)

- Environmentally friendly: The LAMDA process uses no energy-intensive thermal processes and does not rely on organic solvents. All materials used are generally non-hazardous. The LAMDA process compares very favourably to other 3D printing processes in these regards. (met)

LAMDA printing of simple DEA devices has been demonstrated. Electrostatic actuation of a LAMDA DEA with low pre-strain has been shown, however, actuation strain is extremely low. Limitations in the manufacturing process as well as the experimental setup are responsible for this underwhelming performance. Good results can be achieved when using the LAMDA process to fabricate inflatable structures if a few simple design guidelines are respected. Simple pneumatic actuators with large strain and different modes of actuation were demonstrated.

The LAMDA process shows great potential with regard to design flexibility and automated fabrication of soft structures with complex shapes. Particularly the low-cost nature of the LAMDA platform gives it a distinct advantage over other methods, ensuring that the technology will be accessible to a broad community of researchers and hobbyists to explore novel designs for soft and wearable electroactive devices. The LAMDA process is safe and environmentally friendly as it does not require the use of organic solvents or other hazardous substances. Although very promising first results were shown, the process is not reliable enough for widespread use at the moment and the performance of printed devices is not yet competitive. However, several possible improvements to the existing process and printer hardware have been identified which could greatly improve part quality and help to realise the LAMDA platform's full potential. These are discussed in the following section as well as Chapter 6.

5.6. Outlook

The LAMDA process is an interesting new and low-cost approach to fabrication of soft, electroactive devices. However, several challenges still need to be overcome to make the process more reliable and to improve the properties and performance of LAMDA-printed devices. In this section, several ideas for improvements are explored.

5.6.1. Hardware improvements

5.6.1.1. Print substrate

As explained in Section 5.4.3.4, the use of glass slides as print substrate led to great variation in layer thickness since the substrates do not have uniform height when placed too close to the edges of the print bed. The simplest solution to this problem is to place the substrates further from the edge. That alone should greatly reduce the height variation. However, this issue highlights that the process is very sensitive to variations in substrate height. That means that bed levelling is also extremely important. In the current setup, this is done manually. Upgrading to automated bed levelling could greatly improve repeatability. It would also enable probing of the print substrate at regular intervals and compensating for height variations. This is a common feature in the latest generation of FFF printers and is already supported by the printer's current firmware. A high-precision piezo sensor could be added to the print head at the cost of £35[291] and would correct any variations in substrate height to within 5 µm. With automated bed levelling, the type and placement of the substrate would no longer be a concern.

5.6.1.2. Extruder

The deposition mechanism could be upgraded to a purely pneumatic system or a PCP, as discussed in Section 5.3.2.3. Both have advantages and disadvantages. The use of a purely pneumatic system would eliminate the oscillations of the nozzle that were found to cause local variations in silicone layer thickness. It would also reduce cost, since the auger extruders and the extruder motor would no longer be required. On the other hand, a pneumatic controller capable of supplying negative pressure would probably be required to avoid oozing. This could drastically increase the cost of the printer unless a low-cost, custom solution can be found. One potential workaround could be the use of smaller or longer nozzles which restrict material flow enough to prevent oozing. This would increase the overpressure required for printing, but it would remove the need for a negative pressure supply. Since typical extruder pressure for the current system is only 200 mbar, increasing the pressure is relatively unproblematic. If oozing is not a problem, a simple solenoid valve and manual pressure controller, as are

currently used in the LAMDA printer, would be sufficient to effectively control material flow.

The use of a PCP would have the major advantage that it is insensitive to material viscosity. That means that no calibration is required to achieve the desired flow rates regardless of material viscosity (within reasonable limits). This would make the printing process more repeatable and more user friendly. It would also make material preparation easier since materials could be prepared in larger batches. UV Electro 225-1 has a nominal pot life of 3 days. In principle, it can remain usable for weeks after addition of the catalyst if stored properly, but the viscosity of the material starts to increase noticeably after several days. For consistent results, it is therefore recommended to prepare materials fresh and use them within three days. If using a PCP, the impact of small changes in viscosity would be greatly reduced. The biggest problem with PCPs is that no low-cost or disposable PCPs are available that could easily replace the disposable auger extruders currently in use. The use of custom, 3D-printed PCPs has been briefly explored but these suffer from leakage and were not found to be feasible unless considerable effort is invested in developing and optimising them.

5.6.1.3. Laser

One of the difficulties with the current process is that light of a similar wavelength is used for both curing (365 nm) and laser scribing (450 nm). Curing requires the light to penetrate the material, but laser scribing requires it to be absorbed at the surface. This problem could be solved by improving the material formulation to use selectively absorbent pigments, as discussed in Section 4.8.3.1. Alternatively, a different type of laser could be used that emits at a more convenient wavelength. The 450 nm blue-violet diode laser was chosen because this is the cheapest type of high-power diodes currently on the market. Compact laser modules with integrated electronics are available in this wavelength, making them very easy to use. However, other types of laser might be more suitable. A CO_2 laser for example has the advantage of having a very long wavelength of 10,600 nm. At this wavelength, silicone rubber is naturally absorbent and can be laser scribed without any additives.[238,242] This type of laser is used in most commercial laser cutters. However, CO_2 lasers are too expensive, bulky

and powerful to be used in the LAMDA process. Diode lasers are currently the only lasers that are feasible, thanks to their compact size and low cost. Near-infrared laser diodes are a possible alternative to the current 450 nm blue diode. High-power 808 nm diode modules with 1.6 W are currently available on eBay for £100. Unfortunately, UV Electro is no more absorbent at 808 nm than it is at 450 nm (see Figure 53E). Nevertheless, choosing a wavelength that is further from that used for UV curing might make it easier to find a pigment or filler that is selectively absorbent at only the laser wavelength. That being said, there is a distinct advantage to using a blue laser. Because the laser and UV LED wavelength are close together and at the same end of the visible spectrum, the safety enclosure made of orange-tint acrylic can effectively block both wavelengths (see Figure 81). The acrylic glass is highly transparent at 808 nm. If an infrared laser is used, a different (or additional) safety enclosure would have to be built.

In addition to choosing a suitable type of laser, an automated laser focussing capability could greatly increase consistency while also improving user-friendliness and safety. Since laser focus can be adjusted through z-positioning of the print head, an automated bed levelling feature as described in Section 5.6.1.1 could already go a long way in ensuring consistent focussing. Otherwise, some form of optical sensor feedback could be used to aid focussing.

5.6.1.4. Fume extraction

It was shown in Section 5.4.3.8 that silica deposited during laser scribing on the surrounding silicone surface can have an adverse impact on layer adhesion. This might be prevented by adding a miniature fume extractor to the print head, similar to those used for soldering. Such a device could simply be constructed from a miniature fan, a 3D-printed duct and a piece of solder fume extractor filter, which can be bought cheaply and cut to size. This could greatly reduce the required margins around laser-scribed areas for good layer adhesion and thus reduce the possible feature size of pneumatic structures and fluidic channels. Fume extraction and filtering would also reduce health concerns that might arise from the by-products of laser scribing if the printer is used very heavily in a room with inadequate ventilation.

5.6.2. Process optimisation

The LAMDA process is controlled by a large number of important process parameters such as print speed, extrusion width, extruder pressure, layer height, laser scribing speed, laser power, laser focus, UV curing duration, etc. This parameter space has by no means been fully explored to optimise the LAMDA process. Optimising these parameters could have a great impact on the quality of LAMDA-printed parts. One of the biggest problems with the current LAMDA process is the occasional formation of bubbles in silicone layers printed on top of LSSR layers. The presence of even a single bubble usually renders a printed device non-functional. If the formation of bubbles can be suppressed, the reliability of the LAMDA process would be greatly improved.

Investigation of the surface structure of LSSR (Chapter 4, Section 4.6.1.1) shows that LSSR becomes less porous at very low speed and laser power. Reducing the porosity of LSSR could help to avoid trapping gas in the LSSR layer which then escapes by forming bubbles in the silicone printed on top. While printing LAMDA DEAs for actuation tests (see Section 6.4.3.7) it was observed that reducing print speed seemed to decrease the chance of bubbles forming. This is probably because gases trapped in the LSSR have more time to escape on the side where silicone has not yet been deposited. This phenomenon has not yet been properly investigated and it might lead to an effective strategy for suppressing the formation of bubbles. Unfortunately, decreasing both print speed and laser scribing speed will greatly increase print times. However, if reliability can be greatly improved, the increase in print duration would be acceptable since much time can be saved on repeating failed prints.

5.6.3. Design improvements

So far, only very simple models with up to three layers and separate electrodes were printed (see Section 5.4.1). For practical applications, more complex structures and particularly multi-layer DEAs are of interest. To make multi-layer stacks, the electrodes need to be connected together in alternating sequence. Equally, for other more complex designs it might be desirable to produce LSSR layers that are not horizontal. The LAMDA process, like most 3D printing processes, is currently limited to stacked 2D layers. Any non-horizontal electrode layer will have to span several printed layers. Interconnections will be required between these layers to make a

continuous feature. In traditional multi-material 3D printing, this would be achieved easily by ensuring a certain amount of overlap between parts of a layer that are printed with the electrode material. In LAMDA printing however, electrode layers can only be produced on top of silicone layers. A connection between layers is therefore only possible where a silicone surface meets an LSSR surface. It is possible to achieve this intersection by printing a layer in two steps with alternating printing and laser scribing. The fact that the edges of printed layers are inevitably sloped due to the low viscosity of the material is a useful feature in this case. A schematic of the proposed process is depicted in Figure 105A. The same mechanism can be used to produce vertical interconnects between layers of a stacked DEA, as shown in Figure 105B. The ability to produce interconnected LSSR structures across multiple layers can also be useful for LAMDA-printed fluidic actuators, e.g. for bellows structures.

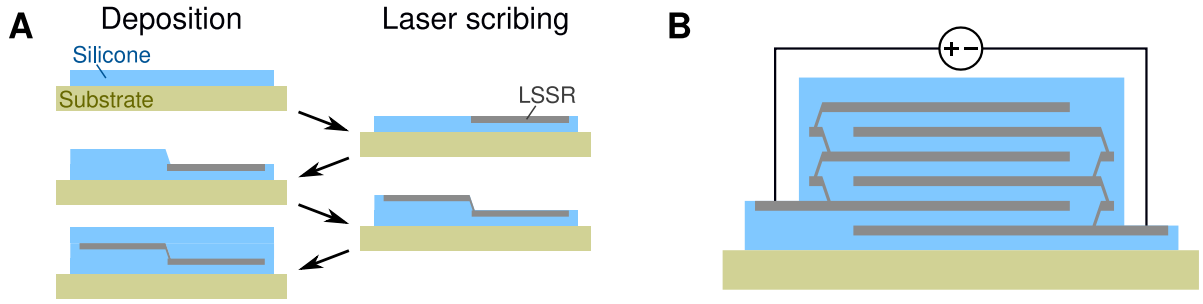

Figure 105. Proposed LAMDA process to print non-horizontal LSSR layers with connections across printed layers. A) Each layer is printed in two alternating printing and laser-scribing steps. B) Schematic of a multilayer DEA printed using the method illustrated in (A).

By reducing the thickness of printed layers to or below the thickness of the LSSR layers, it might be possible to convert an entire continuous volume to LSSR. This could potentially be used as a rigid structural material to produce structures such as an internal rigid skeleton inside a soft part. This has not yet been attempted and predictions about the mechanical properties of bulk LSSR are difficult to make since they will greatly depend on how well adjacent LSSR layers will fuse.

These are just a few of the interesting possibilities that the LAMDA process could enable. Although some improvements still need to be made to the process and the printer hardware to realise its full potential, the LAMDA platform promises to provide manufacturing capabilities for complex, soft, multi-material parts that could not be

manufactured by traditional methods or by other 3D printing techniques in a comparable price range.

Chapter 6

Conclusions and outlook

6.1. Conclusions

We have proposed several new techniques for fabricating soft actuators and devices. Firstly, we showed that LSGO can be used to fabricate functional DEAs and other devices with highly intricate, precisely patterned electrodes. Secondly, we investigated the possibility of direct laser scribing of silicone rubber to produce electrically conductive patterns on soft substrates. Thirdly, we have built a 3D printer capable of fabricating arbitrary, complex shapes from high-performance silicone rubber. Finally, we have introduced the LAMDA process, which combines 3D printing of silicone rubber with laser scribing to fabricate soft, functional, multi-material structures. All of these techniques are simple and use low-cost, easily accessible hardware, which will hopefully make them accessible to a wide community of researchers and enthusiasts and promote innovation in the field.

6.1.1. Laser-scribed graphene oxide

LSGO offers a simple and convenient way to produce high-quality electrodes for DEAs with arbitrary, complex patterns. It requires no pre-fabricated tools, making it an ideal method for research and prototyping. Electrodes are patterned in-situ on the soft substrate, thus reducing potential alignment errors and simplifying the process by eliminating additional transfer steps. DEAs with LSGO electrodes exhibited 19 % higher maximum actuation strain than comparable CG electrodes in our experiments (see Section 3.3.3), although experiments also showed that LSGO only remains

conductive up to ~40 % uniaxial strain and no direct experimental comparison with other common electrode materials such as carbon silicone composites was made.

The process for manufacturing LSGO DEAs, although partially automated, still requires a series of manual steps. Particularly the drying of the GO films takes a long time. This increases the time needed for a full prototyping cycle to about 48 h. Despite this limitation, the LSGO process can be a useful prototyping tool for soft robotics researchers. It is simpler and uses less-expensive hardware than other existing methods with comparable capabilities for patterning electrodes.[146,292] Compared to hand painting CG, which is still a very common method, LSGO can make cleaner, neater, more detailed electrodes that are more stable and less messy. This makes prototypes much easier to handle without the need for encapsulation. Because the laser scribing process is automated, it also has better repeatability than manual methods. Considering all these advantages, LSGO could, after some small refinements, be added to the Soft Robotics Toolkit[48] as a useful new tool that makes fabrication and prototyping of DEA devices easier and more accessible.

6.1.2. LAMDA printing

The LAMDA process is a uniquely simple and low-cost 3D printing process capable of fabricating soft, multi-material functional structures and devices. The printing process is fully automated and requires little preparation and post-processing. We have demonstrated LAMDA-printed devices such as capacitors (Section 5.4.3.4), sensors (Sections 4.6.5 and 5.4.3.6), dielectric (Section 5.4.3.7) and pneumatic actuators (Section 5.4.3.8). Thus, the LAMDA process fulfils the two main objectives of our research, as outlined in Section 1.2: It offers the capability to 3D print highly elastic silicone rubber and can also produce a conductive material to make functional, soft, multi-material devices. However, by using laser scribing instead of multi-material deposition, we chose a slightly different approach to achieve our objectives than originally intended.

Unfortunately, the performance of LAMDA devices is currently still very poor, particularly actuation performance of the DEAs (see Section 5.4.3.7). However, several shortcomings of the current process have been identified which could be mitigated

through minor hardware improvements, as outlined in Sections 4.8 and 5.6. Implementation of these changes could see great improvements in the performance of LAMDA devices. Fabrication of pneumatic actuators has been shown to work well, even with the current process, if certain design rules are followed (see Section 5.4.3.8).

Overall, the LAMDA process represents an exciting new approach to prototyping and fabrication of soft devices. Although it is not yet the powerful, reliable and convenient research tool that we envisioned, some further development could soon see it fulfil its great potential. The focus on low-cost hardware ensures that the LAMDA platform can be made widely accessible. This could make it into a very valuable research tool for soft robotics and related fields. Similar to how low-cost FFF printers have become ubiquitous in modern research labs, the LAMDA platform could become one of the essential tools for soft robotics research in the near future.

6.2. Outlook

6.2.1. Switchable materials

The key factor that enables our LSGO, LSSR and LAMDA processes is the use of switchable materials. In all three, a physical stimulus (laser) is used to selectively convert one material (GO or silicone) to another material with very different properties (LSGO or LSSR). The same fundamental principle is also used in other existing techniques such as SLA (see Section 2.5.4). There, a light is used as the stimulus to switch a material from a liquid to a solid state. In contrast, our work explores materials that can be switched between two solid states with different mechanical and electrical properties. In the LAMDA process, we have combined two stages of switching material: UV curing, which switches from liquid to solid, and laser-scribing, which switches from non-conductive to conductive.

Applying a physical stimulus such as a laser is much simpler and more precise than depositing a material. We have shown in Sections 5.3.3.2 and 5.3.3.3 that multi-material deposition is challenging and greatly increases the complexity and thereby also the cost of the required hardware. It is therefore no surprise that commercial DIW printers with multi-material capabilities, such as those shown in Section 2.5.2, are very expensive. In contrast, the use of switchable materials offers a unique opportunity to

achieve fabrication of functional, multi-material structures using very simple techniques and low-cost hardware. Although the materials for such a process will have to be very carefully formulated and meet very specific requirements, the fact that only a single material is needed could reduce overall material cost as well, compared to other systems where a range of different materials has to be purchased.

In our work so far, only two switchable materials have been explored: GO/LSGO and silicone/LSSR. Neither of the two has the ideal properties for 3D printing of soft devices. GO works well as a switchable material for compliant electrodes, as shown in Chapter 3. However, GO itself is not elastic so it cannot serve as the primary material for printing of soft structures. Silicone rubber, on the other hand, is soft and highly elastic, and also well suited for 3D printing. However, the resulting LSSR is very brittle and therefore not very suitable for the fabrication of compliant electrodes. Despite these shortcomings, we were able to demonstrate printing of functional, soft devices using our LAMDA process. This already demonstrates the great potential of switchable materials in manufacturing. If other switchable materials with more desirable properties can be found, the capabilities of the LAMDA process could increase greatly.

LSGO and LSSR are just two examples of switchable materials. Laser-induced graphene (see Section 2.6.2) is another. Future research could reveal many more such materials with different properties that can undergo different changes in response to different stimuli. The LAMDA process and other novel techniques such as the SMaLL process (see Section 2.5.4) already make use of two different stimuli to trigger two distinct transitions. It may be possible to extend this capability further and formulate materials that respond in different ways to a large number of stimuli and produce a whole palette of different materials from just a single starting material. This represents a completely new paradigm in additive manufacturing where, rather than adding materials, we can selectively add specific properties to a material in certain places to create functional structures. This approach could allow similar flexibility with regard to material properties as inkjet-printed "digital materials" (see Section 2.5.3) but would achieve this with a much simpler system and less-expensive hardware, which can greatly amplify its potential impact.

6.2.2. Designing without constraints

Our vision for the LAMDA system, or its successor, is the realisation of a reliable, automated additive manufacturing process capable of producing soft multi-material parts with a great range of different properties and functions. Such a process could revolutionise our current approach to soft robotics manufacturing. As discussed in Sections 2.2.3 and 2.4, current soft devices are often limited in their capabilities by the available manufacturing methods. A versatile 3D printing process for soft structures could remove many of the design constraints we currently face due to inadequate manufacturing. Lifting these constraints would allow a whole range of novel devices with new functions and unprecedented capabilities.

There are many recent examples of multi-material soft structures with interesting functionality, such as shape morphing elastomers,[51,52] soft actuators with a range of different motion profiles,[186] combinations of fluidic and dielectric actuators such as the HASEL actuator,[87] and even soft machines with integrated fluidic logic, as famously demonstrated in "Octobot".[44] Currently, fabrication of most of these structures still requires many different fabrication steps and involves a lot of manual tasks. At the same time, all of these examples were only possible through recent advances in manufacturing methods. A truly versatile multi-material printing process would greatly simplify the fabrication of such structures and allow even more complex devices with greater functionality to be made. Dielectric or pneumatics muscles, different types of sensors and even some amount of logic could all be integrated into the same printed part. That would enable printing of complete, functional, soft robots in a single, automated process.

The individual functional units would most likely not have the same performance as the same type of device made in a more specialised, dedicated fabrication process, and using materials optimised for the specific application. Some compromises will always need to be made to achieve greater versatility. However, functional structures could now be embedded and integrated into the bodies of soft robots in completely novel ways, in a process that is more akin to biological growth than traditional assembly. Such a technology could enable a new generation of soft robots with unprecedented

capabilities and bring us so much closer to the long-held dream of helpful robotic companions that assist us throughout our daily lives.

Appendix A

Appendix

A1. LSSR in the literature

Table 5. Laser-scribed silicone rubber reported in the literature. Process conditions and reported chemical composition of resulting LSSR are given.

Type of Laser	Wavelength	Exposure	Silicone material	LSSR composition	Application	Reference
CO_2, pulsed	9580 nm	10-750 kJ/m²	Wacker-M 3090	Reduced C/Si and increased O/Si ratios. Carbonate groups present.	Hydrophobic surface modification	Khorasani et al. 1996 [238]
Nd:YAG, pulsed	266 nm	5-20 kJ/m²	PDMS (custom formula)	Amorphous and graphitic carbon (more ordered), silicon, SiC, SiO_x, SiH and SiOH groups	Wettability modification (not demonstrated)	Graubner et al. 2006 [239]
KrF-excimer, pulsed	248 nm	10-40 kJ/m²	PDMS (custom formula)	Amorphous and graphitic carbon (less ordered), silicon, SiC, SiO_x, SiH and SiOH groups	Wettability modification (not demonstrated)	Graubner et al. 2006 [239]
Nd:YAG, pulsed	266 nm	20-30 kJ/m²	Statice Santé MED 4750	Si and SiC nanocrystals in amorphous matrix; matrix has reduced C/Si and increased O/Si ratios.	Surface preparation for Pt metallisation	Dupas-Bruzek et al. 2009 [240]
KrF-excimer, pulsed	248 nm	20-30 kJ/m²	Statice Santé MED 4750	Very few Si and SiC nanocrystals; amorphous and graphitic carbon,	Surface preparation for Pt metallisation	Dupas-Bruzek et al. 2009 [240]
Nd:Glass, pulsed	263 nm	7.5-22 kJ/m²	Statice Santé MED 4860	No Si crystals	Surface preparation for	Atanasov et al. 2016 [241]

					Ni metallisation	
Nd:Glass, pulsed	527 nm	7-32 kJ/m²	Statice Santé MED 4860	Si crystals	Surface preparation for Ni metallisation	Atanasov et al. 2016 [241]
Nd:Glass, pulsed	1055 nm	8-40 kJ/m²	Statice Santé MED 4860	Si crystals, amorphous and graphitic carbon	Surface preparation for Ni metallisation	Atanasov et al. 2016 [241]
Diode, pulsed or continuous	785 nm	150-800 W/m² (dwell time not specified)	Dow Corning Sylgard® 184 with carbon nanoparticles	Carbon nanocrystals, no SiC or SiOC	Laser-etched waveguides	Hautefeuille et al. 2013 [243]
Diode, pulsed or continuous	785 nm	300-800 W/m² (dwell time not specified)	Dow Corning Sylgard® 184 with carbon nanoparticles	Graphitic nanocrystals, carbon nanotubes, no silica	Fluorescent nanocrystal production	Alcántara et al. 2015 [244]
Diode laser, continuous	780 nm	3-3.75 J/m²?	Dow Corning Sylgard® 184 with carbon nanoparticles	Amorphous and crystalline carbon domains; no SiC or SiOC	Fluorescent nanocrystal production	González-Vázquez & Hautefeuille 2017 [245]
Diode laser, continuous	780 nm	0.16-43 MJ/m²	Dow Corning Sylgard® 184 with carbon nanoparticles	(no discussion of residue)	Microfluidic channels	Cruz-Ramírez et al. 2018 [260]
CO_2, pulsed	9400-10600 nm (not specified)	2.8-3.6 W (exposure not specified)	Dow Corning Sylgard® 184	(no analysis performed)	Switchable wettability surface	Wang et al. 2018 [242]
Pumped semiconductor laser, continuous	532 nm	0.4-0.8 W (estimated 1.1-6.4 MJ/m²)	Ecoflex® 00-30	Mostly SiC; formation of SiO_x at higher laser power	Conductive films for strain sensing	Gao et al. 2018 [247]

A2. Material data sheets

All data sheets are shown as received from the supplier. Only pages with relevant information on material properties and composition are included.

A2.1. ELASTOSIL® film technical data sheet

ULTRATHIN SILICONE FILM FOR HIGH-PRECISION SOLUTIONS

A New Product Form for Silicone Elastomers

ELASTOSIL® Film from WACKER is an ultrathin, high-precision film of crosslinked silicone rubber that is available in various layer thicknesses from 20 µm to > 400 µm and is manufactured under clean-room conditions entirely without solvents. The unique patent-pending manufacturing process produces immaculate, high-precision silicone film with a defined thickness that is impossible by other production processes. The maximum thickness variation across the film width is ±5%. This precision, combined with the proven properties of silicone rubber opens up potential applications that were hardly conceivable until now, and could certainly not be realized on an industrial scale.

ELASTOSIL® Film is especially impressive for its durability. Its outstanding dielectric properties, Young's modulus and rebound resilience remain constant over a wide range of temperatures and frequencies, as well as over millions of load cycles. Moreover, ELASTOSIL® Film is chemically inert and suitable for food contact. Like all silicone elastomers, ELASTOSIL® Film is characterized by selective permeability for gases and water vapor.

Diverse Applications

ELASTOSIL® Film is ideal for use as a dielectric precision layer in innovative, future-oriented electronics applications: so-called EAPs (electroactive polymers), especially in:

- Actuator technology ("artificial muscles")
- Electricity generation ("energy harvesting")
- Smart sensors

With its typical silicone properties, ELASTOSIL® Film can also be used in food packaging, technical textiles and an extremely wide variety of industrial applications.

Properties of ELASTOSIL® Film

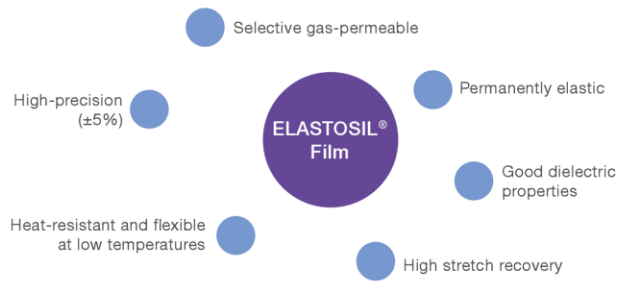

For applications in the medical sector and for wound dressing, ask about our biocompatible SILPURAN® Film.

Form of Delivery and Processing

ELASTOSIL® Film

- Produced under cleanroom conditions, currently on a pilot scale, at a width of 250 mm
- Available as sheet or roll stock on a support film, from which it can be easily stripped off for further processing
- Can be processed by conventional die-cutting or laser techniques
- Can be permanently and reliably bonded using silicone adhesive. Different grades are available for different applications. Ask us, and we will recommend one that is optimum for your application.

ELASTOSIL® Film 2030 Product Data	
Starting material	Addition-curing silicone rubber
Layer thickness	20 µm – 400 µm
Shore A (DIN 53505)	30
Elongation at break (ISO 527-3)	450%
Tear strength (ASTM D624 B)	10 N/mm
Glass transition temperature (Tg)	-126 °C
Operating range	-45 °C to 200 °C
Gas permeability (selectivity)	CO_2/N_2 1:100
Water vapor permeability (JIS 1099 A1)	3,000 g/m²/24 h at 20 µm
Compression set, 22 h, 100 °C (ISO 815-B)	5%
Permittivity ε_r	2.8
Dielectric strength (VDE 0303)	80 V/100µm
Volume resistivity (IEC 60093)	10^{14} Ω·cm
Suitable for food contact (BfR/FDA)[1]	Yes

[1] BfR recommendation:
„XV. Silicones" / FDA CFR 21 § 177.2600
„Rubber articles intended f. repeated use"

These figures are only intended as a guide and should not be used in preparing specifications.

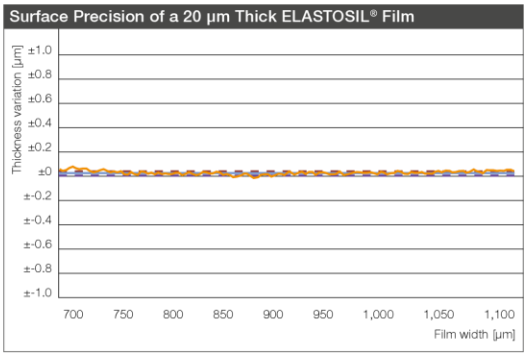

Thickness Precision

The ELASTOSIL® Film process produces films that are a fraction of the thickness of a human hair with state-of-art film thickness uniformity.

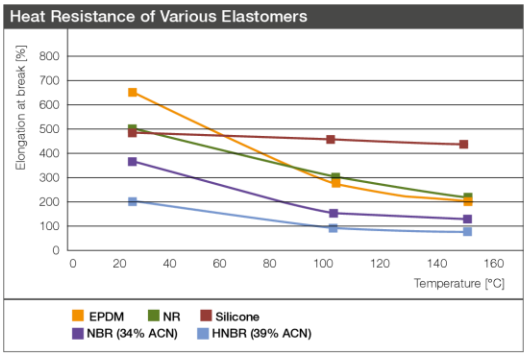

Elongation at Break

Silicones high elongation at break remains practically constant over a wide temperature range.

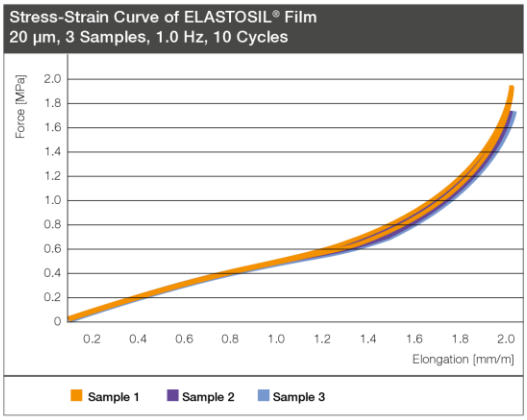

Elasticity and Resilience

ELASTOSIL® Film is highly elastic – permanently.

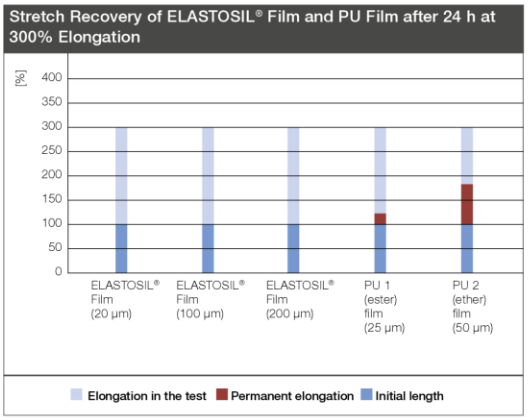

Stretch Recovery

Compared to other materials, silicone, and therefore ELASTOSIL® Film, has excellent elastic recovery.

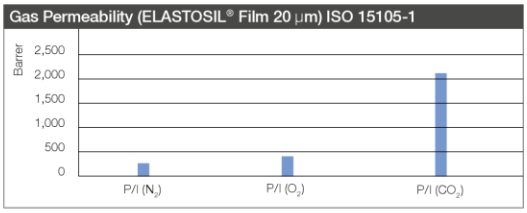

Gas Permeability and Selectivity

ELASTOSIL® Film is water repellent but selectively permeable to gases. This permeability is significantly higher than that of other polymers.

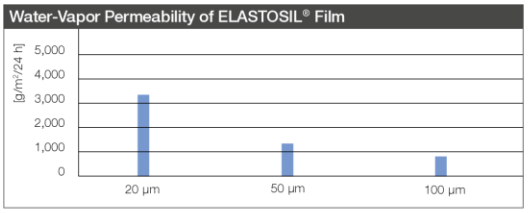

Water-Vapor Permeability

The water-vapor permeability of ELASTOSIL® film depends on the layer thickness.

A2.2. MOMENTIVE UV Electro technical data sheet

MOMENTIVE™ Marketing Bulletin

SILOPREN* UV Electro

LIQUID SILICONE RUBBER

Silopren UV Electro liquid silicone rubbers (LSR) belong to a new family of UV curable materials that can offer the benefit of high cure speed at room temperature in injection molding processes.

Silopren UV Electro LSRs are two-component liquid silicone rubbers with a mixing ratio of 100 to 2.

The processing of Silopren UV Electro LSRs is typically distinguished by:

- **Cure on demand**
- **Very fast curing by UV light at low temperatures**
- **Low clamping forces due to low cavity pressure**
- **Common UV curing systems**
- **Transparent mold materials**

Key Features and Typical Benefits

Vulcanizates consisting of Silopren UV Electro LSRs generally have features similar to conventional LSR materials such as:

- Excellent thermal stability
- High stability and flexibility at low temperatures
- Good rubber-like properties
- Long service life at dynamic stress
- High stability to ozone and ultraviolet light
- Excellent dielectric behavior over a wide range of temperatures
- Ability to be pigmented

Potential Applications

Because of their outstanding properties, Silopren UV Electro LSRs are excellent candidates to consider for use in the following elastomeric articles:

- High voltage plugs
- Cable joints
- Cable terminations
- Insulators

Typical Physical Properties

Typical Physical Properties of the Uncured Rubber

		Silopren UV Electro 235-2		Silopren UV Electro 225-1	
		Base	**Catalyst**	**Base**	**Catalyst**
Appearance		Colorless; translucent	Colorless; translucent	Colorless; translucent	Colorless; translucent
Viscosity in Pa•s gamma = $10s^{-1}$ at 20 °C	DIN 53018	120	10	70	10

The pot-life of the mixture of the two components (closed vessel) at 20 °C is usually one day in the absence of UV light. Increased temperatures reduce the pot-life of the mixture.

Typical Properties of the Vulcanizate

Mixing ratio of components Base : Catalyst = 100 : 2.
Laboratory Vulcanization Conditions: applied to UV light for 2 min at an intensity of 1 kW Power (Fe doted Hg bulb) and distance of 15 cm(1)

			Silopren UV Electro 235-2	Silopren UV UV Electro 225-1
Density	DIN 53 479 A	g/cm3	1.09	1.07
Shore A Hardness	DIN 53 505		35	25
Tensile Strength	DIN 53 504 S2	N/mm2	4.6	4.5
Elongation at Break	DIN 53 504 S2	%	520	580
Tear Strength	ASTM D 624 die B	N/mm	15	9
Tracking Resistance	IEC 60587	Class	1A 3.5	1A 3.5
Volume Resistivity	DIN IEC 60093	Ohm x cm	2.2 x 10^{13}	2.2 x 10^{13}
Dielectric Constant	IEC 60250 (50 Hz)		3.13	3.13
Dissipation Factor	IEC 60250 (50 Hz)		0.0013	0.0013
Dielectric Strength	DIN 53481	KV/mm	24	24

(1) The laboratory vulcanization conditions do not reflect the exposure to UV light during the processing; this time is only recommended for the static curing of slabs with UV light.
Typical data are average data and are not to be used as or to develop specifications.

*Silopren is a trademark of Bayer AG, used under license.

A2.3. MOMENTIVE UV Electro 225-1 Base MSDS

SAFETY DATA SHEET

FOR INDUSTRIAL USE ONLY

UV ELECTRO 225-1 BASE

Section 1. Product and company identification

Product name : UV ELECTRO 225-1 BASE
Chemical name : Silicone Rubber Compound

Manufacturer/Importer/ Distributor Information : Momentive - Performance Materials GmbH
Chempark Leverkusen
Leverkusen 05 51368

Contact person : MomentiveEMEA.productsteward@momentive.com

Telephone : General information
00800.4321.1000 (Customer Service Centre)

1.4
Emergency telephone number : Europe, Israel & All other: +44 (0) 1235239670; Middle East:+44 (0) 1235239671

Section 2. Hazards identification

Classification of the substance or mixture : TOXIC TO REPRODUCTION - Category 2

GHS label elements

Hazard pictograms :

Signal word : Warning
Hazard statements : H361fSuspected of damaging fertility.

Precautionary statements

General : Not applicable.

Prevention : Obtain special instructions before use.
Do not handle until all safety precautions have been read and understood.
Use personal protective equipment as required.

Response : IF exposed or concerned:
Get medical attention.

Storage : Store locked up.

Disposal : P501Dispose of contents and container in accordance with all local, regional, national and international regulations.

Other hazards which do not : None known.

result in classification

Section 3. Composition/information on ingredients

Substance/mixture : Mixture
Chemical name : Not available

Hazardous ingredients	% by weight	CAS number
Octamethylcyclotetrasiloxane	0.1 - 1	556-67-2

There are no additional ingredients present which, within the current knowledge of the supplier and in the concentrations applicable, are classified as hazardous to health or the environment and hence require reporting in this section.
Occupational exposure limits, if available, are listed in Section 8.

Section 4. First aid measures

Description of necessary first aid measures

Eye contact : Immediately flush eyes with plenty of water, occasionally lifting the upper and lower eyelids. Check for and remove any contact lenses. Continue to rinse for at least 10 minutes. Get medical attention if irritation occurs.

Inhalation : Remove victim to fresh air and keep at rest in a position comfortable for breathing. If not breathing, if breathing is irregular or if respiratory arrest occurs, provide artificial respiration or oxygen by trained personnel. It may be dangerous to the person providing aid to give mouth-to-mouth resuscitation. Get medical attention. If unconscious, place in recovery position and get medical attention immediately. Maintain an open airway. Loosen tight clothing such as a collar, tie, belt or waistband.

Skin contact : Flush contaminated skin with plenty of water. Remove contaminated clothing and shoes. Continue to rinse for at least 10 minutes. Get medical attention. Wash clothing before reuse. Clean shoes thoroughly before reuse.

Ingestion : Wash out mouth with water. Remove victim to fresh air and keep at rest in a position comfortable for breathing. If material has been swallowed and the exposed person is conscious, give small quantities of water to drink. Do not induce vomiting unless directed to do so by medical personnel. If vomiting occurs, the head should be kept low so that vomit does not enter the lungs. Get medical attention. Never give anything by mouth to an unconscious person. If unconscious, place in recovery position and get medical attention immediately. Maintain an open airway. Loosen tight clothing such as a collar, tie, belt or waistband.

Indication of immediate medical attention and special treatment needed, if necessary

Notes to physician : Treat symptomatically. Contact poison treatment specialist immediately if large quantities have been ingested or inhaled.

Specific treatments : No specific treatment.

Protection of first aid personnel : No action shall be taken involving any personal risk or without suitable training. It may be dangerous to the person providing aid to give mouth-to-mouth resuscitation.

See toxicological information (Section 11)

A2.4. MOMENTIVE UV LSR Cat MSDS

MOMENTIVE™

SAFETY DATA SHEET *according to Regulation (EC) No. 1907/2006*

UV LSR CAT

Version *1.0* Print Date 28.07.2014
Revision Date 03.11.2010 000000045738

1. IDENTIFICATION OF THE SUBSTANCE/MIXTURE AND OF THE COMPANY/UNDERTAKING

Trade name	:	UV LSR CAT
Usage	:	For industrial use only., Component in personal care products
Company	:	Momentive Performance Materials GmbH Chempark Leverkusen Gebaeude V7 DE - 51368 Leverkusen
Emergency telephone	:	Europe, Israel & All other: +44 (0) 1235239670; Middle East:+44 (0) 1235239671
Further information	:	+ 40 213044229
Environment, Health and Safety Department	:	MomentiveEMEA.productsteward@momentive.com

2. HAZARDS IDENTIFICATION

GHS Classification
Classification according to Regulation (EC) No 1272/2008 as amended:
Not classified

Labelling according to EC Directives

Further information : The product does not need to be labelled in accordance with EC directives or respective national laws.

67/548/EEC

3. COMPOSITION/INFORMATION ON INGREDIENTS

Chemical nature
Polydimethylsiloxane containing vinyl groups.

4. FIRST AID MEASURES

Inhalation : If breathed in, move person into fresh air. If symptoms persist, call a physician.

A2.5. CFS RTV 25 technical data sheet

Revision Date: 17/08/03

FLEXIL-S RTV 25C + 5% Catalyst S

1. DESCRIPTION

***Flexil-S* RTV 25C + 5% Catalyst S** is a two part silicone elastomer which cures at room temperature, to a flexible elastic 25 shore A material.

2. ADVANTAGES

- High elongation
- Good tear strength
- Precise reproduction
- Low shrinkage
- Option of a fast catalyst

3. APPLICATIONS

Suitable for the reproduction of models for scenery, restoration, fibrous plasterwork, palaeontology etc. Useable with thixotropic agents Additive TC and HTC for application by stiff brush or knife.

4. CHARACTERISTICS

a) CONSTITUENTS:

	RTV 25C	Catalyst S	Catalyst F
Appearance	Viscous fluid	Fluid	Fluid
Colour	Beige/White	Green	Yellow
Specific Gravity / gcm^{-3} @20 °C	1.27	1.00	1.00
Viscosity / cps	24,000	55	55

b) MIXING:

RTV + 5% Catalyst	Pot Life/mins	Demould/hours	Full Cure @ 20°C
Catalyst S Green	75	16-24	7 days
Catalyst F Yellow	15-30	2-4	10 hours

c) AFTER CROSSLINKING

Shore Hardness/A [ASTM D2 240 2mm film]	25
Tensile Strength/Mpa [DIN 53504]	4.1
Elongation at break/1% [DIN 53504]	450
Tear Strength KN/m [ASTMS D624 Notched Die B]	20
Linear Shrinkage	<0.5

A2.6. CFS RTV 25 MSDS

Revision Date: 03/10/04

FLEXIL-S RTV 25C

Silicone Rubber Base

1. IDENTIFICATION OF THE SUBSTANCE/PREPARATION AND THE COMPANY

Product Name:	Flexil-S RTV 25C
Chemical Name:	
Supplier:	Jacobson Chemicals Ltd Unit 4 Newman Lane Industrial Estate Alton, Hants GU34 2QR
Telephone:	01420 86934
Fax:	01420 549574
E-mail:	sales@jacobsonchemicals.co.uk

2. COMPOSITION

Substance:	No
Substance Name:	Mixture
EC Index No:	N/a
CAS Number:	391-00-00-09
EEC Number:	N/a

Constituents	Range	Haz Symt	Risk

No hazardous ingredients
Mixture of dimethylpolysiloxane and silane treated fillers.

3. HAZARD INDENTIFICATION

The most important hazards are:	Cause mild irritation to skin and eyes. Slipping hazard if allowed to spill.

4. FIRST AID MEASURES

Immediate medical attention:	No
Professional assistance from physician required?	No
Inhalation:	Treat symptomatically.
Skin Contact:	Remove soiled clothing. Wash affected areas with soap and water.
Eye Contact:	In case of contact, immediately flush with plenty of water for at least 15 minutes. Seek medical attention.
Ingestion:	Do not induce vomiting. Slowly dilute with 1-2 glasses of water or milk and seek medical attention.

A2.7. Smooth-On DragonSkin technical data sheet

Dragon Skin™ Series

Addition Cure Silicone Rubber Compounds

CERTIFIED ISO 10993-10 SKIN SAFE

SMOOTH-ON SINCE 1895

www.smooth-on.com

Cured Material Certified Skin Safe!

PRODUCT OVERVIEW

Dragon Skin™ silicones are high performance platinum cure liquid silicone compounds that are used for a variety of applications ranging from creating skin effects and other movie special effects to making production molds for casting a variety of materials. Because of the **superior physical properties** and flexibility of Dragon Skin™ rubbers, they are also used for medical prosthetics and cushioning applications. Dragon Skin™ rubbers are also used for a variety of industrial applications and have a service temperature range of a constant -65°F to +450°F (-53°C to +232°C).

Great for Making Molds for a Variety of Applications - Available in **Shore 10A, 20A and 30A**, Dragon Skin™ silicones can be used to make exceptionally strong and tear resistant molds for casting plaster, wax, concrete (limited production run), resins and other materials.

Time Tested, Versatile Special Effects Material – Soft, super-strong and stretchy, Dragon Skin™ 10 (**Very Fast, Fast, Medium and Slow speeds**) is used around the world to make spectacular skin and creature effects. An infinite number of color effects can be achieved by adding Silc Pig™ silicone pigments or Cast Magic™ effects powders. Cured rubber can also be painted with the Psycho Paint™ system. Cured material is skin safe and certified by an independent laboratory to ISO 10993-10, Biological evaluation of medical devices, Part 10: Tests for irritation and skin sensitization.

Easy To Use – Dragon Skin™ silicones are mixed 1A:1B by weight or volume. Liquid rubber can be thinned with Silicone Thinner™ or thickened with THI-VEX™. Rubber cures at room temperature (73°F/23°C) with negligible shrinkage. ***Vacuum degassing is recommended to minimize air bubbles in cured rubber.***

TECHNICAL OVERVIEW

	Mixed Viscosity (ASTM D-2393)	Specific Gravity (g/cc) (ASTM D-1475)	Specific Volume (cu. in./lb.) (ASTM D-1475)	Pot Life (ASTM D-2471)	Cure Time	Shore A Hardness (ASTM D-2240)	Tensile Strength (ASTM D-412)	100% Modulus (ASTM D-412)	Elongation at Break % (ASTM D-412)	Die B Tear Strength (ASTM D-624)	Shrinkage (in./in.) (ASTM D-2566)
Dragon Skin™ 10 Very Fast	23,000 cps	1.07	25.8	4 min.	30 min.	10A	475 psi	22 psi	1000%	102 pli	< .001 in./in.
Dragon Skin™ 10 Fast	23,000 cps	1.07	25.8	8 min.	75 min.	10A	475 psi	22 psi	1000%	102 pli	< .001 in./in.
Dragon Skin™ 10 Medium	23,000 cps	1.07	25.8	20 min.	5 hours	10A	475 psi	22 psi	1000%	102 pli	< .001 in./in.
Dragon Skin™ 10 Slow	23,000 cps	1.07	25.8	45 min.	7 hours	10A	475 psi	22 psi	1000%	102 pli	< .001 in./in.
Dragon Skin™ 20	20,000 cps	1.08	25.6	25 min.	4 hours	20A	550 psi	49 psi	620%	120 pli	< .001 in./in.
Dragon Skin™ 30	30,000 cps	1.08	25.7	45 min.	16 hours	30A	500 psi	86 psi	364%	108 pli	< .001 in./in.

Mix Ratio: 1A:1B by volume or weight
Color: Translucent
Useful Temperature Range: -65°F to +450°F (-53°C to +232°C)
Dielectric Strength (ASTM D-147-97a)**:** >350 volts/mil

*All values measured after 7 days at 73°F/23°C

PROCESSING RECOMMENDATIONS

PREPARATION... Safety – Use in a properly ventilated area ("room size" ventilation). Wear safety glasses, long sleeves and rubber gloves to minimize contamination risk. Wear vinyl gloves only. Latex gloves will inhibit the cure of the rubber.

Store and use material at room temperature (73°F/23°C). Warmer temperatures will drastically reduce working time and cure time. Storing material at warmer temperatures will also reduce the usable shelf life of unused material. These products have a limited shelf life and should be used as soon as possible. Mixing containers should have straight sides and a flat bottom. Mixing sticks should be flat and stiff with defined edges for scraping the sides and bottom of your mixing container.

Cure Inhibition – Addition-cure silicone rubber may be inhibited by certain contaminants in or on the pattern to be molded resulting in tackiness at the pattern interface or a total lack of cure throughout the mold. Latex, tin-cure silicone, sulfur clays, certain wood surfaces, newly cast polyester, epoxy, tin cure silicone rubber or urethane rubber may cause inhibition. If compatibility between the rubber and the surface is a concern, a small-scale test is recommended. Apply a small amount of rubber onto a non-critical area of the pattern. Inhibition has occurred if the rubber is gummy or uncured after the recommended cure time has passed.

Because no two applications are quite the same, a small test application to determine suitability for your project is recommended if performance of this material is in question.

A2.8. Smooth-On Ecoflex technical data sheet

Ecoflex™ Series

Super-Soft, Addition Cure Silicone Rubbers

CERTIFIED TESTED SKIN SAFE

SMOOTH-ON SINCE 1896

www.smooth-on.com

Cured Material Certified Skin Safe!

PRODUCT OVERVIEW

Ecoflex™ rubbers are platinum-catalyzed silicones that are versatile and easy to use. **Ecoflex™** rubbers are mixed 1A:1B by weight or volume and cured at room temperature with negligible shrinkage. Low viscosity ensures easy mixing and de-airing, or you can choose to mix and dispense using our convenient dispensing cartridges. Cured rubber is very soft, very strong and very "stretchy", stretching many times its original size without tearing and will rebound to its original form without distortion. **Ecoflex™** rubbers are water white translucent and can be color pigmented with Silc Pig™ pigments for creating a variety of color effects. You can also add Smooth-On's Silicone Thinner™ to further lower the viscosity. THI-VEX™ silicone thickener can be added by weight to Ecoflex™ silicones for brushable aplications.

Soft, Softer, Softest . . . **Ecoflex™** rubbers are based on Smooth-On's Dragon Skin™ technology and are currently available in four different hardness': Shore A-5, Shore 00-10, 00-20, 00-30 and 00-50. They are suitable for a variety of applications including making prosthetic appliances, cushioning for orthotics and special effects applications (especially in animatronics where repetitive motion is required). **Ecoflex™ 5** has a pot life of 1 minute and a demold time of 5 minutes – Available only in dispensing cartridges.

Note: Ecoflex™ 00-10 cures with a "tacky" surface. Cured **Ecoflex™ 00-30 is skin safe** and certified by an independent laboratory to ISO 10993-10, cured **Ecoflex™ 00-20 is skin safe** and certified by an independent laboratory to OECD TG 439.

TECHNICAL OVERVIEW

	Mixed Viscosity (ASTM D-2393)	Specific Gravity (g/cc) (ASTM D-1475)	Specific Volume (cu. in./lb.) (ASTM D-1475)	Pot Life (ASTM D-2471)	Cure Time	Shore Hardness (ASTM D-2240)	Tensile Strength (ASTM D-412)	100% Modulus (ASTM D-412)	Elongation at Break % (ASTM D-412)	Die B Tear Strength (ASTM D-624)	Shrinkage (in./in.) (ASTM D-2566)
Ecoflex™ 5	13,000 cps	1.07	25.8	1 min.	5 min.	5A	350 psi	15 psi	1000%	75 pli	< .001 in./in.
Ecoflex™ 00-50	8,000 cps	1.07	25.9	18 min.	3 hours	00-50	315 psi	12 psi	980%	50 pli	< .001 in./in.
Ecoflex™ 00-30	3,000 cps	1.07	26.0	45 min.	4 hours	00-30	200 psi	10 psi	900%	38 pli	< .001 in./in.
Ecoflex™ 00-20	3,000 cps	1.07	26.0	30 min.	4 hours	00-20	160 psi	8 psi	845%	30 pli	< .001 in./in.
Ecoflex™ 00-10	14,000 cps	1.04	26.6	30 min.	4 hours	00-10	120 psi	8 psi	800%	22 pli	< .001 in./in.

*All values measured after 7 days at 73°F/23°C

Mix Ratio: 1A:1B by volume or weight
Color: Translucent
Useful Temperature Range: -65°F to 450°F (-53°C to 232°C)
Dielectric Strength (ASTM D-147-97a)**:** >350 volts/mil

PROCESSING RECOMMENDATIONS

PREPARATION... Safety – Use in a properly ventilated area ("room size" ventilation). Wear safety glasses, long sleeves and rubber gloves to minimize contamination risk. Wear vinyl gloves only. Latex gloves will inhibit the cure of the rubber.

Store and use material at room temperature (73°F/23°C). Warmer temperatures will drastically reduce working time and cure time. Storing material at warmer temperatures will also reduce the usable shelf life of unused material. These products have a limited shelf life and should be used as soon as possible. Mixing containers should have straight sides and a flat bottom. Mixing sticks should be flat and stiff with defined edges for scraping the sides and bottom of your mixing container.

Cure Inhibition – Addition-cure silicone rubber may be inhibited by certain contaminants in or on the pattern to be molded resulting in tackiness at the pattern interface or a total lack of cure throughout the mold. Latex, tin-cure silicone, sulfur clays, certain wood surfaces, newly cast polyester, epoxy, tin cure silicone rubber or urethane rubber may cause inhibition. If compatibility between the rubber and the surface is a concern, a small-scale test is recommended. Apply a small amount of rubber onto a non-critical area of the pattern. Inhibition has occurred if the rubber is gummy or uncured after the recommended cure time has passed.

Because no two applications are quite the same, a small test application to determine suitability for your project is recommended if performance of this material is in question.

To prevent inhibition, one or more coatings of a clear acrylic lacquer applied to the model surface is usually effective. Allow any sealer to thoroughly dry before applying rubber. Note: Even with a sealer, platinum silicones will not work with modeling clays containing heavy amounts of sulfur. Do a small scale test for compatibility before using on your project.

A3. CAD models and technical drawings

A3.1. Printer steel frame (P3Steel)

The frame design is based on the P3Steel version 2.5 designed by AndrewBCN (reprap.org/wiki/P3Steel). The frame was purchased from Orballo Printing (Spain). CAD assembly by Phil Maddox (grabcad.com/library/prusa-i3-steel-laser-cut-stainless-steel-2-5-dxl-1).

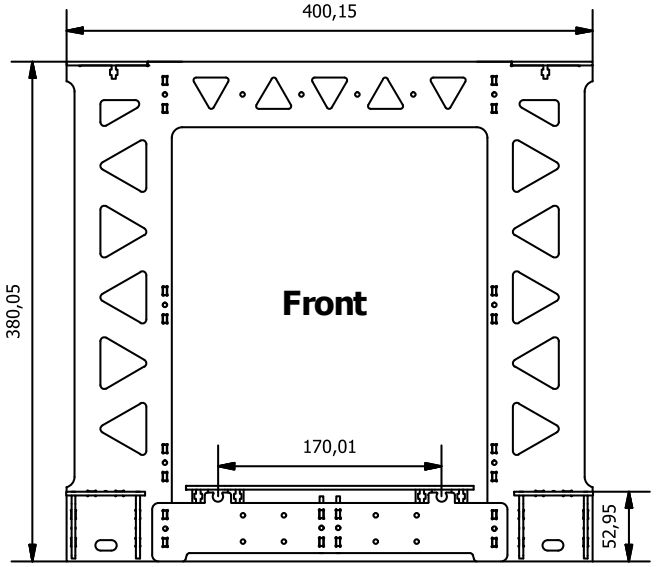

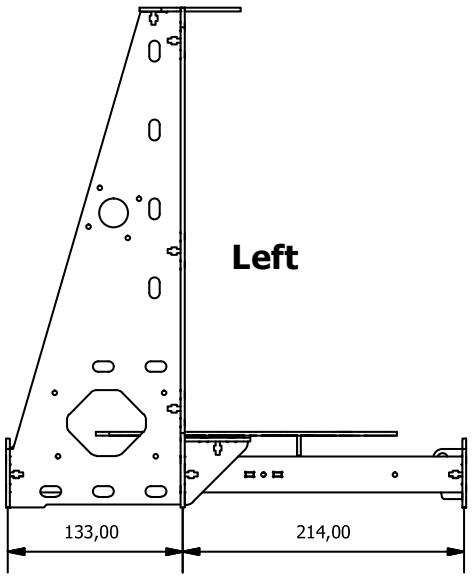

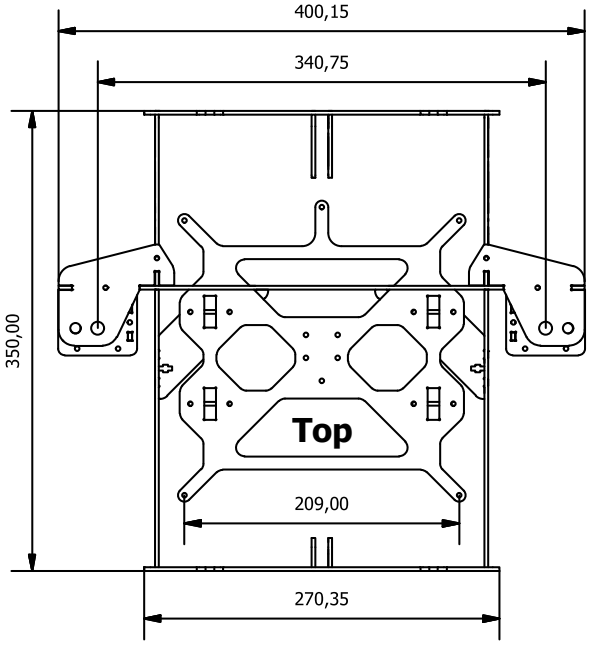

A3.2. Printer enclosure

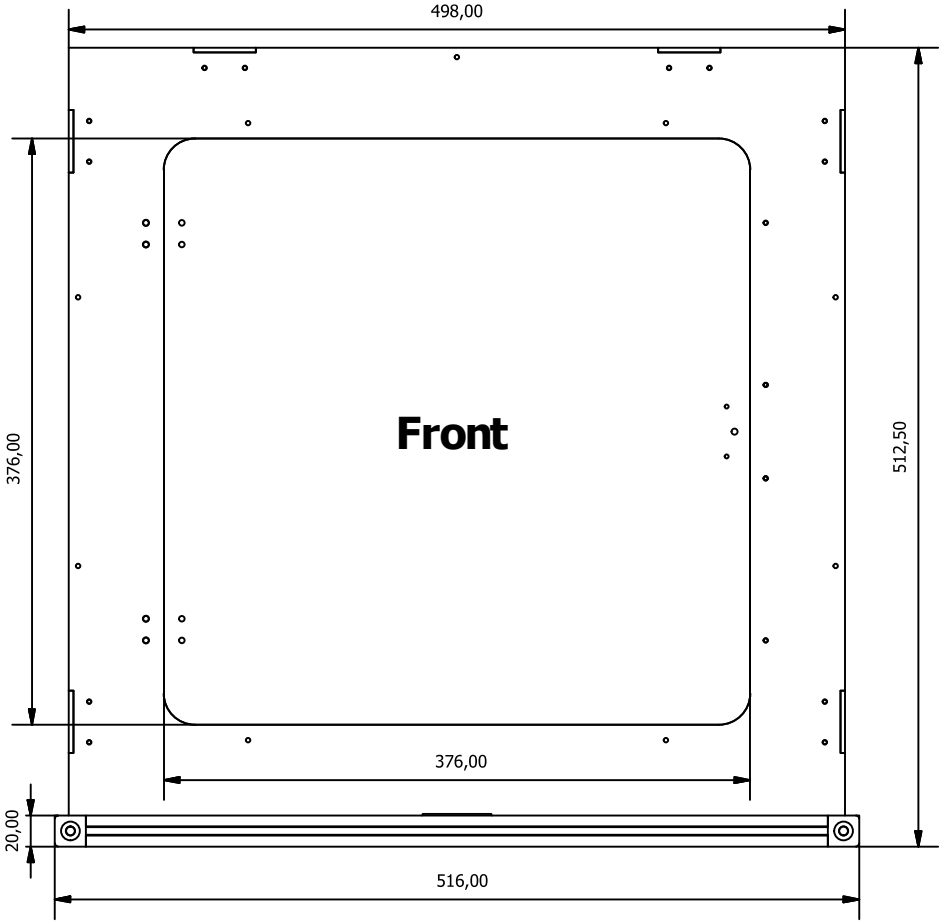

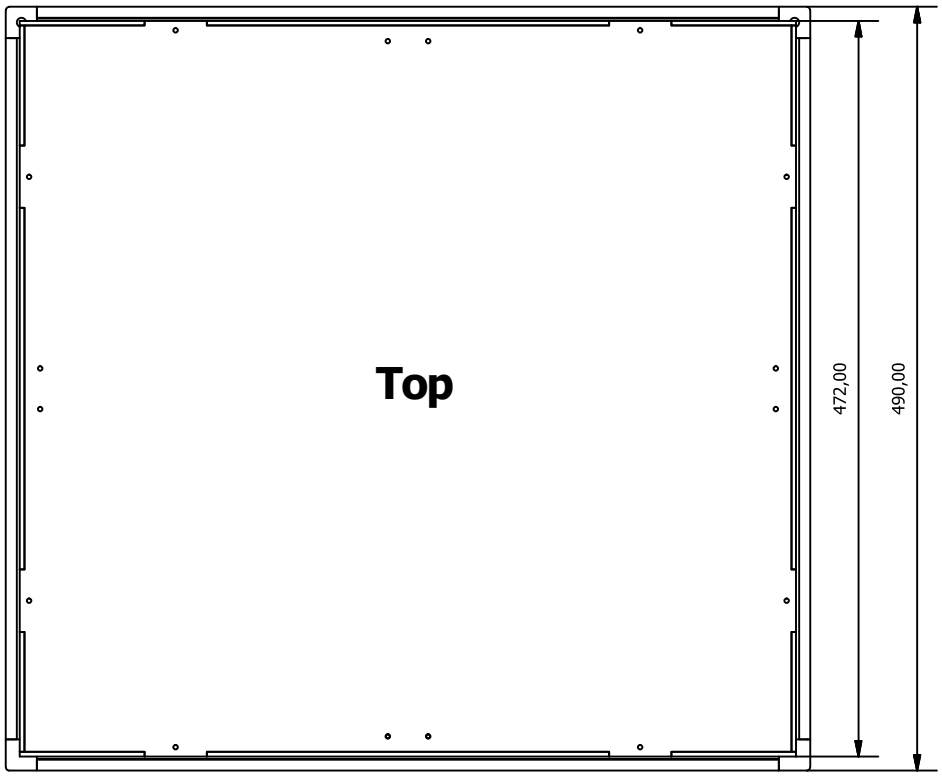

A3.3. LAMDA print head

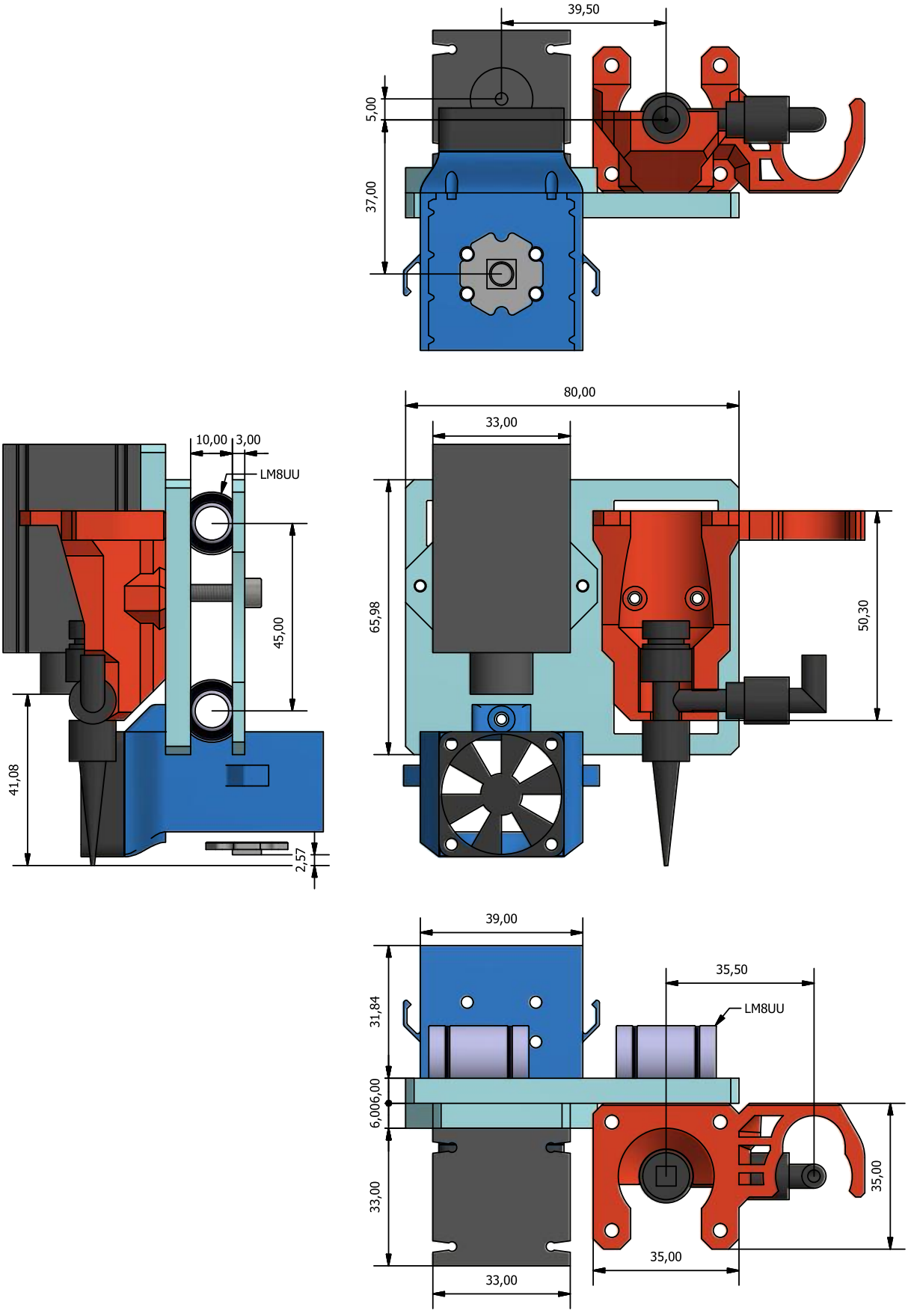

Bibliography

1. Behnke, S. Humanoid Robots – From Fiction to Reality ? *KI-Zeitschrift* **4**, 5–9 (2008).

2. Kemp, C. C., Edsinger, A. & Torres-Jara, E. Challenges for robot manipulation in human environments [Grand challenges of robotics]. *IEEE Robot. Autom. Mag.* **14**, 20–29 (2007).

3. Zinn, M., Roth, B., Khatib, O. & Salisbury, J. K. A New Actuation Approach for Human Friendly Robot Design. *Int. J. Rob. Res.* **23**, 379–398 (2004).

4. Kim, S., Laschi, C. & Trimmer, B. Soft robotics: a bioinspired evolution in robotics. *Trends Biotechnol.* **31**, 287–294 (2013).

5. Laschi, C., Mazzolai, B. & Cianchetti, M. Soft robotics: Technologies and systems pushing the boundaries of robot abilities. *Sci. Robot.* **1**, eaah3690 (2016).

6. Rossiter, J. & Hauser, H. Soft Robotics - The Next Industrial Revolution? [Industrial Activities]. *IEEE Robot. Autom. Mag.* **23**, 17–20 (2016).

7. Polygerinos, P. *et al.* Soft Robotics: Review of Fluid-Driven Intrinsically Soft Devices; Manufacturing, Sensing, Control, and Applications in Human-Robot Interaction. *Adv. Eng. Mater.* **19**, 1700016 (2017).

8. Laschi, C. & Mazzolai, B. Lessons from Animals and Plants: The Symbiosis of Morphological Computation and Soft Robotics. *IEEE Robot. Autom. Mag.* **23**, 107–114 (2016).

9. Mirvakili, S. M. & Hunter, I. W. Artificial Muscles: Mechanisms, Applications, and Challenges. *Adv. Mater.* **30**, 1–28 (2018).

10. Carpi, F., De Rossi, D., Kornbluh, R., Pelrine, R. & Sommer-Larsen, P. Dielectric Elastomers as Electromechanical Transducers. (2008).

11. KIER, W. M. & SMITH, K. K. Tongues, tentacles and trunks: the biomechanics of movement in muscular-hydrostats. *Zool. J. Linn. Soc.* **83**, 307–324 (1985).

12. Maas, J., Tepel, D. & Hoffstadt, T. Actuator design and automated manufacturing process for DEAP-based multilayer stack-actuators. *Meccanica* **50**, 2839–2854 (2015).

13. Tondu, B. Modelling of the McKibben artificial muscle: A review. *J. Intell. Mater. Syst. Struct.* **23**, 225–253 (2012).

14. Sugiyama, Y. & Hirai, S. Crawling and jumping of deformable soft robot. in *IEEE/RSJ International Conference on Intelligent Robots and Systems (IROS)* **4**, 3276–3281 (IEEE, 2004).

15. Menciassi, A., Gorini, S., Pernorio, G. & Dario, P. A SMA actuated artificial earthworm. in *IEEE International Conference on Robotics and Automation (ICRA)* 3282-3287 Vol.4 (IEEE, 2004). doi:10.1109/ROBOT.2004.1308760

16. Shepherd, R. F. *et al.* Multigait soft robot. *Proc. Natl. Acad. Sci.* **108**, 20400–20403 (2011).

17. Ilievski, F., Mazzeo, A. D., Shepherd, R. F., Chen, X. & Whitesides, G. M. Soft robotics for chemists. *Angew. Chemie - Int. Ed.* **50**, 1890–1895 (2011).

18. Petralia, M. T. & Wood, R. J. Fabrication and analysis of dielectric-elastomer minimum-energy structures for highly-deformable soft robotic systems. in *IEEE/RSJ International Conference on Intelligent Robots and Systems (IROS)* 2357–2363 (IEEE, 2010). doi:10.1109/IROS.2010.5652506

19. Polygerinos, P., Wang, Z., Galloway, K. C., Wood, R. J. & Walsh, C. J. Soft robotic glove for combined assistance and at-home rehabilitation. *Rob. Auton. Syst.* **73**, 135–143 (2015).

20. Matysek, M., Lotz, P., Winterstein, T. & Schlaak, H. F. Dielectric elastomer actuators for tactile displays. in *World Haptics 2009 - Third Joint EuroHaptics conference and Symposium on Haptic Interfaces for Virtual Environment and Teleoperator Systems* 290–295 (IEEE, 2009). doi:10.1109/WHC.2009.4810822

21. Boys, H., Frediani, G., Poslad, S., Busfield, J. & Carpi, F. A dielectric elastomer actuator-based tactile display for multiple fingertip interaction with virtual soft bodies. in *Electroactive Polymer Actuators and Devices (EAPAD)* (ed. Bar-Cohen, Y.) 101632D (2017). doi:10.1117/12.2259957

22. Ranzani, T., Gerboni, G., Cianchetti, M. & Menciassi, A. A bioinspired soft manipulator for minimally invasive surgery. *Bioinspir. Biomim.* **10**, 035008 (2015).

23. Shintake, J., Cacucciolo, V., Floreano, D. & Shea, H. Soft Robotic Grippers. *Adv. Mater.* **30**, 1707035 (2018).

24. Arienti, A., Calisti, M., Giorgio-Serchi, F. & Laschi, C. PoseiDRONE: Design of a soft-bodied ROV with crawling, swimming and manipulation ability. in *2013 OCEANS - San Diego* (IEEE, 2013).

25. Sangbae Kim *et al.* Smooth Vertical Surface Climbing With Directional Adhesion. *IEEE Trans. Robot.* **24**, 65–74 (2008).

26. Bauer, S. *et al.* 25th Anniversary Article: A Soft Future: From Robots and Sensor Skin to Energy Harvesters. *Adv. Mater.* **26**, 149–162 (2014).

27. Brown, E. *et al.* Universal robotic gripper based on the jamming of granular material. *Proc. Natl. Acad. Sci.* **107**, 18809–18814 (2010).

28. Shintake, J., Rosset, S., Schubert, B., Floreano, D. & Shea, H. Versatile soft grippers with intrinsic electroadhesion based on multifunctional polymer actuators. *Adv. Funct. Mater.* 1–28 (2015). doi:10.1002/adma.201504264

29. Amend, J. R., Brown, E. M., Rodenberg, N., Jaeger, H. M. & Lipson, H. A Positive Pressure Universal Gripper Based on the Jamming of Granular Material. (2011). doi:10.1109/TRO.2011.2171093

30. Helps, T., Taghavi, M., Manns, S., Turton, A. J. & Rossiter, J. Easy undressing with soft robotics. in *Towards Autonomous Robotic Systems (TAROS)* **10965 LNAI**, 79–90 (Springer, Cham, 2018).

31. Maffli, L., Rosset, S., Ghilardi, M., Carpi, F. & Shea, H. Ultrafast All-Polymer Electrically Tunable Silicone Lenses. *Adv. Funct. Mater.* **25**, 1656–1665 (2015).

32. Knoop, L. E. & Rossiter, J. Towards shear tactile displays with DEAs. in *Electroactive Polymer Actuators and Devices (EAPAD)* (ed. Bar-Cohen, Y.) 905610 (2014). doi:10.1117/12.2044572

33. Lee, H. S. *et al.* Design analysis and fabrication of arrayed tactile display based on dielectric elastomer actuator. *Sensors Actuators A Phys.* **205**, 191–198 (2014).

34. Duduta, M., Clarke, D. R. & Wood, R. J. A high speed soft robot based on dielectric elastomer actuators. in *IEEE International Conference on Robotics and Automation (ICRA)* 4346–4351 (IEEE, 2017). doi:10.1109/ICRA.2017.7989501

35. Kim, S. *et al.* Micro artificial muscle fiber using NiTi spring for soft robotics. in *2009 IEEE/RSJ International Conference on Intelligent Robots and Systems* 2228–2234 (IEEE, 2009). doi:10.1109/IROS.2009.5354178

36. Kühnel, D. T., Helps, T. & Rossiter, J. Kinematic Analysis of VibroBot: A Soft, Hopping Robot with Stiffness- and Shape-Changing Abilities. *Front. Robot. AI* **3**, 60 (2016).

37. Shepherd, C. *et al.* Using Explosions to Power a Soft Robot. *Angew. Chemie* **125**, 2964–2968

38. Bartlett, N. W. *et al.* A 3D-printed, functionally graded soft robot powered by combustion. *Science* **349**, 161–165 (2015).

39. Tolley, M. T. *et al.* An untethered jumping soft robot. in *IEEE/RSJ International Conference on Intelligent Robots and Systems (IROS)* 561–566 (IEEE, 2014). doi:10.1109/IROS.2014.6942615

40. Berlinger, F. *et al.* A Modular Dielectric Elastomer Actuator to Drive Miniature Autonomous Underwater Vehicles. in *IEEE International Conference on Robotics and Automation (ICRA)* 3429–3435 (IEEE, 2018). doi:10.1109/ICRA.2018.8461217

41. Tolley, C. *et al.* A Resilient, Untethered Soft Robot. *Soft Robot.* **1**, 213–223 (2014).

42. Rich, S. I., Wood, R. J. & Majidi, C. Untethered soft robotics. *Nat. Electron.* **1**, 102–112 (2018).

43. Cao, J. *et al.* Untethered soft robot capable of stable locomotion using soft electrostatic actuators. *Extrem. Mech. Lett.* **21**, 9–16 (2018).

44. Wehner, M. *et al.* An integrated design and fabrication strategy for entirely soft, autonomous robots. *Nature* **536**, 451–455 (2016).

45. Josephson, R. Contraction Dynamics and Power Output of Skeletal Muscle. *Annu. Rev. Physiol.* **55**, 527–546 (1993).

46. Chou, C. P. & Hannaford, B. Measurement and modeling of McKibben pneumatic artificial muscles. *IEEE Trans. Robot. Autom.* **12**, 90–102 (1996).

47. FESTO. Fluidic Muscle DMSP. Available at: https://www.festo.com/cat/en-gb_gb/data/doc_engb/PDF/EN/DMSP_EN.PDF. (Accessed: 15th October 2018)

48. Soft Robotics Toolkit | Actuators. Available at: https://softroboticstoolkit.com/actuators. (Accessed: 15th October 2018)

49. Klute, G. K., Czerniecki, J. M. & Hannaford, B. Artificial Muscles: Actuators for Biorobotic Systems. *Int. J. Rob. Res.* **21**, 295–309 (2002).

50. Yang, D. *et al.* Buckling Pneumatic Linear Actuators Inspired by Muscle. *Adv. Mater. Technol.* **1**, 1600055 (2016).

51. Siéfert, E., Reyssat, E., Bico, J. & Roman, B. Bio-inspired pneumatic shape-morphing elastomers. *Nat. Mater.* **18**, 24–28 (2018).

52. Pikul, J. H. *et al.* Stretchable surfaces with programmable 3D texture morphing for synthetic camouflaging skins. *Science* **358**, 210–214 (2017).

53. Mosadegh, B. *et al.* Pneumatic Networks for Soft Robotics that Actuate Rapidly. *Adv. Funct. Mater.* **24**, 2163–2170 (2014).

54. Niu, D. *et al.* Reversible Bending Behaviors of Photomechanical Soft Actuators Based on Graphene Nanocomposites. *Sci. Rep.* **6**, 27366 (2016).

55. Hu, Y. *et al.* A Graphene-Based Bimorph Structure for Design of High Performance Photoactuators. *Adv. Mater.* **27**, 7867–7873 (2015).

56. Haines, C. S. *et al.* Artificial Muscles from Fishing Line and Sewing Thread. *Science* **343**, 868–872 (2014).

57. Lima, M. D. *et al.* Electrically, Chemically, and Photonically Powered Torsional and Tensile Actuation of Hybrid Carbon Nanotube Yarn Muscles. *Science* **338**, 928–932 (2012).

58. Mohd Jani, J., Leary, M., Subic, A. & Gibson, M. A. A review of shape memory alloy research, applications and opportunities. *Mater. Des.* **56**, 1078–1113 (2014).

59. Koh, J. Design of Shape Memory Alloy Coil Spring Actuator for Improving Performance in Cyclic Actuation. *Materials (Basel).* **11**, 2324 (2018).

60. Seok, S., Onal, C. D., Wood, R., Rus, D. & Kim, S. Peristaltic locomotion with antagonistic actuators in soft robotics. in *Proceedings - IEEE International Conference on Robotics and Automation* 1228–1233 (IEEE, 2010). doi:10.1109/ROBOT.2010.5509542

61. Laschi, C. *et al.* Soft Robot Arm Inspired by the Octopus. *Adv. Robot.* **26**, 709–727 (2012).

62. Lin, H.-T., Leisk, G. G. & Trimmer, B. GoQBot: a caterpillar-inspired soft-bodied rolling robot. *Bioinspir. Biomim.* **6**, 026007 (2011).

63. Pelrine, R. *et al.* Dielectric elastomers: generator mode fundamentals and applications. in (ed. Bar-Cohen, Y.) **4329**, 148 (International Society for Optics and Photonics, 2001).

64. Jung, K., Kim, K. J. & Choi, H. R. A self-sensing dielectric elastomer actuator. *Sensors Actuators, A Phys.* (2008). doi:10.1016/j.sna.2007.10.076

65. Pelrine, R., Kornbluh, R. & Kofod, G. High-strain actuator materials based on dielectric elastomers. *Adv. Mater.* **12**, 1223–1225 (2000).

66. Pelrine, R. *et al. High-field deformation of elastomeric dielectrics for actuators. Materials Science and Engineering C* **11**, (2000).

67. Heydt, R., Kornbluh, R., Eckerle, J. & Pelrine, R. Sound radiation properties of dielectric elastomer electroactive polymer loudspeakers. in (ed. Bar-Cohen, Y.) **6168**, 61681M (International Society for Optics and Photonics, 2006).

68. Ji, X. *et al.* Stretchable composite monolayer electrodes for low voltage dielectric elastomer actuators. *Sensors Actuators, B Chem.* **261**, 135–143 (2018).

69. Rosset, S. & Shea, H. R. Small, fast, and tough: Shrinking down integrated elastomer transducers. *Appl. Phys. Rev.* **3**, 031105 (2016).

70. Koh, S. J. A. *et al.* Mechanisms of large actuation strain in dielectric elastomers. *J. Polym. Sci. Part B Polym. Phys.* **49**, 504–515 (2011).

71. Keplinger, C., Kaltenbrunner, M., Arnold, N. & Bauer, S. Rontgen's electrode-free elastomer actuators without electromechanical pull-in instability. *Proc. Natl. Acad. Sci.* **107**, 4505–4510 (2010).

72. Carpi, F. *et al.* Standards for dielectric elastomer transducers. *Smart Mater. Struct.* **24**, 105025 (2015).

73. Ha, S. M., Yuan, W., Pei, Q., Pelrine, R. & Stanford, S. Interpenetrating Polymer Networks for High-Performance Electroelastomer Artificial Muscles. *Adv. Mater.* **18**, 887–891 (2006).

74. Brochu, P., Stoyanov, H., Niu, X. & Pei, Q. All-silicone prestrain-locked interpenetrating polymer network elastomers: free-standing silicone artificial muscles with improved performance and robustness. *Smart Mater. Struct.* **22**, 055022 (2013).

75. Niu, X. *et al.* Synthesizing a new dielectric elastomer exhibiting large actuation strain and suppressed electromechanical instability without prestretching. *J. Polym. Sci. Part B Polym. Phys.* **51**, 197–206 (2013).

76. Duduta, M., Wood, R. J. & Clarke, D. R. Multilayer Dielectric Elastomers for Fast, Programmable Actuation without Prestretch. *Adv. Mater.* **28**, 8058–8063 (2016).

77. Lotz, P., Matysek, M. & Schlaak, H. F. Fabrication and Application of Miniaturized Dielectric Elastomer Stack Actuators. *IEEE/ASME Trans. Mechatronics* **16**, 58–66 (2011).

78. Loverich, J. J., Kanno, I. & Kotera, H. Concepts for a new class of all-polymer micropumps. *Lab Chip* **6**, 1147 (2006).

79. McCoul, D. & Pei, Q. Tubular dielectric elastomer actuator for active fluidic control. *Smart Mater. Struct.* **24**, 105016 (2015).

80. Maffli, L., Rosset, S. & Shea, H. R. Zipping dielectric elastomer actuators: characterization, design and modeling. *Smart Mater. Struct.* **22**, 104013 (2013).

81. Giousouf, M. & Kovacs, G. Dielectric elastomer actuators used for pneumatic valve technology. *Smart Mater. Struct.* **22**, 104010 (2013).

82. Shintake, J., Rosset, S., Schubert, B. E., Floreano, D. & Shea, H. R. A Foldable Antagonistic Actuator. *IEEE/ASME Trans. Mechatronics* **20**, 1997–2008 (2015).

83. Kovacs, G., Lochmatter, P. & Wissler, M. An arm wrestling robot driven by dielectric elastomer actuators. *Smart Mater. Struct.* **16**, S306–S317 (2007).

84. Kovacs, G., Düring, L., Michel, S. & Terrasi, G. Stacked dielectric elastomer actuator for tensile force transmission. *Sensors Actuators A Phys.* **155**, 299–307 (2009).

85. StretchSense Ltd. StretchSense. Available at: https://www.stretchsense.com/. (Accessed: 21st October 2018)

86. SBM Offshore. *WAVE ENERGY CONVERTER CONCEPT DEVELOPMENT*. (2016).

87. Acome, E. *et al.* Hydraulically amplified self-healing electrostatic actuators with muscle-like performance. *Science* **359**, 61–65 (2018).

88. Veale, A. J., Xie, S. Q. & Anderson, I. A. Characterizing the Peano fluidic muscle and the effects of its geometry properties on its behavior. *Smart Mater. Struct.* **25**, 065013 (2016).

89. Kellaris, N., Gopaluni Venkata, V., Smith, G. M., Mitchell, S. K. & Keplinger, C. Peano-HASEL actuators: Muscle-mimetic, electrohydraulic transducers that linearly contract on activation. *Sci. Robot.* **3**, eaar3276 (2018).

90. Taghavi, M., Helps, T. & Rossiter, J. Electro-ribbon actuators and electro-origami robots. *Sci. Robot.* **3**, (2018).

91. Zhang, R., Iravani, P. & Keogh, P. S. Modelling dielectric elastomer actuators using higher order material characteristics. *J. Phys. Commun.* **2**, 045025 (2018).

92. Mullins, L. Softening of Rubber by Deformation. *Rubber Chem. Technol.* **42**, 339–362 (1969).

93. Smooth-On. Ecoflex™ Series Technical Bulletin. (2018). Available at: https://www.smooth-on.com/tb/files/ECOFLEX_SERIES_TB.pdf. (Accessed: 22nd October 2018)

94. Smooth-On. Dragon Skin Series Technical Bulletin. (2018). Available at: http://www.smooth-on.com/tb/files/DRAGON_SKIN_SERIES_TB.pdf. (Accessed: 6th October 2018)

95. Arkles, B., Goff, J. & Sikorsky, A. Ultra-High Elongation Silicone Elastomers. *Rubber World* (2016).

96. Meunier, L., Chagnon, G., Favier, D., Orgéas, L. & Vacher, P. Mechanical experimental characterisation and numerical modelling of an unfilled silicone rubber. *Polym. Test.* **27**, 765–777 (2008).

97. Calisti, M. *et al.* Study and fabrication of bioinspired Octopus arm mockups tested on a multipurpose platform. in *2010 3rd IEEE RAS & EMBS International Conference on Biomedical Robotics and Biomechatronics* 461–466 (IEEE, 2010). doi:10.1109/BIOROB.2010.5625959

98. Shintake, J., Cacucciolo, V., Shea, H. & Floreano, D. Soft Biomimetic Fish Robot Made of Dielectric Elastomer Actuators. *Soft Robot.* **5**, 466–474 (2018).

99. Poulin, A. *et al.* An ultra-fast mechanically active cell culture substrate. *Sci. Rep.* **8**, 9895 (2018).

100. Gerratt, A. P., Balakrisnan, B., Penskiy, I. & Bergbreiter, S. Batch fabricated bidirectional dielectric elastomer actuators. in *2011 16th International Solid-State Sensors, Actuators and Microsystems Conference* 2422–2425 (IEEE, 2011). doi:10.1109/TRANSDUCERS.2011.5969653

101. Lau, G.-K., Lim, H.-T., Teo, J.-Y. & Chin, Y.-W. Lightweight mechanical amplifiers for rolled dielectric elastomer actuators and their integration with bio-inspired wing flappers. *Smart Mater. Struct.* **23**, 025021 (2014).

102. Momentive. SILOPREN UV Electro Marketing Bulletin. **24**, 1–4

103. Wacker Chemie AG. *SEMICOSIL ® UV.*

104. Shin-Etsu Silicone. UV Cure RTV Silicone Rubbers. (2017). Available at: https://www.shinetsusilicone-global.com/catalog/pdf/UV-RTV_E.pdf. (Accessed: 23rd October 2018)

105. Wacker Chemie. New Horizons through innovative applications with Elastosil film. (2014). Available at: https://www.wacker.com/cms/media/publications/downloads/7091_EN.pdf. (Accessed: 13th June 2018)

106. Stratasys. TangoPlus Safety Data Sheet. (2017). Available at: http://www.stratasys.com/-/media/4261911BB0B348EC9D691AB956F17D7C.pdf. (Accessed: 12th November 2018)

107. spot-A materials. Spot-E MATERIAL SAFETY DATA SHEET. (2014). Available at: https://spotamaterials.com/wp/wp-content/uploads/2015/07/Spot-E_MSDS_tmp.pdf. (Accessed: 12th November 2018)

108. Formlabs. Flexible Photoreactive Resin for Form 1, Form 1+, Form 2 SAFETY DATA SHEET. (2016). Available at: https://formlabs.com/media/upload/Flexible-SDS_eSMv2T6.pdf. (Accessed: 12th November 2018)

109. Rossiter, J., Walters, P. & Stoimenov, B. Printing 3D dielectric elastomer actuators for soft robotics. in *SPIE Proc.* (eds. Bar-Cohen, Y. & Wallmersperger, T.) 72870H (2009). doi:10.1117/12.815746

110. Peele, B. N., Wallin, T. J., Zhao, H. & Shepherd, R. F. 3D printing antagonistic systems of artificial muscle using projection stereolithography. *Bioinspir. Biomim.* **10**, 055003 (2015).

111. Ge, L., Dong, L., Wang, D., Ge, Q. & Gu, G. A digital light processing 3D printer for fast and high-precision fabrication of soft pneumatic actuators. *Sensors Actuators A Phys.* **273**, 285–292 (2018).

112. Pelrine, R., Kornbluh, R., Pei, Q. & Joseph, J. High-speed electrically actuated elastomers with strain greater than 100%. *Science* **287**, 836–839 (2000).

113. 3M. VHB™ Tape Specialty Tapes Technical Data. (2015). Available at: http://multimedia.3m.com/mws/media/986695O/3m-vhb-tape-specialty-tapes.pdf. (Accessed: 13th June 2018)

114. McKay, T. G., Calius, E. & Anderson, I. A. The dielectric constant of 3M VHB: a parameter in dispute. in (eds. Bar-Cohen, Y. & Wallmersperger, T.) **7287**, 72870P (International Society for Optics and Photonics, 2009).

115. Kofod, G., Sommer-Larsen, P., Kornbluh, R. & Pelrine, R. Actuation Response of Polyacrylate Dielectric Elastomers. *J. Intell. Mater. Syst. Struct.* **14**, 787–793 (2003).

116. Huang, C. *et al.* Giant, voltage-actuated deformation of a dielectric elastomer under dead load. *Appl. Phys. Lett.* **100**, 041911 (2012).

117. Lau, C. ;, Heng, G.-K. ;, Ahmed, K.-R. S. ; & Shrestha, A. S. Dielectric elastomer fingers for versatile grasping and nimble pinching. *Appl. Phys. Lett.* **110**, 182906 (2017).

118. Christianson, C., Goldberg, N. N., Deheyn, D. D., Cai, S. & Tolley, M. T. Translucent soft robots driven by frameless fluid electrode dielectric elastomer actuators. *Sci. Robot.* **3**, eaat1893 (2018).

119. Tang, C., Li, B., Fang, H., Li, Z. & Chen, H. A speedy, amphibian, robotic cube: Resonance actuation by a dielectric elastomer. *Sensors Actuators A Phys.* **270**, 1–7 (2018).

120. Liu, Q., Chen, J., Li, Y. & Shi, G. High-Performance Strain Sensors with Fish-Scale-Like Graphene-Sensing Layers for Full-Range Detection of Human Motions. *ACS Nano* **10**, 7901–7906 (2016).

121. Yap, H. K., Ng, H. Y. & Yeow, C.-H. High-Force Soft Printable Pneumatics for Soft Robotic Applications. *Soft Robot.* **3**, 144–158 (2016).

122. Valentine, A. D. *et al.* Hybrid 3D Printing of Soft Electronics. *Adv. Mater.* **29**, 1703817 (2017).

123. Petit, L., Guiffard, B., Seveyrat, L. & Guyomar, D. Actuating abilities of electroactive carbon nanopowder/polyurethane composite films. *Sensors Actuators A* **148**, 105–110 (2008).

124. Shankar, R., Ghosh, T. K. & Spontak, R. J. Electroactive Nanostructured Polymers as Tunable Actuators. *Adv. Mater.* **19**, 2218–2223 (2007).

125. Zhang, F., Li, T. & Luo, Y. A new low moduli dielectric elastomer nano-structured composite with high permittivity exhibiting large actuation strain induced by low electric field. *Compos. Sci. Technol.* **156**, 151–157 (2018).

126. Cancarb Limited. Carbon Black Physical and Chemical Properties. Available at: http://www.cancarb.com/docs/pdf/Physical_Chemical_Properties.pdf. (Accessed: 28th November 2018)

127. Asbury Carbons. Asbury Ultra Fine / Ultra High Surface Area Graphite Technical Flyer. (2017). Available at: http://asbury.com/Current Tech Flyers/TF Ultra Fine Graphite.pdf. (Accessed: 29th November 2018)

128. Pelrine, R. E., Kornbluh, R. D. & Joseph, J. P. Electrostriction of polymer dielectrics with compliant electrodes as a means of actuation. *Sensors Actuators A Phys.* **64**, 77–85 (1998).

129. de Saint-Aubin, C. A., Rosset, S., Schlatter, S. & Shea, H. High-cycle electromechanical aging of dielectric elastomer actuators with carbon-based electrodes. *Smart Mater. Struct.* **27**, 074002 (2018).

130. Schlatter, S., Rosset, S. & Shea, H. Inkjet printing of carbon black electrodes for dielectric elastomer actuators. in *SPIE 2017* (ed. Bar-Cohen, Y.) 1016311 (2017). doi:10.1117/12.2258615

131. MG Chemicals. Technical Data Sheet 846 Carbon Conductive Grease. (2018). Available at: https://www.mgchemicals.com/downloads/tds/tds-846.pdf. (Accessed: 28th November 2018)

132. Rosset, S., O'brien, B. M. & Shea, H. R. The need for speed. (2012). doi:10.1117/12.914623

133. Rajamani, A., Grissom, M. D., Rahn, C. D. & Zhang, Q. Wound Roll Dielectric Elastomer Actuators: Fabrication, Analysis, and Experiments. *IEEE/ASME Trans. Mechatronics* **13**, 117–124 (2008).

134. Muth, J. T. *et al.* Embedded 3D Printing of Strain Sensors within Highly Stretchable Elastomers. *Adv. Mater.* **26**, 6307–6312 (2014).

135. MG Chemicals. Safety Data Sheet 846 Conductive Carbon Grease. (2017). Available at: https://www.mgchemicals.com/downloads/msds/01 English UK SDS/sds-846 en uk.pdf.

136. Rosset, S. & Shea, H. R. Flexible and stretchable electrodes for dielectric elastomer actuators. *Appl. Phys. A* **110**, 281–307 (2013).

137. Chemtronics. CircuitWorks Silver Conductive Grease CW7100. (2018). Available at: www.chemtronics.com. (Accessed: 7th December 2018)

138. Bozlar, M. *et al.* Dielectric elastomer actuators with elastomeric electrodes. *Appl. Phys. Lett.* **101**, 091907 (2012).

139. Zhang, R. *et al.* Strain sensing behaviour of elastomeric composite films containing carbon nanotubes under cyclic loading. *Compos. Sci. Technol.* **74**, 1–5 (2013).

140. Liu, H. *et al.* Electrically conductive strain sensing polyurethane nanocomposites with synergistic carbon nanotubes and graphene bifillers. *Nanoscale* **8**, 12977–12989 (2016).

141. Zheng, Y. *et al.* A highly stretchable and stable strain sensor based on hybrid carbon nanofillers/polydimethylsiloxane conductive composites for large human motions monitoring. *Compos. Sci. Technol.* **156**, 276–286 (2018).

142. Guan, L.-Z., Zhao, L., Wan, Y.-J. & Tang, L.-C. Three-dimensional graphene-based polymer nanocomposites: preparation, properties and applications. *Nanoscale* **10**, 14788–14811 (2018).

143. Araki, T., Nogi, M., Suganuma, K., Kogure, M. & Kirihara, O. Printable and Stretchable Conductive Wirings Comprising Silver Flakes and Elastomers. *IEEE Electron Device Lett.* **32**, 1424–1426 (2011).

144. Carpi, F., Salaris, C. & Rossi, D. De. Folded dielectric elastomer actuators. *Smart Mater. Struct.* **16**, S300–S305 (2007).

145. Poulin, A., Rosset, S. & Shea, H. Fully printed 3 microns thick dielectric elastomer actuator. in *SPIE 2016* (eds. Bar-Cohen, Y. & Vidal, F.) 97980L (2016). doi:10.1117/12.2218256

146. Araromi, O. A., Rosset, S. & Shea, H. R. High-Resolution, Large-Area Fabrication of Compliant Electrodes via Laser Ablation for Robust, Stretchable Dielectric Elastomer Actuators and Sensors. *ACS Appl. Mater. Interfaces* **7**, 18046–18053 (2015).

147. Liu, H. *et al.* Electrically conductive polymer composites for smart flexible strain sensors: a critical review. *J. Mater. Chem. C* **6**, 12121–12141 (2018).

148. Guo, S.-Z., Qiu, K., Meng, F., Park, S. H. & McAlpine, M. C. 3D Printed Stretchable Tactile Sensors. *Adv. Mater.* **29**, 1701218 (2017).

149. Shian, S., Diebold, R. M., McNamara, A. & Clarke, D. R. Highly compliant transparent electrodes. *Appl. Phys. Lett.* **101**, 061101 (2012).

150. Lee, P. *et al.* Highly Stretchable or Transparent Conductor Fabrication by a Hierarchical Multiscale Hybrid Nanocomposite. *Adv. Funct. Mater.* **24**, 5671–5678 (2014).

151. Keplinger, C. *et al.* Stretchable, Transparent, Ionic Conductors. *Science* **341**, 984–987 (2013).

152. Chen, B. *et al.* Highly Stretchable and Transparent Ionogels as Nonvolatile Conductors for Dielectric Elastomer Transducers. *ACS Appl. Mater. Interfaces* **6**, 7840–7845 (2014).

153. Wang, H. *et al.* Ionic Gels and Their Applications in Stretchable Electronics. *Macromol. Rapid Commun.* **39**, 1800246 (2018).

154. Bakarich, S. E., Panhuis, M. in het, Beirne, S., Wallace, G. G. & Spinks, G. M. Extrusion printing of ionic–covalent entanglement hydrogels with high toughness. *J. Mater. Chem. B* **1**, 4939 (2013).

155. Tian, K. *et al.* 3D Printing of Transparent and Conductive Heterogeneous Hydrogel-Elastomer Systems. *Adv. Mater.* **29**, 1604827 (2017).

156. Haghiashtiani, G., Habtour, E., Park, S. H., Gardea, F. & McAlpine, M. C. 3D printed electrically-driven soft actuators. *Extrem. Mech. Lett.* **21**, 1–8 (2018).

157. Wang, D. *et al.* Chemical formation of soft metal electrodes for flexible and wearable electronics. *Chem. Soc. Rev.* **47**, 4611–4641 (2018).

158. Verplancke, R., Bossuyt, F., Cuypers, D. & Vanfleteren, J. Thin-film stretchable electronics technology based on meandering interconnections: fabrication and mechanical performance. *J. Micromechanics Microengineering* **22**, 015002 (2012).

159. Kim, D.-H. *et al.* Materials and noncoplanar mesh designs for integrated circuits with linear elastic responses to extreme mechanical deformations. *Proc. Natl. Acad. Sci.* **105**, 18675–18680 (2008).

160. Kim, R.-H. *et al.* Waterproof AlInGaP optoelectronics on stretchable substrates with applications in biomedicine and robotics. *Nat. Mater.* **9**, 929–937 (2010).

161. Benslimane, M., Kiil, H.-E. & Tryson, M. J. Electromechanical properties of novel large strain PolyPower film and laminate components for DEAP actuator and sensor applications. in *Proc. SPIE* (ed. Bar-Cohen, Y.) **7642**, (2010).

162. Low, S. H. & Lau, G. K. Bi-axially crumpled silver thin-film electrodes for dielectric elastomer actuators. *Smart Mater. Struct.* **23**, 125021 (2014).

163. Rosset, S., Niklaus, M., Dubois, P. & Shea, H. R. Metal ion implantation for the fabrication of stretchable electrodes on elastomers. *Adv. Funct. Mater.* **19**, 470–478 (2009).

164. Rosset, S., Niklaus, M., Dubois, P. & Shea, H. R. Large-stroke dielectric elastomer actuators with ion-implanted electrodes. *J. Microelectromechanical Syst.* **18**, 1300–1308 (2009).

165. Niklaus, M. & Shea, H. R. Electrical conductivity and Young's modulus of flexible nanocomposites made by metal-ion implantation of polydimethylsiloxane: The relationship between nanostructure and macroscopic properties. *Acta Mater.* **59**, 830–840 (2011).

166. Liu, Y., Gao, M., Mei, S., Han, Y. & Liu, J. Ultra-compliant liquid metal electrodes with in-plane self-healing capability for dielectric elastomer actuators. *Appl. Phys. Lett.* **103**, 71101 (2013).

167. Tabatabai, A., Fassler, A., Usiak, C. & Majidi, C. Liquid-phase gallium-indium alloy electronics with microcontact printing. *Langmuir* **29**, 6194–6200 (2013).

168. Li, X. *et al.* Liquid Metal Droplets Wrapped with Polysaccharide Microgel as Biocompatible Aqueous Ink for Flexible Conductive Devices. *Adv. Funct. Mater.* **28**, 1804197 (2018).

169. Markvicka, E. J., Bartlett, M. D., Huang, X. & Majidi, C. An autonomously electrically self-healing liquid metal–elastomer composite for robust soft-matter robotics and electronics. *Nat. Mater.* **17**, 1–7 (2018).

170. Mohammed, M. G. & Kramer, R. All-Printed Flexible and Stretchable Electronics. *Adv. Mater.* **29**, 1604965 (2017).

171. Wang, X. & Liu, J. Recent Advancements in Liquid Metal Flexible Printed Electronics: Properties, Technologies, and Applications. *Micromachines* **7**, 206 (2016).

172. Calisti, M., Cianchetti, M., Manti, M., Corucci, F. & Laschi, C. Contest-Driven Soft-Robotics Boost: The RoboSoft Grand Challenge. *Front. Robot. AI* **3**, 55 (2016).

173. Crawford, R. J. & Kearns, M. P. *Practical Guide to Rotational Moulding.* (Smithers Rapra, 2012).

174. Truby, R. L. & Lewis, J. A. Printing soft matter in three dimensions. *Nature* **540**, 371–378 (2016).

175. ten Kate, J., Smit, G. & Breedveld, P. 3D-printed upper limb prostheses: a review. *Disabil. Rehabil. Assist. Technol.* **12**, 300–314 (2017).

176. Taghavi, M., Helps, T., Huang, B. & Rossiter, J. 3D-Printed Ready-To-Use Variable-Stiffness Structures. *IEEE Robot. Autom. Lett.* **3**, (2018).

177. Kuang, X. *et al.* 3D Printing of Highly Stretchable, Shape-Memory, and Self-Healing Elastomer toward Novel 4D Printing. *ACS Appl. Mater. Interfaces* **10**, 7381–7388 (2018).

178. Kong, Y. L. *et al.* 3D Printed Quantum Dot Light-Emitting Diodes. *Nano Lett.* **14**, 7017–7023 (2014).

179. Yirmibesoglu, O. D. *et al.* Direct 3D printing of silicone elastomer soft robots and their performance comparison with molded counterparts. in *2018 IEEE International Conference on Soft Robotics (RoboSoft)* 295–302 (IEEE, 2018). doi:10.1109/ROBOSOFT.2018.8404935

180. Robinson, S. S. *et al.* Integrated soft sensors and elastomeric actuators for tactile machines with kinesthetic sense. *Extrem. Mech. Lett.* **5**, 47–53 (2015).

181. Reid, J. A. *et al.* Accessible bioprinting: Adaptation of a low-cost 3D-printer for precise cell placement and stem cell differentiation. *Biofabrication* **8**, 025017 (2016).

182. RichRap. Universal Paste Extruder for 3D printers. (2012). Available at: https://www.thingiverse.com/thing:20733. (Accessed: 21st December 2018)

183. RepRap Wiki. Paste Extrusion. (2015). Available at: https://reprap.org/wiki/Paste_Extrusion. (Accessed: 21st December 2018)

184. Unfold ~fab. Road to better paste extrusion, episode 2: Auger Valves. (2012). Available at: http://unfoldfab.blogspot.com/2012/08/road-to-better-paste-extrusion-episode.html. (Accessed: 21st December 2018)

185. Sultan, S., Abdelhamid, H. N., Zou, X. & Mathew, A. P. CelloMOF: Nanocellulose Enabled 3D Printing of Metal-Organic Frameworks. *Adv. Funct. Mater.* 1805372 (2018). doi:10.1002/adfm.201805372

186. Schaffner, M. *et al.* 3D printing of robotic soft actuators with programmable bioinspired architectures. *Nat. Commun.* **9**, 878 (2018).

187. Kokkinis, D., Schaffner, M. & Studart, A. R. Multimaterial magnetically assisted 3D printing of composite materials. *Nat. Commun.* **6**, 8643 (2015).

188. Bakarich, S. E., Gorkin, R., Panhuis, M. in Het & Spinks, G. M. 4D Printing with Mechanically Robust, Thermally Actuating Hydrogels. *Macromol. Rapid Commun.* **36**, 1211–1217 (2015).

189. Wei, T.-S., Ahn, B. Y., Grotto, J. & Lewis, J. A. 3D Printing of Customized Li-Ion Batteries with Thick Electrodes. *Adv. Mater.* **30**, 1703027 (2018).

190. Gupta, M. K. *et al.* 3D Printed Programmable Release Capsules. *Nano Lett.* **15**, 5321–5329 (2015).

191. De Maria, C. *et al.* Design and Validation of an Open-Hardware Print-Head for Bioprinting Application. *Procedia Eng.* **110**, 98–105 (2015).

192. McCoul, D., Rosset, S., Schlatter, S. & Shea, H. Inkjet 3D printing of UV and thermal cure silicone elastomers for dielectric elastomer actuators. *Smart Mater. Struct.* **26**, 125022 (2017).

193. Stratasys. PolyJet 3D Printers Systems and Materials Overview. (2018). Available at: https://www.stratasys.com/-/media/files/printer-spec-sheets/polyjet-3d-printers-systems-materials-spec-sheet.pdf. (Accessed: 11th December 2018)

194. Gregory, D. A., Zhang, Y., Smith, P. J., Zhao, X. & Ebbens, S. J. Reactive Inkjet Printing of Biocompatible Enzyme Powered Silk Micro-Rockets. *Small* **12**, 4048–4055 (2016).

195. Wilson, W. C. & Boland, T. Cell and organ printing 1: Protein and cell printers. *Anat. Rec.* **272A**, 491–496 (2003).

196. Waasdorp, R., van den Heuvel, O., Versluis, F., Hajee, B. & Ghatkesar, M. K. Accessing individual 75-micron diameter nozzles of a desktop inkjet printer to dispense picoliter droplets on demand. *RSC Adv.* **8**, 14765–14774 (2018).

197. Wacker Chemie AG. ACEO® - Unique Drop on Demand Technology. Available at: https://www.aceo3d.com/technology/. (Accessed: 13th December 2018)

198. ACEO. 3D printing with silicones IMAGINE …. (2018). Available at: https://s27714.pcdn.co/wp-content/uploads/2018/07/ACEO-Flyer_Imagine_RGB.pdf. (Accessed: 22nd December 2018)

199. Wacker Chemie AG. ACEO® Introduces 20 Shore A for Silicone 3D Printing. (2018). Available at: https://www.aceo3d.com/shore-a/. (Accessed: 14th December 2018)

200. Wacker Chemie AG. ACEO® Introduces 3D Printing With Electrically Conductive Silicone Rubber. (2018). Available at: https://www.aceo3d.com/aceo-introduces-3d-printing-with-electrically-conductive-silicone-rubber/. (Accessed: 12th December 2018)

201. Reitelshöfer, S. *et al.* Aerosol-Jet-Printing silicone layers and electrodes for stacked dielectric elastomer actuators in one processing device. in *SPIE Proc.* (eds. Bar-Cohen, Y. & Vidal, F.) 97981Y (2016). doi:10.1117/12.2219226

202. Deegan, R. D. *et al.* Capillary flow as the cause of ring stains from dried liquid drops. *Nature* **389**, 827–829 (1997).

203. Schlatter, S., Rosset, S., McCoul, D. & Shea, H. *Fully inkjet printed dielectric elastomer actuator with 5 μm thick silicone membrane.* (presented at SPIE EAPAD, 2018).

204. Reitelshofer, S., Landgraf, M., Graf, D., Bugert, L. & Franke, J. A new production process for soft actuators and sensors based on dielectric elastomers intended for safe human robot interaction. in *2015 IEEE/SICE International Symposium on System Integration (SII)* 51–56 (IEEE, 2015). doi:10.1109/SII.2015.7404953

205. Mahajan, A., Daniel Frisbie, C. & Francis, L. F. Optimization of Aerosol Jet Printing for High-Resolution, High-Aspect Ratio Silver Lines. (2013). doi:10.1021/am400606y

206. Vaezi, M., Chianrabutra, S., Mellor, B. & Yang, S. Multiple material additive manufacturing – Part 1: a review. *Virtual Phys. Prototyp.* **8**, 19–50 (2013).

207. Dolinski, N. D. *et al.* Solution Mask Liquid Lithography (SMaLL) for One-Step, Multimaterial 3D Printing. *Adv. Mater.* **30**, 1800364 (2018).

208. Han, D. *et al.* Soft Robotic Manipulation and Locomotion with a 3D Printed Electroactive Hydrogel. *ACS Appl. Mater. Interfaces* **10**, 17512–17518 (2018).

209. Tumbleston, J. R. *et al.* Continuous liquid interface production of 3D objects. *Science* **347**, 1349–1352 (2015).

210. Hummers, W. S. & Offeman, R. E. Preparation of Graphitic Oxide. *J. Am. Chem. Soc.* **80**, 1339–1339 (1958).

211. Pei, S. & Cheng, H.-M. The reduction of graphene oxide. *Carbon N. Y.* **50**, 3210–3228 (2012).

212. Wu, Y. *et al.* Characterization of CVD graphene permittivity and conductivity in micro-/millimeter wave frequency range. *AIP Adv.* **6**, 095014 (2016).

213. Guerrero-Contreras, J. & Caballero-Briones, F. Graphene oxide powders with different oxidation degree, prepared by synthesis variations of the Hummers method. *Mater. Chem. Phys.* **153**, 209–220 (2015).

214. Marcano, D. C. *et al.* Improved Synthesis of Graphene Oxide. *ACS Nano* **4**, 4806–4814 (2010).

215. Zhang, Y. *et al.* Direct imprinting of microcircuits on graphene oxides film by femtosecond laser reduction. *Nano Today* **5**, 15–20 (2010).

216. Gao, W. *et al.* Direct laser writing of micro-supercapacitors on hydrated graphite oxide films. *Nat. Nanotechnol.* **6**, 496–500 (2011).

217. Zhou, Y. *et al.* Microstructuring of Graphene Oxide Nanosheets Using Direct Laser Writing. *Adv. Mater.* **22**, 67–71 (2010).

218. Deng, N.-Q. *et al.* Tunable graphene oxide reduction and graphene patterning at room temperature on arbitrary substrates. *Carbon N. Y.* **109**, 173–181 (2016).

219. El-Kady, M. F., Strong, V., Dubin, S. & Kaner, R. B. Laser Scribing of High-Performance and Flexible Graphene-Based Electrochemical Capacitors. *Science* **335**, 1326–1330 (2012).

220. El-Kady, M. F. & Kaner, R. B. Scalable fabrication of high-power graphene micro-supercapacitors for flexible and on-chip energy storage. *Nat. Commun.* **4**, 1475 (2013).

221. Strong, V. *et al.* Patterning and Electronic Tuning of Laser Scribed Graphene for Flexible All-Carbon Devices. *ACS Nano* **6**, 1395–1403 (2012).

222. Tian, H. *et al.* Scalable fabrication of high-performance and flexible graphene strain sensors. *Nanoscale* **6**, 699–705 (2014).

223. Tian, H. *et al.* A Graphene-Based Resistive Pressure Sensor with Record-High Sensitivity in a Wide Pressure Range. *Sci. Rep.* **5**, 8603 (2015).

224. Griffiths, K. *et al.* Laser-scribed graphene presents an opportunity to print a new generation of disposable electrochemical sensors. *Nanoscale* **6**, 13613–13622 (2014).

225. Tian, H. *et al.* Wafer-scale integration of graphene-based electronic, optoelectronic and electroacoustic devices. *Sci. Rep.* **4**, 3598 (2014).

226. Tian, H. *et al.* Cost-effective, transfer-free, flexible resistive random access memory using laser-scribed reduced graphene oxide patterning technology. *Nano Lett.* **14**, 3214–3219 (2014).

227. Tian, H. *et al.* Graphene Earphones: Entertainment for Both Humans and Animals. *ACS Nano* **8**, 5883–5890 (2014).

228. Tao, L. Q. *et al.* Novel electron devices based on laser scribed graphene. in *China Semiconductor Technology International Conference 2017, CSTIC 2017* 1–4 (IEEE, 2017). doi:10.1109/CSTIC.2017.7919877

229. Park, S., Lee, H., Kim, Y.-J. & Lee, P. S. Fully laser-patterned stretchable microsupercapacitors integrated with soft electronic circuit components. *NPG Asia Mater.* **10**, 959–969 (2018).

230. Le, T.-S. D., An, J. & Kim, Y.-J. Fabrication of graphene-based stretchable strain sensors using femtosecond laser direct writing. in *Proceedings of the 3rd International Conference on Progress in Additive Manufacturing (Pro-AM 2018)* 482–486 (2018). doi:10.25341/D4N30Q

231. Dinh Le, T.-S., An, J. & Kim, Y.-J. Femtosecond laser direct writing of graphene oxide film on polydimethylsiloxane (PDMS) for flexible and stretchable electronics. in *2017 Conference on Lasers and Electro-Optics Pacific Rim (CLEO-PR)* 1–4 (IEEE, 2017). doi:10.1109/CLEOPR.2017.8118629

232. Qiao, Y. *et al.* Multilayer Graphene Epidermal Electronic Skin. *ACS Nano* **12**, 8839–8846 (2018).

233. Lin, J. *et al.* Laser-induced porous graphene films from commercial polymers. *Nat. Commun.* **5**, 5714 (2014).

234. Li, L. *et al.* High-Performance Pseudocapacitive Microsupercapacitors from Laser-Induced Graphene. *Adv. Mater.* **28**, 838–845 (2016).

235. Luong, D. X. *et al.* Laminated Object Manufacturing of 3D-Printed Laser-Induced Graphene Foams. *Adv. Mater.* **30**, 1707416 (2018).

236. Rahimi, R., Ochoa, M., Yu, W. & Ziaie, B. Highly Stretchable and Sensitive Unidirectional Strain Sensor via Laser Carbonization. *ACS Appl. Mater. Interfaces* **7**, 4463–4470 (2015).

237. Chyan, Y. *et al.* Laser-Induced Graphene by Multiple Lasing: Toward Electronics on Cloth, Paper, and Food. *ACS Nano* **12**, 2176–2183 (2018).

238. Khorasani, M. T., Mirzadeh, H. & Sammes, P. G. Laser induced surface modification of polydimethylsiloxane as a super-hydrophobic material. *Radiat. Phys. Chem.* **47**, 881–888 (1996).

239. Graubner, V.-M. *et al.* Local chemical transformations in poly(dimethylsiloxane) by irradiation with 248 and 266nm. *Appl. Surf. Sci.* **252**, 4781–4785 (2006).

240. Dupas-Bruzek, C., Robbe, O., Addad, A., Turrell, S. & Derozier, D. Transformation of medical grade silicone rubber under Nd:YAG and excimer laser irradiation: First step towards a new miniaturized nerve electrode fabrication process. *Appl. Surf. Sci.* **255**, 8715–8721 (2009).

241. Atanasov, P. A. *et al.* Fs-laser processing of medical grade polydimethylsiloxane (PDMS). *Appl. Surf. Sci.* **374**, 229–234 (2016).

242. Wang, J.-N. *et al.* Wearable Superhydrophobic Elastomer Skin with Switchable Wettability. *Adv. Funct. Mater.* 1800625 (2018). doi:10.1002/adfm.201800625

243. Hautefeuille, M. *et al.* New perspectives for direct PDMS microfabrication using a CD-DVD laser. *Lab Chip* **13**, 4848 (2013).

244. Alcántara, J. C. C., Cerda Zorrilla, M., Cabriales, L., Rossano, L. M. L. & Hautefeuille, M. Low-cost formation of bulk and localized polymer-derived carbon nanodomains from polydimethylsiloxane. *Beilstein J. Nanotechnol.* **6**, 744–8 (2015).

245. González-Vázquez, M. & Hautefeuille, M. Controlled Solvent-Free Formation of Embedded PDMS-Derived Carbon Nanodomains with Tunable Fluorescence Using Selective Laser Ablation with A Low-Power CD Laser. *Micromachines* **8**, 307 (2017).

246. Kuhnel, D. T., Rossiter, J. M. & Faul, C. F. J. 3D printing with light: Towards additive manufacturing of soft, electroactive structures. in *Proceedings of SPIE - The International Society for Optical Engineering* **10594**, (2018).

247. Gao, Y. *et al.* Laser Direct Writing of Ultrahigh Sensitive SiC-Based Strain Sensor Arrays on Elastomer toward Electronic Skins. *Adv. Funct. Mater.* **29**, 1806786 (2018).

248. Kuhnel, D. T., Rossiter, J. M. & Faul, C. F. J. Laser-Scribed Graphene Oxide Electrodes for Soft Electroactive Devices. *Adv. Mater. Technol.* **4**, 1800232 (2019).

249. Lerf, A., He, H., Forster, M. & Klinowski, J. Structure of Graphite Oxide Revisited. *J. Phys. Chem. B* **102**, 4477–4482 (1998).

250. Ferrari, A. C. & Robertson, J. Interpretation of Raman spectra of disordered and amorphous carbon. *Phys. Rev. B* **61**, 14095 (2000).

251. King, A. A. K. *et al.* A New Raman Metric for the Characterisation of Graphene oxide and its Derivatives. *Sci. Rep.* **6**, 19491 (2016).

252. T. Szabó *et al.* Evolution of Surface Functional Groups in a Series of Progressively Oxidized Graphite Oxides. *Chem. Mater.* **18**, 2740–2749 (2006).

253. Zhang, J. *et al.* Reduction of graphene oxide via L-ascorbic acid. *Chem. Commun. (Camb).* **46**, 1112–4 (2010).

254. Khodaparast, P., Ghaffarian, S. R., Khosroshahi, M. R., Yousefimehr, N. & Zamani, D. Electrode structures in high strain actuator technology. *J. Optoelectron. Adv. Mater.* **9**, 3585–3591 (2007).

255. C&M Rubber Co. Elastomer Compatibility Chart. (2009). Available at: http://www.cmrubber.com/wp-content/uploads/Elastomer-Compatibility-Chart.pdf.

256. Lee, Y. R., Kwon, H., Lee, D. H. & Lee, B. Y. Highly flexible and transparent dielectric elastomer actuators using silver nanowire and carbon nanotube hybrid electrodes. *Soft Matter* **13**, 6390–6395 (2017).

257. O'Halloran, A. *et al.* A review on dielectric elastomer actuators, technology, applications, and challenges. *J. Appl. Phys.* **104**, 071101 (2008).

258. Yen, T. M. *et al.* Reversing Coffee-Ring Effect by Laser-Induced Differential Evaporation. *Sci. Rep.* **8**, 3157 (2018).

259. Rosset, S., de Saint-Aubin, C., Poulin, A. & Shea, H. R. Assessing the degradation of compliant electrodes for soft actuators. *Rev. Sci. Instrum.* **88**, 105002 (2017).

260. Cruz-Ramírez, A. *et al.* Progress on the Use of Commercial Digital Optical Disc Units for Low-Power Laser Micromachining in Biomedical Applications. *Micromachines* **9**, 187 (2018).

261. Camino, G., Lomakin, S. . & Lazzari, M. Polydimethylsiloxane thermal degradation Part 1. Kinetic aspects. *Polymer (Guildf).* **42**, 2395–2402 (2001).

262. Stabler, C., Ionescu, E., Graczyk-Zajac, M., Gonzalo-Juan, I. & Riedel, R. Silicon oxycarbide glasses and glass-ceramics: "All-Rounder" materials for advanced structural and functional applications. *J. Am. Ceram. Soc.* **101**, 4817–4856 (2018).

263. Kim, K. J., Eom, J.-H., Kim, Y.-W. & Seo, W.-S. Electrical conductivity of dense, bulk silicon-oxycarbide ceramics. *J. Eur. Ceram. Soc.* **35**, 1355–1360 (2015).

264. Lide, D. R. *CRC Handbook of Chemistry and Physics, Internet Version 2005.* (CRC Press, Boca Raton, FL, 2005). doi:10.1016/0165-9936(91)85111-4

265. Ringdalen, E. & Tangstad, M. Softening and Melting of SiO2, an Important Parameter for Reactions with Quartz in Si Production. in *Advances in Molten Slags, Fluxes, and Salts: Proceedings of the 10th International Conference on Molten Slags, Fluxes and Salts 2016* 43–51 (Springer International Publishing, 2016). doi:10.1007/978-3-319-48769-4_4

266. Khavryuchenko, V. D., Khavryuchenko, O. V. & Lisnyak, V. V. Formation of Pyrogenic Silica: Spectroscopic and Quantum Chemical Insight. *Crit. Rev. Solid State Mater. Sci.* **36**, 47–65 (2011).

267. Newbury, D. E. & Ritchie, N. W. M. Is Scanning Electron Microscopy/Energy Dispersive X-ray Spectrometry (SEM/EDS) Quantitative? *Scanning* **35**, 141–168 (2013).

268. Thomas, T. R. Characterization of surface roughness. *Precis. Eng.* **3**, 97–104 (1981).

269. Heaney, M. B. Electrical Conductivity and Resistivity. in *Electrical Measurement, Signal Processing, and Displays* (ed. Webster, J. G.) (CRC Press, 2003).

270. Miccoli, I., Edler, F., Pfnür, H. & Tegenkamp, C. The 100th anniversary of the four-point probe technique: the role of probe geometries in isotropic and anisotropic systems. *J. Phys. Condens. Matter* **27**, 223201 (2015).

271. Ossila. Sheet Resistance: A Guide to Theory. Available at: https://www.ossila.com/pages/sheet-resistance-theory. (Accessed: 15th January 2019)

272. Brennan, K. F. *Introduction to Semiconductor Devices*. (Cambridge University Press, 2005). doi:10.1017/CBO9781139171373

273. Trujillo-Pino, A., Krissian, K., Alemán-Flores, M. & Santana-Cedrés, D. Accurate subpixel edge location based on partial area effect. *Image Vis. Comput.* **31**, 72–90 (2013).

274. Jokinen, V., Suvanto, P. & Franssila, S. Oxygen and nitrogen plasma hydrophilization and hydrophobic recovery of polymers. *Biomicrofluidics* **6**, 16501–1650110 (2012).

275. Owen, M. J. & Smith, P. J. Plasma treatment of polydimethylsiloxane. *J. Adhes. Sci. Technol.* **8**, 1063–1075 (1994).

276. Gómez-García, M., Ochoa-Alejo, N., Gómez-García, M. D. R. & Ochoa-Alejo, N. Biochemistry and Molecular Biology of Carotenoid Biosynthesis in Chili Peppers (Capsicum spp.). *Int. J. Mol. Sci.* **14**, 19025–19053 (2013).

277. Racles, C., Cozan, V., Bele, A. & Dascalu, M. Polar silicones: structure-dielectric properties relationship. *Des. Monomers Polym.* **19**, 496–507 (2016).

278. Santa Cruz Biotechnology, I. Disperse Red 1 Material Safety Data Sheet. *2010* Available at: http://datasheets.scbt.com/sc-214922.pdf. (Accessed: 29th May 2019)

279. ZMorph. ZMorph VX Multitool printer. Available at: https://zmorph3d.com/product/zmorph-vx. (Accessed: 21st May 2019)

280. SNAPMAKER. SNAPMAKER THE 3-IN-1 3D PRINTER. Available at: https://snapmaker.com/. (Accessed: 21st May 2019)

281. Wijnen, B., Hunt, E. J., Anzalone, G. C. & Pearce, J. M. Open-source syringe pump library. *PLoS One* **9**, 1–8 (2014).

282. Structur3D Printing. Discov3ry Paste Extruder. Available at: https://www.structur3d.io/#discov3ry. (Accessed: 21st May 2019)

283. Henri Cholet. *Progressing Cavity Pumps*. (Éditions Technip, 1997).

284. ViscoTec. preeflow eco-PEN300. Available at: https://www.preeflow.com/media/eco-pen300_EN.pdf. (Accessed: 21st May 2019)

285. Duduta, M., Wood, R. J. & Clarke, D. R. Flexible, stretchable electroadhesives based on acrylic elastomers. in *Electroactive Polymer Actuators and Devices (EAPAD)* (eds. Bar-Cohen, Y. & Vidal, F.) **9798**, 97981D (2016).

286. Thingiverse. Octopus Resculpt by Geoffro. (2014). Available at: https://www.thingiverse.com/thing:374048. (Accessed: 21st May 2019)

287. DURAN. DURAN - Microscope slides. Available at: http://www.duran-group.com/en/products-solutions/laboratory-glassware/products/glasware-for-microbiology/microscope-slides.html. (Accessed: 7th May 2019)

288. Supplies, S. SPI Supplies Quartz Microscope Slide, 1 x 3 in. x 1 mm Thick. Available at: https://www.2spi.com/item/01018-ab/quartz-slides-ge124/. (Accessed: 7th May 2019)

289. MOMENTIVE. Silopren UV Electro 235-2 and UV Electro 225-1 Technical Data Sheet. (2016). Available at: https://www.momentive.com/en-us/products/tds/silopren-uv-electro-235-2-and-uv-electro-225-1/. (Accessed: 22nd October 2018)

290. Badran, H. A., Taha, A. Y., Abdulkader, A. F. & Emshary, C. A. Preparation and Study of the Electrical and Optical Properties of a New Azo Dye (4-Acetaminophenol – [2- (4-Azo)] -4- Amino Dipheyl Sulfone). *J. Ovonic Res.* **8**, 161–170 (2012).

291. Precision Piezo. Precision Piezo Z probe kit. Available at: https://www.precisionpiezo.co.uk/product-page/precision-piezo-orion-kit. (Accessed: 20th May 2019)

292. Rosset, S., Araromi, O. A., Schlatter, S. & Shea, H. R. Fabrication Process of Silicone-based Dielectric Elastomer Actuators. *J. Vis. Exp.* e53423 (2016). doi:10.3791/53423